Characterization of Tearing Mode Dynamics with the Radial Interferometer-Polarimeter on DIII-D

by

Rachel A. Myers

A dissertation submitted in partial fulfillment of the requirements for the degree of Doctor of Philosophy

(Physics)

at the

UNIVERSITY OF WISCONSIN–MADISON
2025

Date of final oral examination: 08/08/25

The dissertation is approved by the following members of the Final Oral Committee:

John S. Sarff, Professor, Physics

Brett E. Chapman, Scientist, Physics

Paul W. Terry, Professor, Physics

Benedikt Geiger, Associate Professor, Nuclear Engineering and Engineering Physics

We choose to go to the Moon in this decade and do the other things, not because they are easy, but because they are hard.

— President John F. Kennedy

Abstract

The Radial Interferometer-Polarimeter (RIP) diagnostic on the DIII-D tokamak measures density and magnetic fluctuations throughout the plasma. RIP is particularly useful for detecting core-resonant tearing modes, a potentially dangerous magnetic instability. These modes may not be detected with external sensing coils. Mode amplitudes measured with RIP are compared to those measured with sensing coils and to the output of a linear magnetohydrodynamic stability model that allows inclusion of toroidicity and shaping. Due to its line-averaged nature, RIP cannot detect fluctuations with even poloidal mode number, m. It is confirmed that RIP measures even-m modes through their odd-m sidebands, which are generated by toroidicity and shaping.

Results of a DIII-D experiment measuring shaping effects on RIP measurements and tearing stability at low elongation are presented. These plasmas were dominated by the sawtooth instability, which was expected to trigger tearing modes but did not. Tearing mode appearance was uncommon but tearing modes that did appear were associated with current gradients. Even-m modes were easily measured by RIP because toroidicity induced strong, detectable odd-m sidebands. Odd-m modes were weaker than previously measured, hypothesized to be due to low elongation. Internal measurements show that toroidicity and shaping significantly contribute to RIP-measured mode structure and stability.

ITER and reactors must avoid bursty edge localized modes (ELMs) that may damage plasma-facing components. QH-mode, an advanced scenario, is attractive because it suppresses ELMs via the edge harmonic oscillation (EHO), another magnetic fluctuation. Using RIP and other diagnostics, it is confirmed experimentally that EHO components are non-

linearly coupled throughout QH-mode. This coupling matches simulations predicting that coupling sustains the EHO. When core-resonant tearing modes are present, RIP, but not sensing coils, detects nonlinear coupling between the tearing modes and the EHO. The EHO is interrupted, which prevents access to long-lived QH-mode. These results illustrate that nonlinear coupling sustains the EHO and provide the first evidence that core-resonant tearing modes can modify QH-mode development. Preventing core-edge coupling may help make QH-mode and other advanced scenarios more robust.

Dedicated to the memory of

Joseph K. Myers III

1958–2025

Sarah M. Bailey

1933–2025

Acknowledgments

It's been a long time. Ten years ago, I came into the UW physics department not knowing what I was doing. Five years ago, I thought I had no choice but to leave physics for good. Three years ago, I somehow found myself back here. Now I've made it. It still seems impossible. I'm sure I've missed some people, but I'll do my best to thank everyone who deserves it. I couldn't have done it without such a good group of people around me.

My utmost thanks go out to my faculty advisor, John Sarff, and my PI, Brett Chapman. You took a chance on me and gave me an opportunity that I couldn't have found in any other group. Then, you pushed me to keep learning and progressing while still remaining kind and supportive. It is that balance that has gotten me where I am now. John, I'm thankful for our long meetings spent hammering out concepts I needed to know and going back and forth on on exactly what I was seeing. Brett, thank you for pushing me to put myself out there with my run time and travel to San Diego, and for bringing together such an encouraging and active research group.

Thank you to Paul Terry and Benedikt Geiger for taking the time to serve on my committee and read my thesis, and for your helpful comments. Paul, thank you also for interesting conversations on nonlinear interactions. I would like to thank Carl Sovinec and Dan Mc-Cammon for serving on my prelim committee, and Carl for your help with tearing modes.

To the other members of the UW-D3D group: Karsten, thank you for being involved alongside Brett and John in bringing me into the group, and for asking the hard questions I needed to be able to answer. Mihir and Ruifeng, thank you also for your interest, commentary on talks, papers, and other research, and for working with me in San Diego. I especially

appreciated all your contributions to my experiment.

To my other coauthors, collaborators, and mentors: to the UCLA team, particularly David Brower, Jie Chen, and Weixing Ding, for implementing, operating, and maintaining RIP and for coauthoring all my RIP work. Your contributions keep our research going. To Brian Victor of LLNL, for serving as my mentor during the SCGSR program, for being willing to make time for me, and for teaching me kineticEFIT and DCON even when we had to work out solutions off the cuff. To Richard Fitzpatrick of UT-Austin, for showing me TJ, being so responsive to my questions, and even updating TJ to be more useful for comparing to RIP. To Xi Chen and Zeyu Li of General Atomics, for sparking my interest in QH-mode, interpreting my nonlinear coupling data, and coauthoring my nonlinear coupling paper that forms much of Chapter 6. I look forward to working with you starting in the fall.

To those outside the UW group who lent your time to help me on my DIII-D run day(s): Tyler Cote as chief operator; Jayson Barr, James Yang, and Matthias Knolker as physics operators; Al Hyatt as beam programmer along with Brian again; Nathan Richner as magnetics lead; Tom Benedett of the UCLA-RIP team as RIP operator; and Max Austin and Auna Moser as run coordinators and for fighting to get me contingency time. Thank you for working with me and helping me problem-solve when things went awry. Also to all the DIII-D staff and technicians whose names I may not know or have forgotten, because you are just as vital to operations.

To those who have offered comments, provided help, or answered my questions: everyone I mentioned above, plus Alessandro Bortolon, William Boyes, Keith Burrell, Jim Callen, Jeremy Hanson, Gerrit Kramer, Rob La Haye, Nik Logan, George McKee, Sam Stewart, and Theresa Wilks, to name as many as I can.

To the opportunities that let me spend time at DIII-D: the DIII-D PhD runtime allocation, the Department of Energy Office of Science Graduate Student Research (SCGSR) program for funding and mentorship opportunities in kEFIT and DCON, and to the Wisconsin Physics Department awards committee and Graduate School for travel grants.

To DIII-D itself: being able to spend nine months on site was a formative and integral part of my experience with this group and of my scientific career. I learned the ins and outs of working in a large lab and discovered that I could not have found a better environment. Science is a team enterprise. The ability to walk down the hall and ask a question or chat with someone at the SET meeting was invaluable. Thank you also to the other grad students, postdocs, and scientists for being so welcoming, with particular thanks to the volleyball crew for not judging me too much and to Nathan and Tyler for being familiar Wisconsin faces.

To the Egedal group on TREX/BRB, my first research group here: Jan, Joe, Sam, Emily, Blake, Harsha, and Alex, you taught me how to be a physicist. Though my time in the group didn't work out, I still carry with me those skills. I would also like to thank Michelle Holland for guiding me through the process of leaving, Sharon Kahn for doing the same when I returned, and Lisa Everett and Ellen Zweibel for advocating for me.

To my friends for inspiring and rooting for me, most of all the Westport crew. Tessa, Grace, Jesse Alan, Elizabeth, and Emily, I'm glad we've made it after all this time. I'm so proud of you all. Here's to many more years.

To my family and those who might as well be family. To Estela and Jorge for taking me in as though I were your own child, especially in summer 2020. To Grandma and the rest of my extended family, for always wanting to hear about my work and asking great questions. To Hannah and Christian for your support, care, and enthusiasm for what I'm doing, even when I get annoying about it. To Mom, for taking care of me every step of the way, for being a listening ear in every possible situation, for being so tough, and for helping me be tough. To Dad, for nurturing my intellectual curiosity from the very earliest, for always looking out for me, and for challenging me when I needed it. I miss you so much. Love you forever.

Lastly, to Edward, for being there when I needed you. You believed in me the whole time, even when I didn't believe in myself. You were right. Thank you.

Contents

1	Intr	roduction		
	1.1	The Climate Crisis and Fusion Power	1	
	1.2	Tokamaks and DIII-D	7	
	1.3	Thesis Outline and Key Results	11	
2	Mac	croscopic MHD Instabilities in Tokamaks	17	
	2.1	MHD Equilibrium	18	
	2.2	Ideal Instabilities	24	
	2.3	Resistive Instabilities	29	
	2.4	Nonlinear Mode Coupling	34	
3	Rele	evant Diagnostics and Analysis Tools	41	
	3.1	DIII-D Primary Diagnostics	43	
	3.2	Polarimetry-Interferometry	50	
	3.3	The Radial Interferometer-Polarimeter	55	
	3.4	Computational Tools	60	
		3.4.1 TJ	60	
		3.4.2 EFIT	62	
		3.4.3 DCON	63	
4	Mo	de Detection with RIP and Line-Integration Effects	72	
	4.1	RIP Data and Amplitude Calculations	73	

	4.2	2 Tearing Mode Structure Models	
		4.2.1 Analytic Tearing Mode Structure Model	79
		4.2.2 Linear Computational Tearing Mode Structure Model	82
		$4.2.3 \hbox{Model Comparisons and Shape Effects on Synthetic Eigenfunctions} .$	90
	4.3	Mode Number Effects on RIP Amplitudes	102
	4.4	Additional Mode Detection with RIP	111
		4.4.1 Expanded Mode Detection	111
		4.4.2 ELM Detection	113
5	Plas	sma Shaping, Rotation, and $m, n > 2, 1$ Tearing Mode Origins	119
	5.1	Motivation	120
	5.2	Experimental Approach and Outcomes	121
		5.2.1 Experimental Summary	121
		5.2.2 Data Evaluation	130
	5.3	Tearing Mode and Sawtooth Stability	138
	5.4	Plasma Shape and Mode Detection	150
6	Det	ection and Role of Nonlinear Coupling in QH-Mode Development	167
	6.1	QH-Mode and the EHO	168
	6.2	Bicoherence Analysis	170
	6.3	Nonlinear Coupling Between Edge Harmonics	173
	6.4	EHO and Mode Identification in Post-QH-Mode	178
	6.5	Coupling to Tearing Modes Interrupting EHO Development	184
7	Con	nclusions	194
	7.1	Summary	194
	7.2	Future Work	199
${f A}$	Res	ources and Shot Plan: 2024-34-03	206

B Database Spreadsheet: 2024-34-03

213

Chapter 1

Introduction

This chapter provides a brief motivation for nuclear fusion as an essentially limitless, carbon-free energy source. It introduces the physics of fusion energy along with the current state of research in the field and inherent challenges to deploying power to the grid. The tokamak configuration and the DIII-D fusion research facility, experiments on which form the basis of this thesis, and their significance to the fusion community are described. Lastly, I provide an outline of this thesis and enumerate the most important results therein.

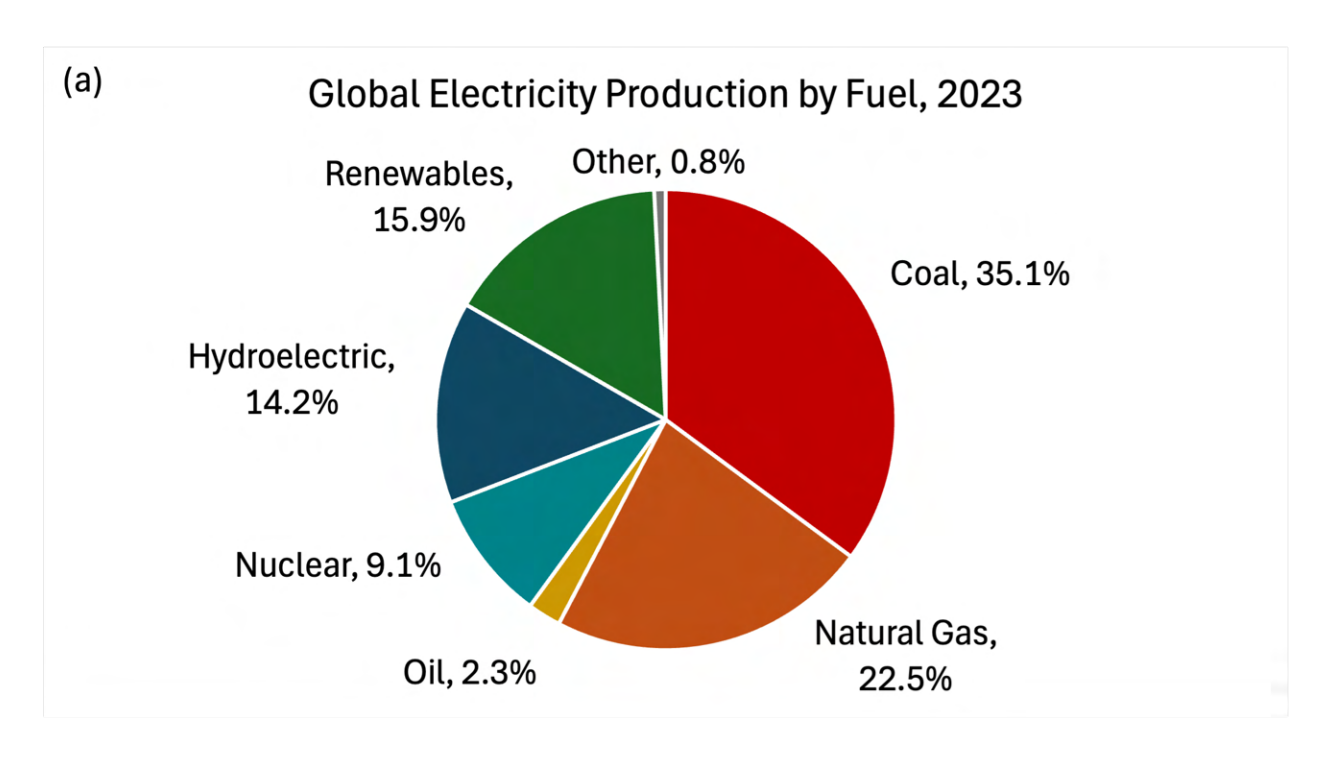
1.1 The Climate Crisis and Fusion Power

Global warming due to the greenhouse effect, induced by human emission of so-called "greenhouse gases" that trap heat in the atmosphere, is one of the foremost concerns facing all life on Earth. Already, global temperatures have risen nearly 1.5°C [1] since the beginning of the industrial era. This has resulted in sea level rises due to melting ice caps, increased frequency of severe weather events, and widespread damage to ecosystems. Combustion of hydrocarbons, or fossil fuels, such as oil, coal, and natural gas for electricity, transportation and heating produces carbon dioxide (CO₂), which is the cause of 65% of human-caused warming thus far [2]. In addition, burning of fossil fuels releases other pollutants into the atmosphere. These include, for example, sulfur dioxide and nitrogen oxide, which cause acid rain [3]. To restrict potential warming to under 2°C, a limit above which much more severe

environmental disasters are expected to occur [4], a major decarbonization of society must take place. Here I discuss the decarbonization of electricity generation as opposed to other sources of carbon emissions.

In 2023, 60% of global electricity production was derived from fossil fuels, and in the United States of America, this figure was very similar at 59.9% [5]. The remainder was derived from renewable sources such as hydroelectric, wind, and solar power as well as nuclear (fission) power and a very small amount of uncategorized generation. Figure 1.1 charts percentages of electricity production for both the world and the US by fuel. Renewable energy, particularly wind and solar, has grown dramatically in capacity since 2000 [6] and shows much promise, but concerns remain. Wind and solar are intermittent, with electricity generation limited by time of day and weather conditions. While energy storage can alleviate some of this burden, it is advantageous for the power grid to have some level of firm capacity. Firm capacity is the amount of electricity a utility can guarantee will be supplied to consumers. Firm capacity at the moment is often provided by fossil fuels, which emit carbon into the atmosphere, or hydroelectric power, new sites for which are growing increasingly difficult to implement. The third main source of firm capacity, which like hydro is carbon-free, is nuclear fission power. Nuclear fission power, produced from the splitting of heavy nuclei such as uranium, can play a beneficial role in the decarbonization process. It is highly efficient and, on average, safer to run than fossil fuels [7]. However, fission still poses concerns of long-lived radioactive waste, pollution from mining, limited fuel supply, and weapons proliferation [8, 9]. Nuclear fusion power, in contrast, poses less concern in all of these categories but remains in the research stage because its scientific challenges are far greater than fission's.

Nuclear fusion is the process that fuels the Sun and other stars. When light elements fuse to form heavier elements with a smaller combined mass and binding energy, the remaining energy is released according to Einstein's equation $\Delta E = \Delta mc^2$. The most easily achievable



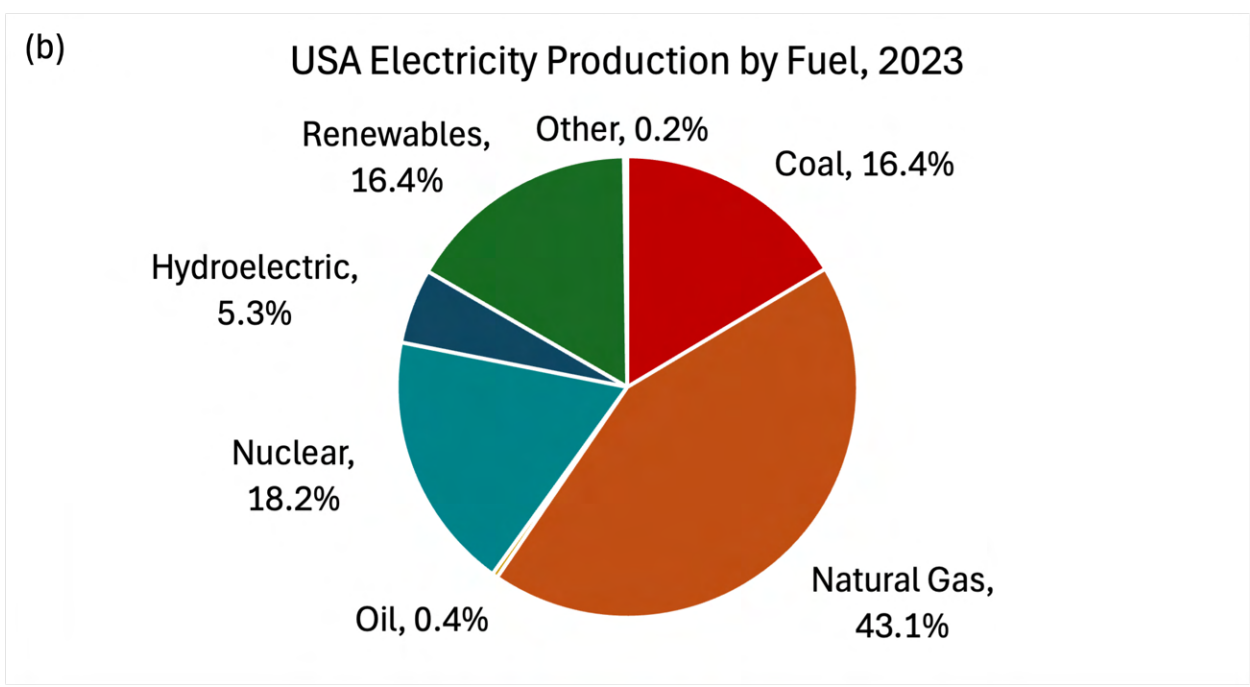


Figure 1.1: (a) Percentage of electricity generation by fuel worldwide in 2023. (b) Percentage of electricity generation by fuel in the USA in 2023. All data taken from [5].

fusion reactions on Earth using current technology are:

$$D + T = {}^{4}He + n + 17.6 \text{ MeV}$$
 (1.1)

$$D + D = T + p + 4.03 \text{ MeV}$$
 (1.2)

$$D + D = {}^{3}He + n + 3.27 \text{ MeV},$$
 (1.3)

with the frequency of each reaction depending on the mix of fuels used. Here, p is the proton, n is the neutron, D is deuterium, and T is tritium. Deuterium is the isotope of hydrogen with one proton and one neutron; tritium is the isotope with one proton and two neutrons. Other reactions such as D-3He are being considered for far-future devices but require temperatures unachievable at this time. After fusion was first harnessed in the form of thermonuclear weapons, it was quickly realized that the energy yields from fusion were superior even to those from fission. In addition, fusion neither requires nor produces long-lived radioactive isotopes. Tritium is radioactive, but its half-life is 12.3 years [10]. Tritium stored at a reactor for fuel or produced on-site would be expected to decay to harmless levels within decades instead of millennia. Deuterium is much less common than ordinary hydrogen but is nevertheless abundant enough to supply the power needs of humanity for billions of years if extracted from seawater. Tritium is artificially produced from lithium, which is also abundant.

Fusion requires relatively stringent conditions to occur in a controlled environment. To overcome the Coulomb forces repelling the like charges of two nuclei and bring them close enough for the strong nuclear force to pull them together, they must be moving very quickly and therefore be at very high temperature. At this temperature, the fusing elements necessarily form a plasma, an ionized gas where electrons have been stripped from the nuclei. The basic question underlying fusion is how to confine the plasma for long enough, and at high enough temperatures, to produce net power. A basic figure of merit for net fusion power output is the Lawson criterion $n_e \tau_E \geq 1.5 \times 10^{20} \text{ m}^{-3} \cdot \text{s}$. Here, n_e is the electron density and

 τ_E is the energy confinement time. A more useful figure of merit $n_e T_e \tau_E$ incorporates the temperature T, since density and temperature can be independently varied in experiments. The criterion for this triple product is $n_e T \tau_E \geq 3 \times 10^{21} \text{ keV} \cdot \text{m}^{-3} \cdot \text{s}$ [11]. Note that T here is the temperature of the ions. The electrons and ions may have different average energies, since electrons and ions are heated by different mechanisms in a reactor and may not have time to equilibrate. The Lawson criterion and triple product vary based on temperature and reaction as shown in Fig. 1.2; for both D-T and D-D fuel, the threshold triple product is minimized at temperatures on the order of 10 kilo-electronvolts (keV) or 100 million kelvin. All is not always well, even if a plasma is both hot and dense. Recall that heating and fueling are only part of the question of achieving the Lawson criterion. The last, trickiest parameter is τ_E , the energy confinement time. Energy confinement time is calculated as

$$\frac{W}{P_{loss}} = \frac{W}{P - \frac{\mathrm{d}W}{\mathrm{d}t}},\tag{1.4}$$

where W is the total energy content of the plasma and P is the heating power, which is both externally driven and internally generated through fusion. Energy confinement time is simply a measure of how quickly energy is lost from the plasma. Device-specific concerns are discussed in Section 1.2, and several internal effects interfering with confinement are detailed in Chapter 2. Confining a very hot plasma for a sufficient length of time is a fundamental scientific and engineering question that drives much of fusion research.

Plasmas at the necessary temperatures to produce net power from fusion cannot be confined using material means and must be confined using externally-applied forces. Two primary methods exist for implementing appropriate confinement levels at scale for power applications. One is inertial confinement fusion (ICF), where fusion reactions are triggered either directly by lasers incident on a D-T pellet or indirectly using lasers to drive X-rays that are then incident on the pellet. ICF lasts a very short time, averting the need to maintain the plasma in place. The other method, which is discussed in this thesis, is magnetic confinement fusion. Since electrons and ions are separate in a plasma, it is composed of charged particles,

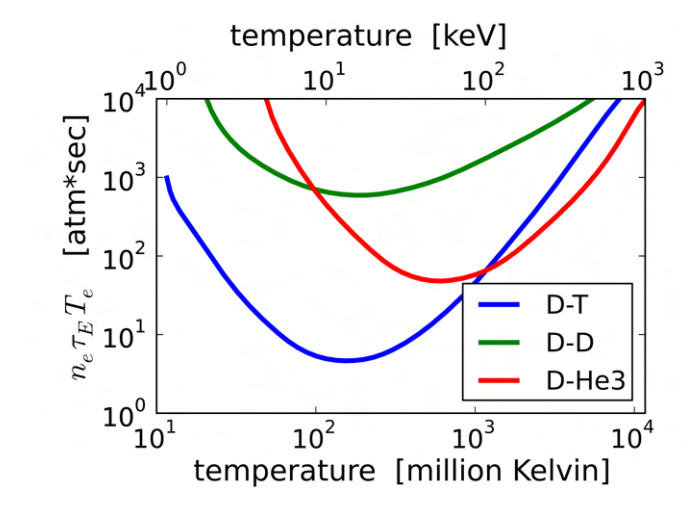


Figure 1.2: A plot of the Lawson triple product for the reactions listed in Equations 1.1-1.3 and the D-³He reaction. This figure assumes $T_e = T_i$. Figure property of D. Strozzi, data taken from [12].

which are then subject to magnetic forces and can be confined using magnetic fields. While magnetic confinement fusion has thus far not been scaled commercially, recent advances in science and technology indicate that despite the challenges facing magnetic fusion, a path forward exists. In this thesis, I investigate various concerns posed by magnetic instabilities, one issue plaguing magnetic confinement devices.

The most popular magnetic confinement configurations are the tokamak and the stellarator, the former of which is the subject of this thesis. Also mentioned is the reversed-field pinch (RFP), another toroidal fusion device that reverses the toroidal magnetic field within the plasma and drives current through a dynamo effect. The Madison Symmetric Torus is an example of a device that can operate with plasmas in the RFP configuration (it can also operate with tokamak plasmas). An important figure of merit in magnetically-confined fusion, aside from the Lawson criterion, is β , the ratio between plasma pressure and magnetic pressure:

$$\beta = \frac{nk_BT}{B^2/2\mu_0}. (1.5)$$

Higher β values are more cost-effective, since they are achieving better performance (pressure) for the same cost (applied magnetic field) [13]. However, a value of β that is too high

can also lead to instability [14, 15]. In tokamaks and in this thesis, β is typically represented as the normalized pressure β_N , which is calculated as follows:

$$\beta_N = \beta \frac{aB_t}{I_p},\tag{1.6}$$

where a is the minor radius, B_t is the toroidal magnetic field, and I_p is the plasma current. It is measured in percent: β_N of 0.03 is typically represented as $\beta_N = 3$.

1.2 Tokamaks and DIII-D

A tokamak [16], derived from a Russian acronym for "toroidal chamber with magnetic coils", is a magnetic confinement fusion device in the shape of a torus, or donut. It evolved from earlier cylindrical pinch designs. Magnetic pinches employ the Lorentz force to compress current-carrying materials such as wires or plasmas. The z-pinch, with current only in the axial (\hat{z}) direction, is at risk of kink-like distortions. Mechanisms for stabilizing the zpinch using internal flows are under development, but current experiments prioritize designs combining characteristics of the z-pinch with other magnetic configurations [17]. The θ pinch, with current only in the azimuthal $(\hat{\theta})$ direction, had very low confinement times. The screw pinch, formed by running currents (and therefore magnetic fields) in both the \hat{z} and $\hat{\theta}$ directions, was successful in creating better confinement with increased stability [18]. Due to its cylindrical shape, the screw pinch still had significant particle losses from its ends as the particles traveled along the field lines to the boundaries of the device. Eventually, it was decided to turn the cylinder in on itself so that escaping particles would remain inside the device; thus, the tokamak was born. The tokamak is at this time the magnetically confined fusion concept closest to reaching breakeven power; the Joint European Torus (JET) achieved a fusion power to auxiliary power ratio Q of approximately 0.67 [19]. The tokamaks SPARC, ARC, and ITER expect to reach Q > 1.

Toroidal (long way around the torus) and poloidal (short way around the torus) currents and magnetic fields are generated by coils outside the vessel. Radio-frequency heating also contributes to current drive, as do the ions that result from neutral beams entering the plasma. A current may also be driven internally; this is known as bootstrap current because it is generated without external contributions [20–22]. As particles travel along field lines, they may become trapped on the outboard side and bounce vertically up and down in so-called banana orbits [23]. Due to the curvature of the field lines, particles spend more time on the outside of the orbit than the inside, resulting in a radial density gradient and electric field pointing outward. The resultant particle motion induces a current. Interactions between trapped and passing particles confer energy to the passing particles and further allow current to develop. A significant fraction of current in future reactors must be bootstrap for them to achieve the required efficiency [22]. The bootstrap current can also drive instabilities [24].

Modern tokamaks typically operate in high-confinement mode, or H-mode. H-mode is induced by strong heating above a threshold that depends on plasma shape, density, and pressure [25]. It is distinguished from low-confinement mode, or L-mode, by increased heat and particle confinement times. In H-mode, temperature and pressure profiles are broad in the core and have a steep gradient near the edge, a formation called the pedestal. The pedestal is maintained by transport barriers that prohibit particle loss across the edge [26]. While H-mode has been very successful in improving plasma performance, it is not without its own issues, as shown in Chapter 2. H-mode is prone to edge instabilities that can damage plasma-facing components, redistribute energy, and have knock-on effects throughout the plasma [27]. These instabilities and their effects appear again in this thesis as drivers of other plasma structures and motivation for scenarios that avoid them.

DIII-D [28], located at General Atomics in San Diego, California and operating since 1986, is the United States' largest working tokamak. DIII-D is a scientific facility that, like many other devices, performs fusion experiments with only deuterium as the working gas. Since there is no expectation of power generation at a research facility, DIII-D avoids the additional difficulty and expense of tritium. Nevertheless, the physical properties of the plasma are sufficient to provide insights into both future scientific devices such as ITER

and fusion pilot plants intended for the power grid. In fact, DIII-D also runs hydrogen plasmas, which do not undergo significant fusion at typical modern tokamak temperatures, for research purposes. Hydrogen will be used during the ITER commissioning phase to test plasma-facing components, so hydrogen operation is another important use of the device. DIII-D is reliable, flexible in terms of parameters, and well-diagnosed, which has made it a leading site for fusion research worldwide. DIII-D can run with conditions similar to the initial planned runs of the ITER campaign, the combination of which is called the ITER Baseline Scenario (IBS). Other scenarios are possible, many of which are targets for future ITER experiments or a reactor. These target scenarios are called advanced tokamak scenarios, one of which is the quiescent H-mode (QH-mode) discussed later in this thesis. Lastly, DIII-D plasmas can be configured for more widely varying shapes, power levels, and other parameters, as are explored in Chapter 5.

Figure 1.3 shows images of DIII-D. DIII-D has an approximate major radius of 1.67 m and a minor radius of 0.67 m, placing it as a medium-sized tokamak compared to larger devices such as JET and ITER and smaller devices such as PEGASUS. DIII-D has a maximum toroidal magnetic field of 2.2 T on-axis and a maximum plasma current of 2.0 MA. The vacuum vessel surrounding the plasma has a D-shaped cross section, and most plasmas in the device have this D shape. The D shape evolved out of the Doublet design that preceded DIII-D and is capable of strong heating and confinement. As particles move around a tokamak, they encounter regions of "good" and "bad" curvature, where the pressure gradient is parallel and antiparallel to the curvature respectively. Bad curvature leads to pressure-driven instabilities that eject plasma outward. The D shape increases the time that particles stay in the good curvature region. Plasmas are shaped using magnetic coils separate from those that drive the plasma current. The wall of the vacuum vessel is covered by graphite tiles to protect the vessel from heat and particles lost or ejected from the plasma. Some losses occur steadily during operation. Some, often associated with higher-than-normal heat fluxes, occur during bursty intermittent events called edge-localized modes (ELMs) or during

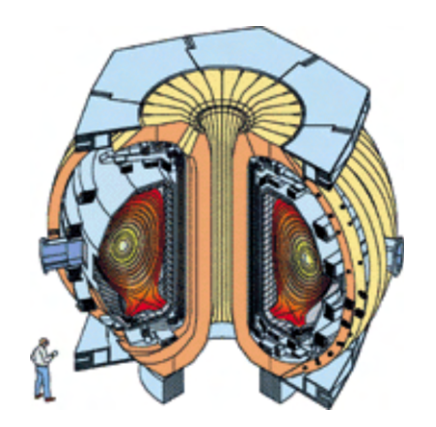




Figure 1.3: Left: A schematic of DIII-D with human for scale. Right: The interior of the DIII-D vacuum vessel. Images property of General Atomics.

a disruption, which is the complete loss of plasma confinement. Most DIII-D experiments also utilize the divertor, which is a magnetic configuration at the top and/or bottom of the device that directs exhausted heat and particles to dedicated plasma-facing components away from the main wall [29]. Any graphite that enters the plasma can be completely ionized at DIII-D temperatures. Heavier materials that may enter the plasma, such as stainless steel, have components (e.g., iron) that ionize incompletely, yielding significant energy losses through radiation. Any species that is neither fuel nor a fusion product is known as an impurity [30].

DIII-D is fueled by a combination of gas puffing and neutral beam injection (NBI) [31]. DIII-D's maximum line-averaged electron density is around 1.5×10^{20} m⁻³, though this is limited by instabilities rather than particle input [32]. In NBI, neutral atoms impinge upon ions or electrons and become ionized themselves. NBI is also a source of heating, with the high velocities of the neutrals transferring to the ions. Electron cyclotron heating (ECH) [33] is another source of heating, and additional methods are being tested for use on future devices. Since plasma has finite resistivity, it is heated to some extent by the current running through it, which is known as ohmic heating. However, ohmic heating is insufficient to raise tokamak plasmas to reactor-relevant fusion temperatures, so auxiliary sources such as NBI and ECH are almost always used. DIII-D has achieved conditions equivalent to Q = 0.32 in a D-T fueled plasma, though the true Q is lower as DIII-D does not use tritium [28].

The vacuum vessel is covered in ports for placement of diagnostics, several of which I discuss in more detail during this thesis [28]. The basic quantities measured in all DIII-D runs include temperature, density, rotation, radiated power, and light emission at a range of wavelengths. Several diagnostics, including some of the basic diagnostics, are equipped to measure fluctuations in temperature, density, and magnetic field. High resolution allows fluctuation measurements to be taken at many spatial and temporal scales. This proves very useful when detecting and tracking instabilities in the plasma.

In a plasma, magnetic field configurations contain free energy that can render them unstable upon perturbation. Such magnetic instabilities are a main challenge of magnetic fusion devices as they can reduce confinement, eject particles and energy from the plasma, and even cause it to disrupt completely. Detection and control of instabilities are therefore priorities for future devices, both for maintaining high performance and avoiding material damage. This thesis will primarily focus on large-scale instabilities that have effects throughout the plasma. Magnetic modes can be detected by measuring the amplitude, frequency, and resonant location of their associated fluctuations, whether in density, temperature, or magnetic field. Magnetic fluctuation amplitudes are typically measured at the wall using external sensing coils, which means that if the fluctuation peak is localized or far from the wall, amplitudes may be weak there. Diagnostics such as the Radial Interferometer-Polarimeter [34], to be discussed in depth in this thesis, can view the entire plasma and thus have an advantage over the sensing coils for modes localized in the plasma core.

1.3 Thesis Outline and Key Results

The remainder of this thesis gives more information about plasma instabilities and how they are measured. The next two chapters provide additional background information. Chapter 2 outlines the physical principles behind large-scale magnetic structures in tokamaks, including both ideal and resistive instability and nonlinear coupling. Chapter 3 details diagnostics including RIP [34], the primary diagnostic used in this research. Capabilities of and recent results from RIP are described. An overview of computational tools used to eval-

uate tearing mode origins and dynamics is given. The following chapters report results from experimental and computational studies of large-scale magnetic instabilities as they pertain to RIP.

The first principle underlying this investigation is to better understand RIP's advantages and capabilities in detection of different modes. Chapter 4 illustrates the physical underpinnings of RIP measurement of macroscopic magnetic instabilities. I show through modeling that plasma toroidicity and shaping break the symmetry of the radial structure of magnetic instability amplitudes that exists in the cylindrical solution to the structure equation. Next, by varying shape in experiment, I more directly study how plasma shaping affects RIP measurements. By comparing these models to experiment, Chapter 5 addresses results from a DIII-D experimental campaign that varies plasma shape and measures its effects on RIP measurements and plasma stability. It is found that in weakly shaped plasmas, magnetic instabilities are driven by current rather than pressure. In these cases, both linear interactions with shaping and nonlinear interactions between modes are significant contributors to mode amplitudes. Chapter 6 provides an example of RIP advantages over sensing coils. It describes first-time measurements of nonlinear coupling to each other of components of a sustained edge magnetic oscillation, called the edge harmonic oscillation (EHO), that inhibits ELMs and distinguishes QH-mode. It then describes nonlinear coupling of core-resonant magnetic instabilities to the EHO, which interrupts it. Chapter 7 provides conclusions and proposals for future work.

Bibliography

- NOAA National Centers for Environmental Information. Monthly Global Climate Report for Annual 2023. Tech. rep. United States National Oceanic and Atmospheric Administration, 2024.
- [2] P. Forster et al. "2021: The Earth's Energy Budget, Climate Feedbacks, and Climate Sensitivity". Climate Change 2021: The Physical Science Basis. Contribution of Working Group I to the Sixth Assessment Report of the Intergovernmental Panel on Climate Change. Ed. by V. Masson-Delmotte et al. Cambridge and New York: Cambridge University Press, 2021, pp. 923–1054.
- [3] T. Kjellstrom et al. Air and water pollution: burden and strategies for control. Disease Control Priorities in Developing Countries, 2nd edition. Washington and New York: The International Bank for Reconstruction and Development/The World Bank/Oxford University Press, 2006.
- [4] W. Steffen et al. "Trajectories of the Earth System in the Anthropocene". *Proceedings* of the National Academy of Sciences 115.33 (2018), pp. 8252–8259.
- [5] J. Davenport, N. Wayth, S. Virley, and R. Debarre. Statistical Review of World Energy 2023. Tech. rep. Energy Institute, 2024.
- [6] J. Prime et al. Renewable Energy Highlights 2024. Tech. rep. International Renewable Energy Agency, 2024.
- [7] A. Markandya and P. Wilkinson. "Electricity generation and health". *The Lancet* 370.9591 (2007), pp. 979–990.

- [8] R. J. Goldston. "Climate change, nuclear power, and nuclear proliferation: Magnitude matters". Science & Global Security 19.2 (2011), pp. 130–165.
- [9] United States Environmental Protection Agency. Radioactive Waste From Uranium Mining and Milling. URL: https://www.epa.gov/radtown/radioactive-waste-uranium-mining-and-milling.
- [10] United States Environmental Protection Agency. EPA Facts About Tritium. 2002.
- [11] J. D. Lawson. "Some criteria for a power producing thermonuclear reactor". *Proceedings of the Physical Society, Section B* 70.1 (1957), p. 6.
- [12] J. D. Huba. NRL Plasma Formulary. United States Naval Research Laboratory, 2023.
- [13] A. J. Creely et al. "Overview of the SPARC tokamak". Journal of Plasma Physics 86.5 (2020), p. 865860502.
- [14] F. Troyon et al. "MHD-limits to plasma confinement". Plasma Physics and Controlled Fusion 26.1A (1984), p. 209.
- [15] E. J. Strait. "Stability limits of high-beta plasmas in DIII-D". Fusion Science and Technology 48.2 (2005), pp. 864–874.
- [16] J. Wesson. Tokamaks. International Monographs on Plasma Physics. Clarendon Press, 2004.
- [17] U. Shumlak, R. P. Golingo, B. A. Nelson, and D. J. Den Hartog. "Evidence of stabilization in the Z-pinch". *Physical Review Letters* 87.20 (2001), p. 205005.
- [18] D. D. Schnack. Lectures in Magnetohydrodynamics: With an Appendix on Extended MHD. Lecture Notes in Physics. Berlin Heidelberg: Springer, 2009.
- [19] EUROfusion. *History of Fusion*. URL: https://euro-fusion.org/fusion/history-of-fusion/.
- [20] M. Kikuchi. "Steady state tokamak reactor based on the bootstrap current". Nuclear Fusion 30.2 (1990), p. 265.

- [21] M. Kikuchi. "Prospects of a stationary tokamak reactor". Plasma Physics and Controlled Fusion 35.SB (1993), B39.
- [22] A. G. Peeters. "The bootstrap current and its consequences". *Plasma Physics and Controlled Fusion* 42.12B (2000), B231.
- [23] F. L. Hinton and R. D. Hazeltine. "Theory of plasma transport in toroidal confinement systems". *Reviews of Modern Physics* 48.2 (1976), p. 239.
- [24] R. Carrera, R. D. Hazeltine, and M. Kotschenreuther. "Island bootstrap current modification of the nonlinear dynamics of the tearing mode". *Physics of Fluids* 29.4 (1986), p. 899.
- [25] F. Wagner et al. "Regime of improved confinement and high beta in neutral-beam-heated divertor discharges of the ASDEX tokamak". Physical Review Letters 49.19 (1982), p. 1408.
- [26] ASDEX Team et al. "The H-mode of ASDEX". Nuclear Fusion 29.11 (1989), p. 1959.
- [27] F. Wagner et al. "Recent results of H-mode studies on ASDEX". 13th International Conference on Plasma Physics and Controlled Nuclear Fusion. International Atomic Energy Agency. 1990, pp. 277–290.
- [28] J. L. Luxon. "A design retrospective of the DIII-D tokamak". *Nuclear Fusion* 42.5 (2002), p. 614.
- [29] ITER Organization. Divertor. URL: https://www.iter.org/machine/divertor.
- [30] R. V. Jensen et al. "Calculations of impurity radiation and its effects on tokamak experiments". *Nuclear Fusion* 17.6 (1977), p. 1187.
- [31] J. T. Scoville et al. "New capabilities and upgrade path for the DIII-D neutral beam heating system". Fusion Engineering and Design 146 (2019), pp. 6–9.
- [32] DIII-D National Fusion Facility. Capabilities and Tools. URL: https://d3dfusion.org/capabilities-tools/.

- [33] M. Cengher et al. "Status and plans for the DIII-D ECH/ECCD System". *IEEE Transactions on Plasma Science* 48.6 (2020), pp. 1698–1702.
- [34] J. Chen et al. "Faraday-effect polarimeter diagnostic for internal magnetic field fluctuation measurements in DIII-D". Rev. Sci. Instrum. 87.11 (2016), 11E108.

Chapter 2

Macroscopic MHD Instabilities in

Tokamaks

Plasmas are not stationary. If all variables are considered, a plasma system has almost innumerable degrees of freedom. A gas at high temperature, held together by finite external forces and contained in a vacuum, will move. Separation of charges produces additional degrees of freedom. Plasmas undergo fluid motion at all scales, from coherent flows to large oscillations to micro-scale turbulence. This thesis is concerned with low-frequency, large-scale magnetic fluctuations in tokamaks, particularly DIII-D. To understand how such fluctuations develop and affect the plasma, I turn to the magnetohydrodynamic (MHD) model. This chapter provides an overview of the concepts necessary to understand the formation, dynamics, and interactions of large-scale MHD instabilities. It then details the most important properties of MHD instabilities in tokamaks and some examples of MHD phenomena.

Section 2.1 covers the basics of the MHD model and important definitions that are used in this thesis. It then describes cylindrical and toroidal equilibrium models. Section 2.2 addresses the ideal (zero-resistivity) instabilities that can affect these equilibria. I devote Section 2.3 to resistive MHD and associated instabilities. I emphasize one type of MHD instability called tearing modes, which are a significant risk to plasma confinement and

performance. I apply physical principles discussed in these sections to the tokamak configuration. Lastly, Section 2.4 gives an overview of how MHD instabilities can interact with each other.

2.1 MHD Equilibrium

MHD is the study of electrically conductive fluids, one type of which includes plasma. More strictly, the name MHD applies to a model where all charged particles are treated together as a single fluid. Other, more complex models exist to describe plasma motion, from the two-fluid (electrons and ions separate) to fully kinetic, statistical models. MHD is a relatively simple, tractable model and is very effective when studying large-scale behavior in collisional plasmas such as those found in fusion. I begin with the basic principles of MHD theory. These are aptly illustrated in [1–3], which form the basis of much of the discussion in this section.

In thie MHD model, electrons (represented e) and ions (represented i) are described using their average motion but are still subject to electromagnetic forces. The fluid has mass density $\rho = \sum_s m_s n_s$, where m_s and n_s are the mass and density of the species, respectively. Each species has a mean velocity \mathbf{u}_s and a charge q_s . The center-of-mass flow velocity is $\mathbf{v} = \frac{1}{\rho} \sum_s m_s n_s \mathbf{u}_s$, and the current density is $\mathbf{J} = \sum_s n_s q_s \mathbf{u}_s$. In all cases presented in this thesis, I assume quasineutrality, $n_e \simeq Z_i n_i$, where Z_i is the average atomic number of the ion distribution, which is appropriate for fusion plasmas. The electric field is written \mathbf{E} and the magnetic field \mathbf{B} . The plasma has a resistivity η . The plasma pressure $p \simeq p_e + p_i$.

The major equations that define the MHD model are as follows:

Continuity equation:
$$\frac{\partial \rho}{\partial t} + \nabla \cdot (\rho \mathbf{v}) = 0$$
 (2.1)

Momentum equation:
$$\rho \frac{\mathrm{dv}}{\mathrm{d}t} = \mathbf{J} \times \mathbf{B} - \nabla p$$
 (2.2)

Adiabatic equation of state:
$$\frac{\mathrm{d}}{\mathrm{d}t} \left(\frac{p}{\rho^{\gamma}} \right) = 0 \tag{2.3}$$

¹The stress tensor Π is the last remaining MHD variable but is neglected in the cases under study.

Ohm's Law:
$$\mathbf{E} + \mathbf{v} \times \mathbf{B} = \eta \mathbf{J}$$
 (2.4)

Ampère's Law:
$$\nabla \times \mathbf{B} = \mu_0 \mathbf{J}$$
 (2.5)

Faraday's Law:
$$\nabla \times \mathbf{E} = -\frac{\partial \mathbf{B}}{\partial t}$$
 (2.6)

No magnetic monopoles:
$$\nabla \cdot \mathbf{B} = 0.$$
 (2.7)

where $\gamma = 5/3$. When $\eta \to 0$, Equation 2.4 becomes $\mathbf{E} + \mathbf{v} \times \mathbf{B} = 0$, and this model is called ideal MHD. Cases with $\eta \neq 0$ are called resistive MHD. In ideal MHD, the magnetic field and the fluid are tied together and cannot move independently of each other. This is called the frozen-flux theorem [4]. Magnetic field lines do not change their topology. Later in this chapter I describe how this condition is violated in the resistive case. The ideal-MHD condition for force balance, i.e., equilibrium, is $\frac{d\mathbf{v}}{dt} = 0$. This leads to the condition $\mathbf{J} \times \mathbf{B} = \nabla p$. I first build up a model of a cylindrical equilibrium then extend to a toroidal model.

I first work in coordinates (r, θ, z) , where r is the radial coordinate of the cylinder, θ is the poloidal coordinate, and z is the axial coordinate. The z-pinch is a simple design created by running an axial current with current density $\mathbf{J} = J_z \hat{\mathbf{z}}$ through the plasma just as in a wire. This induces by Ampére's law a poloidal magnetic field $\mathbf{B} = B_{\theta} \hat{\boldsymbol{\theta}}$. The plasma is confined by $\mathbf{J} \times \mathbf{B}$ forces, which point radially inward. With J_z and B_{θ} and taking the curl in cylindrical coordinates, Equation 2.5 becomes

$$J_z = \frac{1}{\mu_0 r} \frac{\mathrm{d}}{\mathrm{d}r} (rB_\theta) \tag{2.8}$$

and Equation 2.2, by substituting the expression above, becomes

$$\frac{\mathrm{d}p}{\mathrm{d}r} = -J_z B_\theta = -\frac{B_\theta^2}{\mu_0 r} - \frac{\mathrm{d}}{\mathrm{d}r} \frac{B_\theta^2}{2\mu_0}.$$
 (2.9)

These are magnetic pressures induced by field line tension. The plasma is confined effectively.

However, the z-pinch is unstable to asymmetrical perturbations, whether violating ax-

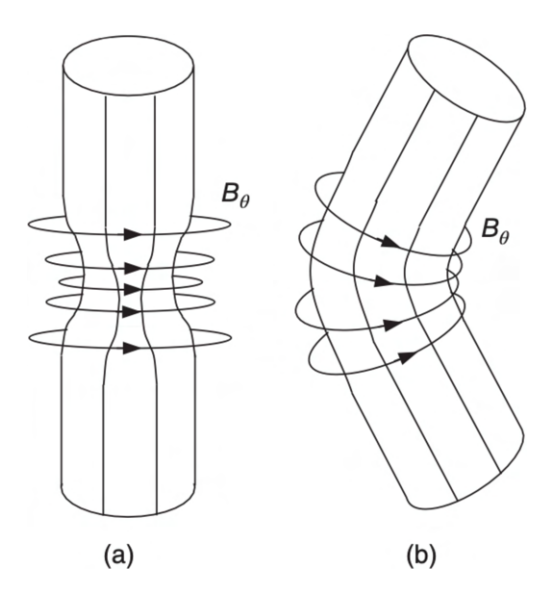


Figure 2.1: (a) The sausage instability in the z-pinch. (b) The kink instability in the z-pinch. Figure reproduced from [3].

isymmetry or radial symmetry. When the plasma is compressed, the magnetic field and magnetic force increase locally, tending to augment the perturbation. Two examples of this type of instability are seen in Figure 2.1. The sausage instability is formed by a radial perturbation that pinches B_{θ} continually inward, while the kink instability is formed by a lateral perturbation.

One may also consider an equilibrium where current \mathbf{J}_{θ} is run poloidally, inducing an axial magnetic field \mathbf{B}_{z} . An axial field is not susceptible to instabilities caused by asymmetrical compression of the field. The $\mathbf{J} \times \mathbf{B}$ force is once again radially inward, creating the θ -pinch.

$$J_{\theta} = -\frac{1}{\mu_0} \frac{\mathrm{d}B_z}{\mathrm{d}r} \tag{2.10}$$

and Equation 2.2 becomes

Here, Equation 2.5 becomes

$$\frac{\mathrm{d}p}{\mathrm{d}r} = J_{\theta}B_z = B_z \left(-\frac{1}{\mu_0} \frac{\mathrm{d}B_z}{\mathrm{d}r} \right) = -\frac{\mathrm{d}}{\mathrm{d}r} \left(\frac{B_z^2}{2\mu_0} \right). \tag{2.11}$$

Once again, the term on the right is a magnetic pressure. The θ pinch has no inherent instability but does not induce strong confinement. The tokamak model is constructed from

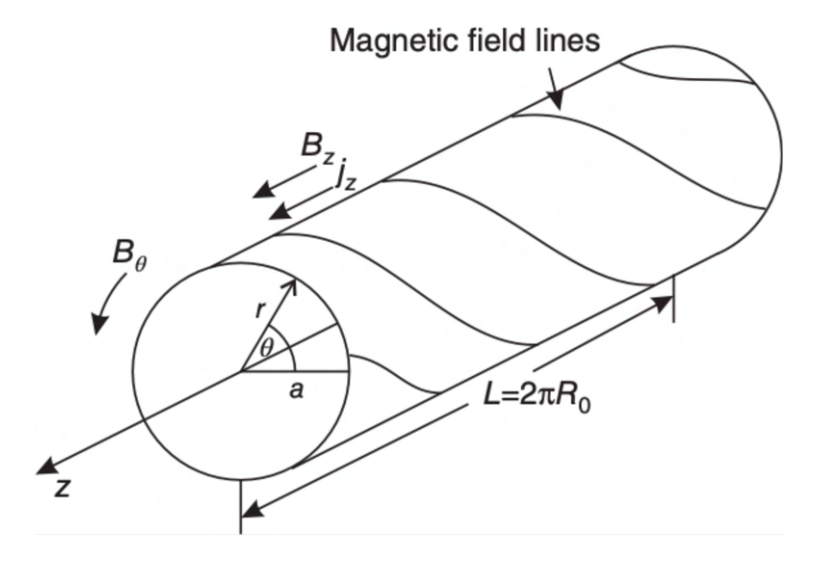


Figure 2.2: A diagram of the screw pinch showing coordinates, currents, and magnetic fields components. Figure reproduced from [3].

a combination of both pinch models.

Assume $\mathbf{B} = B_{\theta}(r)\hat{\boldsymbol{\theta}} + B_z(r)\hat{\mathbf{z}}$; in the pinch model, one assumes that there is no radial magnetic field. Considering each direction separately when appropriate, the MHD equations become

$$\nabla \cdot \mathbf{B} = 0: \qquad \frac{1}{r} \frac{\partial B_{\theta}}{\partial \theta} + \frac{\partial B_z}{\partial z} = 0$$
 (2.12)

$$\mu_0 \mathbf{J}_{\theta} = (\nabla \times \mathbf{B})_{\theta} : \qquad \mu_0 J_{\theta} = -\frac{\mathrm{d}B_z}{\mathrm{d}r}$$
 (2.13)

$$\mu_0 \mathbf{J}_z = (\nabla \times \mathbf{B})_z : \qquad \mu_0 J_z = \frac{1}{r} \frac{\mathrm{d}}{\mathrm{d}r} (rB_\theta)$$
 (2.14)

$$\nabla p = \mathbf{J} \times \mathbf{B}: \qquad \frac{\mathrm{d}p}{\mathrm{d}r} = \frac{\mathrm{d}}{\mathrm{d}r} \left(\frac{B_{\theta}^2 + B_z^2}{2\mu_0} \right) - \frac{B_{\theta}^2}{\mu_0 r}. \tag{2.15}$$

A graphical representation of the screw pinch is shown in Figure 2.2. In the screw pinch, the sausage and kink instabilities can be suppressed through the θ current component bending the field lines. Particle loss from drifts is slowed in the screw pinch compared to the θ -pinch. However, note that there is no constraint on the value of \mathbf{v} in these equations. Particles can flow freely at constant velocity in the axial direction, undergoing gyromotion along the field lines. The field lines extend beyond the plasma, and the plasma encounters end losses.

As discussed briefly in Chapter 1, the problem of end losses can be solved by turning the cylinder's ends in on themselves, creating a torus. The characteristic length L of the screw pinch in Figure 2.2 becomes the circumference while $R_0 = L/2\pi$ is the major radius. The z direction is converted to an angular toroidal coordinate $\phi = \sin^{-1}(z/r)$, yielding an orthogonal coordinate system in (r, θ, ϕ) . The minor radius a should also be noted. To start, I consider these toroidal equilibria to be axisymmetric; all quantities are constant in ϕ . It is also convenient to construct coordinates (R, Z, ϕ) , where R is the major radius of a given point and Z is its height. R and Z then form a rectangular grid while ϕ remains an angular coordinate. The two systems are demonstrated in Figure 2.3. Magnetic fields in a toroidal configuration are typically labeled as poloidal and toroidal: B_{θ} and B_{ϕ} (B_r is zero in equilibrium). In the (R, Z) coordinate system, B_R and B_Z are the cross-sectional components of B_{θ} . The torus can be described by its aspect ratio R_0/a , where R_0 is the major radius and a is the minor radius. The quantity often used to describe the shape of the torus is instead the inverse aspect ratio $\epsilon = a/R_0$. Here I also mention that the cross-section of the plasma may have arbitrary shape, and that in fact, shaped cross-sections are a major factor in the high performance stability seen in so many modern tokamaks. To second order, the cross-section of any flux surface can be parametrized using

Elongation:
$$\kappa = \frac{Z_{max} - Z_{min}}{R_{max} - R_{min}}$$
 (2.16)

Upper triangularity:
$$\delta_u = \frac{R_{\text{max}} - R_{min} - 2RZ_{max}}{R_{max} - R_{min}}$$
 (2.17)

Lower triangularity:
$$\delta_u = \frac{R_{\text{max}} - R_{min} - 2RZ_{min}}{R_{max} - R_{min}}$$
 (2.18)

Since $\nabla p = \mathbf{J} \times \mathbf{B}$, $\mathbf{B} \cdot \nabla p = 0$ as well. Pressure is constant along \mathbf{B} , so magnetic field lines lie on surfaces of constant pressure, which are called flux surfaces. Any quantity that is conserved on a flux surface can be used as a radial coordinate for that surface. For this purpose I use the poloidal magnetic flux $\psi_p = \int \mathbf{B} \cdot d\mathbf{S}_p$. The magnetic field has a fixed

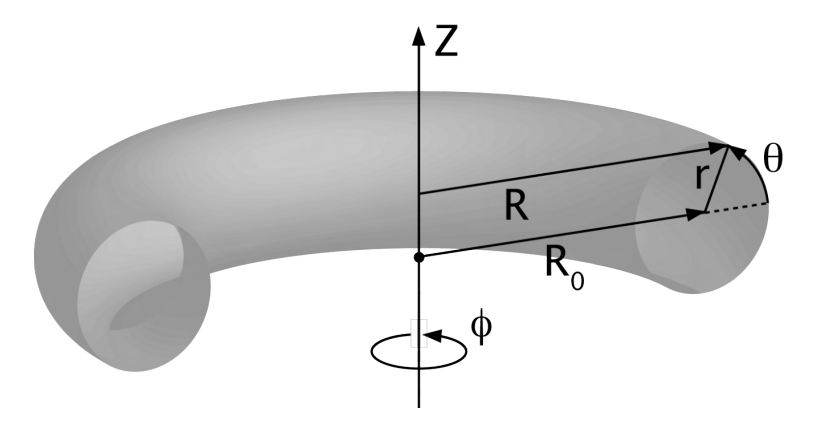


Figure 2.3: The polar (r, θ, ϕ) and rectangular (R, Z, ϕ) toroidal coordinate systems in a circular torus. Image property of CIEMAT.

pitch $d\phi/d\theta$ for every flux surface, which is known as the safety factor q (not to be confused with the power threshold Q). Surfaces where field lines map to their original location after a finite number of toroidal and poloidal transits are called rational surfaces. Flux surfaces where field lines ergodically fill the surface also exist and are called irrational. The safety factor may be positive or negative depending on the orientation of the field lines with respect to the coordinate system origin.

I now state the appropriate MHD equations in toroidal geometry. The poloidal flux function is defined

$$\psi = 2\pi \int_0^R B_Z(R', Z) dR' dZ. \tag{2.19}$$

Using Equations 2.2, 2.5, and 2.7, the radial component of the force-balance equation in toroidal geometry can be written as

$$\Delta^* \psi = -\mu_0 R^2 p' - FF' \tag{2.20}$$

where Δ^* is an operator

$$\Delta^* = R \frac{\partial}{\partial R} \left(\frac{1}{R} \frac{\partial}{\partial R} \right) + \frac{\partial^2}{\partial Z^2}, \tag{2.21}$$

 $p(\psi)$ is the plasma pressure, and $F(\psi) = RB_{\phi}$. This famed equation is known as the Grad-Shafranov equation. In principle, p and F are arbitrary and depend on the configuration

and boundary conditions. The solution ψ can be used to construct equilibrium magnetic flux surface models. Solutions to the Grad-Shafranov equation are not guaranteed to exist, and it is typically solved computationally.

2.2 Ideal Instabilities

I now discuss the dynamics of plasmas perturbed from the equilibria discussed in the previous section. Consider a general spatial displacement $\boldsymbol{\xi}(\mathbf{r},t)$ from an equilibrium position. Then the MHD equations include a velocity $\mathbf{v} = \mathrm{d}\boldsymbol{\xi}/\mathrm{d}t$. In the linear approximation, where all perturbed quantities f are written to first order as $f = f_0 + f_1(\boldsymbol{\xi})$. As the equilibrium is stationary until perturbed, $\mathbf{v}_0 = 0$. In the MHD equations, products of first-order terms u_1v_1 are obtained. When the displacement is small, these terms can be neglected; this is called linearization. The linearized ideal MHD equations become

$$\frac{\partial \rho_1}{\partial t} = -\nabla \cdot (\rho_0 \mathbf{v}_1) \tag{2.22}$$

$$\rho_0 \frac{\partial \mathbf{v}_1}{\partial t} = -\nabla p_1 + \mathbf{J}_0 \times \mathbf{B}_1 + \mathbf{J}_1 \times \mathbf{B}_0$$
 (2.23)

$$\frac{\partial p_1}{\partial t} = -\mathbf{v}_1 \cdot \nabla p_0 - \gamma p_0 \nabla \cdot \mathbf{v}_1 \tag{2.24}$$

$$\frac{\partial \mathbf{B}_1}{\partial t} = \nabla \times (\mathbf{v}_1 \times \mathbf{B}_0) \tag{2.25}$$

where I have used the advective derivative $d/dt = \partial/\partial t + \mathbf{v} \cdot \nabla$. For some known ρ_0 , p_0 , and \mathbf{B}_0 ($\mu_0 J_0 = \nabla \times \mathbf{B}_0$), one can solve for the perturbed quantities, which can also be written in terms of $\boldsymbol{\xi}$. Substituting $\mathbf{v}_1 = d\boldsymbol{\xi}/dt$ and integrating over t where appropriate, the MHD equations become a wave equation for $\boldsymbol{\xi}(t)$:

$$\rho_0 \frac{\partial^2 \boldsymbol{\xi}}{\partial t^2} = J_0 \times [\nabla \times (\boldsymbol{\xi} \times \mathbf{B}_0)] + \frac{1}{\mu_0} [\nabla \times [\nabla \times (\boldsymbol{\xi} \times \mathbf{B}_0)]] \times \mathbf{B_0}$$

$$+ \nabla (\boldsymbol{\xi} \cdot \nabla p_0) + \gamma \nabla (p_0 \nabla \cdot \boldsymbol{\xi})$$

$$= \mathbf{F}(\boldsymbol{\xi}). \tag{2.26}$$

 \mathbf{F} is the ideal MHD force operator. As the system is linear, the perturbed quantities can be represented as Fourier components $f_1(\mathbf{r},t) = f_1(\mathbf{r})e^{-i\omega t}$, and the wave equation becomes

$$-\omega^2 \rho_0 \boldsymbol{\xi} = \mathbf{F}(\boldsymbol{\xi}). \tag{2.27}$$

The force operator is self-adjoint [5], and therefore its solutions ξ form an orthogonal set of eigenfunctions. For $\omega^2 > 0$ the system is stable and will oscillate around the equilibrium. For $\omega^2 < 0$ the system is unstable, and the perturbation will grow or shrink exponentially. The eigenvalue equation cannot, generally, be solved analytically, and later I demonstrate numerical methods to calculate the eigenfunctions.

One can also determine the stability of the system without determining the eigenvalues or eigenfunctions using a variational method called the energy principle [6]. Multiply Equation 2.27 by $\boldsymbol{\xi}^*$ and integrate over volume:

$$\frac{\omega^2}{2} \int \rho_0 |\xi^2| \, dV = -\frac{1}{2} \int \boldsymbol{\xi}^* \cdot \mathbf{F}(\boldsymbol{\xi}) \, dV = \delta W(\boldsymbol{\xi}^*, \boldsymbol{\xi}). \tag{2.28}$$

The left-hand side, also called $K(\boldsymbol{\xi}^*, \boldsymbol{\xi})$, is the kinetic energy in the system, and the right-hand side $\delta W(\boldsymbol{\xi}^*, \boldsymbol{\xi})$ is the potential energy. For $\omega^2 < 0$, at least one of the system's eigenvalues must be negative and the system is unstable [3]. Since $K(\boldsymbol{\xi}^*, \boldsymbol{\xi})$ is positive, the sign of ω^2 depends entirely on the sign of δW . Therefore, if $\delta W > 0$, the system is stable, and if $\delta W < 0$, the system is unstable. An extended energy principle exists for more realistic systems of plasmas surrounded by vacuum and then a conducting wall:

$$\delta W = \delta W_F + \delta W_S + \delta W_V \tag{2.29}$$

where δW_F is the contribution from the fluid (plasma) and therefore δW from Equation 2.28, δW_S is a contribution from the interface between the plasma and the vacuum, and δW_V is the contribution from the vacuum. The definitions of these terms and their boundary conditions in terms of ξ and the equilibrium quantities can be found in [2]. In general, the vacuum

component is always stabilizing, and the surface component may be either stabilizing or destabilizing. Therefore, the δW_F condition below is not a strict boundary. Note that the fluid contribution can be written [6, 7]

$$\delta W_F = \frac{1}{2} \int \left(\frac{|B_{1\perp}|^2}{2\mu_0} + \frac{B_{0\perp}^2}{2\mu_0} |\nabla \cdot \boldsymbol{\xi}_{\perp} + 2\boldsymbol{\xi}_{\perp} \cdot \boldsymbol{\kappa}|^2 + \gamma p_0 |\nabla \cdot \boldsymbol{\xi}|^2 - 2(\boldsymbol{\xi}_{\perp} \cdot \nabla p_0) (\boldsymbol{\kappa} \cdot \boldsymbol{\xi}_{\perp}^*) - \frac{J_{0\parallel}}{B_0} (\boldsymbol{\xi}_{\perp}^* \cdot \mathbf{B}_0) \cdot \mathbf{B}_1 \right)$$
(2.30)

where $\kappa = (\mathbf{B}/B) \cdot \nabla(\mathbf{B}/B)$ is the curvature of the magnetic field, and \parallel and \perp are with respect to the surface. The first three terms are positive-definite and always stable; they correspond to MHD waves. The fourth term is associated with pressure-driven instabilities and the fifth with current-driven instabilities.

I now consider the pinch equilibrium models from Section 2.1, their stability, and their relationship to the energy principle. In an axisymmetric cylindrical system, perturbations can be written as

$$\boldsymbol{\xi}(\mathbf{r}) = \xi(\mathbf{r})e^{i(m\theta + kz)},\tag{2.31}$$

where m and k are the poloidal and axial (toroidal) wave numbers of the oscillatory solution. Some examples of cylindrical perturbations with various values of m and k are illustrated in Figure 2.4. For a plasma column that, unperturbed, has the appearance (a), $m \neq 0$, k = 0 displacements such as (b) and (c) are distortions of the plasma column that vary only in θ . The m = 1 mode is known as the shift mode and is a shift of the plasma off axis. Higher-m modes give, instead of a displacement, an elliptical, triangular, or higher-order variation in cross-sectional shape. The $m = 0, k \neq 0$ mode (d) varies only in z and is the sausage mode discussed in Section 2.1. A perturbation that varies in both θ and z forms a helix as shown in (e), in this case with m = 1 or only one poloidal transit. The kink mode from Section 2.1 is an example of a helical mode. These distortions of the plasma may be external, disturbing the plasma boundary, or internal, distorting only an internal portion of the plasma.

It can be found from the energy principle that the m=0 mode is difficult to stabilize near

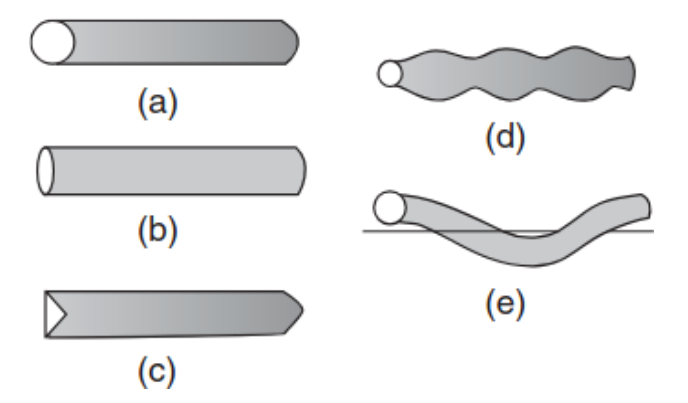


Figure 2.4: Five instability configurations in a plasma column: (a) unperturbed; (b) m = 2, k = 0 (elliptical distortion); (c) m = 3, k = 0 (triangular distortion); (d) m = 0, $k \neq 0$ (sausage); (e) m = 1, $k \neq 0$ (kink). Reproduced from [5].

the boundary of the z-pinch and the m=1 mode is always unstable near the core. These both result from increased magnetic tension when the plasma is compressed, further destabilizing the perturbation. The θ -pinch is MHD stable because the two destabilizing terms in the energy equation are both zero, so the stabilizing terms contribute to the relatively increased stability of the screw pinch compared to the z-pinch. General screw pinch stability can be calculated numerically [8] using trial functions for the radial structure of ξ to solve the Euler-Lagrange equation within the bounds of a known equilibrium [9]. This can be used to test the stability of first internal and then external modes to determine overall stability to ideal modes.

In the limit of large aspect ratio ($\epsilon \ll 1$ or $R_0 \gg a$), a torus can first be modeled as a periodic screw pinch. This allows use of (r, θ, ϕ) coordinate system and transformation of the axial wave number k into a toroidal mode number n. Perturbations can be written as

$$\boldsymbol{\xi}(\mathbf{r}) = \xi(\mathbf{r})e^{im\theta - in\phi}.$$
 (2.32)

Once again, m and n may be either positive or negative depending on the orientation of the mode. On surfaces of constant flux in any torus, q is the number of toroidal transits per poloidal transit and is a rational number m/n. An ideal instability arising in a periodic screw pinch that is particularly relevant to the remainder of this thesis is the sawtooth oscillation

[10, 11]. Sawteeth begin as m=1, n=1 current-driven internal kinks that arise when q(0) < 1, i.e., when the surface on which the 1,1 mode forms exists. While resistivity and toroidicity impart additional complexity to exact mechanism of sawtooth triggering, their initial trigger has m=1, n=1 and forms a kink structure in the core. They are periodic in time and have a two-stage process. Sawteeth form when the current density is increasing. When the current increases to the point that q_0 drops below 1, a 1,1 mode forms, usually an internal kink. This is soon followed by a crash and radial redistribution of current so that q_0 rises above 1 again. During the sawtooth cycle, core temperature repeatedly rises gradually then falls suddenly, forming the sawtooth pattern that gives it its name. They do not necessarily disrupt the plasma and are naturally-occurring in some modern tokamak scenarios but can trigger other modes. Another ideal instability that appears again in this thesis is the fishbone instability [12]. Fishbones also form an internal kink but are triggered by energetic particles at relatively high pressure. They are named as such due to their repetitive ringing signature on magnetic probes and appear in spectrograms to "chirp" rapidly up or down in frequency.

In a torus with finite aspect ratio, the role of curvature becomes important. The term $(\boldsymbol{\xi}_{\perp} \cdot \nabla p_0)(\boldsymbol{\kappa} \cdot \boldsymbol{\xi}_{\perp}^*)$ in the energy principle has opposite signs on the inner and outer surfaces of the torus, since the pressure gradient ∇p is always outwards in r and the curvature $\boldsymbol{\kappa}$ varies along a magnetic field line. Therefore, the inboard condition is referred to as good curvature and the outboard condition as bad curvature, as previously mentioned in Chapter 1. A global pressure-driven instability may develop unless the integral of the term along the field line is balanced. Even so, pressure-driven instabilities may form locally in regions of bad curvature, i.e, on the outer surface. This leads to flux tubes interchanging or locally extending the edge of the plasma in what is known as the ballooning mode. External kinks may also form and are known as peeling modes. The sawtooth as an internal kink remains for $q_0 < 1$. Force balance on the inboard and outboard sides of the plasma also induces an internal shift in the magnetic axis known as the Shafranov shift [11, 13].

Ballooning modes are particularly important in tokamaks when they interact with current-driven external kinks and become peeling-ballooning modes. These modes can drive filamentary structures entirely out of the plasma, where they may contact plasma-facing components. Ballooning modes at the edge are called edge-localized modes (ELMs). ELMs are another generally nondisruptive instability and are seen in modern tokamaks. They are high-m, n external modes that are driven by both pressure and current gradients near the edge in H-mode [14]. In H-mode, some heat and particle transport across the edge is necessary to prevent more damaging instabilities caused by a gradient that has grown too steep. ELMs are also helpful in exhausting impurities from the plasma. However, the energy and particle flux to the wall and divertor caused by large ELMs will be untenable using modern wall materials in higher-power tokamaks such as ITER [15]. ELM avoidance, control, and suppression techniques are major fields of research.

2.3 Resistive Instabilities

So far, I have described only ideal instabilities, where flux is frozen and an entire flux tube deforms. However, fusion plasmas are necessarily collisional and have a finite resistivity, retaining the $\eta \mathbf{J}$ term in Equation 2.4. The conditions for ideal instability remain the same, so ideal instabilities may arise. However, resistivity allows a new set of magnetic dynamics that may cause their own instabilities [16]. The frozen-flux theorem [4] ceases to hold, the plasma diffuses across magnetic field lines, and field lines can slip past each other upon perturbation. When the frozen-flux condition is violated, magnetic field lines can undergo topological change, a process known as magnetic reconnection. Note that magnetic reconnection also occurs in astrophysical contexts such as the solar wind and is often driven by external forces in such contexts [17].

Reconnection forms magnetic islands, regions where the field is locally absent and field lines form closed loops. Typically, islands form chains linked by X-points, where the field lines connect, and O-points, where the field lines are closed. An illustration of magnetic islands is shown in Figure 2.5. An X-point is in the center of the plot, and two O-points

are to either side. Since magnetic field lines are torn, in fusion devices, resistive instabilities forming islands are called tearing modes. A tearing mode can be considered the resistive equivalent of a kink mode; in cylindrical and toroidal devices, tearing modes form helices akin to kink modes. Resistive ballooning modes exist but dynamically are similar to either tearing modes or ideal ballooning modes [18].

While kink modes generally consist of a spatially fixed perturbation, island chains move more or less with the plasma. In a cylinder, a mode can move axially or rotate poloidally. In a torus, this axial motion equates to a toroidal rotation, and poloidal rotation is also possible as in the cylinder. For a moving helix, the directions of motion are indistinguishable, similarly to the apparent vertical motion of stripes on a barber pole [3]. A mode's total angular velocity can be calculated as $\omega = \mathbf{k} \cdot \mathbf{v}$, where \mathbf{k} is the wave vector, and \mathbf{v} is the velocity vector. In a(n infinite) cylinder, this equates to

$$\omega = \frac{m}{r_s} v_\theta + \frac{k}{L} v_z,\tag{2.33}$$

where m is the poloidal mode number, r_s is the radial location of the rational surface, k is the axial wave number, and L is the axial length scale. When the cylinder becomes periodic (a torus), the axial direction z becomes a toroidal direction ϕ , and the angular velocity is equal to

$$\omega = \frac{m}{r_s} v_\theta + \frac{n}{R} v_\phi, \tag{2.34}$$

where n is the toroidal mode number, and R is the major radius of the plasma. Since tearing modes have m > n in most tokamaks, and $R \gg r_s$, one might be concerned about the role of poloidal rotation in the total mode rotation. However, poloidal rotation v_{θ} is often small in a tokamak compared to toroidal rotation v_{ϕ} , by a factor of greater than 10. In addition, the poloidal velocity measurement is typically taken from vertical measurements, which have significant pickup [19], so it can be estimated to be smaller than the measured value. I discuss the role of poloidal rotation again when estimating mode locations in Chapter 4, but even so, $v_{\theta} \ll v_{\phi}$.

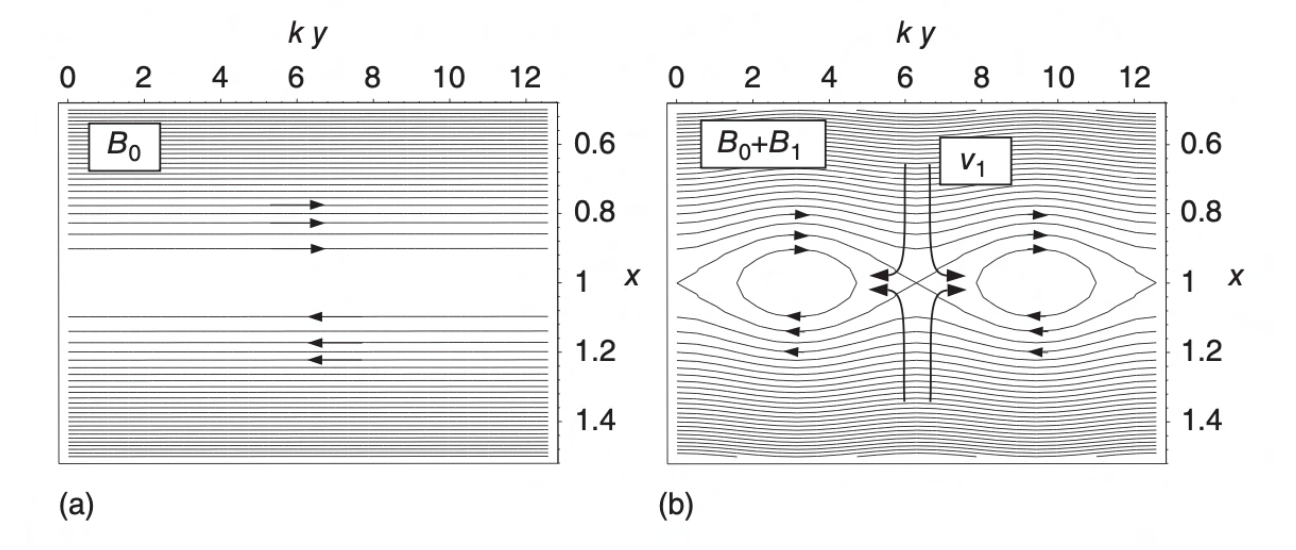


Figure 2.5: A slab model for magnetic field lines (a) before and (b) after reconnection due to a perturbation B_1 , showing magnetic islands and direction of flow. Reproduced from [3].

The original theory of tearing modes entailed a slab model with a magnetic field in the y direction, which changes direction at $x = x_s$, and characteristic length L: $B = B_{0,y}(x-x_s)/L$ [2, 3, 16]. It is typically valid and very useful to model a resistive instability as ideal except for a thin resistive layer around the rational surface where the instability lies. A current layer forms in the resistive layer. For resistive modes, this surface is also known as the resonant surface. Outside the resistive layer, the mode structure spatial eigenfunction Ψ can be described using the infinite-conductivity equation

$$\Psi'' - \Psi \left(\alpha^2 + \frac{F''}{F} - \frac{G}{F^2} \right) = 0 \tag{2.35}$$

where $\alpha = ka$, k is the wavenumber of the slab perturbation, a is the thickness of the current layer, $F = (\mathbf{k} \cdot \mathbf{B})/kB$, and G is an acceleration-related term. In the limit of an infinitely thin layer, $\Psi_1 = \Psi_2$ across the layer, where Ψ_1 and Ψ_2 are the components on each side. Since the solutions must vanish at the boundary, Ψ generally is discontinuous across the layer. The stability of the mode depends on the sign of the discontinuity

$$\Delta' = \frac{\Psi_2'}{\Psi_2} - \frac{\Psi_1'}{\Psi_1}.\tag{2.36}$$

When $\Delta' < 0$, the tearing mode is stable, and when $\Delta' > 0$, it is unstable.

This model was expanded to a cylinder [20] and then to a circular tokamak [21], where for axisymmetric radial perturbations the infinite-conductivity equation appears as

$$\frac{\mathrm{d}}{\mathrm{d}r}\left(H\frac{\mathrm{d}\Psi}{\mathrm{d}r}\right) - \Psi\left[\frac{g}{F^2} + \frac{1}{F}\frac{\mathrm{d}}{\mathrm{d}r}\left(H\frac{\mathrm{d}F}{\mathrm{d}r}\right)\right] = 0. \tag{2.37}$$

Here $F = \mathbf{k} \cdot \mathbf{B}$, $\mathbf{H} = r^3/(k^2r^2 + m^2)$, k = n/r, and

$$g = \frac{(m^2 - 1)rF^2}{k^2r^2 + m^2} + \frac{k^2r^2}{k^2r^2 + m^2} \left(2\frac{\mathrm{d}P}{\mathrm{d}r} + rF^2 + F\frac{2(krB_z - mB_\theta)}{k^2r^2 + m^2} \right).$$

The jump condition at the resonant surface $r=r_s$ is

$$\Delta' = \frac{1}{\Psi(r_s)} \frac{d}{dr} (\Psi_2 - \Psi_1)|_{r_s}.$$
 (2.38)

After the tearing mode arises, its growth quickly becomes nonlinear [22]. While the linear component, inducing exponential growth, is dominant at first [23], eddy currents form and slow the growth rate to quadratic [22]. Good curvature in the outside portion of the island further slows the growth of the mode, resulting in the Rutherford equation [22, 24, 25]

$$\frac{\tau_R}{r_s} \frac{\mathrm{d}w}{\mathrm{d}t} = r_s \Delta'(w) - \beta_p r_s \frac{a_{GGJ}}{w},\tag{2.39}$$

for resistive diffusion time $\tau_R = \mu_0 r_s^2/1.22\eta$, poloidal pressure β_p , and a_{GGJ} the Glasser-Greene-Johnson curvature term [24]. Note here that Δ' depends on w, the island width. A large enough island has a finite current layer and modifies the current gradient nearby. Curvature stabilization and w dependence of Δ' can allow a tearing mode to saturate (dw/dt = 0). Saturated tearing modes can persist without causing disruption. This equation covers a single tearing mode, without linear coupling from geometry or interactions with other modes. The curvature term may also be omitted where appropriate. Modes where $\Delta' > 0$ and that grow quadratically due to current gradients are called classical tearing modes (CTM).

The aforementioned classical theory neglects that magnetic islands of a sufficient size flatten the pressure gradient. The vanishing magnetic field across an island permits particle drift across field lines, which as a general concept is known as neoclassical transport. When an island disturbs the pressure gradient, the bootstrap current is also disturbed. If bootstrap current is a major contributor to overall current, then a hole in the bootstrap current contributes to instability [26, 27]. For a sufficiently large island, it can be assumed that pressure is completely flat and particle drift across the island is halted. For a small island, however, this is not strictly true, and the disturbance to the bootstrap current is reduced [28–31]. As the island moves along the field in time, $\mathbf{E} \times \mathbf{B}$ drifts can create an ion polarization current that is usually stabilizing. If one retains the curvature term in this case, these contributions yield the modified Rutherford equation (MRE):

$$\frac{\tau_R}{r} \frac{\mathrm{d}w}{\mathrm{d}t} = r_s \Delta' + \epsilon^{1/2} \left(\frac{L_q}{L_p}\right) \beta_p \left(\frac{r}{w}\right) \left[\frac{w^2}{w^2 + w_d^2} - \frac{w_{pol}^2}{w^2}\right] - 6.35(q^2 - 1) \frac{L_q^2}{r_s L_p} \frac{\beta}{w}$$
(2.40)

 L_q and L_p are the shear in the safety factor and pressure profiles, and β is the total normalized pressure. There is a characteristic island width w_d related to diffusion rate, and a polarization characteristic size w_{pol} that tends to be larger [32]. The last term is a more explicit (and approximate) representation of Δ'_{GGJ} than in Equation 2.39. It is often neglected in conventional tokamaks [32].

Mode growth in the MRE is linear in time. The existence of terms with both signs in Equation 2.40 demonstrates immediately that the bootstrap term can destabilize a tearing mode in this model even if $\Delta' < 0$. However, the ion polarization term dominates for small w due to its $1/w^3$ dependence, and the w_d term in the bootstrap term means it is negligible for small islands. Curvature is also stabilizing on most flux surfaces, particularly for conventional tokamaks with $R_0/a \gg 1$. This mode is therefore metastable. For the bootstrap term to overcome the stabilizing forces of ion polarization, curvature, and Δ' , a seed island of sufficient size must be present. Seeds can arise from sawteeth, ELMs, or other local instabilities that form islands (in resistive plasmas, sawteeth have both ideal and

resistive components). Modes can also be seeded indirectly. CTMs can form the island [33, 34], which then grows linearly according to the MRE rather than the classical, quadratic growth rate. Nonlinear coupling can also seed tearing modes [35]. Any tearing mode with a linear growth rate, where the pressure gradient is the dominant drive even if Δ' was above 0 at some point during development, is called a neoclassical tearing mode (NTM). NTMs are a major concern in plasma stability because they can emerge under classically stable conditions, and NTM seeds are plentiful in most scenarios. Both NTMs and CTMs can be slowed by resistive drag and lock to the wall, whereupon they are called locked modes and can cause disruptions. This drag can derive from resistivity of the wall or from "error fields", asymmetries in the external magnetic field [36].

2.4 Nonlinear Mode Coupling

Like any coherent fluctuation, tearing modes can couple to each other nonlinearly [37–39]. This is distinct from linear coupling, which arises from two modes coupling to a static structure and does not comprise any higher-order components. The leading component in nonlinear multi-mode interactions is three-wave. This process can link any number of modes, even if the primary interaction is only three-wave in each case. The relationship between three-wave coupled fluctuations can be represented in a basic sense as $\Psi_3 = \Psi_1 \Psi_2$, where as in Equations 2.35–2.37, Ψ are the eigenfunctions. In a general system, as discussed earlier in this section with regard to the displacement ξ , one may approximate the eigenfunction $\Psi = \Psi(\mathbf{x})e^{i\mathbf{k}\cdot\mathbf{x}}$, where \mathbf{k} is the general wavenumber of the mode and \mathbf{x} is the position vector. Then in an axisymmetric torus, $\Psi(\mathbf{x}) = \Psi(r)$ and $\mathbf{k} \cdot \mathbf{x} = m\theta - n\phi$. Including the time component, where the modes oscillate at frequencies ω_i offset by phases φ_i :

$$\Psi_{3}(\mathbf{x},t) = \Psi_{1}(\mathbf{x},t) \cdot \Psi_{2}(\mathbf{x},t)$$

$$= \Psi_{1}(\mathbf{x}) \exp(i\mathbf{k}_{1} \cdot \mathbf{x} - i\omega_{1}t + \varphi_{1}) \cdot \Psi_{2}(\mathbf{x}) \exp(i\mathbf{k}_{2} \cdot \mathbf{x} - i\omega_{2}t + \varphi_{2})$$

$$= \Psi_{1}(r) \exp(im_{1}\theta - in_{1}\phi - i\omega_{1}t + \varphi_{1})$$

$$\cdot \Psi_{2}(r) \exp(im_{2}\theta - in_{2}\phi - i\omega_{2}t + \varphi_{2})$$

$$(2.41)$$

$$= \Psi_1(r)\Psi_2(r) \exp(i[(m_1 + m_2)\theta - (n_1 + n_2)\phi - (\omega_1 + \omega_2)t + (\varphi_1 + \varphi_2)]). \quad (2.42)$$

The three modes lock together. This solution demonstrates the three conditions that must hold for fluctuations to couple nonlinearly:

- 1. Frequency matching, $\omega_1 + \omega_2 = \omega_3$. I represent this as $f_1 + f_2 = f_3$ for real frequencies in kHz.
- 2. Wavenumber matching, $\mathbf{k}_1 + \mathbf{k}_2 = \mathbf{k}_3$. In a torus, this is equivalent to both $m_1 + m_2 = m_3$ and $n_1 + n_2 = n_3$.
- 3. Phase locking, $\varphi_1 + \varphi_2 = \varphi_3$.

When modes interact nonlinearly, they can transfer energy and momentum between each other [37]. It has been proposed that a coupling term be included in the modified Rutherford equation [40]. Nonlinear tearing mode coupling can also negatively affect plasma confinement and was first measured in the reversed-field pinch [38, 41]. Nonlinear tearing mode interactions were later identified in tokamaks as well [39]. Later work has identified that nonlinear coupling is a widespread phenomenon affecting many plasma instability types [38, 41–45]. Tearing modes can also couple to multiscale turbulence [46–49], or to transient edge instabilities [50]. However, core-edge coupling of coherent modes has not yet been measured. Chapter 6 describes the first detected case of this coupling. It has been hypothesized that nonlinear coupling is the cause of the tearing mode cascade. In the cascade, a series of tearing modes with successively smaller m and n (5,4; 4,3; 3,2; 2,1) emerge and precede a collapse in the value of normalized pressure β [51]. Tearing mode three-wave coupling has also been shown to have detrimental effects on plasma performance due to energy transfer to lower, more dangerous modes or seeding of the disruptive m, n = 2, 1 tearing mode [35, 52]. A gap between $f_1 + f_2$ and f_3 , called differential rotation, of 1 kHz or less has been found to be the threshold for coupling [53]. Nonlinear coupling within a single signal is calculated using bispectral analyis [54], which will be detailed in Chapter 6.

Bibliography

- [1] J. D. Callen. "Fundamentals of Plasma Physics". Draft material for "Fundamentals of Plasma Physics" book. 2003.
- [2] D. D. Schnack. Lectures in Magnetohydrodynamics: With an Appendix on Extended MHD. Lecture Notes in Physics. Berlin Heidelberg: Springer, 2009.
- [3] H. Zohm. Magnetohydrodynamic Stability of Tokamaks. Weinheim: WILEY-VCH Verlag GmbH & Co., 2015.
- [4] H. Alfvén. "On the existence of electromagnetic-hydrodynamic waves". Arkiv för matematik, astronomi och fysik 29 (1943), pp. 1–7.
- [5] J. P. Freidberg. *Ideal MHD*. Cambridge: Cambridge University Press, 1987.
- [6] I. B. Bernstein, E. A. Frieman, M. D. Kruskal, and R. M. Kulsrud. "An energy principle for hydromagnetic stability problems". Proceedings of the Royal Society of London. Series A. Mathematical and Physical Sciences 244.1236 (1958), pp. 17–40.
- [7] J. M. Greene and J. L. Johnson. "Interchange instabilities in ideal hydromagnetic theory". *Plasma Physics* 10.8 (1968), p. 729.
- [8] W. A. Newcomb. "Hydromagnetic stability of a diffuse linear pinch". *Annals of Physics* 10.2 (1960), pp. 232–267.
- [9] A. H. Glasser. "The direct criterion of Newcomb for the ideal MHD stability of an axisymmetric toroidal plasma". *Physics of Plasmas* 23.7 (2016), p. 072505.

- [10] B. B. Kadomtsev. "Disruptive instability in tokamaks". Fizika plazmy 1 (1975), pp. 710–715.
- [11] J. Wesson. Tokamaks. International Monographs on Plasma Physics. Clarendon Press, 2004.
- [12] W. W. Heidbrink and G. Sager. "The fishbone instability in the DIII-D tokamak".

 Nuclear Fusion 30.6 (1990), p. 1015.
- [13] V. D. Shafranov. "Equilibrium of a toroidal pinch in a magnetic field". Soviet Atomic Energy 13.6 (1963), pp. 1149–1158.
- [14] F. Wagner et al. "Recent results of H-mode studies on ASDEX". 13th International Conference on Plasma Physics and Controlled Nuclear Fusion. International Atomic Energy Agency. 1990, pp. 277–290.
- [15] A. W. Leonard et al. "The impact of ELMs on the ITER divertor". *Journal of Nuclear Materials* 266 (1999), pp. 109–117.
- [16] H. P. Furth, J. Killeen, and M. N. Rosenbluth. "Finite-resistivity instabilities of a sheet pinch". *Physics of Fluids* 6.4 (1963), pp. 459–484.
- [17] J. W. Dungey. "Interplanetary magnetic field and the auroral zones". *Physical Review Letters* 6.2 (1961), p. 47.
- [18] H. R. Strauss. "Resistive ballooning modes". The Physics of Fluids 24.11 (1981), pp. 2004–2009.
- [19] W. M. Solomon et al. "Experimental test of the neoclassical theory of impurity poloidal rotation in tokamaks". *Physics of Plasmas* 13.5 (2006).
- [20] B. Coppi, J. M. Greene, and J. L. Johnson. "Resistive instabilities in a diffuse linear pinch". *Nuclear Fusion* 6.2 (1966), p. 101.
- [21] H. P. Furth, P. H. Rutherford, and H. Selberg. "Tearing mode in the cylindrical tokamak". *Physics of Fluids* 16.7 (1973), pp. 1054–1063.

- [22] P. H. Rutherford et al. "Nonlinear growth of the tearing mode". *Physics of Fluids* 16.11 (1973), p. 1903.
- [23] G. Van Hoven and M. A. Cross. "Resistive instability of the sheet pinch". *Physics of Fluids* 14.6 (1971), pp. 1141–1142.
- [24] A. H. Glasser, J. M. Greene, and J. L. Johnson. "Resistive instabilities in general toroidal plasma configurations". *The Physics of Fluids* 18.7 (1975), pp. 875–888.
- [25] R. B. White, D. Monticello, M. N. Rosenbluth, and B. V. Waddell. Saturation of the tearing mode. Tech. rep. Princeton Plasma Physics Lab. (PPPL), Princeton, NJ (United States), 1976.
- [26] R. Carrera, R. D. Hazeltine, and M. Kotschenreuther. "Island bootstrap current modification of the nonlinear dynamics of the tearing mode". *Physics of Fluids* 29.4 (1986), p. 899.
- [27] Z. Chang et al. "Observation of nonlinear neoclassical pressure-gradient-driven tearing modes in TFTR". *Physical Review Letters* 74.23 (1995), p. 4663.
- [28] R. Fitzpatrick. "Helical temperature perturbations associated with tearing modes in tokamak plasmas". *Physics of Plasmas* 2.3 (1995), pp. 825–838.
- [29] N. N. Gorelenkov et al. "A threshold for excitation of neoclassical tearing modes".

 Physics of Plasmas 3.9 (1996), pp. 3379–3385.
- [30] A. B. Mikhailovskii et al. "Transport threshold model of subsonic neoclassical tearing modes in tokamaks". *Physics of Plasmas* 10.10 (2003), pp. 3975–3983.
- [31] M. Sato and M. Wakatani. "Study of neoclassical tearing modes based on a reduced MHD model in cylindrical geometry". *Nuclear Fusion* 45.2 (2005), p. 143.
- [32] R. J. La Haye. "Neoclassical tearing modes and their control". *Physics of Plasmas* 13.5 (2006), p. 055501.
- [33] E. D. Fredrickson. "Observation of spontaneous neoclassical tearing modes". *Physics of Plasmas* 9.2 (2002), pp. 548–559.

- [34] H. Reimerdes, O. Sauter, T. Goodman, and A. Pochelon. "From current-driven to neoclassically driven tearing modes". *Physical Review Letters* 88.10 (2002), p. 105005.
- [35] L. Bardóczi, N. C. Logan, and E. J. Strait. "Neoclassical tearing mode seeding by nonlinear three-wave interactions in tokamaks". *Physical Review Letters* 127.5 (2021), p. 055002.
- [36] A. Reiman and D. Monticello. "Tokamak error fields and locked modes". *Physics of Fluids B: Plasma Physics* 3.8 (1991), pp. 2230–2235.
- [37] C. P. Ritz, E. J. Powers, and R. D. Bengtson. "Experimental measurement of three-wave coupling and energy cascading". *Physics of Fluids B: Plasma Physics* 1.1 (1989), pp. 153–163.
- [38] J. S. Sarff et al. "Nonlinear coupling of tearing fluctuations in the Madison Symmetric Torus". *Physics of Fluids B: Plasma Physics* 5.7 (1993), pp. 2540–2545.
- [39] M. F. F. Nave, R. Coelho, E. Lazzaro, and F. Serra. "The influence of mode coupling on the non-linear evolution of tearing modes". European Physics Journal D 8 (2000), pp. 287–297.
- [40] R. M. Coelho, E. Lazzaro, M. F. Nave, and F. Serra. "Nonlinear coupling of rotating magnetic island triplets". *Physics of Plasmas* 6.4 (1999), pp. 1194–1202.
- [41] S. Assadi, S. C. Prager, and K. L. Sidikman. "Measurement of nonlinear mode coupling of tearing fluctuations". *Physical Review Letters* 69.2 (1992), p. 281.
- [42] A. Kleiner et al. "Neoclassical tearing mode seeding by coupling with infernal modes in low-shear tokamaks". *Nuclear Fusion* 56.9 (2016), p. 092007.
- [43] M. Xu et al. "Experimental observation of the localized coupling between geodesic acoustic mode and magnetic islands in tokamak plasmas". Nuclear Fusion 61.3 (2021), p. 036034.
- [44] X. Zhu et al. "Nonlinear mode couplings between geodesic acoustic mode and toroidal Alfvén eigenmodes in the EAST tokamak". *Physics of Plasmas* 29.6 (2022), p. 062504.

- [45] G. Riggs et al. "Time-resolved biphase signatures of quadratic nonlinearity observed in coupled Alfvén eigenmodes on the DIII-D tokamak". Physics of Plasmas 31.4 (2024), p. 042305.
- [46] L. Bardóczi et al. "Modulation of core turbulent density fluctuations by large-scale neoclassical tearing mode islands in the DIII-D tokamak". *Physical Review Letters* 116.21 (2016), p. 215001.
- [47] M. Jiang et al. "Localized modulation of turbulence by m/n= 1/1 magnetic islands in the HL-2A tokamak". Nuclear Fusion 59.6 (2019), p. 066019.
- [48] M. Jiang et al. "Modulation of the trapped electron driven turbulence by m/n = 2/1 tearing mode in the core of HL-2A plasmas". *Nuclear Fusion* 60.6 (2020), p. 066006.
- [49] M. J. Choi et al. "Effects of plasma turbulence on the nonlinear evolution of magnetic island in tokamak". *Nature Communications* 12.1 (2021), p. 375.
- [50] M. Jiang et al. "Coupling among neoclassical tearing modes, edge localized modes and Alfvén eigenmodes in HL-2A high β H-mode plasmas". Nuclear Fusion 62.7 (2022), p. 076025.
- [51] E. J. Strait et al. "MHD instabilities near the β limit in the doublet III-D tokamak". Physical Review Letters 62.11 (1989), p. 1282.
- [52] L. Bardoczi et al. "The root cause of disruptive NTMs and paths to stable operation in DIII-D ITER baseline scenario plasmas". Nuclear Fusion 64.12 (2024), p. 126005.
- [53] N. J. Richner et al. "Use of differential plasma rotation to prevent disruptive tearing mode onset from 3-wave coupling". *Nuclear Fusion* 64.10 (2024), p. 106036.
- [54] Y. C. Kim and E. J. Powers. "Digital bispectral analysis and its applications to non-linear wave interactions". *IEEE Transactions on Plasma Science* 7.2 (1979), pp. 120–131.

Chapter 3

Relevant Diagnostics and Analysis Tools

DIII-D and other fusion devices employ a wide set of diagnostics to measure equilibrium, varying, and fluctuating properties of the plasma and device, both locally and line-integrated over the plasma. One property of DIII-D that sets it apart from its contemporaries is its comprehensive suite of diagnostics. This thesis focuses on measurement of MHD fluctuations, with a particular emphasis on tearing modes. MHD fluctuations are typically comprised of magnetic, temperature, and density fluctuations and can be located anywhere in the plasma. As such, a variety of measurements can and must be be used to glean information about fluctuations in the plasma. For example, magnetic sensing coils on the vessel wall are less sensitive to modes resonant in the core or those that have higher m, n and therefore are more localized. Diagnostics such as the Radial Interferometer-Polarimeter (RIP) that view the entire plasma diameter have proven useful for measuring core-resonant and localized modes. This chapter describes the physics and operation of the DIII-D diagnostics used to collect the data analyzed for this thesis. It notes some advantages and disadvantages of each diagnostic type and how they can be synthesized to form a clear picture of what is occurring in the plasma.

Section 3.1 gives an overview of the most important equilibrium diagnostics on DIII-D and

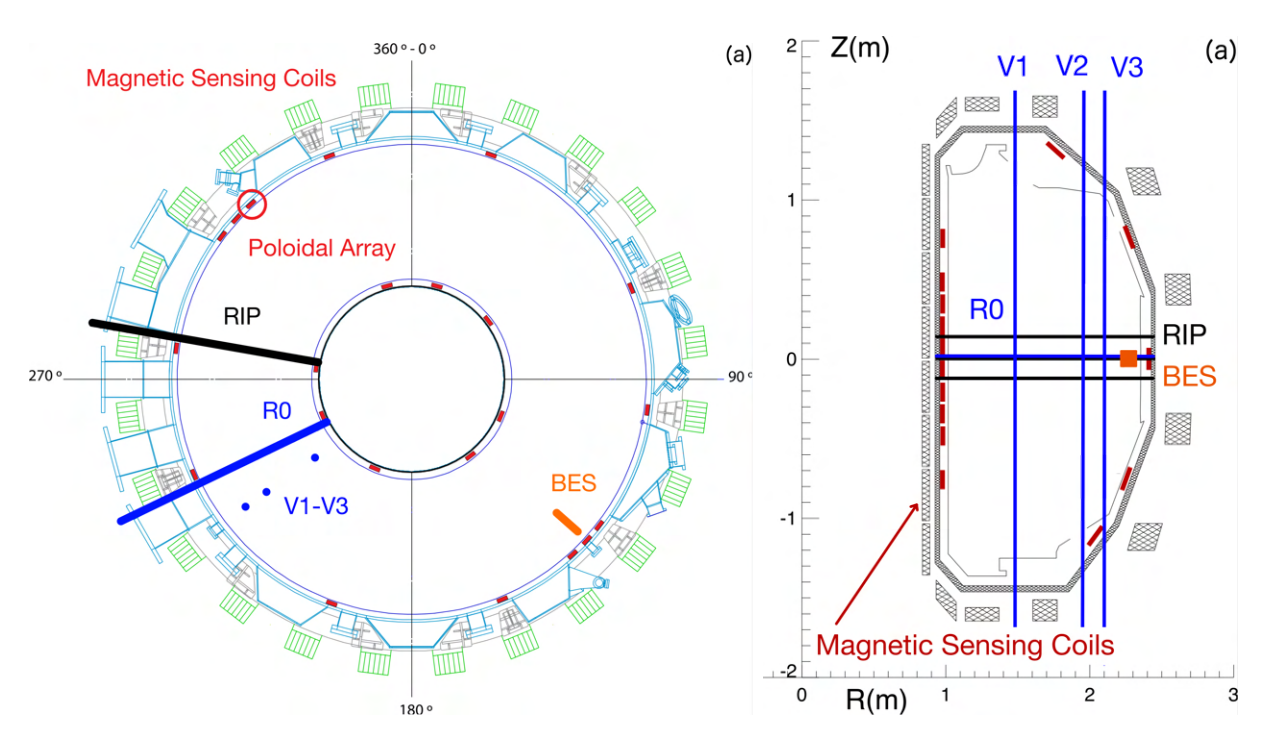


Figure 3.1: (a) Top-down and (b) cross-sectional cartoons of the DIII-D vessel with typical fluctuation diagnostic measurement locations and engineering coordinate system marked. RIP midplane chord vertical location overlaps with interferometry R0 chord. Cross-section collapses multiple toroidal locations into one: true diagnostic locations are as shown in (a). Original images property of General Atomics and altered to show additional diagnostic locations.

the typical fluctuation diagnostics used to characterize MHD modes. Section 3.2 addresses the relatively novel Faraday-effect polarimetry-interferometry method. This section discusses previous uses of polarimetry for plasma measurements and cases where it has an advantage over magnetic sensing coils. Section 3.3 details the RIP diagnostic and its use on DIII-D. A diagram of the locations of all discussed diagnostics is pictured in Figure 3.1. V1–V3 and R0 are chords from the CO₂ interferometer. Note that DIII-D has two angular coordinate systems. The engineering coordinates are used for labeling locations of diagnostics, and the physics coordinates are used for describing plasma current and magnetic fields [1]. The engineering coordinates are marked in Figure 3.1 as diagnostic location labels. The physics coordinates are as stated in Section 2.1, with a top-down view. Section 3.4 details the use of DIII-D diagnostic data in three analysis tools that are essential to the work presented in this thesis.

3.1 DIII-D Primary Diagnostics

Diagnostics on a plasma device can generally be divided into two categories: equilibrium and fluctuation. They may measure material properties, fields, or effects on the vessel, to name only a fraction of measurable quantities. Their measurements may be spatially localized or encompass large portions of the plasma. Equilibrium diagnostics provide snapshotlike measurements reflecting the overall state of the plasma. Fluctuation diagnostics measure more rapid variation in time overlaid on the equilibrium, where the rate of change of the signal is important. In this thesis, I focus on fluctuations in many quantities deriving from MHD modes at relatively low frequency, though I mention higher frequencies occasionally as examples. Equilibrium measurements are required to characterize the plasma state as fluctuations arise and propagate. The most basic diagnostics used on DIII-D are known as routine diagnostics and are standard for every run campaign. Other, more specific diagnostics are also discussed. Both equilbrium and fluctuation diagnostics fall into either or both categories. In general, the highest frequency of fluctuation measurable with a given diagnostic is half the sampling frequency. This is known as the Nyquist frequency or Nyquist limit. However, fluctuations at frequencies marginally below the Nyquist limit may have low amplitude and therefore be obscured by noise. Later in this thesis, one sees that the noise floor for fluctuation measurements depends on frequency and varies between diagnostics.

The most basic equilibrium measurements taken of the plasma in DIII-D are magnetic field, current, temperature, density, and rotation. Magnetic field and current are induced to constrain the scenario and are measured using external flux loops [2]. Temperature is measured locally to construct profiles within the plasma at as many spatial points as possible. Electron temperature may be measured using Thomson scattering [3] and the electron cyclotron emission radiometer (ECE) [4]. Electron density is measured both locally with Thomson scattering and as a line integral with interferometry [5]. All quantities for ions; temperature, density, and rotation; are measured using charge-exchange recombination spectroscopy (CER) [6]. The current profile can be measured using the motional Stark effect

(MSE) polarimeter [7], which are used to construct equilibrium models. Visible-light filter-scopes [8] in the divertor are used to detect ELMs. ECE and interferometry can also be used to measure fluctuations. Beam-emission spectroscopy (BES) [9] can be used for local density fluctuations, and an extensive set of external sensing coils [2] measure magnetic fluctuations.

Thomson scattering [3] measurements are taken using lasers directed on 10 different paths through the plasma: core, tangential, and divertor. The core beams are directed vertically, localizing their measurements at a fixed radial location. The tangential beams pass horizontally near the magnetic axis, and measure closest to the core. One beam views a single location in the divertor. When the beams scatter off electrons, the emitted light yields both temperature and density measurements. The intensity of the light reaching the detector is related to density, and the spectral width and blue shift indicate temperature. The beams are pulsed at 20 and 50 Hz depending on the beam and are therefore best adapted to a longer time frame. Thomson scattering can also be used in "bunch mode", which tunes the phases of each beam such that the profile can be viewed with higher resolution for a short window [10]. This is useful for resolving rapid changes in profile but must be timed precisely.

ECE [4] measures the electron temperature profile. It is both an equilibrium and a fluctuation diagnostic as its data is sampled at both 5 kHz and 500 kHz. It has 48 channels that measure along a single radial chord at a toroidal angle of 81 degrees. Each channel views electron cyclotron radiation emitted from the plasma at a certain frequency between 83.5-129.5 GHz, filtered using band-pass filters. Since the plasma is optically thick, electron cyclotron emission at a radial layer resembles that of a black body, and therefore directly depends on temperature. The radial location of the measurement depends upon the detection frequency using the typical formula for cyclotron radius. This is a major radial component, so the exact ECE locations in minor radial coordinate depends on the size and flux surface shape of the plasma. For high density, certain ECE channels may be cut off or receive little signal. This results from the index of refraction dropping too low and making propagation

of the wave impossible. Density required for cutoff depends on frequency, so only a selection of the channels are ever cut off. This may still leave a significant portion of the T_e profile unable to be fit. Temperature fluctuations are measured with ECE in a similar way to equilibrium temperature; locations are the same, and emission fluctuation amplitudes can be directly converted to temperature fluctuation amplitudes. A separate, localized two-dimensional array of ECE channels varying in both height and frequency is used for ECE imaging (ECE-I) [11]. ECE-I can be used to track mode movement in time [12].

The two-color CO_2 interferometer [5] measures line-integrated electron density and its fluctuations along four chords. One radial chord, called R0, is located at z=0, where z is the vertical distance above the midplane, and the others are vertical and located at R=1.48 m, 1.94 m, and 2.10 m. The vertical chords are called V1, V2, and V3 in the order of their locations. Toroidally, R0 is located at 240 degrees and V1–V3 at 225 degrees. The chord locations are shown in Figure 3.1. Interferometry operates by measuring the phase shift of an incident beam, versus a reference beam, as it traverses a dense material with a different index of refraction. Here, a beam is emitted from a CO_2 laser. A HeNe laser is used to calculate and subtract off a vibration component, not proportional to wavelength, to isolate the interference-related phase shift. This is the origin of the term two-color. In the most basic of senses, interferometry measures the line-integrated electron density:

$$\Phi_I = c_I \int n_e \, \mathrm{d}l \tag{3.1}$$

Here Φ_I is the interferometry phase, λ is the wavelength of the beam, and I define the constant $c_I = 2.82 \times 10^{-15} \lambda$. The CO₂ interferometer is the standard diagnostic used to measure average electron density. It is also a useful source of density fluctuation measurements, once again line-integrated. Line-integrated density fluctuations are taken from the fluctuating component $\tilde{\Phi}_I \sim \int \tilde{n}_e \mathrm{d}l$ of the interferometry phase.

The last important equilibrium diagnostic to discuss is charge-exchange recombination spectroscopy [6]. When neutral atoms from the NBI system impinge upon ions in the plasma,

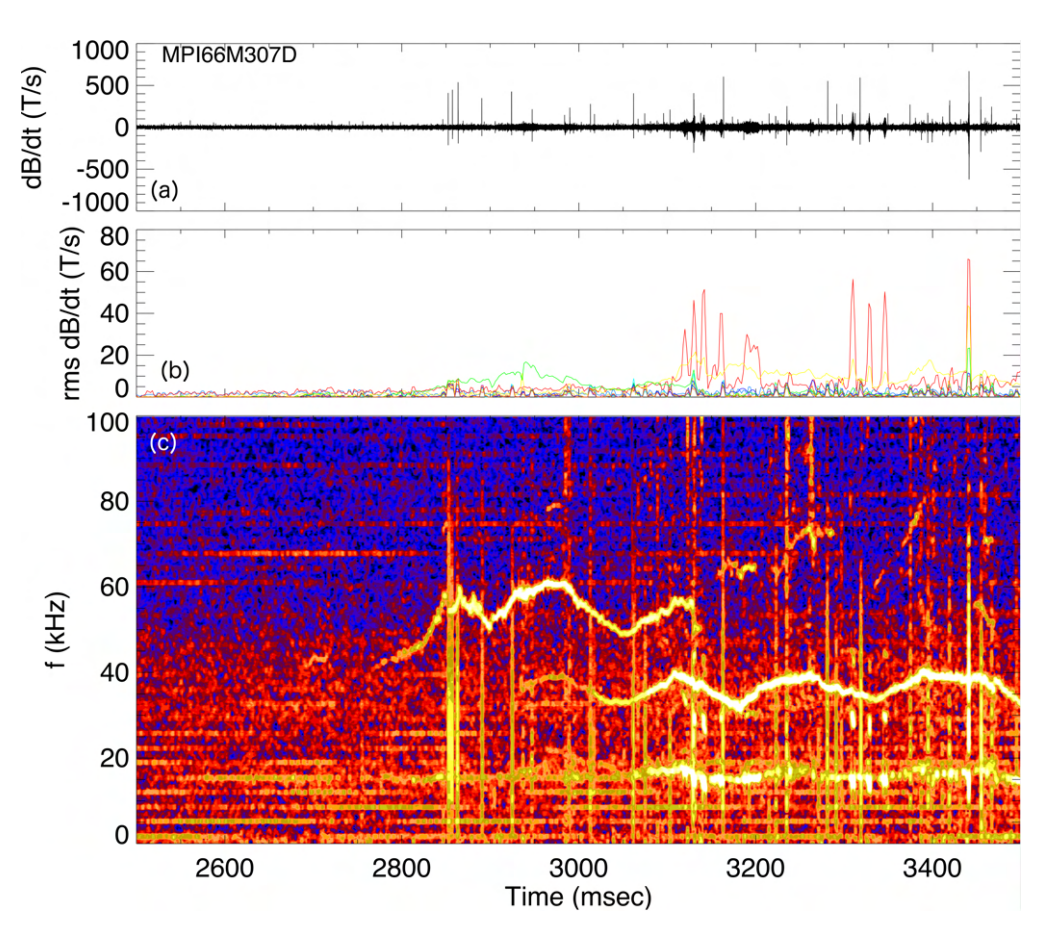
they exchange electrons with the ions and emit radiation. Typically, these measurements are taken from neutral beam atoms as they exchange an electron with carbon impurity ions. DIII-D's graphite walls mean that some degree of carbon impurity is ubiquitous. Carbon is preferred for CER in many cases, since carbon emission lines are easier to measure than deuterium. CER measuring emission from impingement of the beam on deuterium ions exists but is more restricted; carbon is sufficient for most purposes. The carbon system views along 44 tangential chords and 32 vertical chords at fixed locations on the vessel. Emission is measured at the location of charge exchange, which is the intersection of the viewing chord and the beam. CER emission can be classified by its Doppler broadening, Doppler shift, and total spectral intensity. Ion temperature can be calculated from Doppler broadening, rotation from Doppler shift, and density from spectral intensity. Rotation is typically toroidal rotation, measured with the tangential channels and corrected for the angle between the rotation and the chord. Poloidal rotation can also be calculated from the vertical chords but is not automatically corrected. Toroidal rotation is generally an order of magnitude faster than poloidal rotation and can be taken as the total plasma rotation. All three CER-measured quantities can be used to construct radial profiles. The extremeultraviolet SPRED spectrometer is used for measuring impurities [13]. SPRED also measures light emitted as beam neutrals impinge upon impurities, but in the range associated with the impurity rather than the beam neutral. Emission in this frequency range is used to measure impurity density.

Local density fluctuations can be measured by either BES [9] or Doppler backscattering. The research described in this thesis makes use of BES. BES measures emission from collisions between the neutral beams and electrons. The detected wavelength is the deuterium-alpha (D_{α}) line, emitted as an excited deuterium atom decays from the n=3 to n=2 state. BES has 64 sightlines, which are tangential and view the radial and vertical locations where they cross the beam. They can cross the beam at any location, though BES is less effective in the deep core, and arranged in any possible grid configuration. Typically, an 8×8 or 16×4

grid is used. A typical BES location is shown in Figure 3.1.

DIII-D's external magnetic diagnostic system [2] is comprised of a number of magnetic coils and flux loops for measuring plasma and coil current, pressure, local flux, and magnetic fluctuations. I primarily discuss the latter two. Flux loops measure the poloidal flux at the boundary, which can be used in analysis to calculate the plasma shape. They are arranged in an array circling the plasma poloidally; equilibrium reconstruction assumes the plasma is axisymmetric. The sensing coils are used to measure both equilibrium and fluctuating fields. In all cases, magnetic fluctuation amplitudes are calculated using the Fourier transform of the time-integrated \dot{B} signal. The sensing coils are arranged in both toroidal and poloidal arrays, with additional probes located in the divertor. The locations of the sensing coils are depicted in red in both sections of Figure 3.1; the toroidal array is at the midplane, and the poloidal array is at 322 degrees. Most of the magnetic probes are digitized at 200 kHz, giving them a bandwidth of 100 kHz. Five fast magnetic probes are digitized up to 1.1 MHz, but they do not span the device. For this reason, the magnetics are optimized to measure lower-frequency, rotating magnetic fluctuations such as tearing modes.

The existence of a full array allows mode numbers to be measured. Signals at different locations, whether toroidal or poloidal, are offset as the mode moves past. For a coherent mode, the difference in phase between signals of a given frequency at different probes is proportional to the angular coordinate separating the probes multiplied by its respective mode number $(m\theta \text{ or } n\phi)$. The mode makes m or n turns per poloidal or toroidal revolution, respectively. For a full set of probes, the phase difference of the mode from a reference probe can be calculated for the entire array and fit to a linear model to calculate mode number. The code Modespec [14] is used to filter magnetic probe data for a given frequency and fit data at that frequency to its respective mode numbers. Modespec also plots spectrograms of coil data. Data from any fluctuation diagnostic can be converted to a spectrogram, which is a convenient way to identify modes and their frequencies by eye. Sample output from Modespec is shown in Figure 3.2.



Shot 180704 3398.00 - 3402.00 ms 39.25 kHz

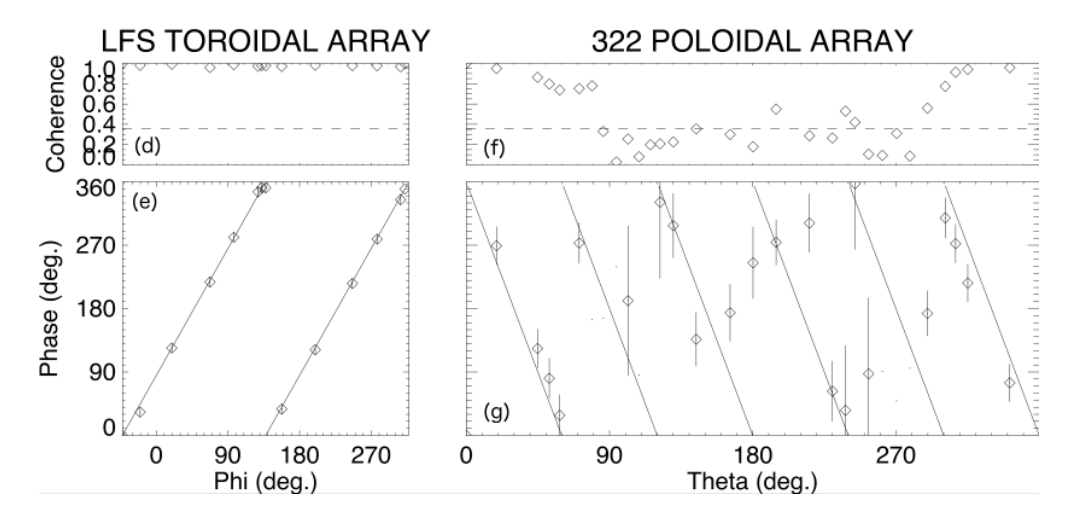


Figure 3.2: Partial Modespec output for DIII-D shot #180704.

The upper half of Figure 3.2 is an overview window showing a portion of a DIII-D shot. A raw B signal from a single magnetic coil is plotted in (a), showing coherent fluctuations in narrow frequency bands due to magnetic modes and vertical stripes due to ELMs. Note the name of the coil, which includes its toroidal location in degrees (307). RMS fluctuation strength is shown in (b). Amplitudes are distinguished by mode number; red (n = 1) dominates due to bursts at lower frequencies, but yellow (n = 2) and green (n = 3) are also visible. A spectrogram of magnetic signals is pictured in (c). Spectrograms are calculated using the short-time Fourier transform and represent through color the strength of a fluctuation at a given frequency at a given time. Modespec spectrograms plot for each frequency and time the cross-power spectral density (CSD) over time between two coils in the toroidal array. Cross-power is the easiest method for distinguishing the phase of toroidally rotating modes and also removes some noise. Here, bright, coherent bands that vary smoothly in frequency are tearing modes. Broadband vertical stripes are ELMs, and background magnetic noise is noticeable up to about 50 kHz as a horizontal band. The horizontal lines are due to pickup or interference from equipment rather than any MHD mode. Note the frequency limit at 100 kHz, the Nyquist limit for all coils when this shot was taken.

The lower half of Figure 3.2 illustrates how mode numbers are calculated from coil data. All phases here are taken from the short-time Fourier transform of the signal over a 4 ms window for a fixed frequency. On the left is data from the toroidal array on the low-field (outboard) side. The x-axis, Phi, is the toroidal separation of each coil from the machine origin. The phase offset of each signal is compared to a reference signal, set at 0 degrees. A linear fit with optional corrections is made to the phase data, returning to zero if necessary. The mode makes two full transits over one revolution of the machine. The signals are coherent, as seen in (d). The linear fit to the phase offset data, pictured in (e), is repeated for each specified mode number, and the best fit using the χ^2 method is reported as the mode number. Here, χ^2 is lowest for n=2 for the 39.25 kHz mode. The right plots (f) and (g) measure the same quantities for the poloidal array situated at machine location 322

degrees. The coils in this array vary in poloidal angle, represented as θ on the x-axis. For this array, mode phase and number must be estimated, since half of the array is positioned on the high-field (inboard) side and less sensitive to modes that peak on the low-field side. In addition, those coils are detecting harmonics of those modes, generated by the plasma geometry, with a variety of mode numbers. Note the low coherence between 90 and 270 degrees. The role of harmonics will be discussed further in Chapter 4. In this case, m is reported as -6, so the mode is moving in the $-\hat{\theta}$ direction. I describe mode numbers using their absolute values. Often, especially for m > 5 and n > 5, it is better to refer to mode numbers as an estimate. For mode numbers above these values, fitting to the same number of coils becomes more complicated.

3.2 Polarimetry-Interferometry

While the magnetic coils are very successful at measuring magnetic fluctuations and mode numbers near the edge, they are less successful when addressing core-localized modes because the fluctuation amplitudes decay as r^{-m-1} far from the resonant surface. I now outline the principles of Faraday-effect polarimetry, which is the primary diagnostic used in this thesis and is shown to be very effective in the core. Polarimetry also measures magnetic field and its fluctuations. When linearly polarized light passes through a magnetic field, its polarization is rotated through the Faraday effect. This effect can be explained through the decomposition of linearly polarized light into left- and right-hand circularly polarized components, each of whose electric fields rotate in opposite directions at the frequency of the light. Faraday rotation is derived as follows: [15]

Assume an electromagnetic wave of frequency ω and electric field components E_x and E_y , propagating along the z-axis in the presence of a magnetic field $B_0\hat{z}$. Then the wave electric field can be described by

$$\mathbf{E} = E_{+}e^{i(k_{+}z-\omega t)}\mathbf{e}_{+} + E_{-}e^{i(k_{-}z-\omega t)}\mathbf{e}_{-}$$
(3.2)

where $\mathbf{e}_{\pm} = \frac{1}{2}(\hat{x} \mp i\hat{y})$ and $E_{\pm} = E_x \pm iE_y$. The first term represents right-hand circularly polarized light and the second term left-hand circularly polarized light. If $E_x \neq E_y$ and both are nonzero, then the light is called elliptically polarized.

In a magnetized material, the electric field of each component causes a separation of charges and, due to the rotating polarization, circular motion of the charges, which induces an additional magnetic field. The magnetic fields induced for each component are in opposite directions. The magnetic field then slows one of the components with respect to the other and causes a phase shift, which corresponds to a rotation of the plane of polarization when the components are recombined. Another interpretation of this mechanism is that the dielectric constant of a material in a magnetic field is different for left- and right-handed circularly polarized light:

$$\epsilon_{\pm} = 1 - \frac{\omega_p^2}{\omega(\omega \pm \Omega)},\tag{3.3}$$

which causes the index of refraction to vary based on polarization and each polarization to have a different wave number

$$k_{\pm} = k \pm \Delta k$$

$$= \omega \left(1 - \frac{1}{2} \left(\frac{\omega_p^2}{\omega^2} \right) \right) \pm \frac{1}{2} \left(\frac{\omega_p^2}{\omega^2} \right) \frac{\Omega}{c}.$$
(3.4)

The angle by which the plane of polarization of the wave rotates is equal to $\varphi = \tan^{-1}(E_y/E_x) = \Delta kz$. Therefore, as the wave propagates, the plane rotates by an angle proportional to the frequency and path length. The rotation of the beam thus induced, known as Faraday rotation, is also proportional to the magnetic field and density. A diagram of Faraday rotation is presented in Figure 3.3. Measurement of Faraday rotation is called Faraday-effect polarimetry and can be used to measure magnetic field in plasmas in addition to solid-state materials. The understanding that magnetic fields in the ionosphere led to Faraday rotation [16] led to the development of polarimetry for measuring internal magnetic fields in fusion devices such as tokamaks.

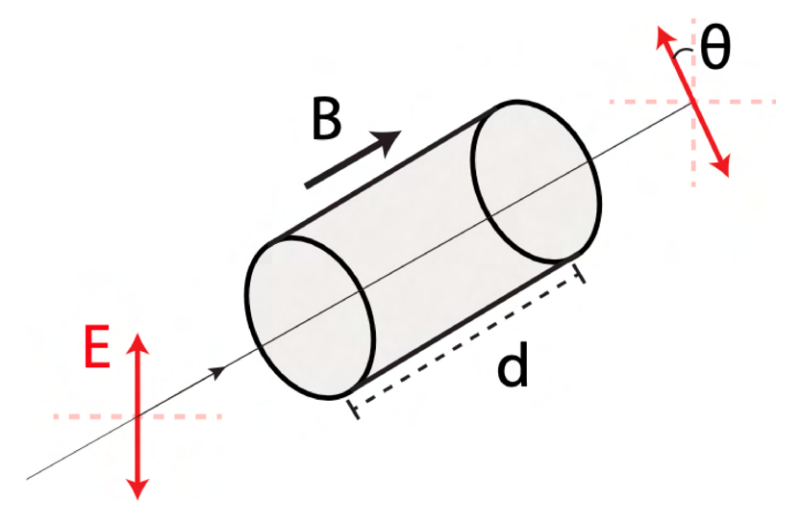


Figure 3.3: A diagram of the Faraday effect. The electric field \mathbf{E} of the light is rotated by angle θ in response to passing through a material with magnetic field \mathbf{B} along the path with length d. Reproduced from [17].

The first combined Faraday-effect polarimeter for use in plasmas was developed by Dodel and Kunz [18] for measurement of poloidal magnetic field on the TFR tokamak [19]. Dodel and Kunz's system is known as a two-wave system due to its use of two separately created collinear laser beams. The superimposed right-hand and left-hand circularly polarized beams differ in frequency by ω_m and form a linearly polarized beam whose plane of polarization rotates at frequency $\omega_m/2$. The so-called modulation frequency, now typically called the intermediate frequency (IF), is tuned so as to be compatible with detectors sensitive to frequencies of that magnitude. Prior to rotation, the detected signal is proportional to $\cos(\omega_m t)$. After passing through a magnetized plasma, the polarizations of the left- and right-handed beams undergo phase shifts ϕ_L and ϕ_R respectively, proportional to the line-integrated magnetic field and density along the beam path. Given that the beams are superimposed, this once again forms a linearly polarized beam whose plane of polarization is rotated, in comparison to a reference beam whose signal varies as $\cos(\omega_m t)$, by $2\Phi_F$, where $\Phi_F = (\phi_L - \phi_R)/2$. The Faraday rotation of the beam is equal to

$$\Phi_F = c_F \int n_e \ B_l \mathrm{d}l. \tag{3.5}$$

As in Equation 3.1, λ is the wavelength of the incoming light beam. The integration variable l is the spatial coordinate along the path of the beam. I henceforth define the constant $c_F = 2.62 \times 10^{-13} \lambda^2$.

The Dodel-Kunz polarimeter configuration included a Véron interferometer [20] using the same beams to measure both density and magnetic field, with the resultant interferometry phase Φ_I being calculated as in Equation 3.1. Simultaneous interferometry produces an absolutely calibrated measurement and allows the magnetic field amplitude to be extracted from the Faraday rotation. Since Faraday rotation $\Phi_F \sim \int n_e B_l dl$ and interferometry phase $\Phi_I \sim \int n_e dl$, one can obtain a line-averaged measurement $B_l \sim (\int n_e B_l dl)/(\int n_e dl) \sim \Phi_F/\Phi_I$. This calculation assumes a flat density profile.

Since Kunz's initial implementation, both the capabilities and configurations of interferometer-polarimeter systems have been expanded. A heterodyne system, where after the beam passes through the plasma a beam splitter separates the components into those parallel and perpendicular to the reference beam for measurement, reduces noise [21]. Experiments on MTX incorporated a small degree of elliptical polarization to reduce refraction effects [22]. In addition, various interferometer-polarimeter configurations have been applied to fusion devices for measuring quantities other than line-integrated magnetic field. Expanding the diagnostic to include multiple vertical beams, passing through the plasma at a single toroidal location but different radii, allows measurement of the poloidal magnetic field, current, and safety factor profiles [22, 23].

Polarimetry-interferometry has also been expanded [24] [25], with the advent of increasingly precise detectors, to measure fluctuations in the magnetic field. Polarimetric and interferometric fluctuation measurements are taken from fluctuations in the polarimetry and interferometry phases:

$$\delta\Phi_F = c_F \left(\delta \int n_e B_l dl\right) = c_F \left(\int \delta n_e B_l dl + \int n_e \delta B_l dl + \int \delta n_e \delta B_l dl\right)$$
(3.6)

$$\delta\Phi_I = c_I \left(\delta \int n_e \, \mathrm{d}l\right) = c_I \int \delta n_e \, \mathrm{d}l. \tag{3.7}$$

The second-order term in the polarimetry can be neglected for small fluctuations. Therefore, Faraday angle fluctuations contain a magnetic and a density fluctuation component. The density component, being proportional to the absolute magnetic field, is small for small absolute magnetic field or beam paths perpendicular to the magnetic field, as shown quantitatively in section 3.3.

Faraday-effect interferometry-polarimetry has been used to great effect [26, 27] on the Madison Symmetric Torus (MST) reversed field pinch (RFP) to measure equilibrium magnetic field and current profiles, as in TEXTOR, and fast internal magnetic fluctuations associated with both the sawtooth dynamo [28] and tearing modes [29]. This system is usually referred to as the far-infrared (FIR) system and consists of eleven chords. As in TEXTOR, the FIR beams cross the plasma vertically and are used to measure the Faraday rotation profile. The spatial derivative of the Faraday rotation profile is used to find the central current density:

$$J(0) = \frac{2}{c\mu_0} \frac{d\Psi}{dx} \frac{1}{\int n_e f(r, \alpha) dz}$$
(3.8)

where c is a constant, Ψ is the profile of the Faraday rotation found from all chords, and $f(r,\alpha)$ is a function representing the current profile shape.

I particularly note the use of the FIR system to measure the strength, spectra, and profiles of magnetic fluctuations associated with tearing modes. The FIR chord at the vertical midplane measures radial fluctuations, which for symmetrical resonant surfaces equate to the line-integrated tearing mode amplitude. This chord approximately passes through the magnetic axis, though this varies due to Shafranov shift or distortions due to sawtooth crashes. In MST, the m, n = 1, 6 tearing mode is typically dominant and interacts with tearing modes at nearby resonant surfaces through interaction with a m, n = 0, 1 mode [30]. The vertical FIR interferometer chords were able to localize the m, n = 1, 6 tearing mode to a region where q = m/n as expected.

In addition to TEXTOR and MST, other notable interferometry-polarimetry systems are located on J-TEXT [31] and EAST [32, 33]. The system on EAST is particularly relevant to

this thesis because of its double-pass, radially-viewing configuration. The radial configuration is advantageous for diverted, shaped plasmas as it crosses the plasma in a region of relative local symmetry and obtains, to good approximation, magnetic field measurements that are purely radial. In the double-pass configuration, retro-reflectors are employed to reflect the beams back to the origin point. In contrast, the FIR system on MST was single-pass, with detectors on the far side of the plasma from the lasers. The double-pass configuration preserves space, since both the source and the detector are on the outboard side. The beam also undergoes double the Faraday rotation versus the single-pass configuration.

3.3 The Radial Interferometer-Polarimeter

A fast Faraday-effect polarimetry system, the Radial Interferometer-Polarimeter (RIP), has now been implemented on DIII-D [34, 35]. RIP is double-pass and radially-viewing like the polarimetry system on EAST, incorporating three vertically-separated chords at (z=0), above (z = 13.5 cm), and below (z = -13.5 cm) the midplane, as also shown in Figure 3.4. Note that for a double-pass system, the direction of Faraday rotation of the beam reverses in the lab frame upon 180° reflection. However, since the wavenumber of the beam also reverses, the polarization rotation in the beam's frame of reference is in the same direction for the returning beam as for the incident beam. This system is specifically designed for high time resolution, able to measure fluctuations of frequencies up to 2.5 MHz for polarimetry and 5 MHz for interferometry. These frequency ranges include micro-tearing modes and broadband electromagnetic turbulence in addition to large-scale tearing modes [36, 37]. RIP uses the original two-wave configuration of Dodel and Kunz [34], as shown in Figure 3.4. In this case of the two-wave system, the superimposed waves at intermediate frequency ω_m feed into a reference detector before being transformed into left- and right-handed polarized beams and sent through the plasma. By passing the probe beam through a beam splitter, half of the beam is sent through the plasma, and the other half is reflected. The reflected portion is used as the local oscillator, which is combined with the return beam to form the interferometry measurement [34].

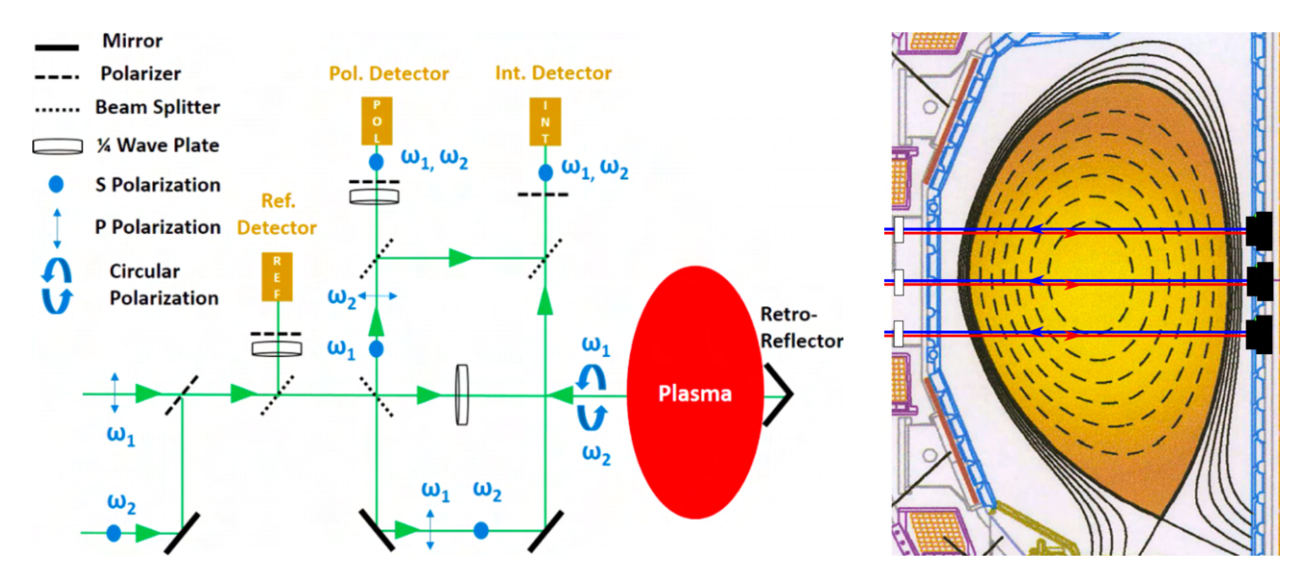


Figure 3.4: Left: A schematic of the two-wave principle, with the two frequencies, separate polarimetry and interferometry detectors, and retro-reflector highlighted. Replicated from [34]. Right: A diagram of RIP on DIII-D showing the three horizontal chords. Image courtesy D. L. Brower and J. Chen.

Several other interferometer-polarimeters instead used a three-wave configuration, where the two waves at ω_1 and ω_2 are mixed with a wave at a third reference frequency and phases are measured from signals at $|\omega_2 - \omega_1|$, $|\omega_3 - \omega_2|$, and $|\omega_3 - \omega_1|$ within a single signal spectrum. This allows the interferometric phase shift to be calculated from the latter two measurements and removes the need for a separate interferometry detector [26, 38]. However, the three-wave configuration increases phase noise, which is most important to minimize when the desired signal is of high frequency [34].

RIP was initially set up with 432 μ m CO₂ lasers as its beam sources and a signal bandwidth of 2 MHz. Initial results showed good correspondence between density measurements from the RIP interferometer midplane chord and the CO₂ interferometer radial chord, with a difference of approximately 2% between their values in the flattop [34]. RIP was then upgraded with 650 GHz, 461 μ m solid-state sources, supplied by Virginia Diodes, to improve beam power and frequency stability. These sources enabled an increased maximum bandwidth of 10 MHz (5 MHz for polarimetry) and decreased the standard deviation of the beam frequency by a factor of five [35]. Once the upgrade to solid-state sources was completed,

absolute measurement of magnetic fluctuations began and RIP data could be compared to other magnetic fluctuation diagnostics on DIII-D.

As described in Section 3.1, measurements of magnetic fluctuations within DIII-D are typically carried out using the magnetic sensing coils [2, 39], as is also done on many other devices. However, magnetic fluctuation eigenfunction amplitudes away from the resonant surface r_s can be estimated to decay radially as $(r/r_s)^{-(m+1)}$, where m is the poloidal mode number [40]. The coils' external location proves disadvantageous when measuring localized or core-resonant magnetic fluctuations, as can arise from both tearing modes and high-frequency turbulence. The advantage of RIP in this context is the ability to measure fluctuations at any radial location within the plasma, agnostic to the resonant surface location aside from the density-weighting of Faraday rotation measurements. This allows detection of modes whose eigenfunctions have decayed significantly toward the plasma edge, where the coils are effective. RIP has detected core-resonant, localized tearing modes earlier than magnetic coils, demonstrating its capabilities and motivating further investigation of tearing mode detection [41].

RIP's lowest sampling rate of 2 MHz and Nyquist frequency of 1 MHz are an order of magnitude larger than the sampling rate of 200 kHz and Nyquist frequency of 100 kHz for the main toroidal and poloidal coil arrays. RIP's large frequency bandwidth has allowed it to be used for magnetic turbulence measurements up to 500 kHz [36, 37]. However, RIP's line-integrated nature does not allow it to measure fluctuation origin or phase, which means it cannot be used to determine mode numbers. A fourth chord, located vertically at the midplane and toroidally separated from the other chords by 3.6° , has been implemented to partially account for this drawback. The purpose of the toroidally-separated chord is to measure the toroidal mode number n of MHD instabilities such as large-scale tearing modes and micro-tearing modes in the pedestal. This is done by measuring the phase shift of the mode between the midplane and toroidal chords similarly to the method used for the coils. As it rotates past the chords, a mode of mode number n undergoes a phase shift equal to

the toroidal separation of the chords multiplied by n. Mode numbers of both tearing modes and turbulence have been identified up to n = 50 [42].

RIP data may be confounded by several factors, including polarization distortion, the Cotton-Mouton (CM) effect, non-collinearity of the two probe beams along each chord, and optical feedback, all of which have been considered and mitigated [35]. The CM effect is a separate polarization rotation of the beam, dependent on the perpendicular magnetic field component, as follows:

$$\varphi_{CM} = 2.46 \times 10^{-11} \lambda^3 \int n_e \ B_{\perp}^2 dl.$$
 (3.9)

The CM effect becomes relevant at high density and magnetic field and couples to the Faraday effect, restricting the degree to which it can be removed from the data [35, 43]. For this reason, RIP data is not recommended to be used above $n_{e,avg}B_T^2 \approx 20 \text{ T}^2\text{m}^{-3}$, where $n_{e,avg}$ is the line-averaged electron density and B_T is the toroidal magnetic field. This corresponds to a density of $5 \times 10^{19} \text{ m}^{-3}$ for a typical DIII-D toroidal field of 2 T and is generally sufficient. The addition of the toroidally separated chord, which operates at higher frequency, allows a higher limit of $n_{e,avg}B_T^2 \approx 58$, covering all accessible regimes on DIII-D. A first-order estimate of the CM effect contribution for typical plasmas of interest is calculated in Section 4.1. Highly peaked core plasma density can also cause refraction of the beams, as is relevant in Chapter 5.

A method for reducing error in RIP not mentioned in [35] is correlation polarimetry-interferometry (CPI). Correlation between diagnostics is useful for reducing noise and detecting fluctuations below the noise floor of either diagnostic [44]. If a single diagnostic detects multiple signals, then the correlation technique can be used without relying on multiple diagnostics. This method was applied to the FIR system on MST, where the single beams for each chord were split using a beam splitter after having passed through the plasma and being Faraday-rotated [45]. Each half of the beam passed through a separate lens and into a separate mixer. The reference beam was also split and the Faraday-rotated beam compared to it as in the original single-mixer system. This provides two separate signals

for a single chord, called A and B, with independent noise and, ideally, otherwise identical signals. The Faraday rotation for a single signal is [45]

$$\Psi = \psi_{probe} - \psi_{ref} = \psi_{plasma} + \psi_{n,probe} + \psi_{n,ref}$$
(3.10)

where each ψ_n is the noise in the measurement from each beam. When two signals Ψ_a and Ψ_b are correlated, since ψ_{plasma} is the "true" value, $\psi_{plasma,a} = \psi_{plasma,b}$ and

$$\langle \Psi_a \Psi_b \rangle = \langle (\psi_{plasma,a} + \psi_{n,a}) (\psi_{plasma,b} + \psi_{n,b}) \rangle$$
$$= \langle \psi_{plasma} \psi_{plasma} \rangle + \langle \psi_{n,a} \psi_{n,b} \rangle$$
(3.11)

since one can assume the noise is incoherent and uncorrelated. The noise component $\langle \psi_{n,a}\psi_{n,b}\rangle$ can then be subtracted and the signal component retained. The correlation method reduced noise on the MST FIR system by an order of magnitude across the entire frequency spectrum in bench tests [45].

CPI was then in turn implemented on the DIII-D RIP system and also proved successful in bench tests, reducing noise by over an order of magnitude in both polarimetry and interferometry measurements. After the completion of the bench test, RIP was used to detect broadband, high-frequency MHD fluctuations below the previous noise floor in the H-mode flattop [46]. As of the writing of this thesis, CPI continues to be operational on RIP but has not been used in quantitative measurements of mode amplitude. This thesis uses the correlation method in both interferometry and polarimetry to obtain increased accuracy in amplitude measurements of low-frequency fluctuations.

CPI, in addition to detecting low-amplitude fluctuations, can be used to evaluate RIP data quality [47]. When measurement uncertainty is high, the signals a and b may exhibit significant deviations from each other, particularly in polarimetric data. In that case, the correlation is low and $\langle \Psi_a \Psi_b \rangle$ may be low in turn, significantly less than $\langle \Psi_a \rangle \langle \Psi_b \rangle$ indicating that the majority of the signal is made up of uncorrelated components. Methods to

account for uncertainty in datasets detected using CPI include time-averaging for lengthy signals such as tearing modes and ensemble-averaging for dynamic, repeated events such as sawteeth [47]. Causes of uncertainty and noise in RIP data include vibration effects, beam deflection, refraction caused by peaked core density profiles, and variation in incident beam magnitude. Measurement of fluctuations by interferometry is generally more robust to uncertainty and decorrelation. This is because fluctuations make up a much greater portion of the overall polarimetry signal than the interferometry signal, so for a fixed noise ratio, the noise amplitude is closer to the polarimetry amplitude.

Some measures for RIP data quality using CPI are:

Cross-power spectral density:
$$CSD = |S_{xy}(f)|^2$$
 (3.12)

Cross-coherence:
$$C_{xy} = \frac{|S_{xy}(f)|^2}{S_{xx}(f)S_{yy}(f)}$$
 (3.13)

Cross-phase:
$$\Im(S_{xx}(f))$$
 (3.14)

where $S_{xy} = F_x F_y^*$ is the cross-correlation between the signals and $S_{xx} = |F_x|^2$ is the auto-correlation between each signal and itself, also known as the auto-power spectral density or periodogram. High RIP data quality is indicated by (1) a strong CSD that tracks with the amplitude on both channels, (2) a cross-coherence near 1, and (3) a consistent cross-phase over time. It should also be noted that these measures may be applied to any pair of signals. They are used later to identify that a single mode has been observed on multiple signals.

3.4 Computational Tools

3.4.1 TJ

I use the code TJ^1 [48] to solve the infinite-conductivity equation (Equation 2.37) for the structure of a single mode in a specified equilibrium. In the case of TJ, the equilibrium shape is parametrized by an arbitrary number of shaping constraints, pressure, and q profile. This

¹The TJ code is freely available at https://github.com/rfitzp/TJ.

yields a radial eigenfunction for B_R that can be line-integrated to create a synthetic RIP measurement. TJ is linear, which means that only modes with a single n are considered, and modes do not interact. This model is valid immediately after mode birth, and it will be evaluated to measure the linear contributions to mode amplitudes detected by RIP in experiment. TJ also calculates Δ' , the stability parameter, in the linear limit.

The code T7 [49] was previously used to calculate differences in stability between coupled and uncoupled tearing mode systems. T7 generates the tearing mode dispersion relation through a shooting method incorporating an expansion to seven different poloidal harmonics (same n, different m) of the base mode, with magnitudes parametrized by the inverse aspect ratio $\epsilon = a/R_0$. The resistive layer is assumed to be narrow. Two possible assumptions were considered: reconnection only at a single rational surface or locking together of all coupled rational surfaces at the same frequency. T7 was also optimized for large aspect ratio, weak shaping, and low pressure. This is used to find not only the eigenfunctions but also the tearing stability index Δ' . It was determined, for example, that toroidicity and greater shaping stabilized the 2,1 tearing mode.

The T7 concept of considering poloidal harmonics as an expansion in inverse aspect ratio has been extended to an arbitrary number of harmonics [50], and therefore an arbitrary cross-sectional shape described using an arbitrary number of parameters, with the code TJ [48]. TJ still requires a relatively large aspect ratio, but its allowed value can approximately reach the DIII-D aspect ratio ($R_0/a \sim 3$). Not only can TJ extend the shaping to arbitrary harmonics, but it can also produce a vertically asymmetric plasma, which T7 could not. In addition, TJ modeling can be done with no wall (free-boundary), an ideal wall at some distance from the plasma, or a fixed boundary [51]. I will show in Chapter 4 my linear solutions, using TJ, for mode eigenfunctions constructed of many poloidal harmonics, which will be line-integrated to model measurements taken by RIP.

3.4.2 EFIT

The various equilibrium diagnostics on DIII-D all present disparate data that must be synthesized to create an accurate picture of the plasma and glean all required information. These data-driven equilibrium snapshots, upon which much further analysis is based, are called reconstructions. Such reconstructions contain information about the plasma boundary; flux surface locations; stored energy; and internal profiles such as current, pressure, and q. For reconstructions, it is assumed that the plasma is isotropic, axisymmetric, and stationary. Since reconstructions are usually used to identify whether the system is stable, this is acceptable because the qualities of the stationary equilibrium are most important. Equilibrium reconstructions are carried out using a code called Equilibrium Fitting (EFIT) [52]; reconstructions are often themselves called EFITs. EFIT solves the Grad-Shafranov equation 2.20 with constraints set using experimental data. This is a nonlinear optimization problem, and the precision of an EFIT is set by the degree to which it converges.

EFITs have varying degrees of complexity depending on the number of diagnostics included. The simplest, EFIT01, uses only the external magnetics, i.e., flux loops and magnetic probes, to construct the plasma boundary. The Rogowski loops measure total plasma inductance, from which current can be derived. Similarly, the diamagnetic loops measure the pressure β , which can be related to the total thermal energy. However, neither of these quantities gives any information about the internal profiles. As a result, current, pressure, and q profiles are constructed based on assumptions about the flux surface shape rather than any internal quantities. The next step is to add the motional Stark effect (MSE) polarimeter, which measures the current profile internally. MSE functions by measuring the splitting of the Balmer alpha lines of neutral beam atoms in the presence of angled magnetic and electric field. The pitch of the magnetic field, and from there the local current density, can be identified from the beam velocity and E. EFITs including MSE are called EFIT02. EFIT02 can be corrected for background radial electric field E_r , estimated using the electron temperature and density profiles. E_r -adjusted EFITs are denoted EFIT02ER.

Kinetic EFIT (kEFIT) [53] is the next expansion of EFIT and includes a full set of internal profiles of equilibrium quantities. These include the aforementioned electron temperature and density, ion temperature and density, ion rotation, and where possible, radiated power. These profiles are collectively called kinetic profiles, since they derive from particle effects, and are used to constrain the reconstruction. KineticEFIT begins by fitting a standard, non-kinetic equilibrium reconstruction such as EFIT02ER to visualize flux surface locations, therefore developing a coordinate system. Recall that in toroidal geometry, magnetic flux is used as a minor radial coordinate since flux surfaces are not radially symmetric. Initial current, pressure, and q profiles are also created as a baseline. Once the initial reconstruction is fit, kinetic profiles are re-fit to the new equilibrium. These profiles are then input into a particle transport simulation code such as TRANSP [54]. Among many other quantities, current and pressure profiles form based on particle motion. These are heavily affected by initial conditions, so appropriate corrections must be made. Plasmas with high beam power but lower density may require artificial fast ion losses to balance particle number. Once simulations are complete, output current and pressure profiles are then passed to EFIT as additional constraints to the Grad-Shafranov equation. As the pressure profile $p(\psi)$ is a direct constraint to the Grad-Shafranov equation, and the modified poloidal field $F(\psi)$ is obtainable from the current profile, the kinetic constraints are relatively stringent. While typical EFITs have convergence limits of approximately 1×10^{-4} (unitless solution), kinetic EFITs strive for convergence of 1×10^{-8} . Along with matching to the externally-measured flux and MSE, these are the most accurate reconstructions available and are needed for precise further computational work such as MHD stability analysis.

3.4.3 DCON

Here, I use ideal MHD stability analysis to develop insights about the resistive tearing stability of experimental plasmas containing a variety of MHD activity. One useful marker for ideal stability is the normalized pressure β_N above which the equilibrium is expected to become unstable, often known as the β_N limit. One might expect that ideal stability anal-

ysis would not be useful in shots exhibiting resistive modes, since overall, resistive stability limits are lower than ideal stability limits. However, comparison to resistive stability codes has found a connection between resistive stability and the β_N limit corresponding to ideal stability with a conducting wall. NIMROD [55] and PEST3 [56] simulations have found that as the ideal-wall β_N limit is approached from below, proximity to the limit is correlated with a strong increase in Δ' . The ideal-wall limit therefore also represents a tendency toward classical tearing instability. Once the β_N limit is crossed in these simulations, Δ' drops below 0, which is acceptable given that the plasma is now ideally unstable. Resistive stability is no longer a consideration. I use proximity to the ideal-wall β_N limit as a proxy for resistive stability.

The primary stability analysis code I use in this thesis is the Direct Criterion of Newcomb (DCON) [57]. TJ can also calculate stability, but that is not the primary objective of its use here. A version of DCON that incorporates resistive effects and calculates Δ' also exists and is called RDCON [58] but is much more complex and is not used here. DCON uses the Newcomb energy principle [59] with toroidal corrections to identify the ideal stability of an equilibrium to both internal and external modes. It expands the Newcomb method to general, axisymmetric toroidal geometry. Instead of a single equation, DCON solves a system of equations to simultaneously determine the sign of the perturbation ξ and the potential energy δW for all components in an equilibrium. Each n is treated separately, with stability calculated for all possible m in a given q profile. The most unstable mode may be kink or ballooning, internal or external; DCON does not distinguish between them. Even so, DCON is useful as a benchmark for whether an equilibrium will disrupt or to explain plasma phenomena. For ξ and δW to be calculated and converge to consistent values, a high-quality equilibrium must be input. Such equilibria are often reconstructed with kineticEFIT, which is the method used in this thesis. DCON runs on a set of equilibria representing any range of shots and times though is usually used for one shot at a time. This calculation is done both with no wall (plasma in vacuum) and an ideal or perfectly conducting wall (magnetic

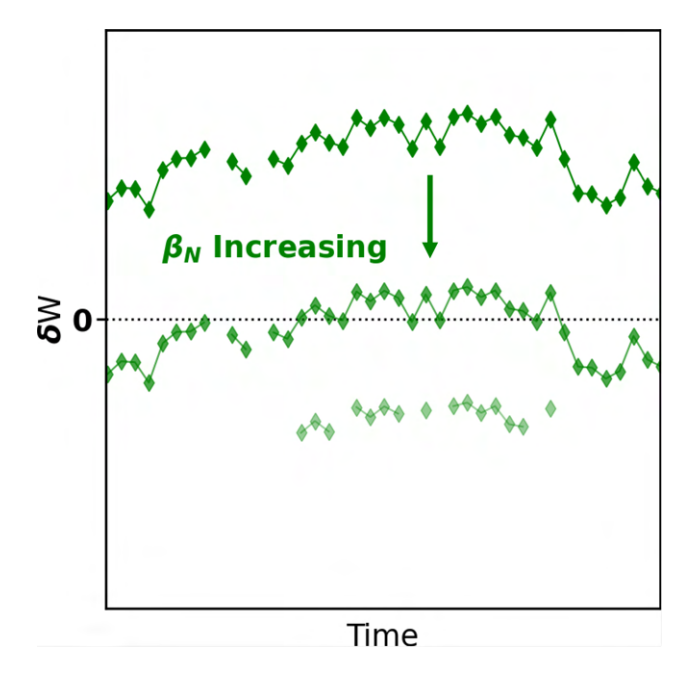


Figure 3.5: A cartoon of how β_N limits are calculated in DCON using δW . Top is the experimental equilibrium where all points are stable. Middle is a scaled equilibrium, and bottom is the further scaled equilibrium where all points are unstable.

field parallel to the wall at the boundary).

Input equilibria to DCON may also be scaled to induce either stability or instability and measure the stability limits for each equilibrium. Often, the parameter being scaled is the normalized pressure β_N . Higher values of β_N tend to induce instability on their own. When β_N calculation is active, DCON is run for each equilibrium and its standard β_N , then for a series of scaled pressure values until δW crosses zero and the plasma stability changes. This is repeated for each time point. These are the no-wall and ideal-wall β_N limits for each n. See Figure 3.5 for a visual depiction of β_N scaling. The plasma may cross the β_N limit over the course of a shot. Once that has occurred or a large instability has developed, the plasma is no longer axisymmetric and simulation convergence is reduced. Both δW and β_N can oscillate. For this reason, DCON is most effective before a large mode occurs.

Bibliography

- [1] E. Strait and T. Taylor. Sign Convention of Magnetics Signals. General Atomics. 1986.
- [2] E. J. Strait. "Magnetic diagnostic system of the DIII-D tokamak". Review of Scientific Instruments 77.2 (2006), p. 023502.
- [3] T. N. Carlstrom et al. "Design and operation of the multipulse Thomson scattering diagnostic on DIII-D". Review of Scientific Instruments 63.10 (1992), pp. 4901–4906.
- [4] M. E. Austin and J. Lohr. "Electron cyclotron emission radiometer upgrade on the DIII-D tokamak". Review of Scientific Instruments 74.3 (2003), pp. 1457–1459.
- [5] M. A. Van Zeeland et al. "Fiber optic two-color vibration compensated interferometer for plasma density measurements". Review of Scientific Instruments 77.10 (2006), 10F325.
- [6] R. P. Seraydarian et al. "Multichordal charge exchange recombination spectroscopy on the Doublet III tokamak". *Review of Scientific Instruments* 57.2 (1986), pp. 155–163.
- [7] D. Wroblewski and L. L. Lao. "Polarimetry of motional Stark effect and determination of current profiles in DIII-D". Review of Scientific Instruments 63.10 (1992), pp. 5140– 5147.
- [8] R. J. Colchin et al. "The filterscope". Review of Scientific Instruments 74.3 (2003), pp. 2068–2070.
- [9] G. McKee et al. "The beam emission spectroscopy diagnostic on the DIII-D tokamak".

- Review of Scientific Instruments 70.1 (1999), pp. 913–916.
- [10] A. Diallo et al. "Correlations between quasi-coherent fluctuations and the pedestal evolution during the inter-edge localized modes phase on DIII-D". *Physics of Plasmas* 22.5 (2015), p. 056111.
- [11] B. Tobias et al. "Commissioning of electron cyclotron emission imaging instrument on the DIII-D tokamak and first data". Review of Scientific Instruments 81.10 (2010).
- [12] G. Yu et al. "ECEI characterization of pedestal fluctuations in quiescent H-mode plasmas in DIII-D". *Plasma Physics and Controlled Fusion* 64.9 (2022), p. 095014.
- [13] R. J. Fonck, A. T. Ramsey, and R. V. Yelle. "Multichannel grazing-incidence spectrometer for plasma impurity diagnosis: SPRED". Applied Optics 21.12 (1982), pp. 2115– 2123.
- [14] E. Strait. Poloidal Mode Identification Using MODESPEC. Presented at the DIII-D3D and Stability Physics Meeting. Aug. 2020.
- [15] R. Fitzpatrick. "Classical Electromagnetism". Lectures. URL: https://farside.ph.utexas.edu/teaching/em/lectures/lectures.html.
- [16] T. Hatanaka. "The Faraday Effect in the Earth's Ionosphere with Special Reference to Polarization Measurements of the Solar Radio Emission". Publications of the Astronomical Society of Japan 8 (1956), p. 73.
- [17] S. Vandendriessche. "The influence of magnetic fields on light–matter interaction". PhD thesis. KU Leuven, 2014.
- [18] G. Dodel and W. Kunz. "A far-infrared 'polari-interferometer' for simultaneous electron density and magnetic field measurements in plasmas". Infrared Physics 18.5-6 (1978), pp. 773–776.
- [19] W. Kunz and Equipe TFR. "First measurement of poloidal-field-induced Faraday rotation in a tokamak plasma". *Nuclear Fusion* 18.12 (1978), p. 1729.

- [20] D. Véron. "High sensitivity HCN laser interferometer for plasma electron density measurements". *Optics Communications* 10.1 (1974), pp. 95–98.
- [21] H. Soltwisch and Equipe TFR. "Experimental test of far-infrared polarimetry for Faraday rotation measurements on the TFR 600 Tokamak". Infrared Physics 21.5 (1981), pp. 287–298.
- [22] B. W. Rice. "Fifteen chord FIR polarimetry system on MTX". Review of Scientific Instruments 63.10 (1992), pp. 5002–5004.
- [23] H. Soltwisch. "Current distribution measurement in a tokamak by FIR polarimetry".

 Review of Scientific Instruments 57.8 (1986), pp. 1939–1944.
- [24] H. R. Koslowski, H. Soltwisch, and W. Stodiek. "Polarimetric measurement of m= 1 sawtooth precursor oscillations in the TEXTOR tokamak". *Plasma Physics and Controlled Fusion* 38.3 (1996), p. 271.
- [25] H. Soltwisch and H. R. Koslowski. "Observation of magnetic field perturbations during sawtooth activity in tokamak plasmas". Plasma Physics and Controlled Fusion 39.5A (1997), A341.
- [26] D. L. Brower et al. "Laser polarimetric measurement of equilibrium and fluctuating magnetic fields in a reversed field pinch". Review of Scientific Instruments 74.3 (2003), pp. 1534–1540.
- [27] W. X. Ding, D. L. Brower, W. F. Bergerson, and L. Lin. "Upgrade of far-infrared laser-based Faraday rotation measurement on MST". Review of Scientific Instruments 81.10 (2010), p. 10D508.
- [28] W. X. Ding et al. "The Hall dynamo effect and nonlinear mode coupling during sawtooth magnetic reconnection". *Physics of Plasmas* 13.11 (2006), p. 112306.
- [29] A. Almagri, S. Assadi, J. Beckstead, et al. "Physics of alternative magnetic confinement schemes". Proc. Workshop Varenna. Ed. by S. Ortolani and E. Sindoni. Bologna, Italy: Societa Italiana di Fisici, 1990.

- [30] J. Sarff et al. "Magnetic reconnection and self-organization in Reversed Field Pinch laboratory plasmas". The Magnetized Plasma in Galaxy Evolution. 2005, pp. 48–55.
- [31] J. Chen et al. "Design of far-infrared three-wave polarimeter-interferometer system for the J-TEXT tokamak". Review of Scientific Instruments 81.10 (2010).
- [32] H. Q. Liu et al. "Design of far-infrared polarimeter/interferometer system for EAST tokamak". *Journal of Instrumentation* 8.11 (2013), p. C11002.
- [33] H. Q. Liu et al. "Faraday-effect polarimeter-interferometer system for current density measurement on EAST". Review of Scientific Instruments 85.11 (2014), p. 11D405.
- [34] J. Chen et al. "Faraday-effect polarimeter diagnostic for internal magnetic field fluctuation measurements in DIII-D". Rev. Sci. Instrum. 87.11 (2016), 11E108.
- [35] J. Chen et al. "A Faraday-effect polarimeter for fast magnetic dynamics measurement on DIII-D". Review of Scientific Instruments 89.10 (2018), 10B101.
- [36] J. Chen et al. "Internal measurement of magnetic turbulence in ELMy H-mode tokamak plasmas". *Physics of Plasmas* 27.12 (2020), p. 120701.
- [37] J. Chen et al. "Pedestal magnetic turbulence measurements in ELMy H-mode DIII-D plasmas by Faraday-effect polarimetry". *Physics of Plasmas* 28.2 (2021), p. 022506.
- [38] J. H. Rommers and J. Howard. "A new scheme for heterodyne polarimetry with high temporal resolution". *Plasma Physics and Controlled Fusion* 38.10 (1996), p. 1805.
- [39] J. D. King et al. "An upgrade of the magnetic diagnostic system of the DIII-D tokamak for non-axisymmetric measurements". Review of Scientific Instruments 85.8 (2014), p. 083503.
- [40] R. J. La Haye et al. "Dimensionless scaling of the critical beta for onset of a neoclassical tearing mode". *Physics of Plasmas* 7.8 (2000), pp. 3349–3359.
- [41] M. D. Pandya et al. "Early internal detection of magnetic tearing and implications for tokamak magnetohydrodynamic stability". *Physics of Plasmas* 31.7 (2024), p. 070706.

- [42] J. Chen. RIP update: toroidal mode number measurement, 5/10 MHz bandwidth, and real-time outputs to PCS. Presented at the DIII-D Science, Engineering, and Technology Meeting. Apr. 2025.
- [43] J. Chen, W. X. Ding, and D. L. Brower. "Impact of the Cotton–Mouton effect on Faraday polarimetry measurements using circular polarization". *Plasma Physics and Controlled Fusion* 60.8 (2018), p. 085001.
- [44] D. E. Smith, E. J. Powers, and G. S. Caldwell. "Fast-fourier-transform spectral-analysis techniques as a plasma fluctuation diagnostic tool". *IEEE Transactions on Plasma Science* 2.4 (1974), pp. 261–272.
- [45] E. Parke, W. X. Ding, and D. L. Brower. "Correlation polarimetry for broadband magnetic fluctuation measurements". Review of Scientific Instruments 89.10 (2018), 10B112.
- [46] J. Chen et al. "Correlation polarimeter-interferometer in the DIII-D tokamak". Review of Scientific Instruments 92.4 (2021), p. 043502.
- [47] J. Chen. Private communication. July 2024.
- [48] R. Fitzpatrick. "Calculation of tearing mode stability in an inverse aspect-ratio expanded tokamak plasma equilibrium". *Physics of Plasmas* 31.10 (2024), p. 102507.
- [49] R. Fitzpatrick, R. J. Hastie, T. J. Martin, and C. M. Roach. "Stability of coupled tearing modes in tokamaks". *Nuclear Fusion* 33.10 (1993), p. 1533.
- [50] R. Fitzpatrick. "Inverse aspect-ratio expanded tokamak equilibria". *Physics of Plasmas* 31.8 (2024), p. 082505.
- [51] R. Fitzpatrick. "Investigation of tearing mode stability near ideal stability boundaries via asymptotic matching techniques". *Physics of Plasmas* 32.6 (2025).
- [52] L. L. Lao et al. "Reconstruction of current profile parameters and plasma shapes in tokamaks". *Nuclear Fusion* 25.11 (1985), p. 1611.

- [53] L. L. Lao et al. "Equilibrium analysis of current profiles in tokamaks". *Nuclear Fusion* 30.6 (1990), p. 1035.
- [54] R. J. Hawryluk. "An empirical approach to tokamak transport". *Physics of Plasmas Close to Thermonuclear Conditions*. Elsevier, 1981, pp. 19–46.
- [55] D. P. Brennan et al. "Tearing mode stability studies near ideal stability boundaries in DIII-D". *Physics of Plasmas* 9.7 (2002), pp. 2998–3006.
- [56] F. Turco et al. "Sensitivity of transport and stability to the current profile in steady-state scenario plasmas in DIII-D". *Physics of Plasmas* 19.12 (2012), p. 122506.
- [57] A. H. Glasser. "The direct criterion of Newcomb for the ideal MHD stability of an axisymmetric toroidal plasma". *Physics of Plasmas* 23.7 (2016), p. 072505.
- [58] A. H. Glasser, Z. R. Wang, and J.-K. Park. "Computation of resistive instabilities by matched asymptotic expansions". *Physics of Plasmas* 23.11 (2016), p. 112506.
- [59] W. A. Newcomb. "Hydromagnetic stability of a diffuse linear pinch". *Annals of Physics* 10.2 (1960), pp. 232–267.

Chapter 4

Mode Detection with RIP and

Line-Integration Effects

Thus far I have discussed the principles of polarimetry-interferometry and obtaining the fluctuating component of a signal. I now move into a discussion of fluctuation amplitude computation, modeling, and interpretation, with particular emphasis on RIP. RIP measurements are marked by a number of physical constraints that affect the measured signal. Not least of these constraints is the line-integrated nature of the measurements. Since RIP is line-integrated, it cannot be used to measure local amplitudes. It instead is used to measure a signal averaged over the path. Depending on mode numbers, this may provide a more or less accurate measurement of the actual mode amplitude at the resonant surface. Synthetic RIP measurements are assessed using a series of linear eigenfunction models, from an analytic high-m approximation to a computational model with an arbitrary number of harmonics. These models are then used to explain differences between RIP and coil measurements.

Section 4.1 describes the short-time Fourier transform method for measuring fluctuation amplitudes for any diagnostic. A method for obtaining magnetic field fluctuations from RIP fluctuations is described. Section 4.2 describes the eigenfunction models used in this thesis. The first is an analytic model using the cylindrical approximation. This section also introduces a potential drawback of RIP's line-integrated nature when measuring even-m modes.

This drawback motivates the incorporation of toroidal and shaping effects into the model and investigation of the strength of their effects. Section 4.3 compares the eigenfunction models with RIP measurements. It details these models and uses them to test potential explanations for mode-number-dependent inconsistencies between RIP and magnetic sensing coils. Section 4.4 discusses other cases in which RIP shows advantages over sensing coils.

4.1 RIP Data and Amplitude Calculations

I now detail how fluctuations in RIP data are represented and how amplitudes are calculated. Magnetic fluctuations on RIP are frequently investigated visually using spectrograms, similarly to the STFT method used in MODESPEC [1]. The primary difference between RIP and Modespec spectrograms is that RIP spectrograms typically use a single signal and plot the auto-power spectral density (PSD), or product of the Fourier transform with itself, for all frequencies and times. A demonstration spectrogram of RIP data is shown for DIII-D shot #184794 in Figure 4.1. When calculating the short-time auto-power for spectrogram plotting, the data is windowed using the Hann function to improve smoothing. In RIP spectrograms, low-frequency MHD modes, including tearing modes, appear as coherent bands centered at the mode frequency. ELMs typically appear as vertical spikes up to approximately 200 kHz. This shot had infrequent ELMs, and this window was chosen to avoid ELMs. During this period, four ELMs appear as vertical stripes. These specific ELMs occur in pairs, though this is not required. The shot also contained several coherent fluctuations of relatively stable frequencies. The mode whose amplitude I calculate generates fluctuations at 11 kHz, and fluctuations at 22 and 33 kHz are also visible along with several other modes. Modespec analysis, using the same process demonstrated in Chapter 3, shows that this mode has m, n = 2, 1. The phase of the mode is fit to the location of each coil in the poloidal array, and Modespec performs a linear fit to determine how many cycles of the mode go by per poloidal transit in the machine. Some of the modes at frequencies greater than 33 kHz are not detected with sensing coils; other examples where RIP detects modes the coils do not are given in Section 4.4 and Chapter 6.

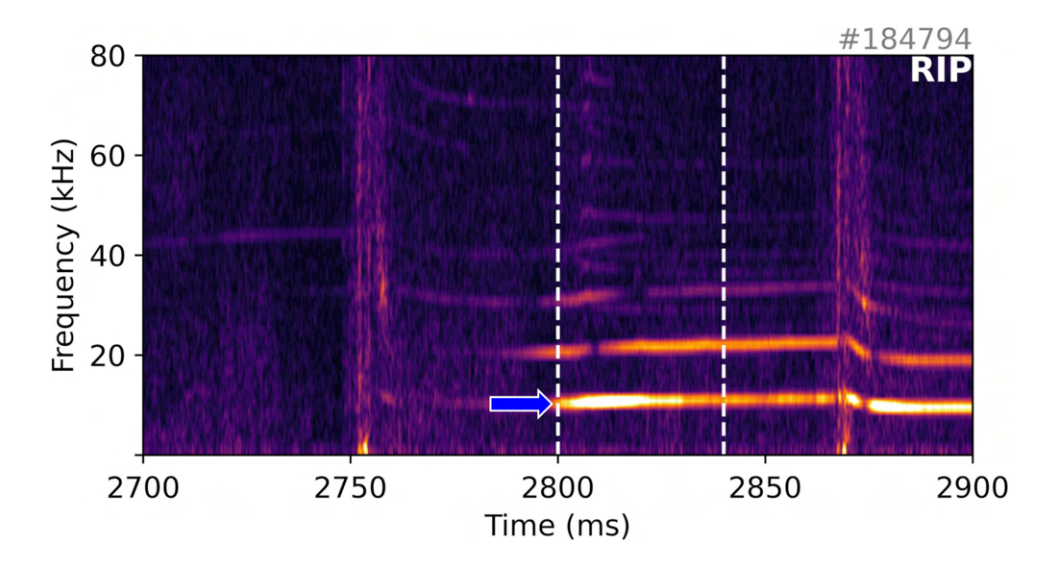


Figure 4.1: Spectrogram of a RIP polarimetry signal showing ELMs (vertical stripes) and low-frequency MHD modes (coherent bands, lowest-frequency mode denoted by blue arrow). White vertical lines mark the period to be depicted in Figures 4.2 and 4.3.

I also use the PSD of the fluctuating component to measure mode amplitude, since it represents the total power of the signal at a given frequency. Since mode frequency may vary over the period of the Fourier transform and most modes considered in these experiments have some finite range of frequencies, the total power within the mode, at all frequencies, is a more accurate representation of the amplitude than the value at a single frequency. For this reason it is preferable to use the PSD rather than the standard Fourier transform to calculate amplitudes. The spectral density in the case of a discrete signal is represented using the periodogram, which is the average of the squared PSD over all samples in a signal. The power spectrum is frequency-adjusted, and its units are those of the square of the original signal divided by the frequency. The power spectrum can then be integrated over a finite frequency range, encompassing the mode width in frequency, with limits f_1, f_2 , to obtain the total mode power. The square root is taken to find the final amplitude. The PSD method is frequently useful to measure changes in a mode's amplitude over time. In this case, I repeat this method and find amplitudes for a series of time windows. The window length is optimized based on the sampling rate; narrower windows produce a higher time resolution for the time-varying amplitude but reduce frequency resolution within each window. In this

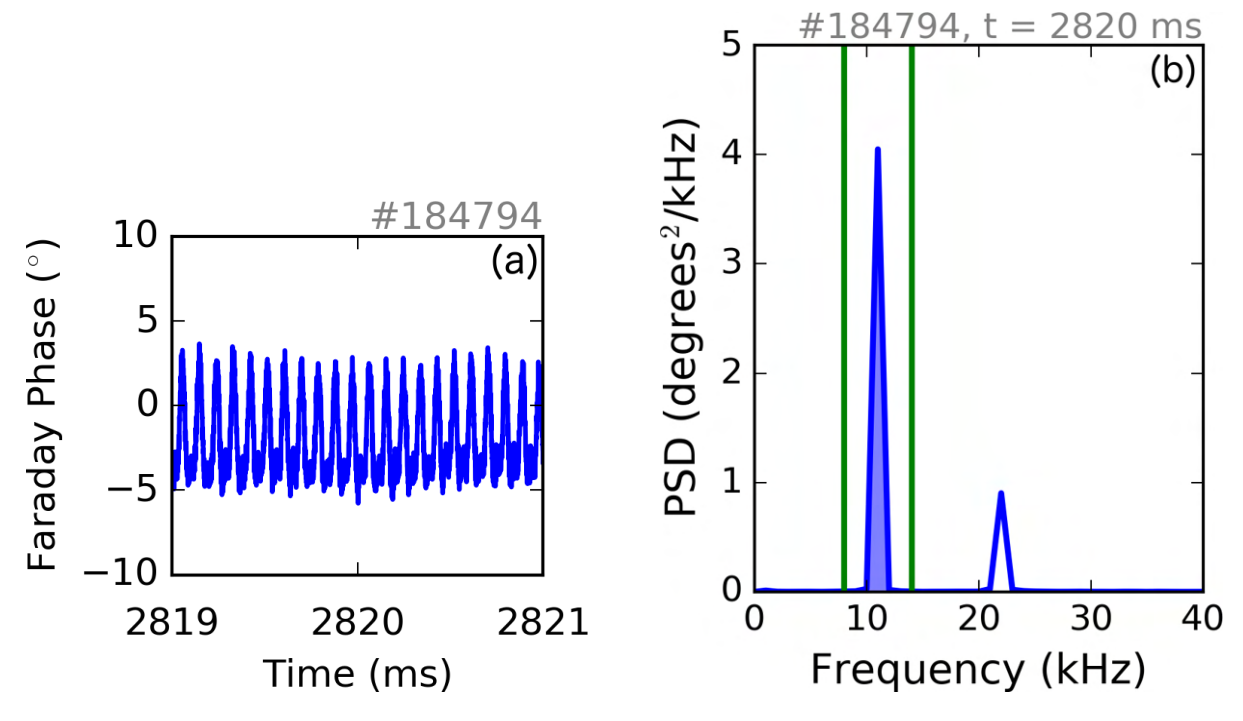


Figure 4.2: (a) Raw polarimetry signal from the RIP midplane chord from t=2819-2821 ms in DIII-D shot #184794, demonstrating coherent fluctuations. (b) An illustration of the integration method for calculating mode amplitudes using the periodogram at t=2820 ms in the same shot. The Fourier transform is denoted in blue and the window of integration in green, with the area under the curve for the lowest-frequency mode highlighted.

thesis, I have used 1 ms windows, which yield a frequency resolution of 1 kHz, or 0.5 ms windows, which yield a frequency resolution of 2 kHz, depending on window size.

I present an example of the STFT calculation. Figure 4.2(a) shows a short section of the raw signal from the RIP polarimeter in DIII-D shot #184794, depicted in Figure 4.1, from t=2819 ms to t=2821 ms. The PSD is calculated, as plotted in Figure 4.2(b); I refer to this as the PSD for the midpoint of that window or t=2820 ms. Since the Faraday rotation is in units of degrees, the units of the PSD are degrees²/kHz. Note the peaks in the spectrum at 11 and 22 kHz, which represent peaks in mode amplitude at those frequencies. There is also a small peak at 33 kHz, which is small enough that it is not resolved by the plot; that mode is very low in amplitude compared to the other two. The goal is to find the amplitude of the 11 kHz mode, so I integrate the PSD over a frequency range covering the entire mode and, ideally, as little background noise as possible:

$$\tilde{\Phi}_{F,amp} = \sqrt{\int_{f_1}^{f_2} PSD(f)df}.$$
(4.1)

The frequency range covering the entire mode has a fixed width of 4 kHz. Its center is automatically determined by finding the window of maximum integrated PSD that covers the specified mode. Here, the mode is identified to be centered at 11 kHz because the window of maximum PSD amplitude lies from $f_1 = 9$ kHz to $f_2 = 13$ kHz.

Using this estimate, I calculate a line-averaged magnetic field fluctuation amplitude. The magnetic fluctuation amplitude can be found by dividing the line-integrated density-weighted amplitude found from the polarimetric measurement by the line-integrated density found from the interferometric measurement, both along the central RIP chord [2]:

$$\bar{\tilde{B}}_r \approx \bar{\tilde{B}}_l = \frac{\int n_e \ \tilde{B}_l \mathrm{d}l}{\int n_e \ dl} = \frac{c_I}{c_F} \frac{\tilde{\Phi}_F}{\Phi_I},\tag{4.2}$$

for a beam path that is approximately radial. The local amplitude of the magnetic field may be higher, but \bar{B}_r is the average magnetic fluctuation amplitude along the path of RIP. The amplitude \bar{B}_r is taken for each window within the time span of interest and yields the amplitude of the mode as it varies in time. I visually represent the mode as an amplitude for a single frequency. An example is shown in Figure 4.3(a) for a series of points centered in frequency around the sample from Figure 4.2, also marked by vertical lines in Figure 4.1. Note that the amplitude of the mode over time tracks with the brightness of the lowest-frequency band in Figure 4.1. Similar principles can be applied to broadband fluctuations to yield the total fluctuation power within a range of any width, as has been done to measure the stored energy in the turbulence spectrum 150–500 kHz [3]. This plays a role in subtracting noise from RIP measurements and detecting ELMs in Section 4.4.

Figure 4.3 also compares the measured mode amplitude to contributions from additional terms in the Faraday rotation. Recall from Equation 3.6 that the fluctuating Faraday angle,

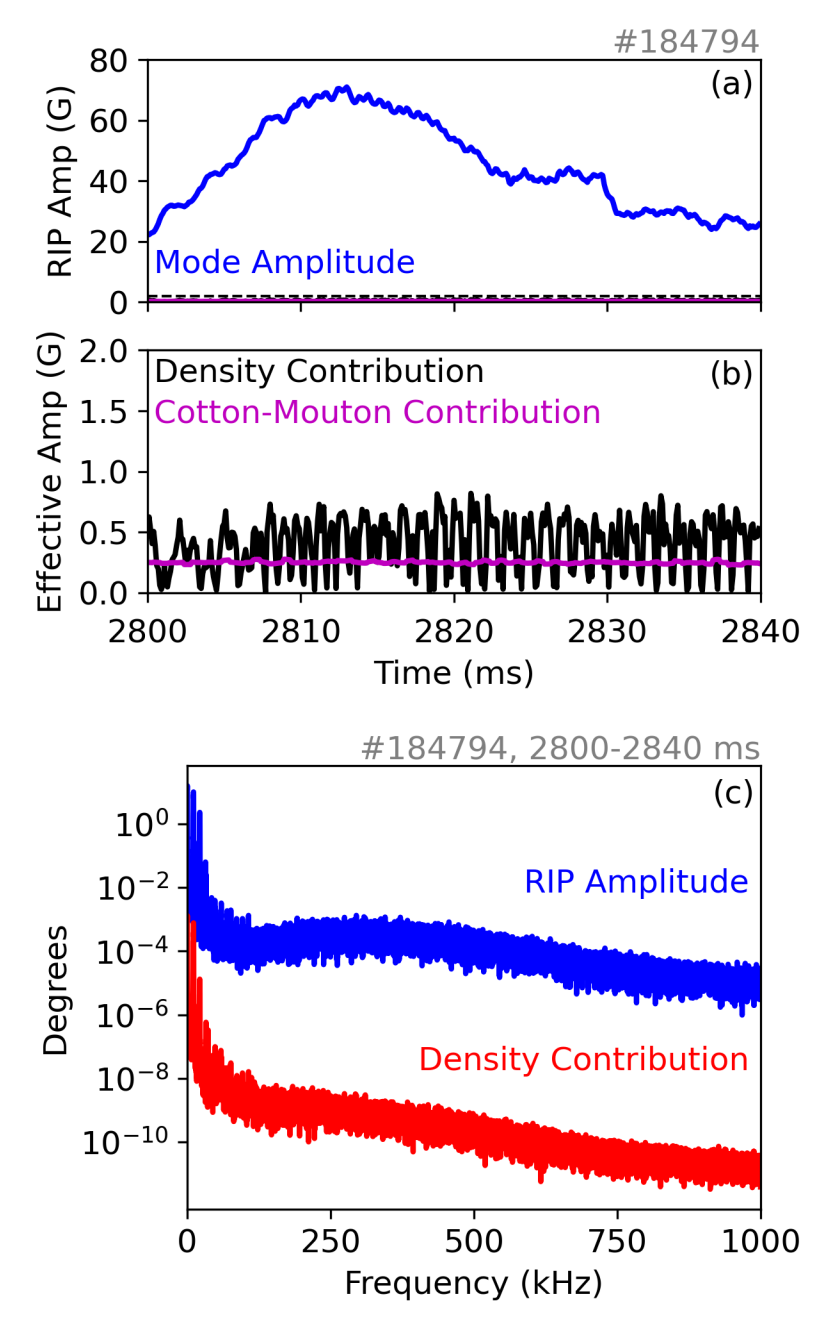


Figure 4.3: (a) Magnetic fluctuation amplitude (blue, solid) over time for a m, n = 2, 1 mode at f = 11 kHz in DIII-D shot #184794 with density fluctuation (black) and Cotton-Mouton effect (magenta) signal contributions. Corrected magnetic amplitude given by blue dashed line. (b) Plot (a) with lower y-axis limit, showing the correction amplitudes. (c) Spectra of the relative strength of the measured Faraday rotation fluctuation and the measured density component.

to first order, is made up of two components

$$\tilde{\Phi}_F = c_F \int n_e \ \tilde{B}_l \mathrm{d}l + c_F \int \tilde{n}_e B_l \mathrm{d}l.$$

For magnetic fluctuation measurements using RIP, the second term is small for two reasons. The density fluctuations associated with MHD modes are much smaller than the overall density, $\tilde{n}/n \sim 10^{-2}-10^{-4}$, reducing the second term's relative magnitude to the first, which is proportional to the overall density. Additionally, B_l , the equilibrium component of the magnetic field along the path of the beam, is the radial field B_R in the case of a radial diagnostic like the midplane RIP chord. In the case of a radial diagnostic at the midplane, the beam path is perpendicular to the magnetic surfaces, so the line integral of B_R is very small. Since B_R is so small, the magnitudes of B_R and its fluctuations \tilde{B}_R are comparable: $B_R/B_R \sim 0.1-1$. Both of these factors combine to shrink the density contribution with respect to the magnetic fluctuation contribution. If desired, to increase accuracy, the density component $c_F \int \tilde{n}_e B_R dR$ can be subtracted from calculated Faraday amplitudes. Figure 4.3(a-b) illustrate the comparative strength of the density and magnetic fluctuations. Figure 4.3(a-b) also compares the approximate value of the Cotton-Mouton effect contribution [4] to the beam rotation with the Faraday contribution. This is an estimate because it covers only the first-order contribution and not coupling to the Faraday rotation. Nevertheless, it is sufficient to provide a general comparison. At the magnetic field and density associated with the given shot, both the density and Cotton-Mouton errors are less than 1% of the portion due to magnetic fluctuation. The density contribution is small for all frequencies. The comparative sizes of the first (magnetic) and second (density) terms, plotted versus frequency, for shot #184794, 2800–2840 ms are given in Figure 4.3(c). At all frequencies, the density contribution to the Faraday amplitude is 3–5 orders of magnitude less than the total amplitude.

4.2 Tearing Mode Structure Models

This thesis provides deeper insight into the nature of magnetic amplitudes measured with RIP and how they compare to other diagnostics such as the sensing coils. It also reveals internal aspects of mode structure and their implications in different ways than external coils reveal. Since RIP measurements are line-integrated, to develop models and synthetic RIP data, I consider the scalar RIP value as the integral of some modeled eigenfunction. I henceforth describe the radial structure of tearing modes through a series of models. This will be used later to represent the magnetic field fluctuation spatial profile over which RIP is integrating, predict and compare to actual RIP findings, and investigate the properties of line-integrated measurements.

4.2.1 Analytic Tearing Mode Structure Model

I begin with a simple analytic model that, far from the mode resonant surface, is a first step towards understanding the overall shape of tearing eigenfunctions. I will show that mode amplitude decays more markedly away from the rational surface as the poloidal mode number m increases, which results in the eigenfunctions being more peaked. In the limit of large aspect ratio $(R_0/a \gg 1)$ used by this model, the plasma can be approximated as a periodic cylinder. Recall the development of the tearing model in Section 2.3. In cylindrical geometry, radial magnetic field perturbations follow $\tilde{B}(r) = i\psi(r)e^{im\theta}$, where ψ is the magnetic flux function, m is the poloidal mode number, and axial/toroidal and time dependence have been suppressed. The cylindrical limit of the toroidal infinite-conductivity Equation 2.37 is: [5, 6]

$$r\frac{\mathrm{d}}{\mathrm{d}r}\left(r\frac{\mathrm{d}\psi}{\mathrm{d}r}\right) - m^2\psi - \frac{q}{1 - nq/m}r\frac{\mathrm{d}}{\mathrm{d}r}\left[\frac{1}{r}\left(\frac{\mathrm{d}}{\mathrm{d}r}\frac{r^2}{q}\right)\right]\psi = 0,\tag{4.3}$$

where $q = \frac{rB_z}{RB_\theta} = m/n$ is the safety factor at the rational surface.

For $m \gg 1$, the second term dominates over the third except near the resonant surface,

and the infinite-conductivity equation becomes approximately equal to

$$r\frac{\mathrm{d}}{\mathrm{d}r}\left(r\frac{\mathrm{d}\psi}{\mathrm{d}r}\right) - m^2\psi \simeq 0. \tag{4.4}$$

I assume that the wall at r = b is a perfect conductor. Then the boundary conditions for the outer portion of the function are that $\psi(r = b) = 0$, and that the poloidal magnetic flux at the boundary is equal to the measured poloidal magnetic flux: $B_{\theta}(b) = \frac{\mathrm{d}\psi}{\mathrm{d}r}|_{r=b} = B_{\theta b}$. This dependence on $B_{\theta,b}$ applies to all eigenfunction models and will be used later to normalize synthetic RIP measurements with respect to synthetic sensing coil data. I institute a trial function:

$$\psi = a_{-} \left(\frac{r}{b}\right)^{-m} + a_{+} \left(\frac{r}{b}\right)^{m} \tag{4.5}$$

After some algebra,

$$\psi = \frac{B_{\theta b}}{2m} \left(\left(\frac{r}{b} \right)^{-m-1} - \left(\frac{r}{b} \right)^{m+1} \right). \tag{4.6}$$

The poloidal and radial magnetic field eigenfunctions in r for $r \geq r_s$ are

$$B_{\theta}(r) = \frac{\mathrm{d}\psi}{\mathrm{d}r} = \frac{B_{\theta b}}{2} \left[\left(\frac{r}{b}\right)^{-m-1} + \left(\frac{r}{b}\right)^{m-1} \right] \tag{4.7}$$

$$B_r(r) = im\frac{\psi}{r} = \frac{iB_{\theta b}}{2} \left[\left(\frac{r}{b}\right)^{-m-1} - \left(\frac{r}{b}\right)^{m-1} \right]. \tag{4.8}$$

I now solve for ψ for small radii $r < r_s$. The boundary conditions here are $\psi(0) = 0$ and the continuity of the normal component of B, $\hat{n} \cdot B$, at the rational surface r_s . Let $a = a_+$. Then for $0 \le r \le r_s$:

$$\psi = \frac{B_{\theta b} r_s}{2m} \left[\left(\frac{r_s}{b} \right)^{-2m} - 1 \right] \left(\frac{r}{b} \right)^m \tag{4.9}$$

$$B_{\theta}(r) = \frac{B_{\theta b} r_s}{2b} \left[\left(\frac{r_s}{b} \right)^{-2m} - 1 \right] \left(\frac{r}{b} \right)^{m-1} \tag{4.10}$$

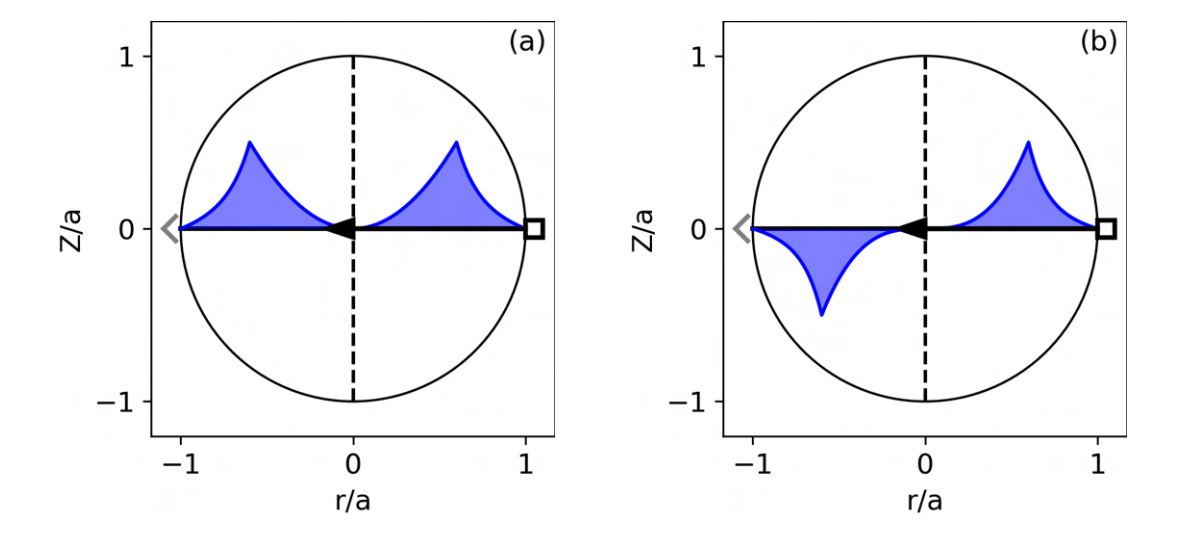


Figure 4.4: Cartoon of a cylindrical vessel with overlaid magnetic eigenfunctions for (a) m=3 (odd-m) and (b) m=4 (even-m) tearing modes resonating at normalized radius $\rho=0.6$ in the analytic model. Area under the eigenfunction curve highlighted in blue. Arrows show the direction of line-integration for a radial polarimeter at the midplane. Black box is a cartoon representation of the RIP detector. Gray V is a cartoon representation of the RIP retro-reflector.

$$B_r(r) = \frac{iB_{\theta b}r_s}{2b} \left[\left(\frac{r_s}{b}\right)^{-2m} - 1 \right] \left(\frac{r}{b}\right)^{m-1}. \tag{4.11}$$

The approximation given in Equation 4.4 is most useful to detect trends in eigenfunction behavior. For example, modes become more localized as m grows larger. The mode peaks at the resonant surface and decays quickly toward the edge. Line-averaging using a diagnostic like RIP can detect the peaked amplitudes in the core instead of the low amplitudes at the edge where the coils measure. Near the resonant surface, particularly when m < 5, the model breaks down. The q term becomes increasingly important as m decreases because the $m^2\psi$ term becomes less dominant. A full solution to the infinite-conductivity equation generates more accurate eigenfunctions and will provide a better understanding of the degree of peaking measured by RIP near the resonant surface.

In polarimetry, line-integration introduces additional complications that must be considered when constructing models and interpreting data. RIP integrates across the entire plasma. As seen in Section 4.2.1, for $m \gg 1$, in the cylindrical approximation, tearing mode

radial eigenfunction amplitudes decay roughly as $(r/r_s)^{-m-1}$. Figure 4.4 presents a cartoon of a cylindrical plasma with magnetic eigenfunctions corresponding to odd and even m for r inboard and outboard of the magnetic axis. A radius inboard of the magnetic axis, r < 0, corresponds to a phase shift of $\theta \to \theta + \pi$ in the $e^{im\theta}$ factor in ψ . Together with the r^{-m-1} dependence, this shift means that the B_R eigenfunction for even m switches sign across the magnetic axis while the eigenfunction for odd m does not. When line-integrated over a radial path such as the RIP midplane chord, even m yields a tearing mode amplitude of 0, whereas odd m yields a finite amplitude. The eigenfunction is integrated (area under the curve filled in blue), which results in a value of zero for even m and finite for odd m. The cylindrical model states that even-m modes should not be visible with polarimetry at the midplane. However, evidence of even=m mode detection in RIP dataindicates that even-mmodes are detected with RIP. Radial polarimetry at the midplane cannot detect even-mcomponents, as even-m modes switch signs across the magnetic axis in all models of eigenfunction structure. RIP must be detecting some odd-m component. Full toroidal modeling [7] of mode eigenfunctions as measured by RIP, including toroidicity and shaping reveals additional harmonics that yield a finite amplitude for even-m modes.

4.2.2 Linear Computational Tearing Mode Structure Model

I now show that adding toroidicity and shaping to the tearing eigenfunction model yields components measurable by polarimetry, even when m is even. When including the effects of toroidicity and shaping, the linearization method applied to solve for ξ in Section 2.2 no longer holds. The plasma is no longer symmetric in θ , so the perturbations are no longer independent. When this occurs, perturbations can couple to plasma shape:

$$\xi_n = \sum_{m=1}^{\infty} \xi_{mn}(\psi, \theta) e^{im\theta - in\phi}$$
(4.12)

Here the first term (m = 1) is a coupling of the mode to the toroidicity, m = 2 to elongation, and so on. These couplings exist because plasma shape is equivalent to a spatially station-

ary n = 0 ideal MHD mode. Toroidicity induces a Shafranov shift (1,0), and elongation, triangularity, and higher-order parameters are equivalent to (m,0) modes. As a result, the couplings illustrated in Equation 4.12 can occur. The coupled ξ_{mn} are poloidal harmonics or sidebands to the dominant perturbation and and originate at the same rational surface with the same toroidal rotation frequency [8].

The contributions of toroidicity and shaping to mode stability and structure are significant [9]. Linear modeling is the first step to determining stability in a plasma of realistic shape, and I will employ it to predict profiles and model what RIP would be expected to detect. To first (linear) order, all Fourier harmonics of a mode with the same m are coupled to each other. The modes are represented as a sum of sidebands with different m. I employ a computational model for the linearized solution to the infinite-conductivity equation including the q profile, toroidicity, shaping, and sideband amplitudes. The linear code TJ, published in 2024, is used for these computations [7, 10, 11]. These more advanced models apply matched asymptotic expansions to incorporate the reconnection region [12]. The computational model now adds a resistive layer of finite width. In asymptotic matching, the domain is divided into sections, and the ideal and resistive solutions match on both sides of the resistive layer. I first describe computational solutions in a cylinder and then include toroidal effects. Nonlinear (higher-order) interactions between perturbations are ignored, which is valid for the short linear growth phase just after mode birth. A full nonlinear treatment is computationally expensive and beyond the scope of this thesis. I show that toroidal linear computational models are sufficient to compare diagnostics. This thesis contains the first experimental test of TJ-calculated amplitudes compared to direct measurement of mode amplitudes. While TJ is used to find line-integrated radial magnetic field here, amplitudes of sidebands are expected to prove useful for modeling mode amplitudes measured with other fluctuation diagnostics such as BES and ECE [13].

The magnetic field shape is asymmetric in the poloidal coordinate θ , and therefore the major-radial coordinate R, for any toroidally confined plasma. The Shafranov shift is the

simplest manifestation of this asymmetry; magnetic field lines are more compressed on the outboard side than the inboard side. The magnetic field strength itself is modified by toroidicity, and so in turn are the eigenfunctions. In a toroidal system with arbitrary shaping as can be modeled in TJ, the R and Z coordinates of the flux surfaces are parametrized in the inverse aspect ratio $\epsilon = a/R_0$ and the shaping parameters H_j, V_j as follows [10]:

$$R_{surf} = R_0 \left[1 - \epsilon \cos \theta + \epsilon^2 \sum_{j>0} H_j(r) \cos[(j-1)\theta] + \epsilon^2 \sum_{j>1} V_j(r) \sin[(j-1)\theta] + \epsilon^3 L(r) \cos \theta \right]$$

$$Z_{surf} = R_0 \left[\epsilon \sin \theta + \epsilon^2 \sum_{j>0} H_j(r) \sin[(j-1)\theta] + \epsilon^2 \sum_{j>1} V_j(r) \cos[(j-1)\theta] + \epsilon^3 L(r) \sin \theta \right].$$

$$(4.14)$$

Here H_j are arbitrary shaping parameters related to Shafranov shift, elongation, triangularity, and other typical metrics. V_j represent vertical tilts of each axis to induce asymmetry of the flux surfaces. H_j and V_j are set by the TJ user. V_1 is a vertical shift that cancels when coordinates are normalized. L(r) is a labeling parameter calculated within TJ [10]. In this formula, θ is the typical polar coordinate $\tan^{-1}(Z/R)$, and r is a flux-surface label.

In experiment, shaped plasma cross-sections are parametrized by the elongation κ and the upper and lower triangularity δ_u , δ_l . Higher-order parameters such as squareness can be used and are included in the arbitrary number of harmonics permitted in TJ. Here $\kappa = (Z_{\text{max}} - Z_{\text{min}})/2a$, where Z_{max} and Z_{min} are the maximum and minimum value of the plasma's Z coordinate along the boundary, and a is the minor radius. Triangularities are calculated as

$$\delta_u = \frac{1}{a} \left(\frac{R_{max} - R_{min}}{2} - R_{upper} \right), \quad \delta_l = \frac{1}{a} \left(\frac{R_{max} - R_{min}}{2} - R_{lower} \right). \tag{4.15}$$

 R_{max} and R_{min} are the minimum radii along the boundary, R_{upper} is the major radius of the highest vertical (Z) point of the boundary, and R_{upper} is the major radius of the lowest vertical point. The experimental parameters are also a useful reference when constructing

TJ models parametrized in H_j , V_j , since they can be calculated from the dimensions of the resulting equilibrium.

In each case, I calculate the full eigenfunction, with as many harmonics as feasible, using the TJ code. TJ constructs the harmonics through a matching procedure carried out by simultaneously solving differential equations for each harmonic. The magnetic flux eigenfunction ψ , from which magnetic fields are derived, can be understood as a Fourier expansion:

$$\psi_m = \psi_m' + \frac{\epsilon}{2}(\psi_{m+1} + \psi_{m-1}) + \frac{\epsilon^2}{4} \sum_{j>0}^{\infty} H_j^2(\psi_{m+j} + \psi_{m-j})$$
(4.16)

where, for example, the first-order components can be expanded as

$$\psi_{m+1} = \psi'_{m+1} + \frac{\epsilon}{2}(\psi_m + \psi_{m+2}) + \dots$$

$$= \psi'_{m+1} + \frac{\epsilon}{2}(\psi'_m + \frac{\epsilon}{2}(\psi_{m-1} + \psi_{m+1}) + \psi'_{m+2} + \frac{\epsilon}{2}(\psi_{m+3} + \psi_{m+1}) + \dots)$$

$$= \psi'_{m+1} + \frac{\epsilon}{2}(\psi'_m + \psi'_{m+2}) + \frac{\epsilon^2}{4}(\psi_{m-1} + 2\psi_{m+1} + \psi_{m+3}) + \dots), \tag{4.17}$$

and ψ'_m are the fundamentals of each mode, without any sidebands. The sidebands in turn are expected to yield their own sidebands. All terms contain an expansion in all orders of ϵ , encompassing all modes. Toroidicity is expected to induce $m \pm 1$ sidebands parametrized by the inverse aspect ratio ϵ , elongation is expected to induce $m \pm 2$ sidebands parametrized by $\epsilon^2 H_2^2$, and so on. The factor of two in the denominator derives from the splitting of the sideband energy into two harmonics. Extrapolating to each order and including H_1 , the overall ψ_m contribution is proportional to $1 + (\epsilon - \frac{\epsilon^2 H_1^2}{4})^2 + \frac{\epsilon^4 H_2^4}{16} + \dots$ This is important when discussing mode number effects on measured amplitudes. Note that TJ requires a finite value of ϵ . In this thesis, when cylindrical plasmas are discussed in the context of TJ, this means that $\epsilon = 0.01$, a small but finite value. An example of an equilibrium calculated using TJ's shaping parameters [7] is depicted in Figure 4.5. $H_{j>1}$ and V_j are fixed at the boundary, and $H_j(r)$ and $V_j(r)$ are generated accordingly. This includes H_1 , which is generated from the Shafranov shift induced by the input ϵ . Observe that the flux surfaces are plotted with

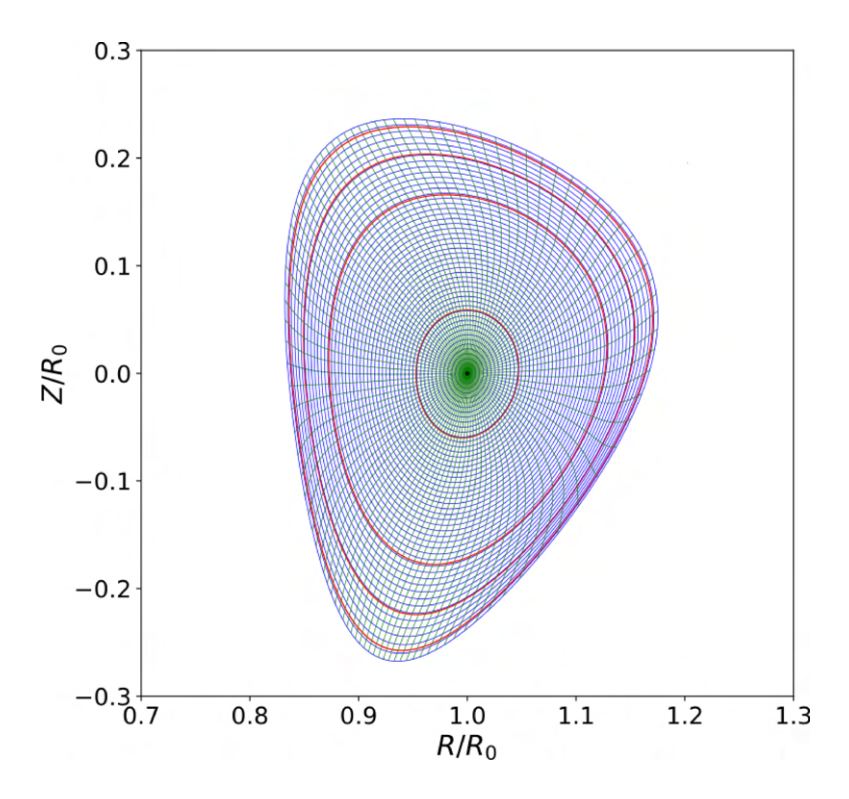


Figure 4.5: An example equilibrium generated by TJ with $\epsilon = 0.2$, $H_{2,a} = 1$, $H_{3,a} = 0.5$, $V_{2,a} = 0.2$, and $V_{3,a} = -0.375$, and $H_{j>3,a}$ and $V_{j>3,a} = 0$. Blue contours represent surfaces of constant radial flux coordinate, and green contours represent surfaces of constant angular flux coordinate. Black dot marks the magnetic axis. Red contours mark n = 1 resonant surfaces. Lengths normalized to major radius R_0 . Adapted from [7].

respect to a grid where flux surface radius is constant, as in the formulae for R and Z. Flux surface angle is also constant. In terms of the standard parameters, this plasma has $\kappa = 1.29$, $\delta_u = 0.342$, and $\delta_l = 0.370$. The simulation is performed with no wall; later calculations in this section will use a perfectly conducting wall at some finite distance from the plasma boundary [11].

Using TJ, I calculate a set of harmonics fixed in the inputs, not all of which have corresponding resonant surfaces, but which have a finite value regardless if the corresponding parameter ϵ (for the $m\pm 1$ harmonic) or H_j (for higher harmonics) is finite. TJ calculates and sums the sideband eigenfunctions in the linear expansion for a fixed set of n; these simulations were carried out for $-10 \le m \le 20$, giving a total of 31 harmonics. Obviously, not all of these have corresponding rational surfaces, but they exist as components of the full function [7]. A demonstration of sideband amplitudes, using the magnetic flux eigenfunction ψ calculated

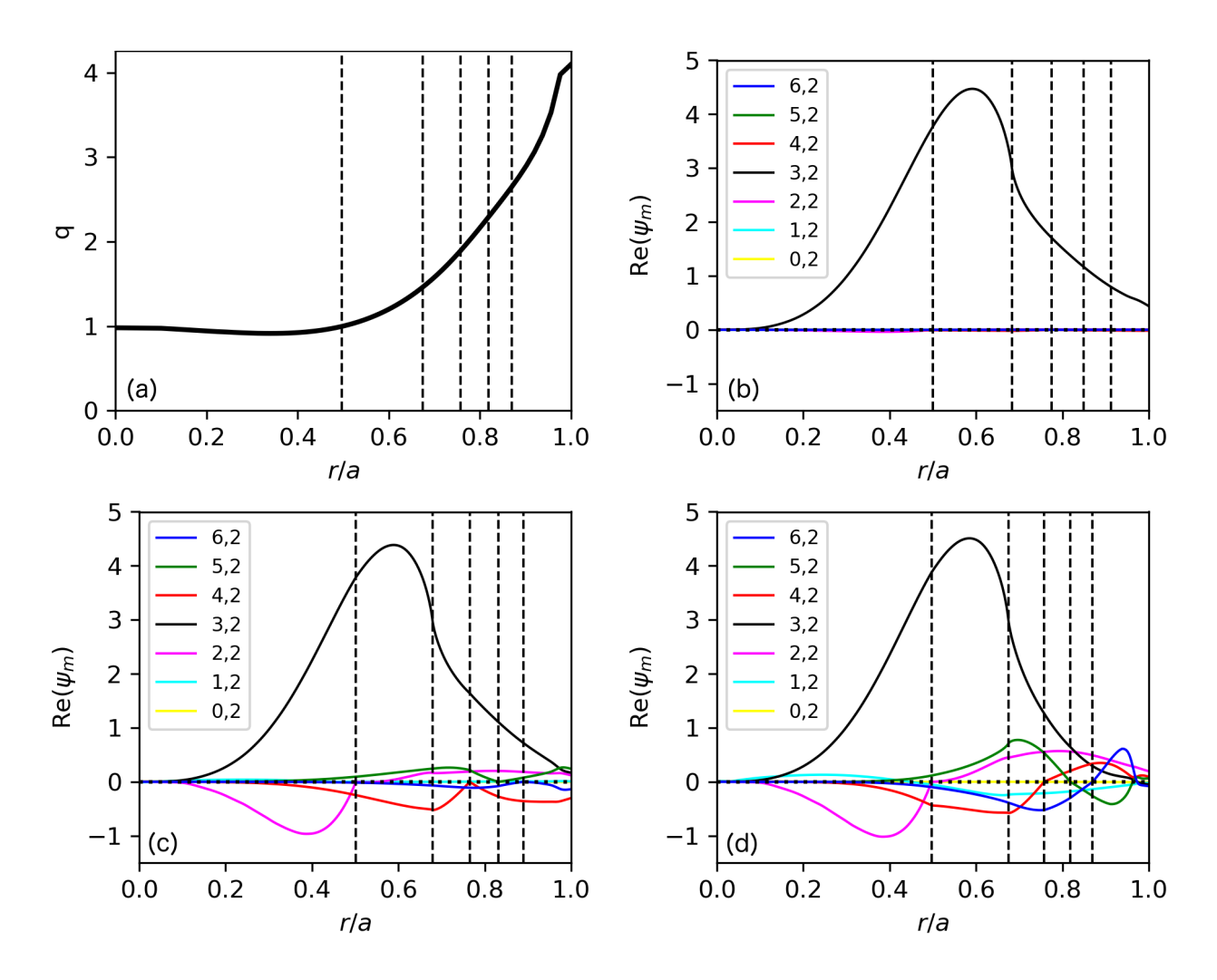


Figure 4.6: (a) TJ input safety factor profile, corresponding to DIII-D shot #182771. Tearing mode (black) and sideband (colors) magnetic flux eigenfunctions, calculated with TJ, for cylindrical (b, $\epsilon = 0.01$, $H_2 = 0$), toroidal (c, $\epsilon = 0.3$, $H_2 = 0$), and elongated (d, $\epsilon = 0.3$, $H_2 = 0.5$) plasmas for the given q profile. Vertical dashed lines indicate rational surfaces.

with TJ, for an m, n = 3, 2 tearing mode in ρ for cylindrical, toroidal, and toroidal-elongated plasmas is given in Figure 4.6. Figure 4.6(a) gives an experimental q profile used in TJ to calculate the sideband structure. The cylindrical plasma ($\epsilon = 0.01, H_2 = 0$, Figure 4.6(b)) demonstrates sidebands with an amplitude near zero, with the original m, n = 3, 2 mode (black) dominating. The toroidal ($\epsilon = 0.3, H_2 = 0$, Figure 4.6(c)) and elongated ($\epsilon = 0.3, H_2 = 0.5$, Figure 4.6(d)) plasmas demonstrate finite sidebands (colored), up to $m \pm 3$, where the plotted portion of the expansion truncates. The sideband amplitudes are dependent on plasma shaping. Notice that in Figure 4.6(c), the highest-amplitude sidebands are the m+1

(red) and m-1 (magenta) modes, which are generated by coupling to the Shafranov shift. The other sidebands are generated through the further coupling of the $m\pm 1$ sidebands to toroidicity, since there is no elongation coupling. This expansion results in the maximum amplitude of the, e.g., m+2 sideband (green) being lower than the maximum of the m+1 (red) sideband by a factor of ϵ . This ratio is not followed exactly in the elongated plasma, because there is now a second component to the m+2 mode: note the strong 5,2 and 6,2 sidebands near the edge, which are generated by a combination of toroidicity and elongation coupling. Also recall here that the so-called cylindrical plasma is not exactly cylindrical and instead has a small, finite ϵ . This value is what results in the small visible sidebands in the cylindrical case. Each successive addition to the shaping parameters affects the size of the generated sidebands and moves the model closer to representing an actual DIII-D plasma, or what RIP is expected to measure in the linear model.

TJ simulations take input q and pressure profiles. The automatically generated plasma shape also changes the rational surface locations somewhat to maintain angular momentum conservation. The modifications to the q profile affect the edge, with the rational surfaces in the core undergoing less drastic change. TJ conserves angular momentum by ensuring that the electromagnetic torque between the magnetic axis and any surface inside the plasma is negligible. This also sets the net torque at the boundary to be zero, which is required for the plasma to rotate as a rigid body. The only exception to this rule is at rational surfaces, where one would expect instabilities to exert torque on the plasma [7]. TJ's modification of the q and pressure profiles ensures that the appropriate torques are exerted at all radii.

From the flux eigenfunction ψ , the horizontal (B_R) and vertical (B_Z) components of the magnetic field are calculated in TJ and can therefore be compared to RIP and sensing coil measurements respectively. My first choice is the cylindrical model ($\epsilon = 0.01$, $H_j = 0$) to establish that to lowest order in a full model with all terms, an odd-m mode gives a finite line integral at the midplane while an even-m mode gives zero. The q profile corresponds to DIII-D shot #182771. Figure 4.7(a-b) illustrates the 3,2 case and plots the line integral

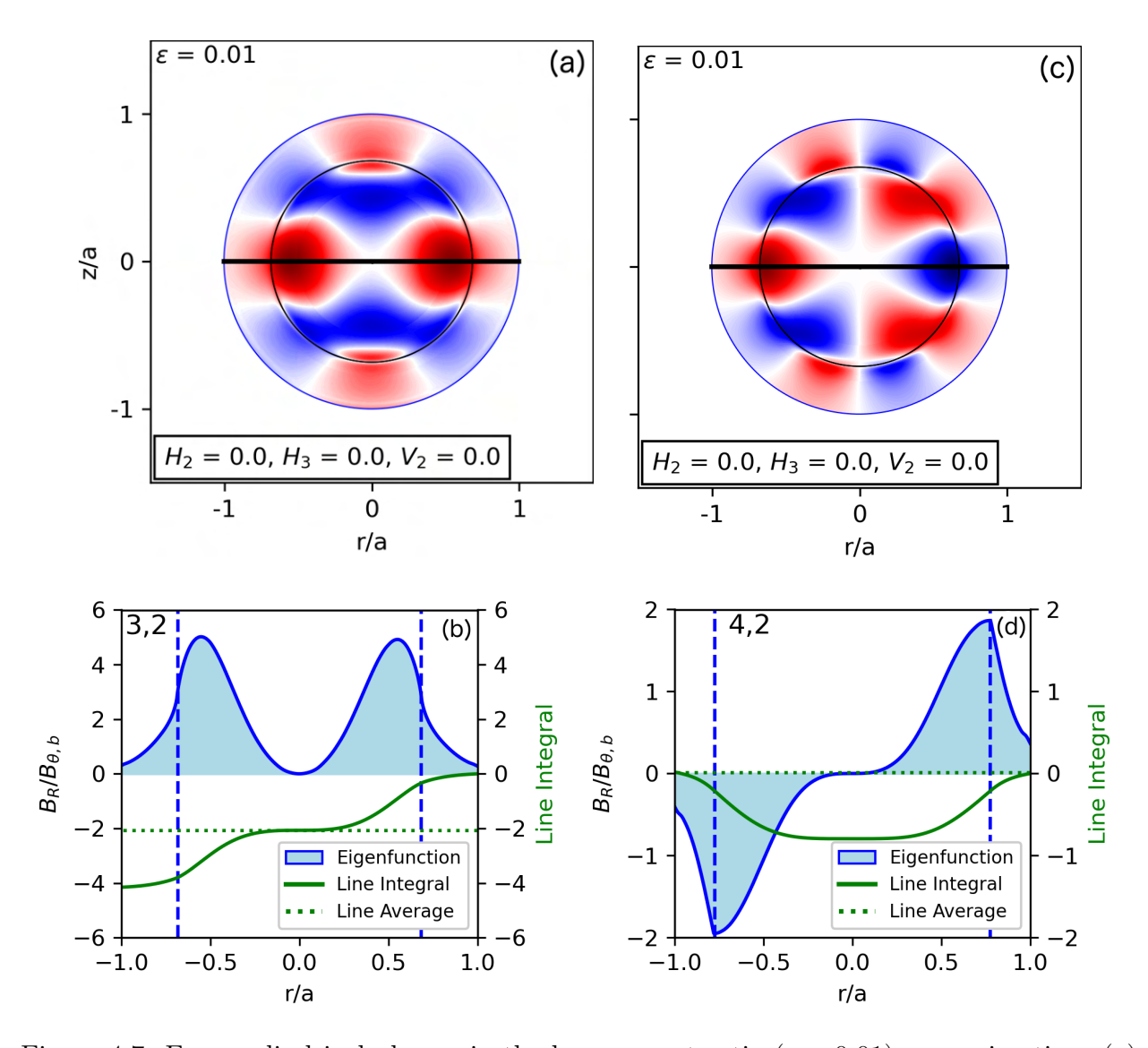


Figure 4.7: For a cylindrical plasma in the large aspect ratio ($\epsilon = 0.01$) approximation: (a) Contour plot of B_R for a 3,2 mode. Red represents positive values and blue negative values. (b) B_R along the chord (blue, filled), line integral (green, solid), and line average (green, dotted) in the -R direction. Blue vertical dashed lines mark the resonant surface on each end of the chord. (c-d) The same plots for the 4,2 mode.

of B_R at the midplane. Plot (a) shows B_R for the 3,2 mode in two dimensions and the path of the midplane RIP chord. Plot (b) shows B_R along the chord and shows both the line-integral and the line average. B_R along the chord is normalized to B_Z at the edge, which is the synthetic analogue of the sensing coil measurement. Here, the measurement is made at the midplane. The synthetic polarimetry diagnostic can measure at any height above or below the midplane. Since the coordinate system in TJ is polar in (r,θ) , the synthetic polarimetry diagnostic integrates over each (r, θ) point closest to the specified location. RIP integrates in the -R direction, or from left to right as represented in the figures. Therefore, the sign of $\int B_R dR$ in the figures is the opposite of the sign of B_R ; this corresponds to the trough of the fluctuation and does not affect the actual RIP measurement as it is an absolute value. The magnetic field is symmetric over reflection in R for odd m, so the line integral is finite. Figure 4.7(c-d) illustrates B_R and its line integral in the 4,2 case. Plot (c) shows B_R in two dimensions and the path of the chord. Plot (d) shows B_R along the chord, the line integral, and the line average. The magnetic field is antisymmetric over reflection for even m, so the line integral is near zero. The small residual is due to a mandatory small level of toroidicity in TJ that creates small sidebands. In the cylindrical approximation, even-mmodes are not detected by polarimetry at the midplane.

4.2.3 Model Comparisons and Shape Effects on Synthetic Eigenfunctions

Here, I use the linear model with toroidal and shaping effects, computed using TJ, to develop a model for what RIP would be expected to measure, relative to the magnetic field measured by the coils. The line integral of B_R is taken as a synthetic RIP measurement. The value of the line integral is then compared to the $B_{Z,b}$ output by TJ, i.e., a synthetic coil amplitude, in the same way that mode amplitudes can be compared between RIP and the coils. This is a useful method because coils can detect all mode numbers, and eigenfunctions are directly proportional to $B_{Z,b}$. RIP cannot measure B_{θ} at the midplane, and the sensing coils are the only other diagnostic that measures magnetic fluctuations. Therefore, the

coils are an appropriate normalization factor for RIP when comparing to the line-integrated eigenfunction models. It should be recognized that coil measurements are susceptible to local MHD effects such as toroidal asymmetry (as the low-noise coils are toroidally separated from RIP) and shielding of fluctuations by other modes. However, coil data quality is good in the shots measured, and there is no evidence of shielding or local effects. I test the synthetic measurements, with and without considering the antisymmetry in the B_R eigenfunction for even m, against RIP to determine the effect of even and odd m on RIP amplitudes. Lastly, I develop scalings to estimate the effects of toroidicity and chord location on projected RIP amplitudes.

I assess the relative contribution of the q term in Equation 4.3 [14, 15] by comparing the analytic high-m model to the TJ cylindrical model. The simulation is performed with an ideally conducting wall, located at $b_w = (a + d_{gap})/a = 1.1$ and q profile corresponding to DIII-D shot #182771. Here a is the location of the plasma boundary, and b is the location of the wall. A comparison image between TJ simulations and the analytic model for modes with m = 3-5 in the cylindrical limit, with the wall gap included, is provided in Figure 4.8. The plasma is parametrized with the same wall gap and q profile as DIII-D shot #182771 but a cylindrical plasma. Section 4.3 will directly compare RIP and coil data for the three given modes in #182771. The analytic model was a basic statement of the eigenfunction effect on RIP amplitudes. The TJ model is a more complete model of the actual eigenfunction. The functions are more localized as m increases, even for similar resonant surface locations. The TJ cylindrical model and analytic model correspond closely for $|r| > r_s$, and both decay as $(r/b)^{-m-1}$. The two solutions diverge from each other for $|r| < r_s$ due to the q term, which increases mode amplitude in that region. The analytic model has a sharp discontinuity in its derivative at the rational surface, while the TJ model is smooth. In TJ, the resistive layer has finite width, and the $(r/b)^{-m-1}$ model breaks down. Asymptotic matching at the boundaries of the resistive region generates a function whose derivative is continuous [7].

Some corrections have been made to the cylindrical eigenfunctions in Figure 4.8. The

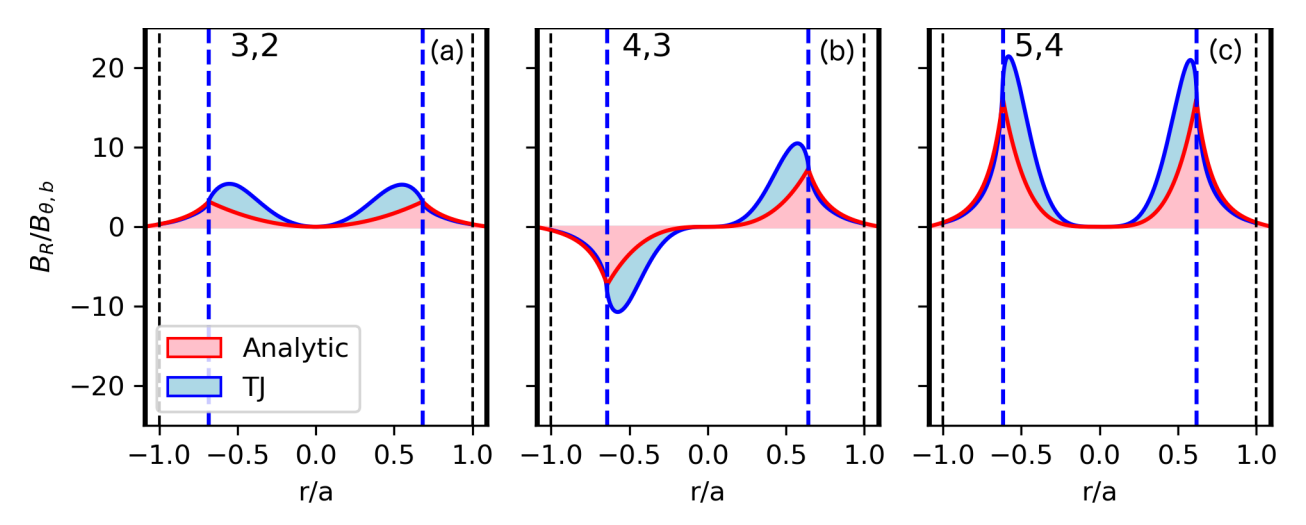


Figure 4.8: Comparisons between the analytic (red) and TJ (blue) cylindrical eigenfunction models for (a) 3,2; (b) 4,3; and (c) 5,4 modes. Vertical blue dashed lines denote resonant surfaces. Vertical black dashed lines denote plasma boundary.

sensing coils are located on the wall, so the $B_{\theta,b}$ they measure is not the same as $B_{\theta,a}$, which is the boundary of B_Z in TJ. The true eigenfunction model extends to the wall, since B_R is finite at the plasma boundary and only goes to zero at the wall. B_Z is finite and continues decaying to its external value $B_{Z,b}$ at the wall (= $B_{\theta,b}$ measured by the sensing coils at the midplane). However, TJ does not output B_R or B_Z in the vacuum region. I must therefore introduce corrections corresponding to estimates for these quantities at the wall. According to the analytic model (Equation 4.8), B_r and B_θ decay as $(r/b)^{-m-1}$ far from the resonant surface for $|r| > r_s$. This can be used to approximate that B_R and B_Z decay accordingly outside the plasma. Because the wall is assumed to be a perfect conductor, $B_R = 0$ at the wall. B_Z decays toward the wall and is expected to have a smaller value at the wall than at the plasma surface. A demonstration of this approximation for b > a, for both B_R and B_Z , is shown in Figure 4.9. In the 3,2 case, for $b_w=1.1,\ B_{Z,b}/B_{Z,a}\approx (1/1.1)^4=0.683,$ a decrease in amplitude of over 30%. Plasma distance from the wall strongly affects the normalization of the TJ-generated eigenfunctions to the coil value. The model also includes a contribution to $\int B_R dR$ from the portion of B_R lying outside the plasma. Depending on the mode, the vacuum component contributes between 1–3% of the total line average, a small value. RIP does not measure the magnetic field in the vacuum, because Faraday rotation measurements

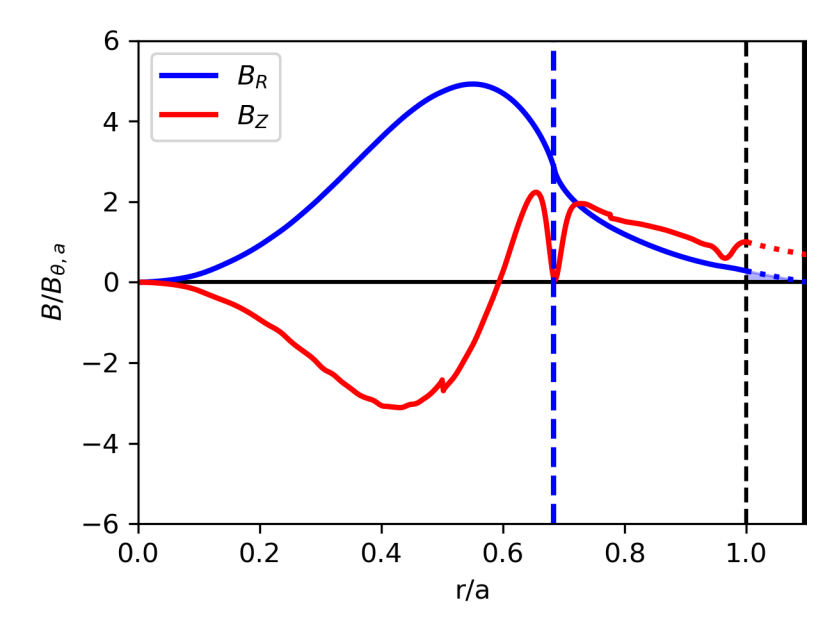


Figure 4.9: B_R (blue) and B_Z (red) profiles for a 3,2 mode in a cylindrical TJ equilibrium. r/a = 1 (vertical black dashed line) is the plasma boundary, and plot boundary is the wall at r/a = 1.1. Dotted lines denote extrapolations of each magnetic field component to the wall under the approximation that they decay as $(r/b)^{-m-1}$. Vacuum component of B_R integral highlighted in blue. Vertical blue dashed line denotes resonant surface.

are density-weighted, and density is near zero in the vacuum region. Therefore, the vacuum component may be neglected when developing synthetic analogues to RIP data based on the linear TJ model.

Next, I add toroidicity and shaping to the model to bring it closer to a realistic configuration. Using cylindrical models, one can only estimate the effects of mode number and toroidicity on mode amplitudes and their ratios, making any estimate of the effects of shaping even more uncertain. The two-dimensional model in TJ inherently incorporates the sign flip across the magnetic axis for even-m modes, and the eigenfunction includes mode number, toroidicity, and shaping effects by adding all harmonics together. Figure 4.10 shows example B_R from TJ for a 4,2 tearing mode in cylindrical, toroidal, toroidal-elongated, and toroidal-shaped plasmas. In the shaped case, I tune the elongation and triangularity to approximate the shape of DIII-D shot #182771, which will be compared directly to TJ later in this chapter. The q profile is close to the q profile of #182771; TJ automatically makes slight adjustments to conserve angular momentum. Pressure is zero to simplify calculations,

as it does not appear to have an effect on the eigenfunctions. I choose a 4,2 mode to visually illustrate the antisymmetry of B_R for even-m modes in the cylindrical approximation and the breaking of antisymmetry in toroidal and shaped plasmas.

When I use a model with lower aspect ratio ($\epsilon = 0.3$) i.e., a toroidal plasma, the eigenfunction gains $m \pm 1$ toroidal harmonics, which are visible in Figure 4.10(b) as distortions to the overall function. Once the plasma has been made toroidal, additional shaping parameters can be added: elongation (represented by H_2 , added in (c)), triangularity (represented by H_3 , added in (d)), and so on. Adding parameters to the plasma structure distorts the eigenfunctions further, with increasingly higher-order fluctuations visible at the edge. These higher-order fluctuations are due to the harmonics, as represented in the radial ψ in Figure 4.6. For example, the outer portion of Figure 4.10(c) has 13 lobes of each color. Resonant surfaces with m = 2, 3, 4, 5, 6, 7 exist in this plasma. The 13-lobe pattern results from the presence of both the 5,2 (first order in toroidicity) and 6,2 (second order in toroidicity, first order in elongation) harmonics in the outer section, as the interference pattern between m=6 and m=5 has 13 intersections. Plasma (a) has $\epsilon=0.01$, the cylindrical approximation, and all other shaping parameters zero. Plasma (b) has $\epsilon = 0.3$, a DIII-D-like toroidicity, with all shaping parameters zero. Plasma (c) has $\epsilon = 0.3$ and elongation parameter $H_2 = 0.8$, yielding an elongation value of approximately $\kappa = 1.8$. Plasma (d) has $\epsilon = 0.3$, $H_2 = 0.8$, and triangularity parameter $H_3 = 0.4$, which together result in an elongation of $\kappa = 1.5$ and a top and bottom triangularity of approximately $\delta = 0.4$. The q profile for all four of these plasmas is close to the profile shown in Figure 4.6(a). Observe that the distortion due to each successive addition of a shaping parameter changes the relative amplitudes of the inboard and outboard components. This is expected to result in a finite line-integrated polarimetry measurement for an even mode.

The next step is to quantitatively determine the relative effect of the sidebands on the measured dominant mode amplitude. Using TJ, I perform a scaling analysis of simulated toroidal plasmas with circular cross-sections and varying aspect ratios to confirm that in

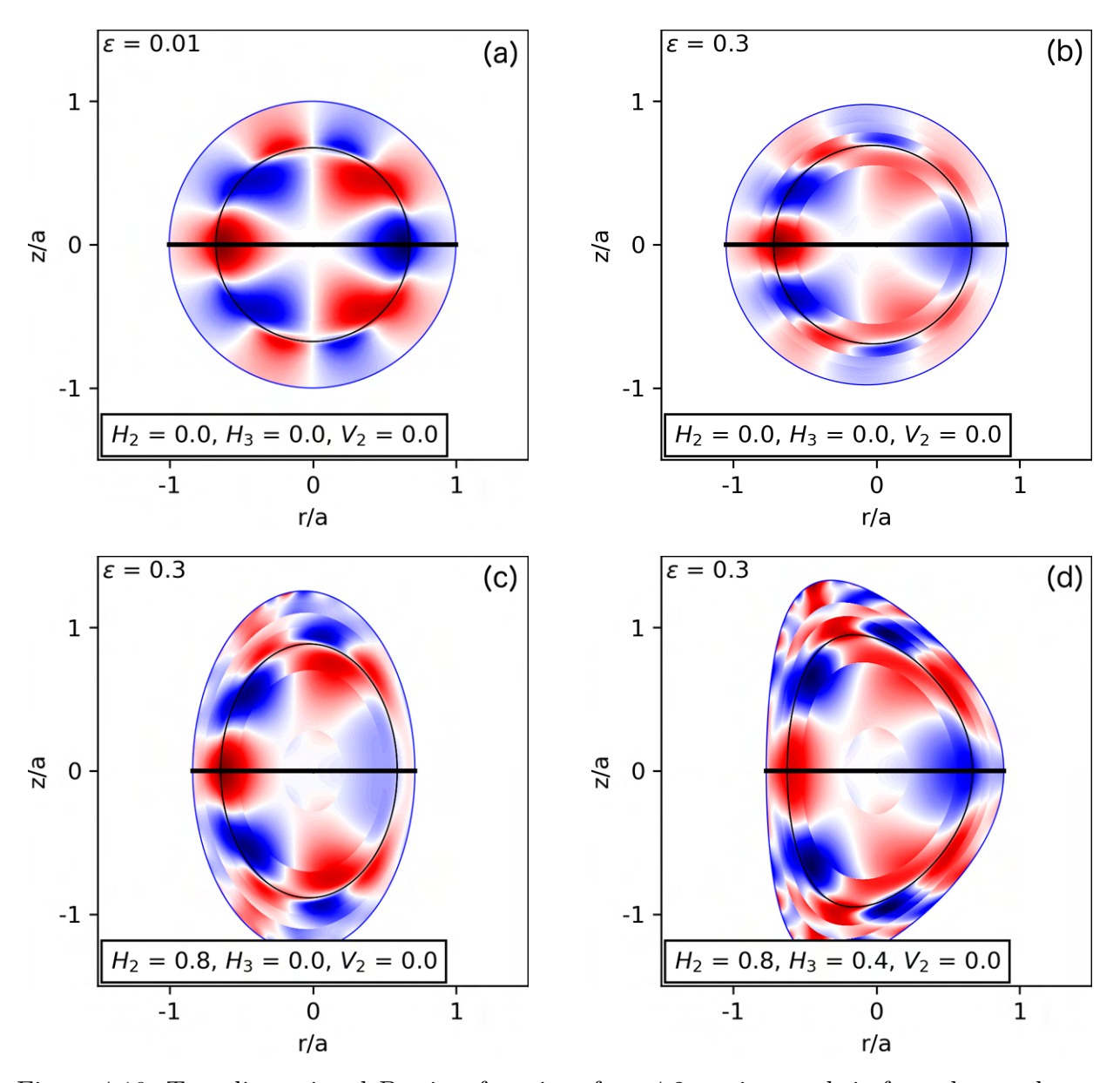


Figure 4.10: Two-dimensional B_R eigenfunctions for a 4,2 tearing mode in four plasma shapes parametrized as shown: (a) cylindrical, (b) toroidal-circular, (c) toroidal-elongated, and (d) toroidal-triangular. Red represents positive values and blue negative values. Resonant surface marked with black contour and plasma boundary with blue contour.

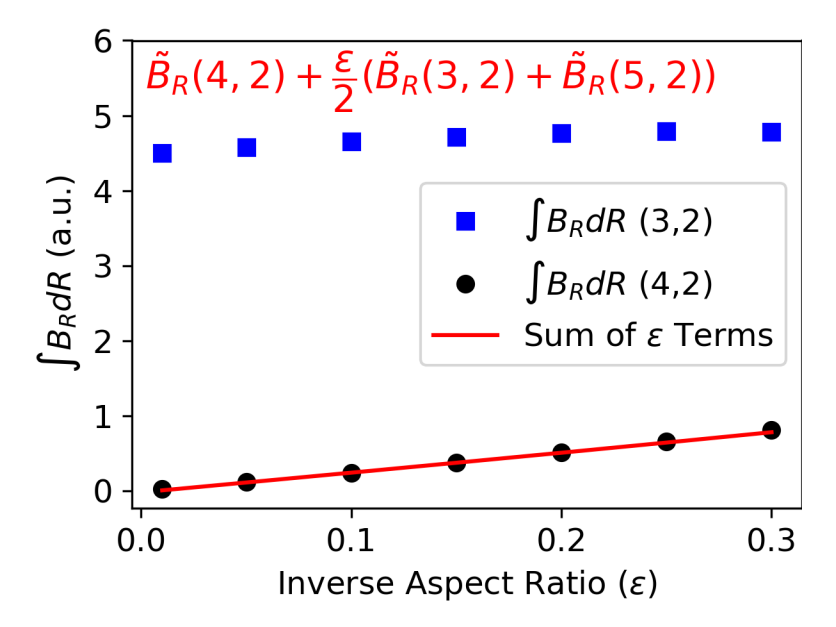


Figure 4.11: Line-integrated amplitudes at the midplane of the 3,2 (blue squares) and 4,2 (black circles) modes in the TJ model compared with the projected odd-*m* component of the 4,2 mode, calculated from its cylindrical sidebands (red solid line, terms written in red) in the same model.

TJ, even-m modes are detected only from their sidebands. Here I use several inverse aspect ratios a/R ranging from 0.01 to 0.3 to confirm that the model is consistent. For the example of an even-m mode, I consider a 4,2. The 4,2 mode is expected to produce 3,2 and 5,2 sidebands attenuated by ϵ . Expanding as in Equation 4.16 to leading order, the measurable portion of the 4,2 mode appears as

$$\tilde{B}_R(4,2) = \frac{\epsilon}{2} (\tilde{B}_R(3,2) + \tilde{B}_R(5,2)) \tag{4.18}$$

or, to leading order, linearly dependent on ϵ . This is the portion I expect RIP to detect.

I now investigate the properties of the TJ model and the role of the sideband amplitudes in building up the total mode amplitude measurement. I first test directly, using TJ measurements of both the 4,2 mode and the 3,2 and 5,2 sidebands, whether Equation 4.18 holds. I therefore use TJ to calculate and plot the left side $(\int \tilde{B}_R(4,2)dR)$ of Equation 4.18 versus the right side $(\int \frac{\epsilon}{2}(\tilde{B}_R(3,2) + \tilde{B}_R(5,2))dR)$ to determine whether they match. Here $\tilde{B}_R(3,2)$ and $\tilde{B}_R(5,2)$ are the values in the cylindrical approximation, since the toroidal model is con-

structed out of cylindrical sidebands. I repeat the process for two modes at multiple values of ϵ , shown in Figure 4.11. While aspect ratio does not vary in experiment, this test of the ϵ dependence of the 4,2 mode, as compared to the dependence of the sidebands that should make it up, should indicate how much of the measured 4,2 mode amplitude in TJ is attributable to these two sidebands. If the match is close, odd mode amplitudes, parametrized to the inverse aspect ratio, can be used as a predictor for even mode amplitudes measured with RIP.

The 3,2 mode shows relatively constant line-integrated amplitude (blue squares) for all ϵ , reflecting a small contribution from its order- ϵ^2 and higher odd-m sidebands. The 4,2 (black circles) grows nearly linearly, matching closely to the expected ϵ scaling of its two odd-m cylindrical sidebands (red line). At $\epsilon = 0.3$, a DIII-D-like value, to first order the 4,2 mode (sum of 3,2 and 5,2 sidebands) is attenuated versus the sum of the projected 3,2 and 5,2 dominant mode amplitudes by a factor of 0.146, within 3% of the predicted value of 0.15. This close relationship between the 4,2 amplitude and the projected value of the sidebands holds for all ϵ , indicating the consistency of the model. The scaling result indicates that RIP should detect even modes through their odd sidebands, attenuated by a factor of ϵ .

I test a similar scaling by varying elongation. The elongation component is expected to scale as

$$\tilde{B}_R = \tilde{B}_R(m,n) + \frac{\epsilon^2}{2} H_2^2(\tilde{B}_R(m+2,n) + \tilde{B}_R(m-2,n)) + \dots$$
(4.19)

where H_2 is the elongation parameter fixed in TJ. Note that the elongation terms will all have the same parity as the dominant term. In the limit of large aspect ratio, elongation is not expected to affect amplitudes, since the elongation harmonic is proportional to ϵ^2 . When aspect ratio is finite, elongation contributes an extra odd component for odd modes. It is expected to contribute an order- ϵ^3 effect for even-m modes, where the toroidal sidebands will interact with elongation and generate their own sidebands. To isolate the elongation effect and increase it as much as possible, I fix $\epsilon = 0.3$ and vary H_2 from 0 to 1, which in a plasma with zero triangularity is approximately equivalent to varying $\kappa = 1-2$. The 3,2 and

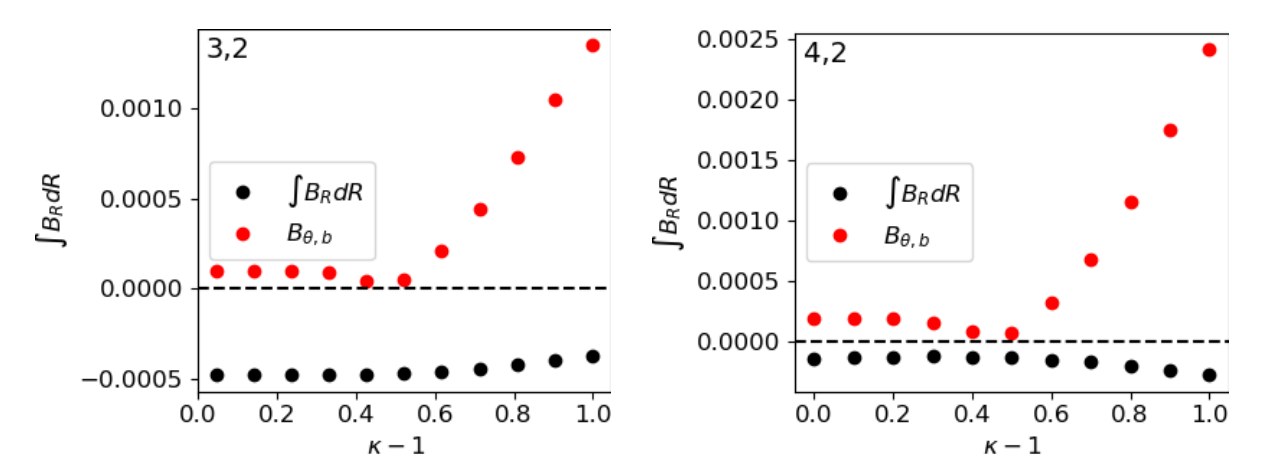


Figure 4.12: Line-integrated B_R and edge B_θ in arbitrary units in TJ-modeled m, n = 3, 2 (a) and m, n = 4, 2 (b) modes for plasma elongation from $\kappa = 1 - 2$.

4,2 line-integrated amplitudes, along with $B_{\theta b}$, are plotted in arbitrary units versus $\kappa - 1$ in Figure 4.12.

Without normalization, $\int B_R \, dR$ shrinks in magnitude for the 3,2 mode, representing $m \pm 2$ sidebands of the opposite sign that add to the 3,2 fundamental, reducing its value. The same integral for the 4,2 mode grows in time slightly. Since the $m \pm 2$ component also has even m and is not visible in the line integral, I infer that the growth in the 4,2 mode with elongation is related to the coupling of the elongation sidebands in turn to toroidicity, which produces $m \pm 1$ and $m \pm 3$ sidebands. These results are consistent with what might be expected from a pure linear model. However, the value of B_{θ} at the edge shows a dramatic departure from expectation. Due to the formation of a magnetic structure at the outboard midplane at higher elongations, B_{θ} increases drastically in value as κ grows higher than 1.5. In Sections 4.3 and 5.4, B_R is normalized to B_{θ} to compare RIP to the sensing coils. The influence of the outboard structure on synthetic mode amplitudes with TJ will significantly affect the normalization.

Above or below the plasma midplane, B_R contains both radial (B_r) and poloidal (B_θ) components. The B_θ components do not have the same even/odd parity as the B_r components, so less cancellation of even-m components due to antisymmetry is expected to occur. I investigate the effect of chord height on line-integrated mode amplitude in preparation for

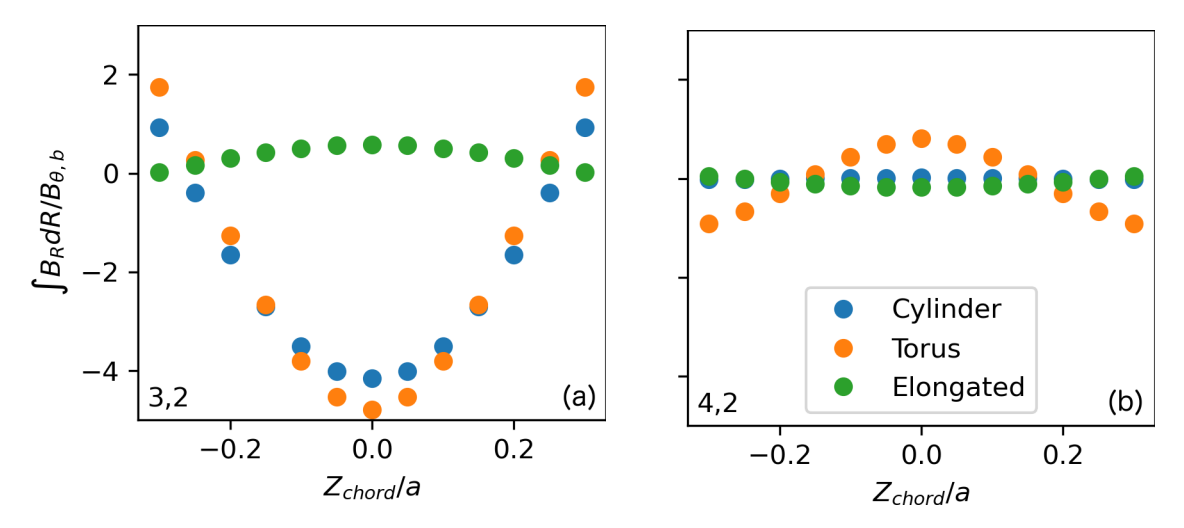


Figure 4.13: (a) Integral of B_R for heights Z/a above and below the midplane, normalized the minor radius, for a 3,2 mode in three plasma shapes: cylindrical (blue, $\epsilon = 0.01$, $H_2 = 0$), toroidal (orange, $\epsilon = 0.3$, $H_2 = 0$), and toroidal-elongated (green, $\epsilon = 0.3$, $H_2 = 0.8$). (b) The same integrals for a 4,2 mode.

the experimental work done in Chapter 5. I compare synthetic RIP amplitudes at chord heights from 25% of the minor radius below the midplane to 25% above the midplane for three different plasmas, depicted in Figure 4.13. The cylindrical plasma has $\epsilon = 0.01$ and $H_{2,a} = 0$. The toroidal plasma has $\epsilon = 0.3$ and $H_{2,a} = 0.8$ ($\kappa \approx 1.8$ if there is no triangularity).

The magnitude and shape of B_R as well as the magnitude of $B_{\theta,a}$ for the cylindrical and toroidal 3,2 (Figure 4.13(a)) are very similar under vertical translation to the extent studied, resulting in similar integrals. This is understandable because toroidicity only generates even-m sidebands, which integrate to near zero at the chord heights analyzed. The elongated plasma has a very different dependence on chord height, attributable to a structure that develops at the outboard midplane in plasmas with $\kappa \geq 1.5$ and affects $B_{Z,b}$. The structure has B_R of the opposite sign to the internal structure, so this results in $\int B_R dR$ of the opposite sign of the cylindrical and toroidal cases. For the m, n = 4, 2 mode (Figure 4.13(b)), the integral in the cylindrical case is small for all Z_{chord} , reflecting antisymmetry in the eigenfunction. The breaking of antisymmetry due to toroidal effects and the addition of the odd-m sidebands results in a nonzero integral. The synthetic RIP diagnostic integrates over

the sidebands, but these are attenuated by ϵ and therefore lesser in magnitude compared to the contributions in the odd-m case. Once again, the elongated case is dominated by the structure at the outboard midplane. $\int B_R dR$ changes sign as the chord moves up in the cylindrical and toroidal cases, associated with the regions of strongest symmetry or asymmetry moving off the chord location.

The linearized nature of TJ, where each tearing mode is developed as a sum of eigenfunctions for a single n, still leaves the question of where and at what frequency the sidebands resonate. In the TJ linear expansion, reconnection takes place only at a single rational surface. As a result, sidebands with the same n rotate at the same toroidal frequency (nf_{ϕ}) as the main mode [12]. Therefore, in a spectrogram or other measure of power at a given frequency, each mode should be coherent. Poloidal rotation is relatively flat in the core. As a result, the ratio of the poloidal to toroidal rotation contribution to total mode frequency (see Equation 2.34) should be the same up to a factor of m/n. Given that poloidal rotation is weak in DIII-D [16], the shift between sideband total frequencies due to poloidal rotation should be minor. Since tearing modes are not perfect sinusoids, sidebands should appear as a broadening of the mode in frequency space. As shown in Section 4.1, the finite frequency width of the mode is already considered when measuring amplitudes. Thus, sidebands are already included in amplitudes on both RIP and the coils, which are distinguished by frequency, in the same way they are in the TJ eigenfunctions. This also means that sidebands of a dominant mode do not interfere with the measured amplitude of other modes present in the plasma at distinct frequencies.

I conclude with a discussion of how the sidebands interact with independent modes. Linear geometric coupling can be described with a similar formulation to Chapter 2.4's example on nonlinear coupling, but with the shaping components coupling like (m, 0) modes because the plasma is axisymmetric. The geometry of the plasma has no time dependence. I confirm that the sideband is in phase with the dominant mode. This should yield a sideband with the following structure:

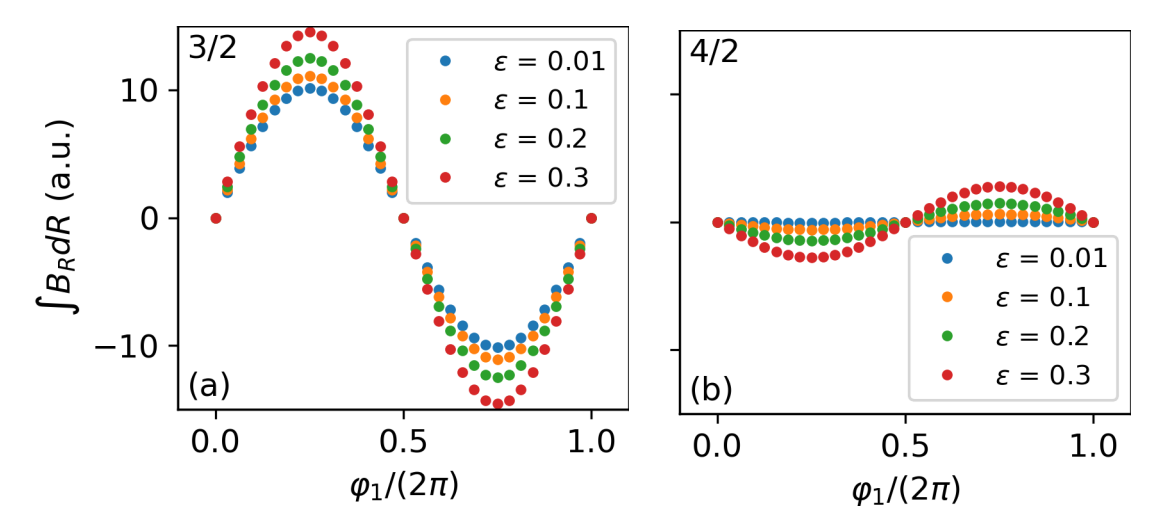


Figure 4.14: Amplitudes of (a) the 3,2 mode and (b) 4,2 mode versus input phase for four different inverse aspect ratios (blue, orange, green, red).

$$\Psi_3 = \Psi_1(r) \exp(im_1\theta - in_1\phi - i\omega_1t + \varphi_1) \cdot \Psi_2(r) \exp(im_2\theta)$$

= $\Psi_1(r)\Psi_2(r) \exp(i[(m_1 + m_2)\theta - n_1\phi - \omega_1t + \varphi_1]).$

Using TJ, I can calculate $\int B_R dR$ for odd- and even-m modes rotated by an arbitrary phase φ_1 . By the barber pole principle discussed in Section 2.3, this phase corresponds to a rotation in the toroidal direction and to motion in time. I am searching for the relative phase between the 3,2 mode and the odd-m sidebands of the 4,2 mode. The relationship between the line-integrated midplane amplitudes of the 3,2 and 4,2 modes and the phase φ_1 is shown in Figure 4.14. Once again, it is evident that the 3,2 mode has a finite amplitude for all ϵ , augmented at higher ϵ by the addition of sidebands. The 4,2 mode has amplitude near zero for small ϵ but increases as ϵ and the amplitudes of the sidebands increase, in line with the scaling already established in Figure 4.11. The visible odd-m sidebands of the 4,2 mode are phase-locked to the 3,2 dominant mode, and this does not change with either aspect ratio or the overall phase shift. Each relation is a pure sinusoid, showing that all sidebands have the same frequency and phase as well. All sidebands of the mode are phase-locked both to each other and to the dominant mode, with no drift. This in turn means that in a case of nonlinear coupling, the sidebands should interact with the coupled mode in the same way

that the dominant mode interacts.

4.3 Mode Number Effects on RIP Amplitudes

I now compare the TJ models to DIII-D data. In the cylindrical limit, it is expected that even-m modes should not be detected with RIP. However, when linear sidebands are included, even modes become detectable in models of RIP line-integration. I test against RIP data on DIII-D predictions in toroidal and shaped plasmas of relative even- and odd-m mode amplitudes on RIP. If the even mode's amplitude corresponds to the measured sideband contribution, then linear factors are the primary contributors to what RIP measures for even modes. The ITER Baseline Scenario (IBS) is a useful scenario for comparing RIP and coil measurements due to the frequent presence of multiple tearing modes. IBS combines an ITER-similar shape with low torque and q(0) < 1, making the plasma susceptible to the sawtooth instability, which can trigger tearing modes. A major concern in IBS is preventing disruptions due to the m, n = 2, 1 NTM [17]. The 2,1 is often preceded by a cascade of tearing modes beginning with 5,4; 4,3; and 3,2 modes, with the 2,1 triggered by a sawtooth, an ELM, [18] or nonlinear coupling [19]. DIII-D shot #182771, whose shape and q profile were already investigated with TJ above, is chosen. In this shot, multiple tearing modes with both even and odd m are present simultaneously at high amplitude on both RIP and the coils, which is useful for comparing the two diagnostics' detection of modes with even and odd m. I begin with a comparison at a single time point between the n = 2 - 4 modes. Data from the RIP midplane chord and a single midplane magnetic sensing coil from shot #182771 are shown in Figure 4.15.

Note that RIP measures B_R and the coils measure B_θ , so the mode amplitudes cannot be directly compared without a synthetic eigenfunction for B_R , normalized to edge B_θ measured on coils. To begin, I observe the relative amplitudes between the modes on RIP and the coils to reveal information about the quantities being measured. I focus in particular on t = 2480 ms but also on amplitude trends. On RIP, the m, n = 3, 2 mode has the strongest amplitude, with 4, 3 and 5, 4 lesser in amplitude. On the coils, however, the 5, 4 is the smallest, with

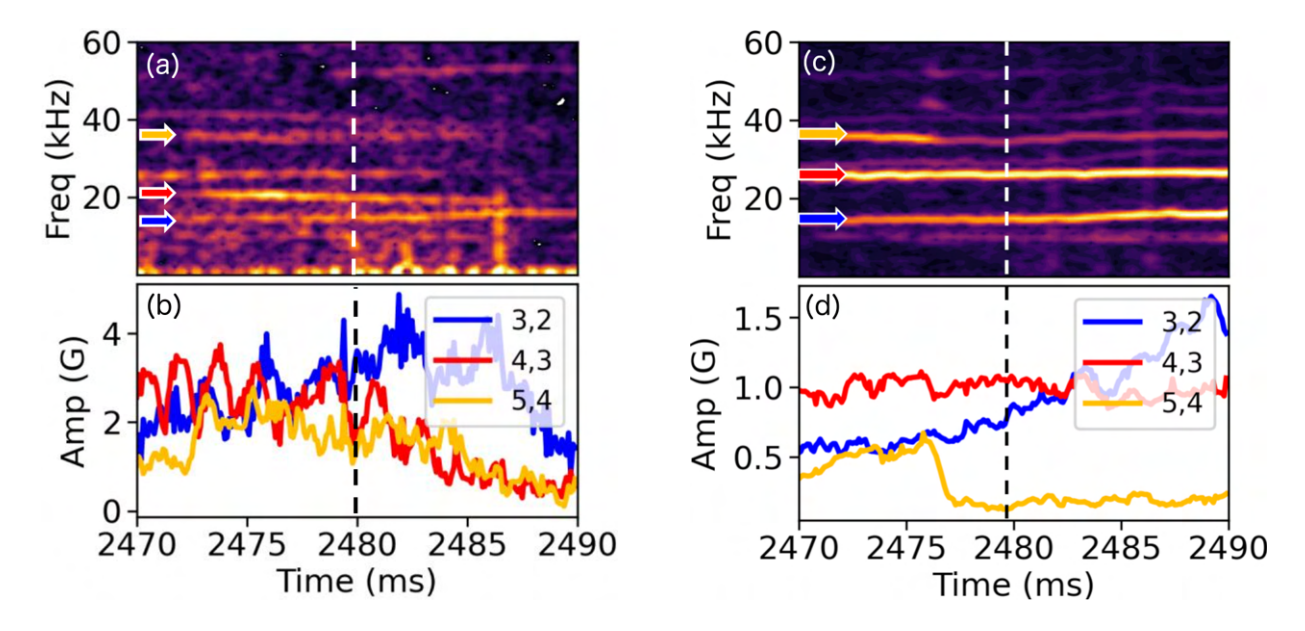


Figure 4.15: (a) Spectrogram of RIP magnetic signals. Tearing modes marked with arrows. (b) RIP magnetic fluctuation amplitudes (\tilde{B}_r) of tearing modes marked in (a). Line colors correspond to arrows in (a). (c) Spectrogram of magnetic signals for a single sensing coil. Same modes are marked. (d) Sensing coil magnetic fluctuation amplitudes (\tilde{B}_{θ}) for the same modes. Dashed lines mark t = 2480 ms, where further calculations are done.

the 4,3 more prominent than on RIP. The 3,2 is strong on both diagnostics. The ratio of RIP to coil-measured mode amplitudes $(B_R/B_{\theta,b})$ is given in Table 4.1: it is much higher in the 3,2 and 5,4 than the 4,3 by a factor of 2.74 and 6.29 respectively. While the 4,3 mode is visible, its amplitude is attenuated on RIP with respect to the value measured by coils. Modeling indicates that RIP is measuring not the even-m mode, which cancels to zero under line integration, but its odd-m harmonics. The toroidicity-related harmonics m=3 and m=5 should be attenuated by a factor of ϵ compared to the dominant mode. The elongation-related sidebands m=2 and m=6 should then be attenuated by $\epsilon^2 H_2$ and the triangularity sidebands m=1 and m=7 by $\epsilon^2 H_3$, where H_2 and H_3 are set in TJ [7]. This places the $m\pm 1$ sidebands as the likely greatest contributor to the detection of the 4,3 mode on RIP. I can test this by measuring the degree to which the 4,3 mode is attenuated compared to the 3,2 and 5,4 modes.

The next step is to make an apples-to-apples comparison of RIP and coil data for evenand odd-m modes. To do this, I compare the ratio between RIP and coil-measured ampli-

	Amplitudes (G)		RIP/Coil Ratios $\int B_R dR/B_{Z,b}$				
				TJ	TJ	TJ	TJ
Mode	RIP	Coil	RIP/Coil	Cylindrical	Toroidal	Elongated	Triangular
3,2	4.20	0.877	4.79	4.48	4.52	0.156	9.75
4,3	1.85	1.06	1.75	0.051	1.44	0.157	0.039
5,4	1.66	0.151	11.0	11.4	8.42	1.51	8.25

Table 4.1: Mode amplitudes and their ratio for DIII-D #182771, 2480 ms for five cases: DIII-D data, TJ cylindrical model ($\epsilon = 0.01$, $H_2 = 0$, $\kappa = 1$, $H_3 = 0$, $\delta = 0$), TJ toroidal model ($\epsilon = 0.3$, $H_2 = 0$, $\kappa = 1$, $H_3 = 0$, $\delta = 0$), TJ elongated model ($\epsilon = 0.3$, $H_2 = 0.4$, $\kappa = 1.4$, $H_3 = 0$, $\delta = 0$), and TJ triangular model ($\epsilon = 0.3$, $H_2 = 0.8$, $\kappa = 1.5$, $H_3 = 0.4$, $\delta = 0.4$).

tudes to its synthetic counterpart in TJ. The synthetic model for B_R is scaled so that B_Z at the edge is equal to the B_Z (B_θ) measured by the coils. I take the B_R for each model as a mock eigenfunction from r=0 to r=b. The next step is to line-integrate the mock eigenfunction over a double-pass contour: $\int_1^{-1} B_R dR + \int_{-1}^1 B_R dR$. As the polarization of the beam continues to rotate in the same direction in the lab frame after reflection, this integral is equal to $2\int_r^{-r} B_R dR$, a synthetic "RIP" value on TJ. This is divided by $B_{Z,b}$, the synthetic coil value. The integral of any even mode is zero without including sidebands; I compare RIP and the coil data to determine whether sidebands are the cause of finite amplitudes of even modes detected with RIP.

I compare RIP to the line integrals for cylindrical, toroidal, toroidal-elongated, and toroidal-triangular models, assuming integration across the midplane, at 2480 ms in shot #182771. I begin by normalizing the TJ computational, cylindrical B_R model [7] to B_{Zb} . The q profile input to TJ is shown in Figure 4.16(a), with the locations of the rational surfaces for each mode also marked. This q profile is taken from shot #182771, t = 2480 ms, except for the point q_a , which is set to 4.1 to encourage computational convergence and does not affect rational surface locations. It is plotted in both positive and negative r in the figure and is symmetric in the normalized coordinate r/a. TJ also slightly modifies the input q

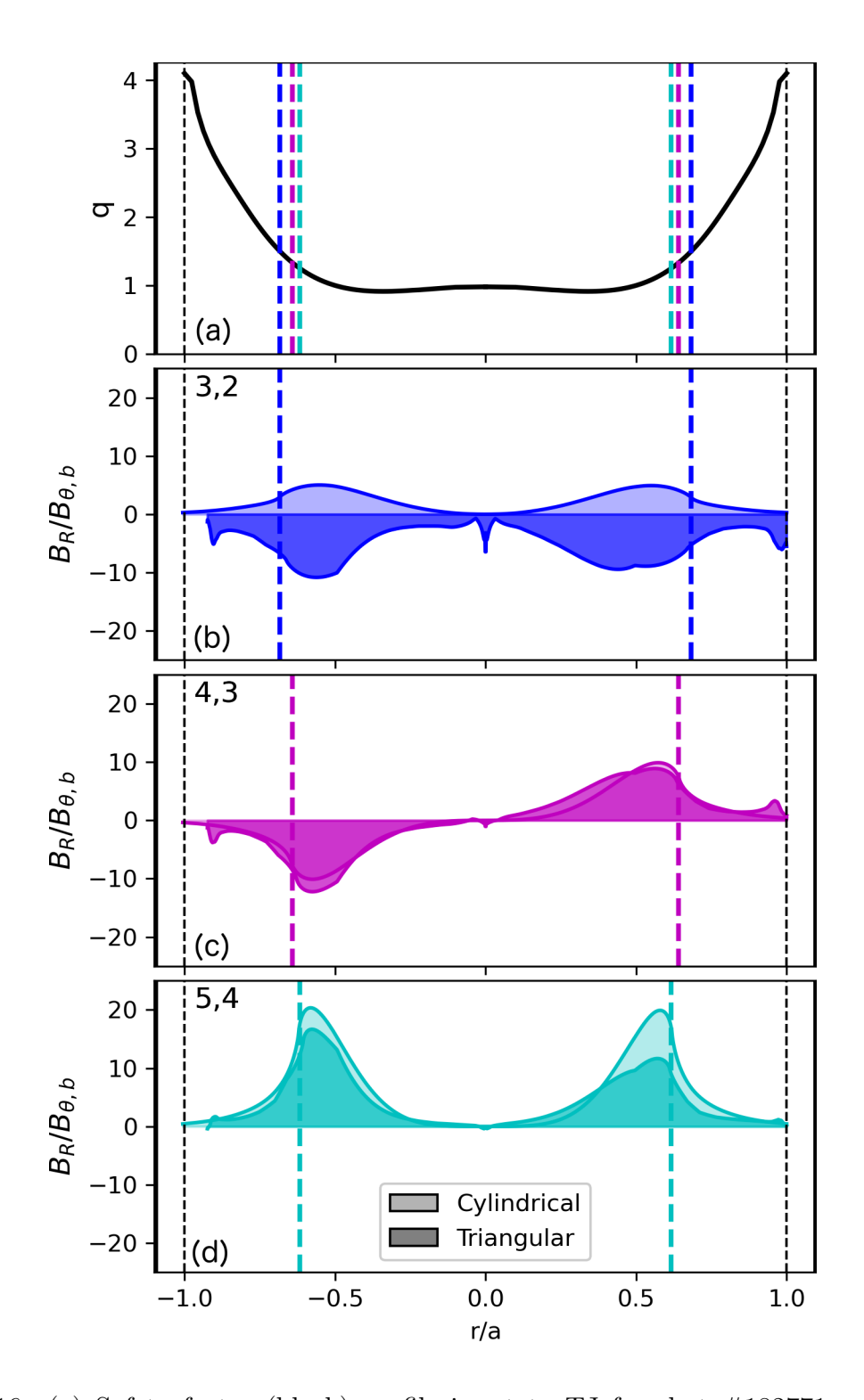


Figure 4.16: (a) Safety factor (black) profile input to TJ for shot #182771 and location of resonant surfaces for 3,2 (blue); 4,3 (magenta); and 5,4 (cyan) tearing modes. (b–d) Eigenfunctions for the 3,2 (b), 4,3 (c), and 5,4 (d) modes, generated in TJ for cylindrical (light) and triangular (dark) plasmas. Colored dashed lines denote resonant surface locations. Black dashed line represents plasma boundary.

profile within the code to conserve angular momentum [7]. This primarily affects q near the edge and does not significantly affect the locations of the rational surfaces, though there is still some error in the profiles. The plasma pressure is set to zero. The density profile is assumed to be flat, so RIP amplitudes \tilde{B} can be calculated by dividing through by $\int n_e \ \mathrm{d}R$ from the interferometry chord. This is an appropriate approximation because the density is near-constant outside the pedestal and in the region of greatest \tilde{B}_R for all three modes. Eigenfunctions for all three modes in both the cylindrical and triangular TJ models are presented in Figures 4.16(b-d). The 3,2 mode in the triangular plasma has opposite sign, versus in the cylindrical plasma, across the entire plasma. This changes the sign of the integral but does not affect the amplitude of a measured fluctuation. It also has greater magnitude, overall. The eigenfunction for the 4,3 mode is distorted in the triangular model, but the primary sidebands appear to be even and therefore not measurable by RIP. The amplitude of the 5,4 mode is reduced overall in the triangular model. In the triangular model, a peaked structure in B_R is present at both the inboard and outboard midplanes. I assert that this is related to the torque balance calculation in TJ, previously addressed in the elongation scaling in Section 4.2.2, and compare directly to RIP data to identify whether this structure is experimentally accurate.

As shown in Table 4.1, the 4,3 mode has finite RIP amplitude, as was evident from the spectrogram. It is smaller, compared to RIP, than the other two modes. The 5,4 mode is significantly stronger than either of the other modes, most likely due to the peaking of the eigenfunction. The ratio between RIP and the coils is close to the result for the cylindrical model for the two odd modes, which is unexpected. Finite elongation would be expected to contribute significantly to the eigenfunction, whether in phase (positive change) or out of phase (negative change). I add more steps successively to the inverse aspect ratio expansion of the shape, first adding a finite ϵ , then elongation, then triangularity. The toroidal model produces a first-order sideband in toroidicity and successive higher-order sidebands from the back-coupling of the first order. In this model, the ratio $\int B_R dR/B_{Z,b}$ is close to the

experimental RIP/coil ratio for both the 3,2 and 4,3 modes, indicating that the toroidicity sideband is a good leading-order model for the m=4 amplitude. The 5,4 mode is somewhat attenuated compared to both RIP and the cylindrical model, indicating that a structure has formed out of phase with the fundamental for that mode or that there is some experimental variation or higher-order effect in play. One would expect that the addition of an $m \pm 1$ (even) component to the 5,4 would not affect the line integral significantly.

The elongated model shows all modes much smaller than both RIP and the other models. Despite the fact that this model was constructed to have $\kappa < 1.5$ and reduce the amplitude of the B_{θ} structure at the outboard midplane, I still find that $B_{Z,b}$ is large and therefore that $\int B_R \, \mathrm{d}R/B_{Z,b}$ is small. In the triangular model, which includes all toroidal and shaping effects, the ratio $\int B_R \, \mathrm{d}R/B_{Z,b}$ is somewhat attenuated compared to both RIP and the cylindrical model for both RIP and the coils, indicating some cancellation from other components and a role for the outboard B_{θ} structure, though somewhat masked by the triangular components. The even mode has a small contribution in both models, which might also be unexpected. The even mode amplitude in the TJ triangular model is likely washed out by modifications to the edge magnetic structure from TJ. It should also be noted that even the TJ triangular model is an estimate: the DIII-D plasma was vertically asymmetrical, even more elongated, and had an X-point at the bottom of the vessel due to employing the divertor.

Given evidence that RIP amplitudes are both finite and attenuated for even-m modes compared to odd-m modes using multiple models for line-integrated coil data, I expand to a dataset of six shots. All six shots are from the same IBS series and contain 3,2; 4,3; and 5,4 tearing modes. RIP and coil data are taken for all six shots at times when the three modes are clearly visible on both diagnostics. Figure 4.17 shows the ratio between RIP and coil amplitudes for the six shots. The 4,3 mode is more attenuated than the 3,2 mode, and the 5,4 is much larger in all cases due to its peaking. The ratios are compared to the inverse aspect ratio $\epsilon = a/R_0$, which is the extent to which the RIP data is expected to be attenuated if

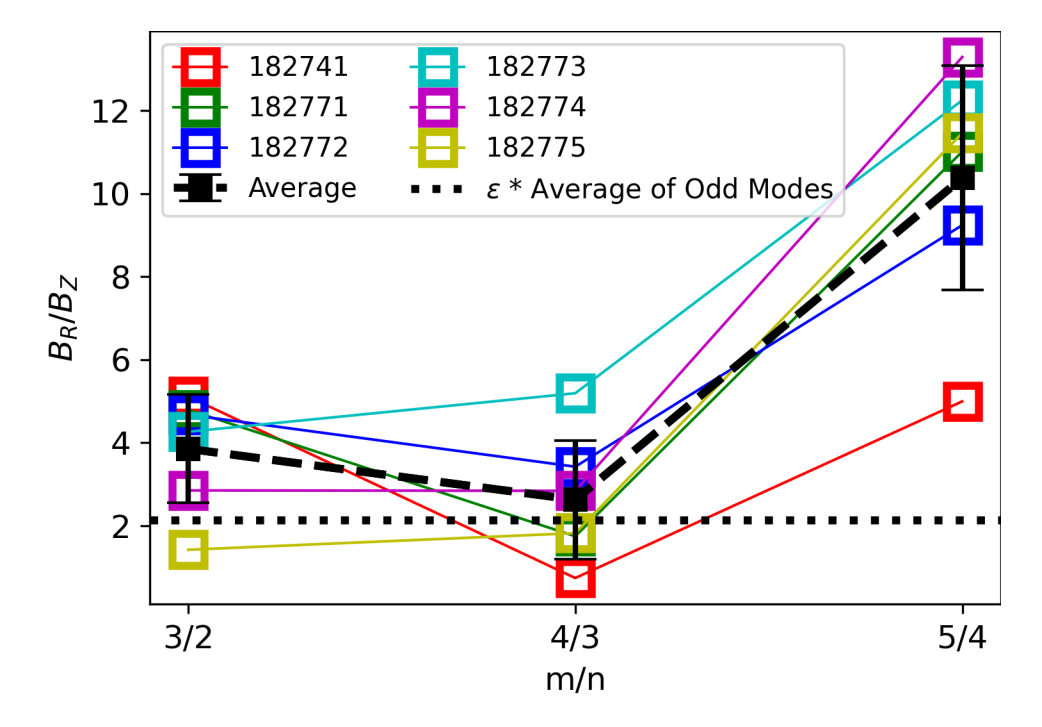


Figure 4.17: RIP/coil amplitude ratios for three modes in six IBS shots. Heavy dashed black line and black markers denote average RIP/coil ratio.

RIP measures the odd-m harmonics (m=3 and m=5) of the even-m mode (m=4). The value of ϵ used in Figure 4.17 is the inverse aspect ratio for the last shot in the series and is nearly the same for all DIII-D plasmas. The average attenuation is calculated from both the 3,2 and 5,4 modes to approximate the expected value of the 3,3 and 5,3 ($m\pm1$) sidebands. While Equation 4.16 uses a factor of $\epsilon/2$, the factor of 1/2 is already present in the average amplitude: $(\tilde{B}(3,2)+\tilde{B}(5,4))/2$. The average RIP/coil ratio of the even-m mode, compared to the odd-m mode, is lower but noticeably larger than what the ϵ factor might predict, suggesting a role for additional sidebands. It should also be noted that the 3,2 mode and the 3,3 sideband of the 4,3 mode, while they have the same m and therefore the same r dependence, have different rational surfaces. A direct comparison cannot be drawn, as the 3,3 and 5,3 sidebands have the same frequency and cannot be separated from the 4,3 mode in RIP or coil data. However, since far from the resonant surface the mode's radial decay is dependent on m rather than n, and all B_Z are small at the wall, we may take this as a first estimate.

	Amplitudes (G)		RIP/Coil Ratios $\int B_R dR/B_{Z,b}$				
				TJ	TJ	TJ	TJ
Mode	RIP	Coil	RIP/Coil	Cylindrical	Toroidal	Elongated	Triangular
3,2	4.26	0.877	4.86	0.700	0.404	0.049	2.65
4,3	12.28	1.06	11.6	0.057	1.56	0.155	0.495
5,4	2.66	0.151	17.6	6.91	5.65	0.543	4.09

Table 4.2: RIP upper chord and coil mode amplitudes and their ratios for DIII-D #182771, 2480 ms.

	Amp	litudes (G)	RIP/Coil Ratios $\int B_R dR/B_{Z,b}$				
				TJ	TJ	TJ	TJ
Mode	RIP	Coil	RIP/Coil	Cylindrical	Toroidal	Elongated	Triangular
3,2	4.25	0.877	4.85	0.700	0.404	0.049	2.65
4,3	4.69	1.06	4.42	0.057	1.56	0.155	0.495
5,4	3.63	0.151	24.0	6.91	5.65	0.543	4.09

Table 4.3: RIP lower chord and coil mode amplitudes and their ratios for DIII-D #182771, 2480 ms.

Thus far I have only considered the midplane chord. The integral of an even-m mode off-midplane is nonzero, even for a cylindrical plasma. I expect that odd-m modes, since their line integral is strongest at midplane, would be attenuated when integrated at an offset compared compared to the midplane. I test the strength of the off-midplane components by comparing the mode amplitude and attenuation on RIP versus the coil for the 3,2; 4,3; and 5,4 modes with the chords at \pm 13.5 cm from the midplane. RIP is still normalized to the B_{θ} value at the outboard midplane, since this is what the coils measure. For a DIII-D minor radius of 56 cm, 13.5 cm above or below the midplane is 24% of the radius. Tables 4.2 and 4.3 give the mode amplitudes from RIP and from the TJ models and their ratios for the other two chords. Tables 4.4 and 4.5 compare the upper and lower chords to the midplane chord both directly and in TJ models.

	Upper/Midplane						
		TJ	TJ	TJ	TJ		
Mode	RIP	Cylindrical	Toroidal	Elongated	Triangular		
3,2	1.01	0.156	0.089	0.314	0.272		
4,3	6.64	1.12	1.08	0.987	12.7		
5,4	1.60	0.606	0.671	0.360	0.496		

Table 4.4: Ratio of mode amplitudes observed at z = 13.5 cm and z = 0 cm on RIP and in TJ models for DIII-D #182771, 2480 ms.

	Lower/Midplane						
	TJ		TJ	TJ	TJ		
Mode	RIP	Cylindrical	Toroidal	Elongated	Triangular		
3,2	1.01	0.156	0.089	0.314	0.272		
4,3	2.54	1.12	1.08	0.987	12.7		
5,4	2.19	0.606	0.671	0.360	0.496		

Table 4.5: Ratio of mode amplitudes observed at z = -13.5 cm and z = 0 cm on RIP and in TJ models for DIII-D #182771, 2480 ms.

The differences in RIP measurements between the upper and lower chords can be attributed to vertical asymmetry in the plasma in DIII-D. Overall, the two chords demonstrate similar trends with respect to the midplane. Note immediately that the 3,2 modes are very similar, that the 4,3 mode is less attenuated than at midplane, and the 5,4 mode is stronger overall. The side chords show higher amplitudes for all modes than the midplane chord, indicating some data quality differences or cancellation of terms due to antisymmetric mode structure components at the midplane.

Inspecting the TJ eigenfunctions, the integral of the 3,2 mode at \pm 13.5 cm has both positive and negative components, leading to a small value for its line integral. The elongated and triangular nature of the DIII-D plasma means that this cancellation occurs near the RIP chord in the triangular model, meaning that the TJ eigenfunction is small there. The 5,4

mode encounters this effect only for the triangular plasma; the peaking effect is still present in the cylindrical plasma. The antisymmetry still appears to be present off-midplane for the 4,3 mode compared to the midplane. This may also be an effect of resonant surface location or of additional magnetic structure near the edge, generated by elongation or triangularity. The edge structure is particularly noticeable for the elongated plasma without triangularity, just as for the midplane case. Considering the side chords in the TJ models, there was significant variation, but the 4,3 and 5,4 modes were more prominent on the side chords, in comparison to the midplane chord, than the 3,2 mode. This comparison was intended to avoid the structure at the outboard midplane, but it appears that variation within the structure still contributed to differences between the chords. It should also be noted that due to the structure of the coordinate system in TJ, the chord height of integration was an approximation. A synthetic line-integrated diagnostic in TJ, which measures at each chord height exactly rather than approximating based on the TJ coordinate system, will be useful for resolving numerical issues. In general, the triangular case best reflected the true differences between the upper, midplane, and lower chords, but there was still significant offset, likely related to the portion of the outboard structure that was still detected by the synthetic RIP chord.

4.4 Additional Mode Detection with RIP

RIP's internal view into the plasma lets it detect modes close to the noise floor, at high frequencies, and at any radial location. I give a few examples of scenarios, other than the aforementioned early detection, in which RIP shows advantages over other diagnostics. RIP can be more sensitive to coherent MHD modes than the coils in some contexts, and it can detect ELMs earlier than the filterscopes.

4.4.1 Expanded Mode Detection

In addition to early detection, RIP shows mode detection advantages over the coils in a number of contexts. These can be named extended, continuous, and extra detection. In

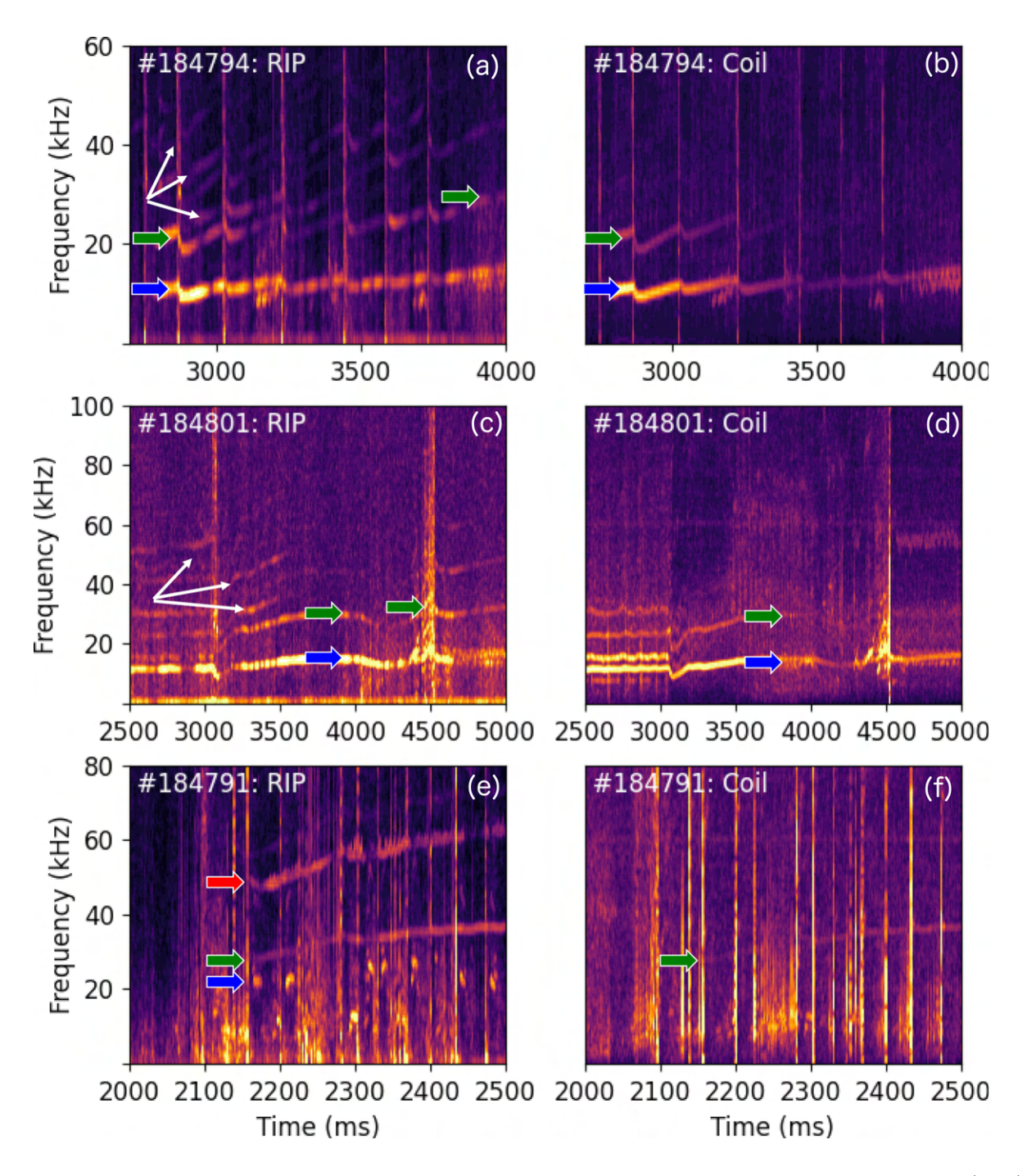


Figure 4.18: RIP magnetic and single external sensing coil spectrograms for shots (a–b) #184794, (c–d) #184801, and (e–f) #184791, demonstrating modes that appear on RIP but not coils or disappear on coils but remain present on RIP.

extended detection, a mode remains visible on RIP after it has disappeared on coils. In continuous detection, a mode weakens or disappears and then reappears on coils but is strongly visible throughout on RIP. In extra detection, some modes are visible on RIP that are never seen on coils, whether due to location or amplitude. Figure 4.18 compares RIP and coil spectrograms for three shots where RIP shows advantages over the coils. Shot #184794, previously mentioned in Section 4.1 due to its strong coherent modes before 3000 ms, displays extended detection of the second-lowest frequency mode, marked with a green arrow in both plots and a second green arrow in (a) where extended detection is seen. The shot demonstrates extra modes at higher frequencies (white arrows). The lowest mode (blue arrow) also remains strong on RIP while it weakens from 3200–3800 ms on coils. Shot #184801 is unusual in that it contains multiple different types of magnetic modes under ELM-free conditions [20]. It displays continuous strong detection on RIP of the first mode (marked with a blue arrow), where it fades temporarily around 4000 ms on coils. This shot also displays extended detection of the second-lowest mode (green arrow) and additional modes (white arrows). Shot #184791 displays multiple examples of extra modes (blue and red arrows) both above and below the tearing mode visible on coils (green arrow). This shot is discussed further in Chapter 6. All three shots are from the same series and begin in QHmode, which maintains the H-mode pedestal without ELMs, before transitioning to ELMy H-mode. As modes' resonant location moves within the plasma, their measured amplitude with coils may weaken due to the $r^{-(m+1)}$ radial amplitude decay. In addition, RIP's high signal-to-noise ratio allows modes to be detected at low amplitude or far from the edge.

4.4.2 ELM Detection

Typically, ELMs are detected using filterscopes that measure spikes in visible light in the divertor. The emission line used for ELM measurements is the deuterium-alpha (D_{α}) line at 656 nm. An ELM is detected when the D_{α} signal is over a certain magnitude. RIP can also be used to independently detect ELMs, which is useful when the filterscope algorithm has failed to detect an ELM and to detect ELMs earlier than the filterscopes. In spectrograms,

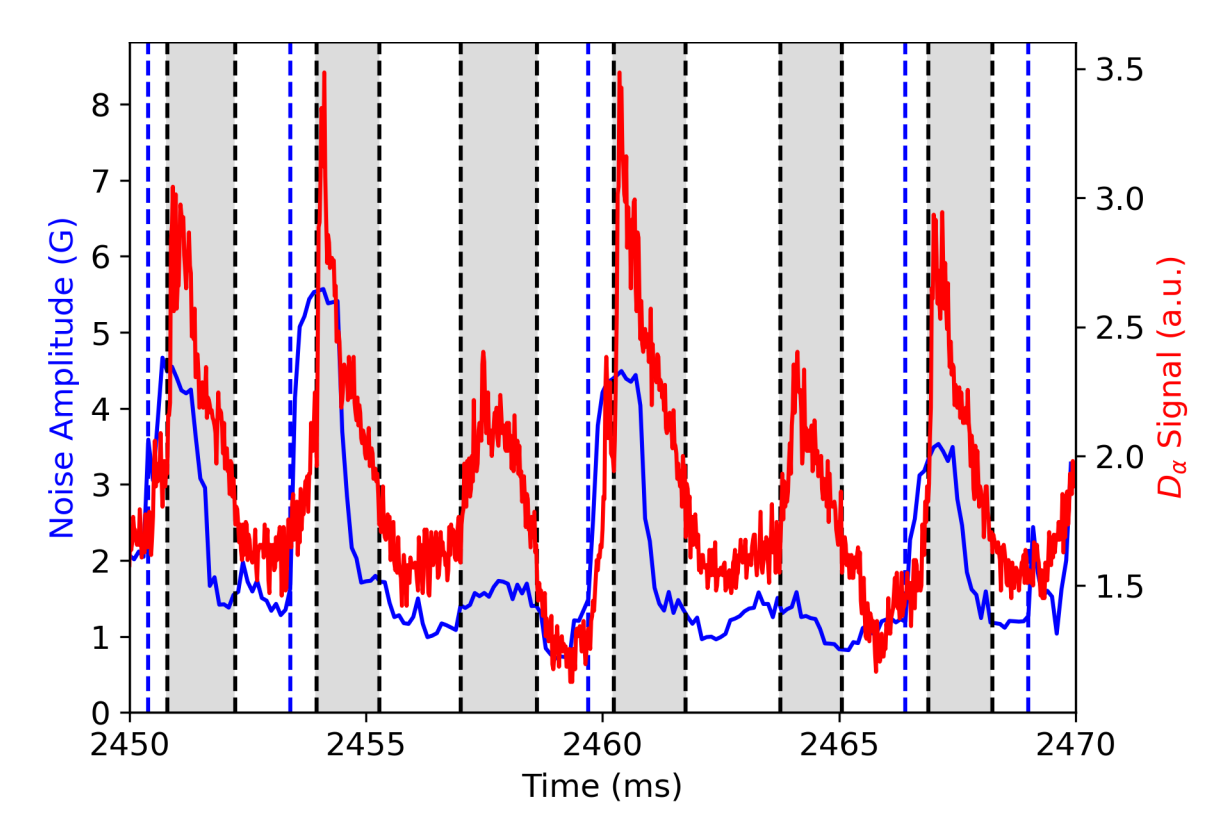


Figure 4.19: RIP background noise from 10–80 kHz (blue), ELM starts detected by RIP (blue dashed lines), D_{α} emission measured by the filterscopes (red), and ELM periods as measured by DIII-D's default ELM detection algorithm, which uses D_{α} (gray, black dashed lines).

ELMs appear on RIP as broadband spikes reaching up to about 200 kHz. The short-time Fourier transform can be used to measure the broadband mode amplitude by integrating the PSD over a wide frequency range. The most effective lower limit for ELM detection is between 5–10 kHz and, and upper limit is between 80–200 kHz. The amplitude of any tearing or other large fluctuation can be subtracted, which has the additional advantage of removing any noise that may have been detected at that frequency. I call the amplitude resulting from integrating fluctuation power over all non-mode frequencies the noise amplitude.

ELMs can automatically be detected by measuring jumps in the broadband amplitude within a short time frame. The most effective method for ELM detection measures the mean noise amplitude for the most recent ELM-free period. An ELM is detected if the noise amplitude is more than one standard deviation above the mean of the ELM-free period. A comparison between RIP broadband data, filterscope data, and ELMs detected by the

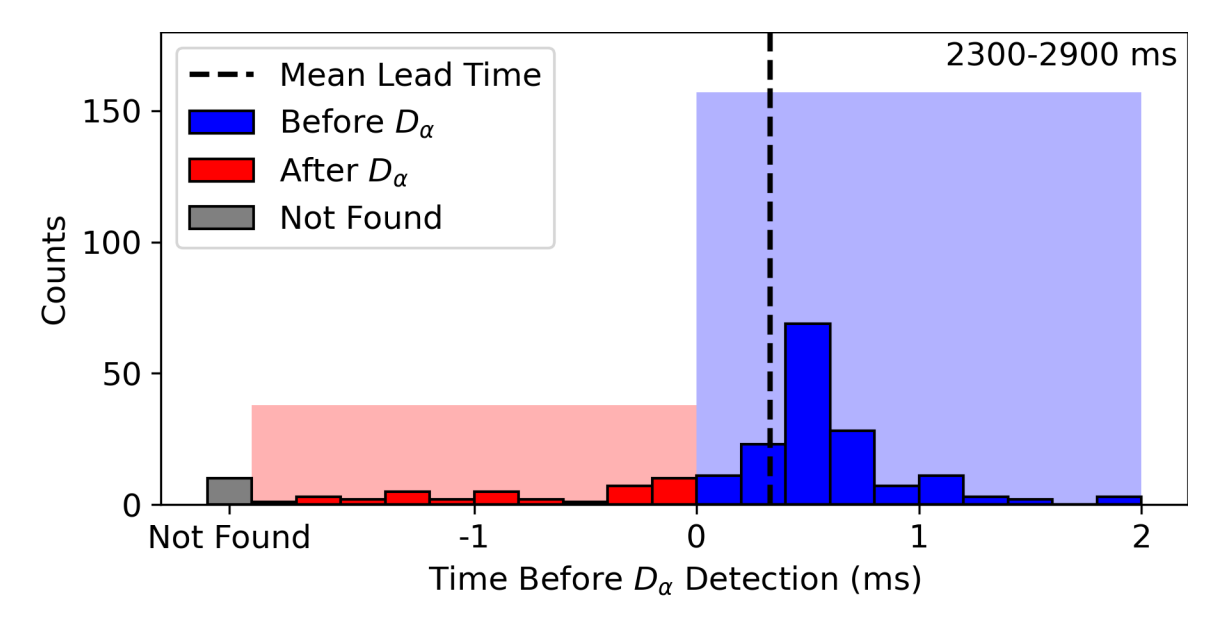


Figure 4.20: Histogram of time between RIP and D_{α} ELM detections from 2300–2900 ms in DIII-D shot #180704. Blue marks ELMs detected with RIP first, red marks ELMs detected with D_{α} first, and gray marks ELMs not detected with RIP. Large bars represent all early and late detection. Mean lead time marked with black dashed line.

filterscopes in shot #180704 is shown in Figure 4.19. For five out of the six ELMs shown in the plot, RIP shows an increase in background signal around 0.5 ms before the D_{α} signal marks the ELM start. The one exception in this case occurs for a weak ELM, where RIP and D_{α} rise simultaneously. The detection algorithm is effective for the strongest four of the six ELMs and confirms that ELMs can be detected automatically using RIP earlier than D_{α} .

A more extensive study of ELMs on RIP from 2300–2900 ms in DIII-D shot #180704 shows that on average, when RIP shows an ELM-related increase in background signal, ELMs are detected on RIP 0.33 ms before the filterscopes. The peak of the distribution occurs around 0.5 ms, corroborating the observations from the previous period. Out of 205 ELMs detected on filterscopes during this period, 157 (76.6%) were detected on RIP first, 38 (18.5%) were detected on filterscopes first, and 10 (4.9%) were not detected on filterscopes at all. Figure 4.20 illustrates the distribution of ELM start times. As before, ELMs are detected on RIP by measuring significant peaks in broad-spectrum "noise", with mode-related fluctuations excluded. ELMs on D_{α} are detected with the default algorithm. Overall, RIP shows an advantage over the filterscopes in detecting ELMs. However, the

algorithm requires more refinement. Since ELMs are localized and sometimes do not display a signal on RIP, it is likely most advantageous to use both diagnostics simultaneously for the best possible detection of ELMs.

Bibliography

- E. Strait. Poloidal Mode Identification Using MODESPEC. Presented at the DIII-D
 and Stability Physics Meeting. Aug. 2020.
- [2] J. Chen et al. "A Faraday-effect polarimeter for fast magnetic dynamics measurement on DIII-D". Review of Scientific Instruments 89.10 (2018), 10B101.
- [3] J. Chen et al. "Internal measurement of magnetic turbulence in ELMy H-mode tokamak plasmas". *Physics of Plasmas* 27.12 (2020), p. 120701.
- [4] J. Chen, W. X. Ding, and D. L. Brower. "Impact of the Cotton–Mouton effect on Faraday polarimetry measurements using circular polarization". *Plasma Physics and Controlled Fusion* 60.8 (2018), p. 085001.
- [5] H. P. Furth, J. Killeen, and M. N. Rosenbluth. "Finite-resistivity instabilities of a sheet pinch". *Physics of Fluids* 6.4 (1963), pp. 459–484.
- [6] H. P. Furth, P. H. Rutherford, and H. Selberg. "Tearing mode in the cylindrical tokamak". *Physics of Fluids* 16.7 (1973), pp. 1054–1063.
- [7] R. Fitzpatrick. "Calculation of tearing mode stability in an inverse aspect-ratio expanded tokamak plasma equilibrium". *Physics of Plasmas* 31.10 (2024), p. 102507.
- [8] H. Zohm. Magnetohydrodynamic Stability of Tokamaks. Weinheim: WILEY-VCH Verlag GmbH & Co., 2015.
- [9] J. W. Connor et al. "Tearing modes in toroidal geometry". *Physics of Fluids* 31.3 (1988), pp. 577–590.

- [10] R. Fitzpatrick. "Inverse aspect-ratio expanded tokamak equilibria". *Physics of Plasmas* 31.8 (2024), p. 082505.
- [11] R. Fitzpatrick. "Investigation of tearing mode stability near ideal stability boundaries via asymptotic matching techniques". *Physics of Plasmas* 32.6 (2025).
- [12] R. Fitzpatrick, R. J. Hastie, T. J. Martin, and C. M. Roach. "Stability of coupled tearing modes in tokamaks". *Nuclear Fusion* 33.10 (1993), p. 1533.
- [13] R. Fitzpatrick. "Investigation of Neoclassical Tearing Mode Detection by ECE Radiometry in Tokamak Reactors via Asymptotic Matching Techniques". arXiv preprint arXiv:2506.05553 (2025).
- [14] B. Coppi, J. M. Greene, and J. L. Johnson. "Resistive instabilities in a diffuse linear pinch". *Nuclear Fusion* 6.2 (1966), p. 101.
- [15] D. C. Robinson. "Tearing-mode-stable diffuse-pinch configurations". Nuclear Fusion 18.7 (1978), p. 939.
- [16] W. M. Solomon et al. "Experimental test of the neoclassical theory of impurity poloidal rotation in tokamaks". *Physics of Plasmas* 13.5 (2006).
- [17] R. J. La Haye. "Neoclassical tearing modes and their control". *Physics of Plasmas* 13.5 (2006), p. 055501.
- [18] O. Sauter et al. "Beta limits in long-pulse tokamak discharges". *Physics of Plasmas* 4.5 (1997), pp. 1654–1664.
- [19] L. Bardóczi, N. C. Logan, and E. J. Strait. "Neoclassical tearing mode seeding by nonlinear three-wave interactions in tokamaks". *Physical Review Letters* 127.5 (2021), p. 055002.
- [20] G. Yu et al. "ECEI characterization of pedestal fluctuations in quiescent H-mode plasmas in DIII-D". *Plasma Physics and Controlled Fusion* 64.9 (2022), p. 095014.

Chapter 5

Plasma Shaping, Rotation, and m, n > 2, 1 Tearing Mode Origins

Nondisruptive m, n > 2, 1 tearing modes can affect plasma dynamics but are understudied due to emphasis on the disruptive 2, 1 mode. In particular, they may be triggered more easily than n = 1 modes, reduce confinement, and seed deleterious n = 1 modes. As part of the FY2024 PhD runtime allocation, I carried out an experiment, also titled "Plasma Shaping, Rotation, and m, n > 2, 1 Tearing Mode Origins", to investigate the triggering of m, n > 2, 1 modes¹. In Section 5.1, I describe the experimental motivation, which was to measure the effects of varying plasma shape and rotation on frequency and detection with RIP of sawtooth-triggered tearing modes in inner-wall limited (IWL) plasmas. IWL plasmas are magnetically configured to touch the vessel wall. Instead of exhausting particles and energy into the divertor, IWL exhausts particles directly to the wall. In Section 5.2, I describe the experimental design and give an overview of the experiment's performance. Section 5.3 describes the MHD instabilities that appeared during the experiment. This section also covers post-experiment computational analysis conducted in kineticEFIT [1]

¹Portions of this chapter are reproduced or derived from the DIII-D Miniproposal I wrote and submitted to the Run Coordination team prior to the experiment.

and DCON [2] to further understand the stability of limited plasmas². Section 5.4 outlines the effects of plasma shape on instability development and detection with RIP. Appendix A comprises a copy of the Resources and Experimental Plan sections of the Miniproposal as well as the Shot Plan distributed to the run team. Appendix B consists of a spreadsheet containing more extensive notes on all shots from the campaign.

5.1 Motivation

Tearing modes are a major cause of disruptions in tokamaks. ITER's high projected stored energy makes disruptions very damaging; reactor-relevant scenarios must be optimized to avoid disruptive tearing modes. Current research emphasizes early and accurate detection of tearing modes to help control or avoid modes. Two major actuators of tearing mode dynamics in both scenario design and control are plasma shaping and mode structure. For example, the onset probability of a disruptive m, n = 2, 1 tearing mode is strongly correlated with both increased plasma elongation and triangularity in the ITER Baseline Scenario (IBS) [3]. I am interested in building on these results to determine the role of shaping on m, n > 2, 1 tearing mode incidence, particularly in scenarios beyond IBS. This experiment was designed to expand the parameter dependence study beyond the existing m, n = 2, 1database. Higher-m, n modes can emerge at lower β_N than lower-m, n modes, preceding them [4, 5]. The interest of this experiment was in small-amplitude modes that might trigger deleterious modes that can strongly affect confinement. RIP is a useful diagnostic for small-amplitude and high-m, n modes studies because it is particularly effective, when compared to the coils, in detecting small-amplitude modes. It also has advantages when measuring modes that are more localized, as occurs with higher m, n, and may be farther from sensing coils despite being dynamically important. All these modes were expected to be resistive tearing modes rather than ideal kinks.

Plasma rotation was also expected to influence tearing mode seeding. Increasing differ-

²Portions of this section are reproduced or derived from my final report from the DOE SCGSR program.

ential rotation between the plasma and the coupling frequency can prevent tearing mode seeding by nonlinear coupling [6]. Seeding by coupling is a particular concern for ITER, where torque and plasma rotation are planned to be low. The research described herein was also intended to identify whether high plasma rotation could by itself increase differential rotation and reduce coupling-related mode seeding.

Shape was varied to expand the studied parameter space of plasma shape for tearing stability and measure shaping effects on RIP amplitudes. This research investigated the comparative magnitude of toroidal, elongation, and triangularity contributions, induced by linear coupling, to tearing mode amplitudes. This was done by harnessing RIP's inherent sensitivity to these contributions. Chapter 4 addressed that in the cylindrical limit, tearing modes with even m are not detected with RIP. The finite even-m mode amplitudes shown in the small-database analysis of multi-tearing shots are compatible with estimates of the amplitudes of $m \pm 1$ sidebands. This supports the hypothesis that even modes are visible with RIP through their sidebands and motivates further study of elongation and triangularity effects. Elongation is particularly important for odd-m modes, since it induces the lowest-order visible sidebands. The even-m4 toroidicity sidebands of odd modes are not visible with line-integrated diagnostics. The proposed multi-tearing shots in this experiment provided opportunity to compare odd and even m outside IBS, while varying elongation and triangularity would allow measurement of the contributions of their corresponding coupled sidebands. In turn, the research would also cover the role of linear sidebands in nonlinear seeding of tearing modes. Section 4.2.2 indicates that linear sidebands are in phase with the fundamental and can therefore phase lock to the same modes.

5.2 Experimental Approach and Outcomes

5.2.1 Experimental Summary

In DIII-D, experimental plans typically involve replicating a target shot, performed during a previous experiment. Subsequent shots make changes to the target. The initial target

shot for my experiment was #194784, a low-elongation sawtoothing shot. The inner-wall limited configuration was chosen to ensure sawteeth for easy tearing mode triggering. IWL accesses a lower-elongation regime than is possible in diverted plasmas and is therefore expected to induce mode sidebands, as described in Chapter 4, of different sizes than ITER-like highly shaped plasmas. Shape in the target had elongation $\kappa = 1.25$ and upper and lower triangularities $\delta_u = 0.1$, $\delta_l = 0.1$. A plasma with elongation this low is colloquially called "circular." Initial plasma outer radius at the midplane was $0.54~\mathrm{m}$. Goal q_{95} for all shots was planned to be 4.5, the same as the target shot; the planned current was modified for each elongation to maintain this value in accordance with existing models [7]. It was believed that with higher input power, lower q would promote tearing activity. The experiment was designed to reach a wide range of elongations, to modify the size of the sideband components of RIP data and investigate shaping effects on RIP data. The scenario for this study included an initial plasma current of 0.8 MA in the standard direction, counterclockwise when seen from above. The density target was between $4-5\times10^{19}~\mathrm{m}^{-3}$, and target toroidal magnetic field was 2 T in the standard direction, clockwise when seen from above. These figures resemble those from the target shot. RIP's sensitivity to low-amplitude core-resonant magnetic fluctuations is also maximized, since RIP magnetic measurements are density-weighted. These figures also avoid the Cotton-Mouton effect, which limits density and magnetic field to $n_{e,avg}B_T^2 \approx 20$ [8].

This experiment modified plasma conditions between shots, rather than within a shot, in order to promote long-lived steady tearing modes. I scanned NBI power in four torque configurations ($P_{inj} = 5, 8, 10, 11 \text{ MW}$), depending on the shot, to quantify tearing mode development in the rotation profiles with maximum MHD activity. NBI power was maximized to maximize differential rotation between modes and held approximately steady in time to aid in detection of mode coupling. Coupling is easier to measure when mode frequencies are steady, since phase locking is measured between frequencies. One beam was modulated on a 50% duty cycle to improve performance of the CER diagnostic, whose spatial accuracy is

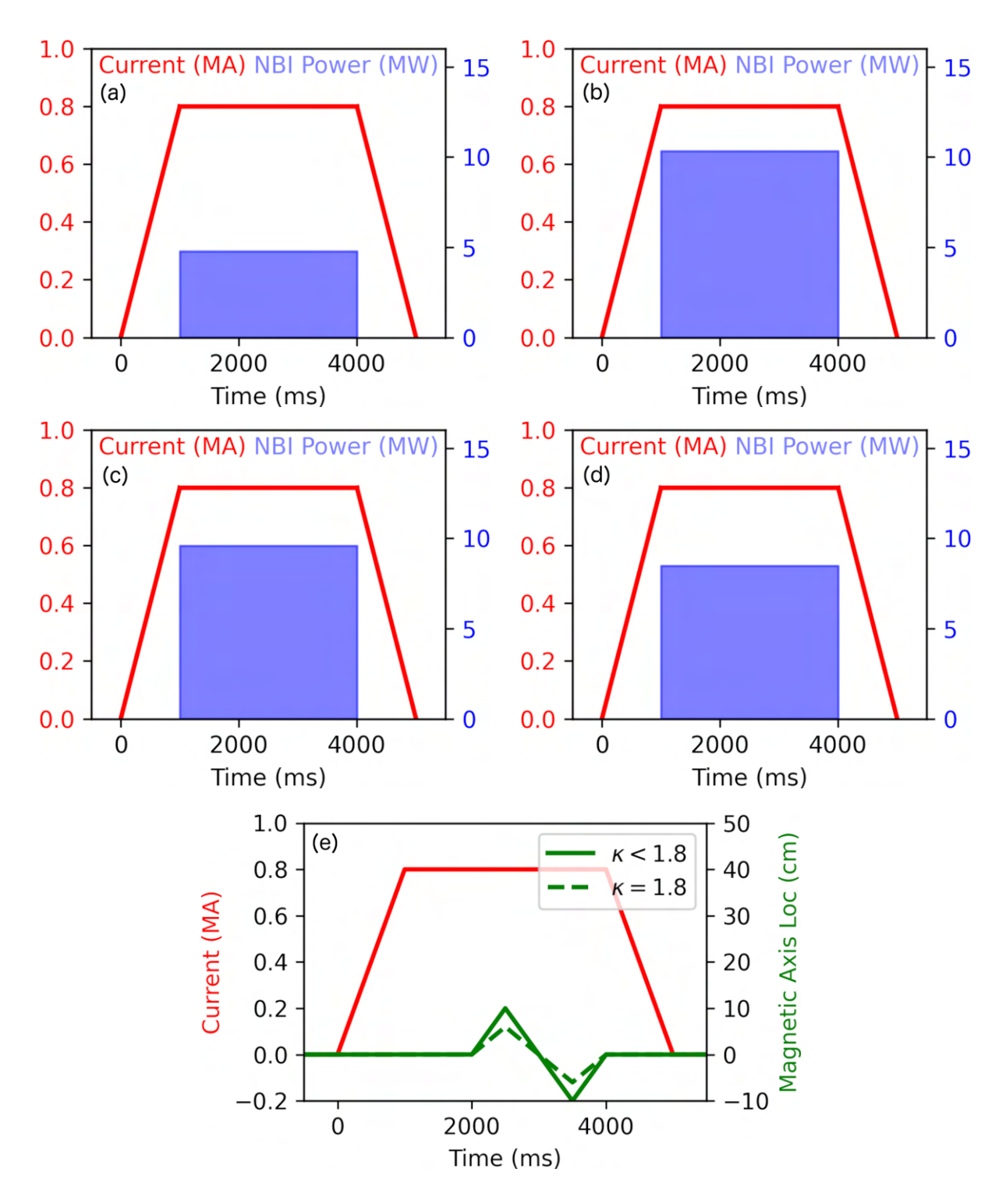


Figure 5.1: (a–d) Planned time traces of plasma current (red) and injected NBI power (blue, filled) for the four different torque configurations in the experiment. (e) Planned time traces of plasma current (red) and magnetic axis height (green) for different plasma elongations.

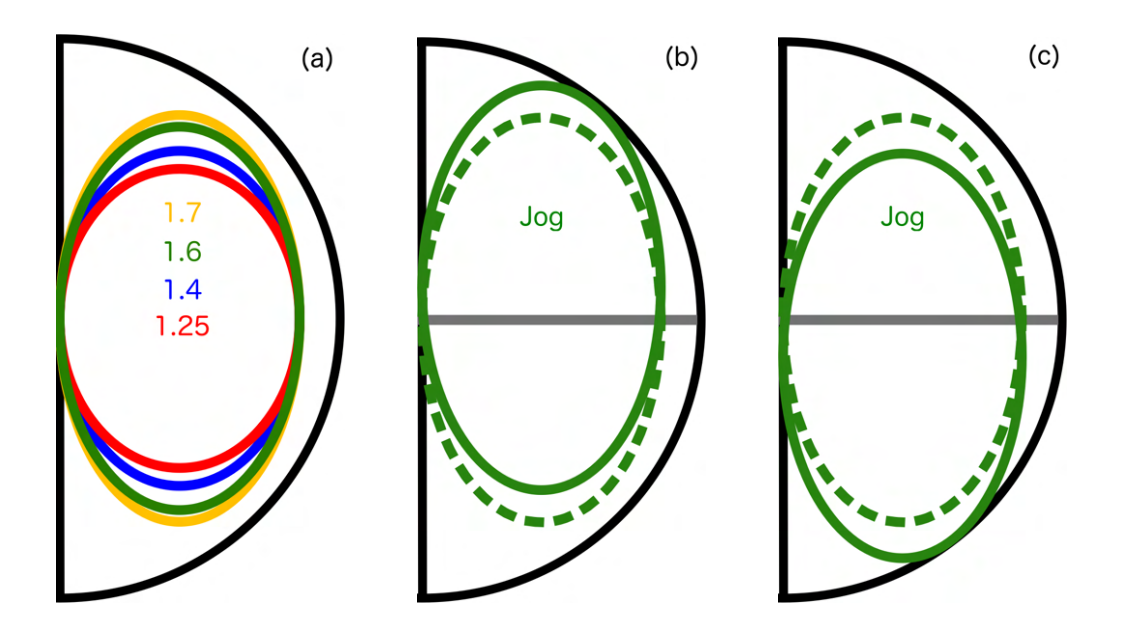


Figure 5.2: (a) Cartoon of plasma boundaries for the four different plasma elongations programmed into the experiment: 1.25 (red), 1.4 (blue), 1.6 (green), and 1.7 (yellow). (b–c) Cartoon of the path of the plasma during the jog. Solid green lines represent boundary at upper and lower limits ($Z = \pm 10$ cm) of jog, and dotted green lines represent boundary for magnetic axis at Z = 0. Gray line marks midplane.

reduced if both beams at the same toroidal location are injecting. Time traces of plasma current and NBI power for the four torque configurations are shown in Figure 5.1. Tearing mode dynamics were studied for four plasma elongations, depicted in a conceptual diagram in Figure 5.2(a). In addition to the target shot $\kappa = 1.25$, elongations of $\kappa = 1.4$, 1.6, and 1.7 were planned, again depending on the shot rather than the time. Most of the shots had triangularity $\delta = 0.1$, but the last few shots reached $\delta = 0.2$ in both the upper and lower half of the plasma. The only condition varied within the shot was the magnetic axis position, which was vertically swept from +10 to -10 cm, depicted in a conceptual diagram in Figure 5.2(b-c), in each shot to increase RIP coverage of mode structure. It was hoped that the the jog would be extensive enough to sweep the RIP chords across an entire island. This was intended to allow comparison of on- and off-axis magnetic signatures, identification of magnetic axis location, and measurement of magnetic axis location effect on tearing mode development. The shots experienced vertical displacement events (VDEs), a common consequence of lack of control [9], at the highest elongations. This placed constraints on the

achievable elongation in experiment.

It was predicted that the highest levels of tearing mode activity when perturbed by a sawtooth, as measured by onset time, amplitude, number of modes, or likelihood to tear, would be present in shots with higher elongation and triangularity. Tearing modes with m, n > 2, 1 would be larger in amplitude and triggered earlier when rotation was high but more likely to seed m, n = 2, 1 modes by nonlinear coupling when rotation was low. RIP tearing mode amplitude measurements would be boosted relative to the coils in highly elongated and/or vertically asymmetrical plasmas. The experiment was planned to use internal measurements to measure tearing mode growth as early as possible. Another goal was to apply the data to investigate birth amplitudes of modes triggered by transient events such as sawteeth and the role of nonlinear coupling in the early stages of such triggers. The experiment was planned to be used to validate and expand on previous findings, using polarimetry, of nonlinear tearing mode coupling and coupling drivers, which could be applied to avoiding such drivers in the future.

The initial run day comprised seventeen plasma shots, eight of which disrupted at various times. A loose tile and exposed wire on the floor of the vessel, a result of in-vessel work conducted just before my run, caused a large influx of carbon and iron. Carbon is a typical impurity, though the tile caused a larger influx than usual. Iron was highly elevated compared to typical experiments. High-Z impurities such as iron radiate power at a higher rate than lower-Z impurities such as carbon, so iron was the most concerning impurity that day [10]. The iron radiation interfered with instrument performance, particularly diagnostics. Impurity radiation was measured with core SPRED only [11]; since the plasma was innerwall limited and did not contact the divertor, divertor SPRED was not available. Examples of carbon and iron emission are shown in Figure 5.3. All shots had significant carbon radiation, particularly from the carbon-VI line, representing complete stripping of electrons from carbon atoms. During disruptions, all carbon lines and iron-XVI showed spikes. Carbon emission was constant, consistent with both wall and tile contact, whereas iron emission

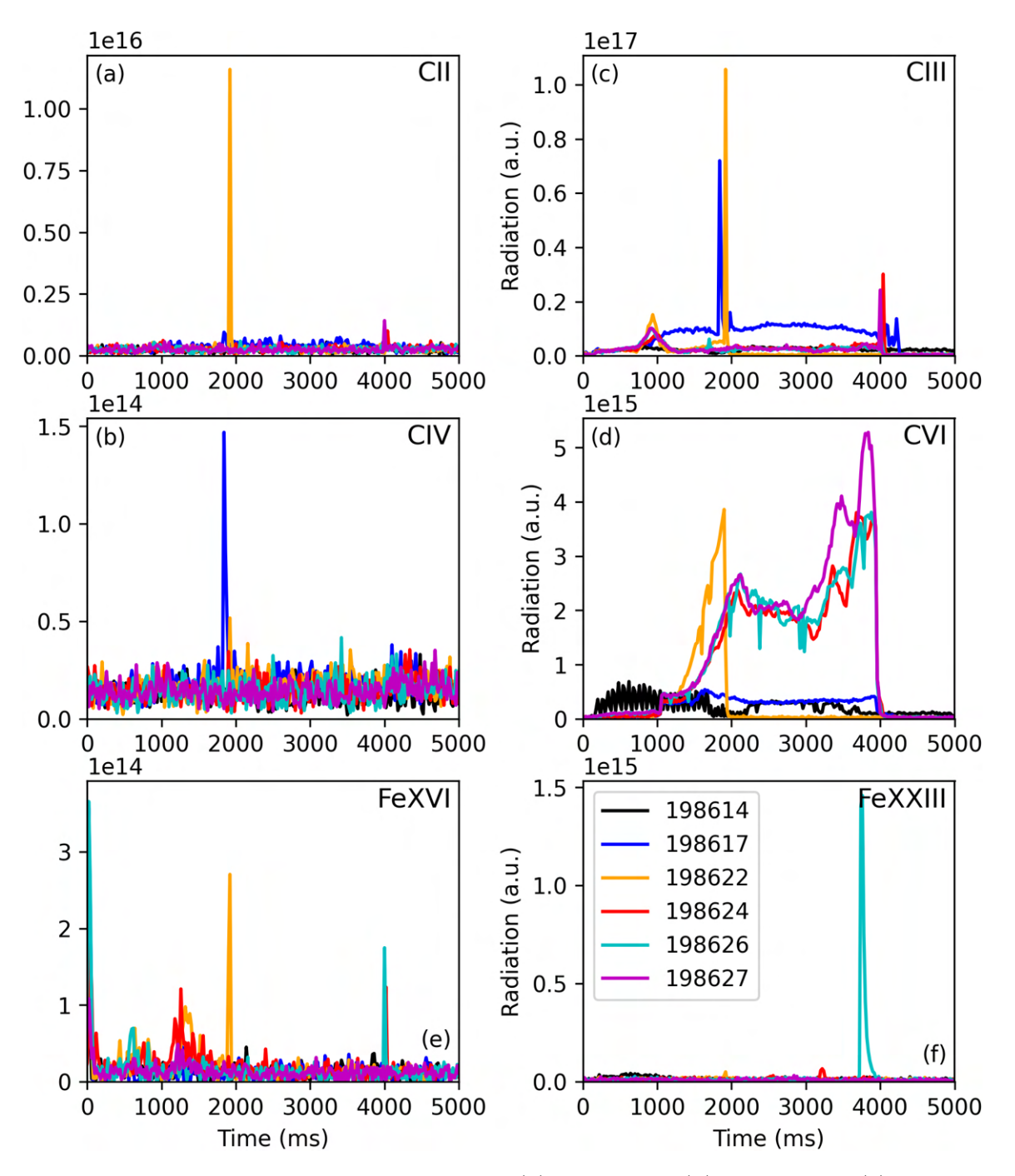


Figure 5.3: Time traces of radiation from the (a) carbon-II, (b) carbon-III, (c) carbon-IV, (d) carbon-VI, (e) iron-XVI, and (f) iron-XXIII emission lines for several shots in the initial run day.

Cleat	D:12	Density (10^{19} m^{-3})	Beam	Goal	G
Shot	Disrupted?	(10° m°)	Power (MW)	Elongation	Comments
198614	No	2.5	7.6	1.25	Small sawteeth
198617	No	5.1	8.02	1.25	Fishbones
198622	Yes	5.5	9.54	1.7	Locked mode
198624	No	4.6	9.40	1.6	Giant sawteeth with fishbones
198626	No	3.9	9.45	1.6	Tearing modes
198627	No	4.4	9.53	1.6	Giant sawteeth,
					higher triangularity

Table 5.1: Basic characteristics of six shots representative of the initial run day.

was spiky, reflecting occasional arcs from the wire. Note that emission line is numbered in Roman numerals by its level of ionization; neutral is I, so the number of stripped electrons is one less than the numeral. Radiation also led to disruption through radiative collapse, or complete energy exhaust from the plasma [12]. Arcs and iron emission were associated with disruptions in the experiment, matching predicted increased risks posed by high-Z impurity radiation as stated in the literature [10]. Due to the impurity influx and repeated disruptions, very little high-quality data was available on any diagnostic, and significant time was lost, because shots disrupted and their data was unusable. As a result, after repairs were completed to remove the exposed tile and wire, one half-day of contingency was granted. This day comprised twelve shots, none of which disrupted.

A summary of several shots, chosen to represent the variety of conditions that occurred throughout the two run days, are described in Tables 5.1 (initial run day) and 5.2 (contingency run day). The lowest-elongation shots did not display tearing modes, and the sawteeth that were present were smaller and more frequent than seen in more elongated shots. The fishbone instability was also present and combined with the sawteeth, with repeated fishbones exhibited in many shots just before a sawtooth crash. Fishbones are an m, n = 1, 1 ideal instability that gain free energy from energetic particles [13], which were present in

		Density	Beam	Goal	
Shot	Disrupted?	(10^{19} m^{-3})	Power (MW)	Elongation	Comments
199319	No	2.5	5.69	1.25	Small sawteeth
199321	No	3.9	6.97	1.25	Fishbones
199322	No	4.5	10.5	1.25	3,2 tearing modes
199324	No	5.1	8.33	1.7	Giant sawteeth
199328	No	3.9	10.6	1.5	H-mode,
					2,1 tearing mode
199329	No	4.1	10.7	1.5	H-mode,
					3,2 tearing modes

Table 5.2: Basic characteristics of six shots representative of the contingency run day.

abundance in this experiment due to high input power and relatively high density. They appear in spectrograms as intermittent fluctuations that rapidly chirp up and down and in raw magnetic signals with a distinct ringing pattern that lends them their name. Fishbones were associated with higher density, which matches the energetic-particle nature of the instability. The elongated shots demonstrated a variety of phenomena: (1) High-amplitude sawteeth with a long period; (2) At highest elongation for shots that disrupted late, several tearing modes that then locked to the wall, bringing plasma rotation to zero and causing disruption; and (3) m, n = 3, 2 and 2,1 tearing modes, identified by sensing coil analysis, alongside small sawteeth. Also important to note is that all the shots with giant or fishboning sawteeth contained compound sawteeth, or smaller crashes preceding a larger crash. Compound sawteeth are a subject of ongoing research with RIP [14]. Shots #199328-#199330 also entered H-mode, which is difficult to achieve in IWL plasmas [15].

I evaluate data quality using the RIP signal magnitudes. Signal magnitudes are the intensity of the light beam entering the detector and are not affected by Faraday rotation. If external factors are affecting mode detection, they may do so by altering the incoming beam, which will then be reflected in the signal magnitude. RIP was noisy in both the initial and contingency days, likely due to variation in signal magnitude due to radiation

and instrumental noise, particularly on the upper chord. In addition, RIP signal magnitude was lower than in typical shots. This is hypothesized to be due to refraction caused by high impurity density in the core. Figure 5.4 demonstrates the low amplitude and substantial noise in RIP signals in the initial and contingency run days. Shot #180704, the early detection shot where RIP was known to be effective, is used as a control. #198626 belonged to the initial run day, and #199322 belonged to the contingency run day. All three contained tearing modes.

The upper chord, Z=13.5 cm, shown in 5.4(a), had poor data quality for both run days. It is immediately evident that the signal magnitude for the upper chord is both low and very noisy for the run shots, particularly the high-power shots. This may be because the wall has a shelf near that location, which could cause the plasma to contact more of the wall surface area. The signal magnitude also increases, yet remains noisy, when the magnetic axis moves closer to the chord at 2500 ms. The upper chord was noisy on #180704 but was not dominated by noise like the initial run day shots. Spectrograms from the upper chord on the run day show high-amplitude background noise at all frequencies and no fluctuation activity. The spectrogram for the upper chord in #180704 did not show these issues and, while noisier than the spectrograms for the other chords in that shot, was effective in showing tearing mode activity. I consider the low, noisy signal that does not appear to correspond to any phenomenon within the plasma to be a sign of poor data due to radiation.

Both the midplane (Z = 0 cm, Figure 5.4(b)) and lower (Z = -13.5 cm, Figure 5.4(c)) showed higher data quality than the upper chord during the run days and were usable, but they experienced more broadband noise than #180704. This is reflected in the signal magnitudes of shots #198626 and #199322 on the two chords. Signal magnitude is less strong by a factor of over two compared to #180704, which results in the Faraday rotation being partially washed out by instrumental noise, external radiation, and other factors. Modes are harder to identify.

RIP magnitudes are compared to carbon-VI emission (Figure 5.4(d)), which was the line

most boosted by the extra influx from the wall and tile. As already shown in Figure 5.3, carbon was elevated in both run days, though more in the initial run day, compared to a more typical shot like #180704. The spikes in C-VI emission in #180704 are due to ELMs. It should be noted that C-VI is relatively high early in #180704, but the time period of interest, corresponding to tearing modes, does not begin until after the emission drop. In contrast, tearing modes are of interest late in the shot in #198626 and #199322 as well but are confounded by emission that is still present.

5.2.2 Data Evaluation

RIP data quality for the Z=0 and Z=-13.5 cm chords can also be assessed using correlation polarimetry. As described in Chapter 3, correlation between signals can be used to correct signal amplitudes, and cross-coherence can be used to measure whether a significant fraction of the RIP signal at a given frequency is noise. The RIP A and B channels are expected to detect the same mode, and its fluctuations, independently. Uncorrelated (noise) signal components should vanish when the two RIP signals [16] are cross-correlated. The quantities used to compare signals are the cross-power spectral density (CSD) and coherence, taken between the RIP A and B signals at the midplane. They are then compared to the auto-power spectral density (PSD) of each signal. Using these measures, I compare two shots that contained steady m, n = 3, 2 tearing modes, as determined by sensing coil analysis, and did not undergo the L-H transition. Shot #198626 was from the initial run day with higher impurities, and shot #199322 was from the contingency day with lower impurities. Figures 5.5 shows auto-power and cross-power spectral densities and coherence between the A and B RIP signals for shots #198626 and #199322 along with spectrograms of the tearing modes. The comparisons are made for both polarimetry (δB) and interferometry (δn) from RIP. Interferometry typically has less noise than polarimetry, as illustrated in Chapter 4 due to the small value of the density fluctuation amplitude. On interferometry, the fluctuation magnitude is significantly less than the equilibrium value, whereas for polarimetry the fluctuation and equilibrium values are of the same order. The same time window, 2600–

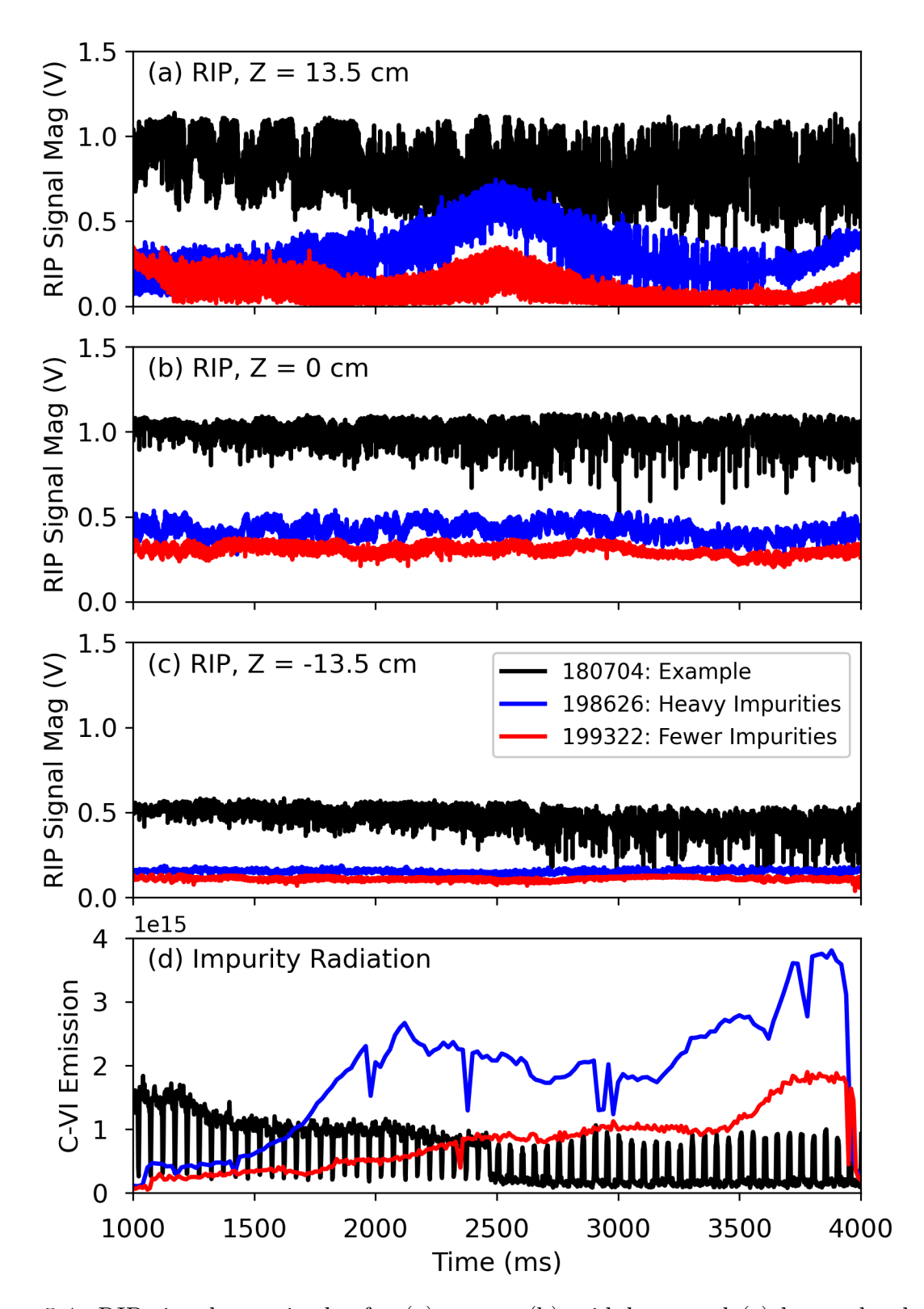


Figure 5.4: RIP signal magnitudes for (a) upper, (b) midplane, and (c) lower chords and (d) emission from the carbon-VI line for three shots. #180704 (black) is an example shot to demonstrate good RIP signals. #198626 (blue) from initial run day, #199322 (red) from contingency run day.

2800 ms, is used for both comparisons.

The spectral densities show striking differences in their measurements between the two shots. In the initial run day, high-impurity shot, the two PSDs are almost independent, coherence drops near zero at times, and the CSD and spectrogram are choppy despite the tearing mode being strong. In the contingency shot, the PSDs track together despite having different scales, and the CSD tracks with them both. Coherence is more consistent. While the spectrogram is noisy, likely due to refraction and the remaining elevated carbon radiation, the evolution of the tearing mode in time is clearly distinguished; amplitude is flat for about 50 ms and then begins a general upward trend. In both cases, cross-correlation of interferometry measurements between the two channels demonstrated very good coherence despite background noise in the signal as shown in the spectrogram. The A and B power spectral densities matched almost completely and also tracked with the cross-power spectral density. I posit that interferometry was more successful because it is not confounded by radiation. However, as magnetic fluctuations are directional, the polarimetry channels are still vital to understanding the dynamics of the shots. Only polarimetry is affected by phase shifts across the magnetic axis in even-m modes. While both tearing modes remained steady in frequency, the shot with higher impurities had significantly more variation in time than the shot with lower impurities.

While not a common mode of operation and therefore not expected in my experiment, inner-wall limited plasmas can achieve H-mode. H-mode is rarely pursued or achieved in IWL in DIII-D due to high power requirements, though other devices such as TFTR, which was fully circular ($\kappa = 1$) and only ran limited plasmas, successfully employed it [17]. Both TFTR and early DIII-D limiter H-mode results found that the required input power scaled linearly with the product of the line-averaged density and magnetic field on-axis [15, 17]:

$$P_{\text{TFTR}} = 9.2\bar{n}_e B_t \tag{5.1}$$

$$P_{\text{DIII-D}} \approx 12.7 \bar{n}_e B_t. \tag{5.2}$$

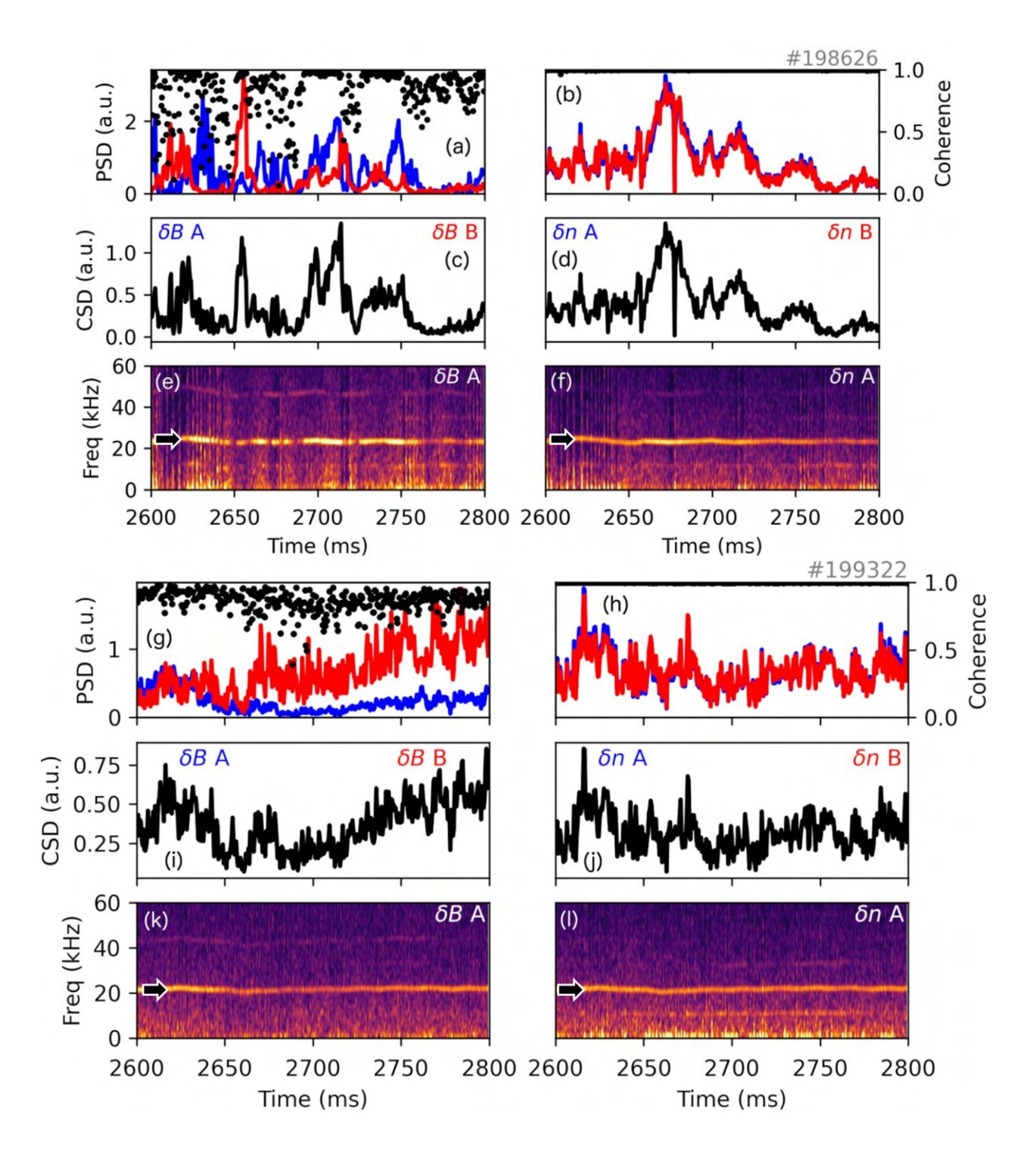


Figure 5.5: (a–b) Power spectral densities and cross-coherence from the midplane A (blue) and B (red) RIP polarimetry and interferometry channels. Black dots represent coherence between signals. (c–d) Cross-power spectral density between the A and B polarimetry and interferometry channels. (e–f) Spectrogram showing tearing mode for shot #198626, 2600-2800 ms. (g–l) The same signals for shot #199322 and the same window. Black arrows mark dominant tearing modes.

Plasmas near the L-H power threshold, in both limited and diverted plasmas, may instead enter dithering H-mode, a borderline regime. In dithering H-mode, the plasma transitions repeatedly between L-mode and H-mode [18]. This is associated with small ELM-like bursts in the D_{α} signal but not strong pedestal formation or large ELMs.

Though this was not planned, three shots reached H-mode, as evidenced by a drop in D_{α} emission followed by a transition to spiky behavior associated with ELMs. However, the H-mode behavior was different than in typical shots. The ELMs in D_{α} had different time dependence than ELMs in typical H-mode, did not appear as broadband in RIP or magnetic data, and were more frequent than the ELMs seen in shots such as #180704. A temperature pedestal did not form. The density pedestal was lower than in standard H-mode, and the density was strongly peaked in the core as in the L-mode shots. I conclude that H-mode was not robust in these shots. Nine other shots exhibited regular spikes in D_{α} but had no drop in D_{α} prior to the start of spikes and therefore no transition phase. I conclude that these shots entered dithering H-mode and denote the shots that did not undergo the transition as having dither only.

Figure 5.6 illustrates both types of H-mode behavior found in my experiment. It compares a dithering-only shot (#199322) and an H-mode shot (#199329) that both contained 3,2 tearing modes. Figure 5.6(a) shows the D_{α} traces of each shot along with the transition time and first ELM for shot #199329. The significant dip, followed by a large spike, is an H-mode transition. The shot then exhibits small ELMs. #199322 has no drop. Figure 5.6(b) compares the input power for each shot to the $\bar{n}_e B_t$ scaling threshold above which H-mode is predicted to begin in DIII-D. Both shots have a B_t of 2 T and similar input power, which is modulated between 8 and 10 MW. The dithering-only shot has higher density throughout, which leads it to sit just below the required input power even at maximum power. The lower density in the H-mode shot meant that the maximum power lay above the threshold.

Due to the unexpected finding of H-mode, I investigate whether the power threshold to achieve H-mode complied with existing density and temperature scalings from other devices.

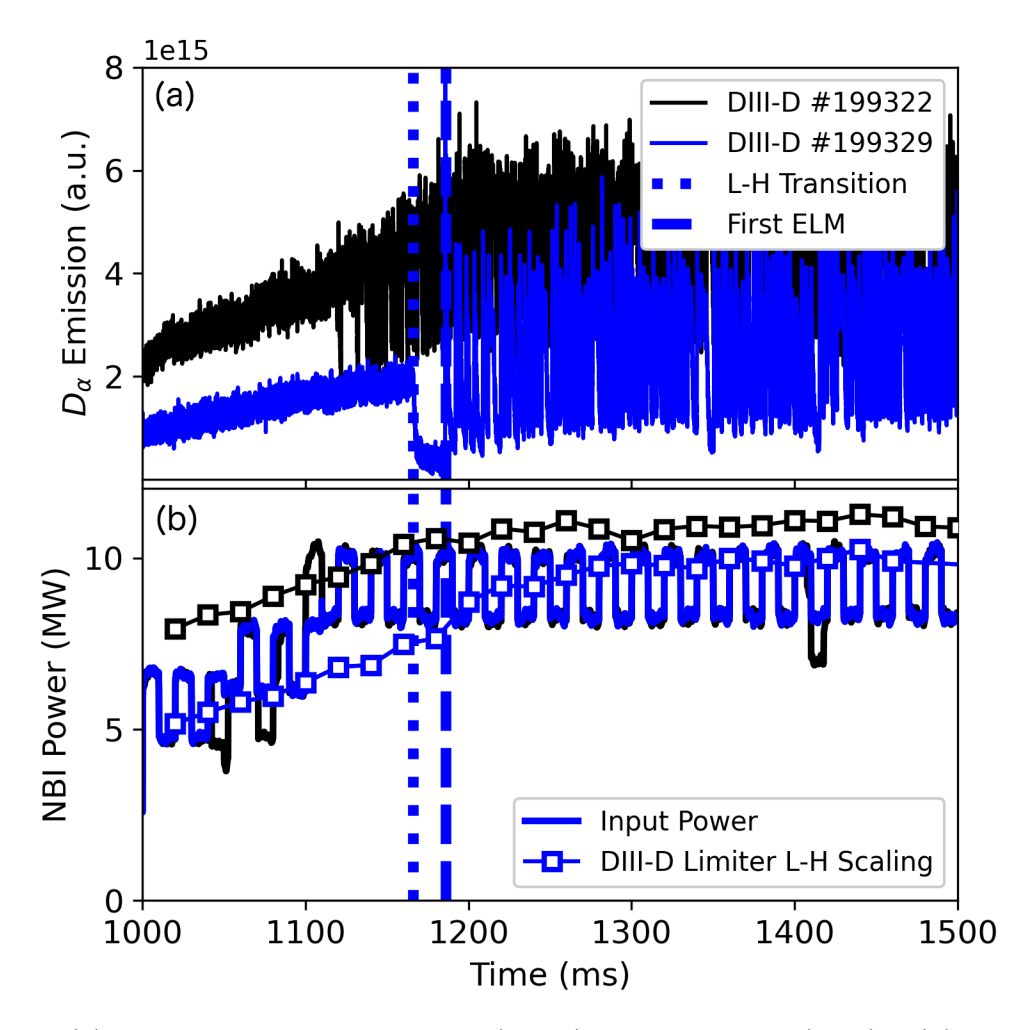


Figure 5.6: (a) D_{α} emission for #199322 (black) and #199329 (blue). (b) Input power (solid) and DIII-D $\bar{n}_e B_t$ scaling (squares) over time. Vertical dotted and dashed lines mark H-mode transition times for #199329.

I compare all shots to the TFTR and DIII-D scalings to identify whether this series more closely replicated TFTR (circular, even less weakly shaped than these plasmas) or DIII-D. Each shot can be categorized by its D_{α} behavior: full H-mode transition, dither only without a transition, or no dither. Figure 5.7 plots each shot, combining my run days. For each, the magnetic field-weighted line-averaged density at 1200 ms, which is an approximation to the H-mode transition time of shots #199328-#199320, and input power are plotted. All three H-mode shots (blue circles, two of which almost overlap) lay above the DIII-D threshold. Dithering shots (black circes) lay below the threshold overall, closer to the TFTR threshold, and L-mode shots (white circles) lay below that. The lowest $\bar{n}_e B_t$ values were associated

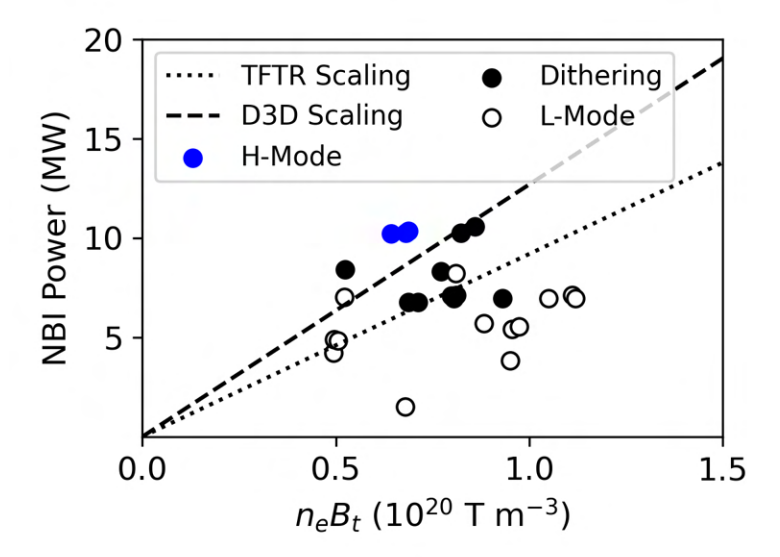


Figure 5.7: DIII-D IWL shots classified by regime: H-mode (blue), dithering (black), or L-mode (white) versus $\bar{n}_e B_t$ and input NBI power. TFTR and DIII-D power scalings marked with dotted and dashed lines.

with higher requirements to reach H-mode; around $\bar{n}_e B_t = 0.5 \times 10^{20}$ T m⁻³, a shot well above the DIII-D threshold experienced dither, and another one near the threshold did not reach H-mode at all. Overall, for this campaign, H-mode proximity reflected typical DIII-D scalings rather than the circular TFTR scalings, corroborating previous results.

Due to the ineffectiveness of many diagnostics on the initial run day, I primarily analyze data from the contingency day. As Tables 5.1 and 5.2 briefly describe, the MHD activity in the high-power IWL shots was dependent on the elongation in addition to density. Elongation values submitted to the Plasma Control System (PCS) varied from 1.25–1.7. However, due to restrictions on the shaping coils and the plasma response to the controls, the range of elongations was much narrower than intended. Actual elongation in the experiment ranged from approximately 1.25–1.5. The target shots reached $\kappa = 1.25$ as expected. Figure 5.8 shows elongation over time for the three other categories: near-circular shots, elongated shots, and tearing shots. Variation in time was not requested, but the PCS takes some time to establish the correct shape after plasma startup. The tearing shots all shared very similar elongation, around 1.4. The shots with fishbones and κ lowest after the flattop had

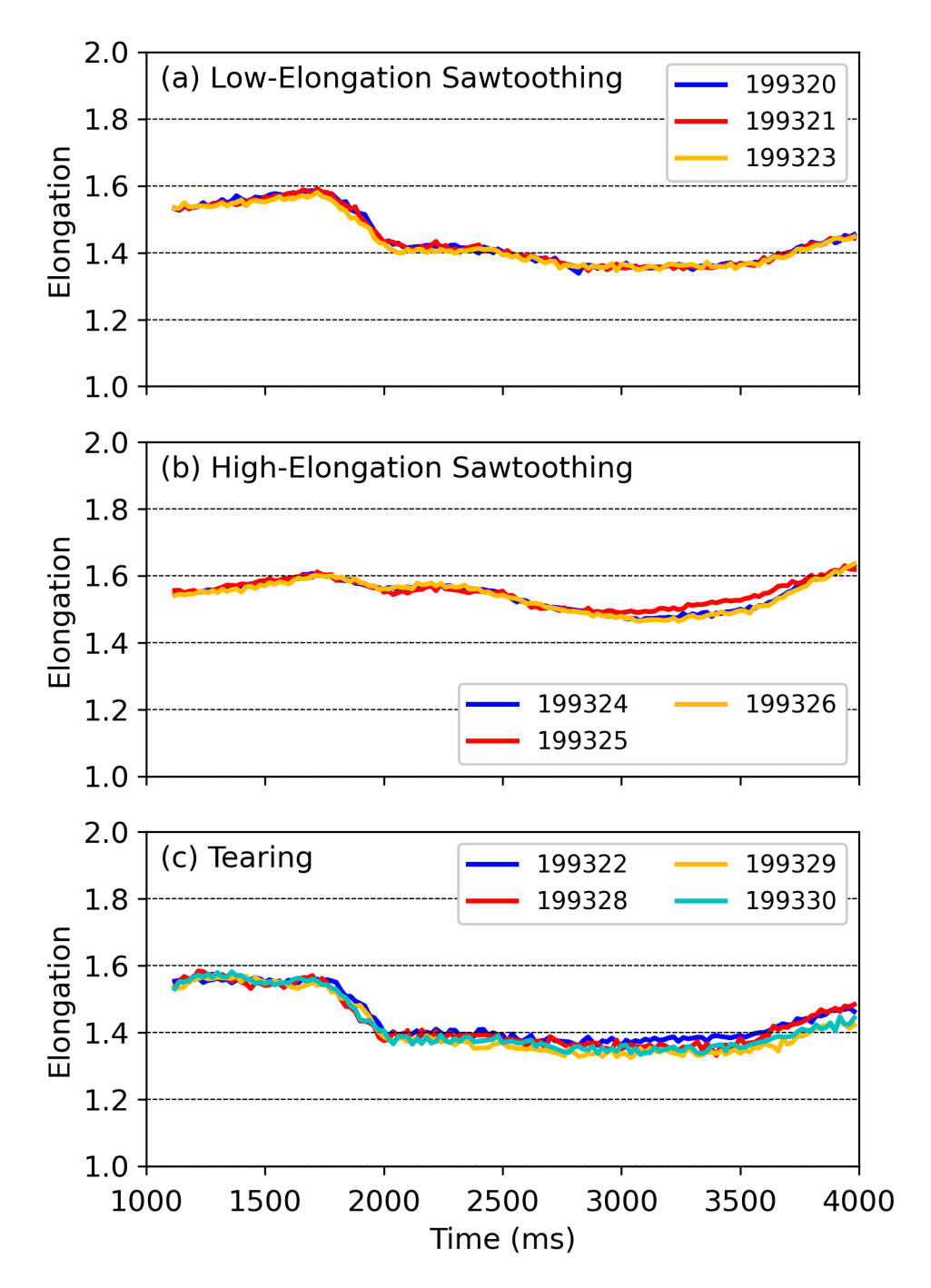


Figure 5.8: Plots of plasma elongation for each non-disrupting, non-target shot in the contingency day from flattop to rampdown in (a) near-circular shots, (b) elongated shots, and (c) tearing shots. Dotted lines mark increments of 0.2 in κ .

a value near 1.35. The elongated shots maintained elongation around 1.5 throughout. In addition, the elongation was reduced during the period the plasma was swept across the three RIP chords. Tearing occurred only for shots with relatively higher elongation, qualitatively matching the hypothesis that the pattern of greater instability at high elongation [3] would hold for the remainder of the elongation space. However, some shots with higher elongation did not contain tearing. Tearing modes may be attributable to higher q and lower density, particularly the 2,1 mode, which had the highest q of all. Section 5.3 discusses in greater detail the reasons for inconsistent tearing mode triggering.

5.3 Tearing Mode and Sawtooth Stability

My next goal is to identify in more detail the reasons why the plasma experienced tearing modes, sawteeth, fishbones, or some combination of the three under the conditions specified in Section 5.2. Assessing tearing and other types of MHD stability is a nontrivial process, and codes to calculate resistive stability are either complicated to use or require assumptions to be made. The ideal stability limit with a perfectly conducting wall has a good qualitative correlation with the tearing stability boundary $\Delta' = 0$ [19]. Specifically, Δ' asymptotically increases just below the ideal-wall limit [20]. Plasmas become more resistively unstable as they approach the ideal-wall boundary. Therefore, to measure general stability trends in plasmas near the resistive stability boundary, one can use the ideal-wall limit as a proxy. To calculate the comparative stability of tearing modes of different n using the ideal-wall approximation, I use DCON [2] to conduct ideal stability analysis with a conducting wall at the experimental wall locations given, for example, in Tables 5.1 and 5.2. DCON analysis requires the input of kinetic EFITs [1] for an accurate picture of temperature, current, and pressure gradients in the plasma interior. EFITs additionally provide the safety factor q, which is used in DCON to identify rational surface locations and is also instrumental to the sawtooth cycle, since sawteeth are believed to be triggered by the minimum safety factor q_{min} falling below 1 [21].

I carried out full kinetic EFITs for each shot. I input into TRANSP [22] electron and

ion temperature, electron and ion density, and ion rotation to produce current and pressure constraints. Since these plasmas had high power and typically moderate density, TRANSP results required inclusion of a fast ion loss term to obtain appropriate neutron emission rates in the model and account for beam power not absorbed by the plasma. Fast ion diffusion is important because disregarding fast ion losses overestimates density, pressure, and current. I constructed the fast ion loss term by first making multiple TRANSP runs with different values of the fast ion diffusivity from 0–20000 cm²/s. From there, at each time point, I ran a linear regression to identify the appropriate diffusivity value to recreate the experimental neutron emission rate. This was the final TRANSP run for each shot. EFIT combined the kinetic constraints with magnetic data to constrain the boundary and MSE data to improve the current constraint.

I found that the typical pressure and current constraint shapes were ineffective for innerwall limited plasmas. To solve the Grad-Shafranov equation (Equation 2.20), EFIT constructs P' and FF', called basis functions, using a spline model. The plasma was marked by no or weak pedestals in pressure and current, differing from standard H-mode. Current constraints are typically weighted toward the edge, again to generate a pedestal but also to numerically stabilize the q profile there. However, the constraints generated by the current and magnetic field at the edge were not fully consistent. This resulted in Grad-Shafranov solutions that converged to unphysical plasma shapes. Removing the current constraint solved the plasma shaping issue but left the q profile unconstrained in the edge, which interfered with DCON by yielding inconsistent β_N limits. A weak, radially uniform current constraint, balanced with magnetic constraints through a series of optimizations, was the best solution to ensure convergence.

Once the EFITs were finished, I ran DCON for each shot based on the experimental equilibrium reconstructions. The free energy δW and the no-wall and ideal-wall β_N limits were calculated for as many shots and time points as possible. As previously described in Section 3.4.3, no-wall and ideal-wall β_N limits are calculated by scaling β_N in an experimental

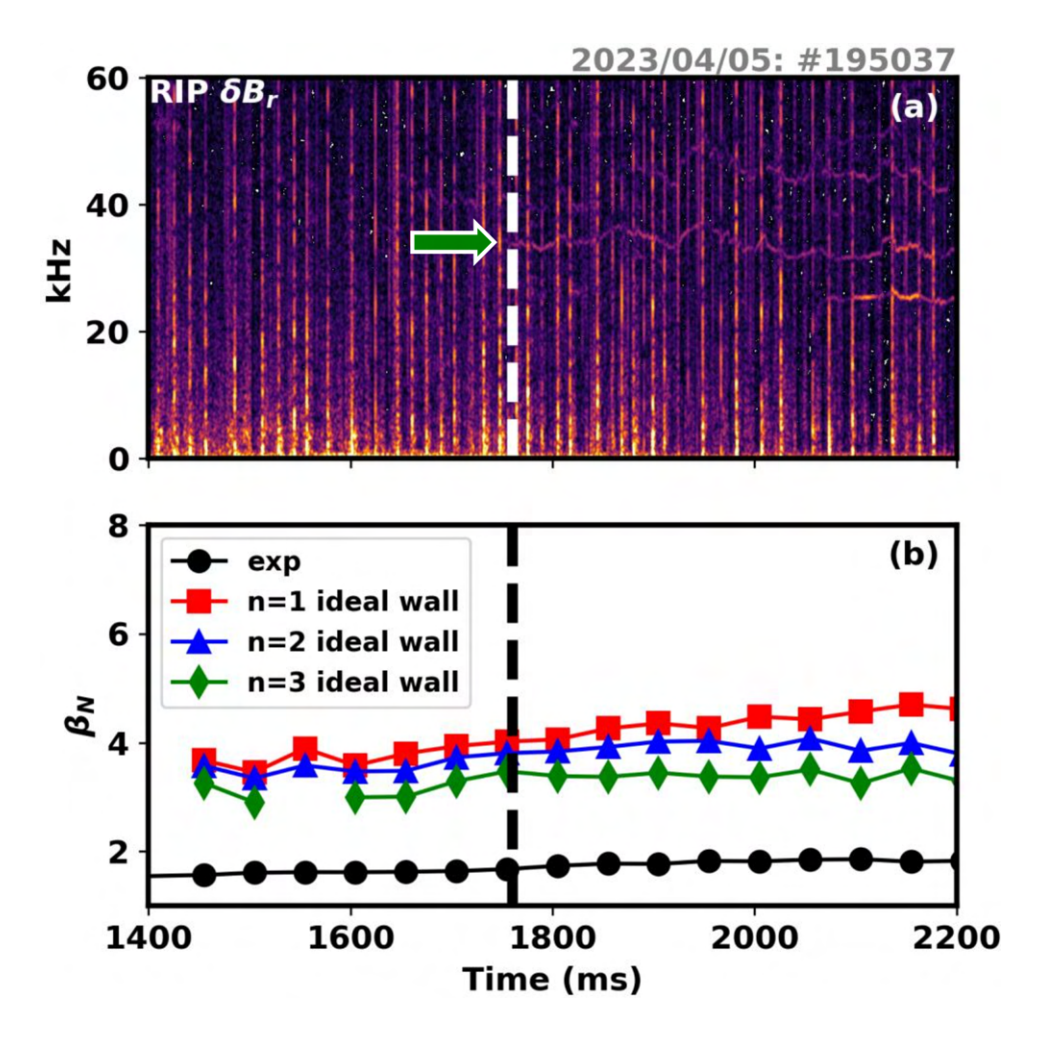


Figure 5.9: (a) A spectrogram of RIP data for shot #195037, demonstrating several low-amplitude tearing modes. The first mode to arise, marked with a green arrow, has n = 3. (b) Experimental β_N (black circles) and ideal-wall β_N limits for the n = 1 (red squares), n = 2 (blue triangles), and n = 3 (green diamonds) modes, calculated using DCON.

equilibrium reconstruction, re-running DCON, and repeating the process until all time points yield unstable plasmas. The β_N limit could not be resolved for some points, which were discarded. The most important use of DCON in this study was to compare experimental β_N to ideal-wall limits and identify if MHD instabilities in these shots were related to proximity to the limit. I hypothesized that β_N would remain below the n=2 and n=3 ideal-wall stability limits but that n=2 modes would arise regardless. This would result from a trigger, in the form of a sawtooth, to destabilize a classically stable system and induce neoclassical growth. Shot #180704, where RIP detected a tearing mode before the coils, was an example

of a mode arising below the corresponding ideal-wall limit. Another example, of a shot similar to #180704, is shown in Figure 5.9. In this shot, an n = 3 tearing mode arises on RIP just before coils and well below the n = 3 ideal-wall limit. This is a marker for an NTM. I expected that the IWL plasma would show similar signatures due to the ability of sawteeth to trigger tearing modes.

The results for the inner-wall limited plasmas departed from the hypothesis that NTMs would be triggered below the β_N limits. These modes were resistive as predicted, as potential energy remained stationary and $\delta W < 0$ was not required to trigger modes. However, in most cases, n=2 and n=3 modes did not arise, and sawteeth did not trigger them. When tearing modes did not arise, the n=1 limit determined the shot dynamics. One example of the effect of the n=1 limit on dynamics occurred in shot #199323, in which sawteeth dominated. RIP signatures and stability conditions before and just after the first sawtooth crash, between 1000–2000 ms, are shown in Figure 5.10(a–c). When the ideal-wall β_N limit for the n=1 mode drops below the measured β_N value, reflecting an approximate resistive stability boundary, a sawtooth precursor arises and causes a brief loss of axisymmetry, resulting in δW and β_N oscillating then recovering. The sawtooth precursor appears on RIP as a bright band below 20 kHz, dropping slightly in frequency. This precursor contains fishbone oscillations, associated with energetic particles induced by high beam power. RIP also shows a short-lived tearing mode as a bright band; it disappears after the crash. When the β_N limit drops again, the sawtooth crash occurs, and the limit remains below the experimental β_N thereafter. The precursor low-frequency MHD mode disappears. I was unable to determine whether the sawtooth triggering by the n = 1 limit corresponded to the same sawtooth trigger as the target shot, because the MSE diagnostic encountered an error. As a result, I was unable to construct EFITs for that shot.

Sawteeth have precursor modes that are often described as ideal internal kink modes. However, in practice, their precursor modes have a resistive component, making them similar to tearing modes [21]. The fact that the β_N limit triggers a sawtooth indicates that (1)

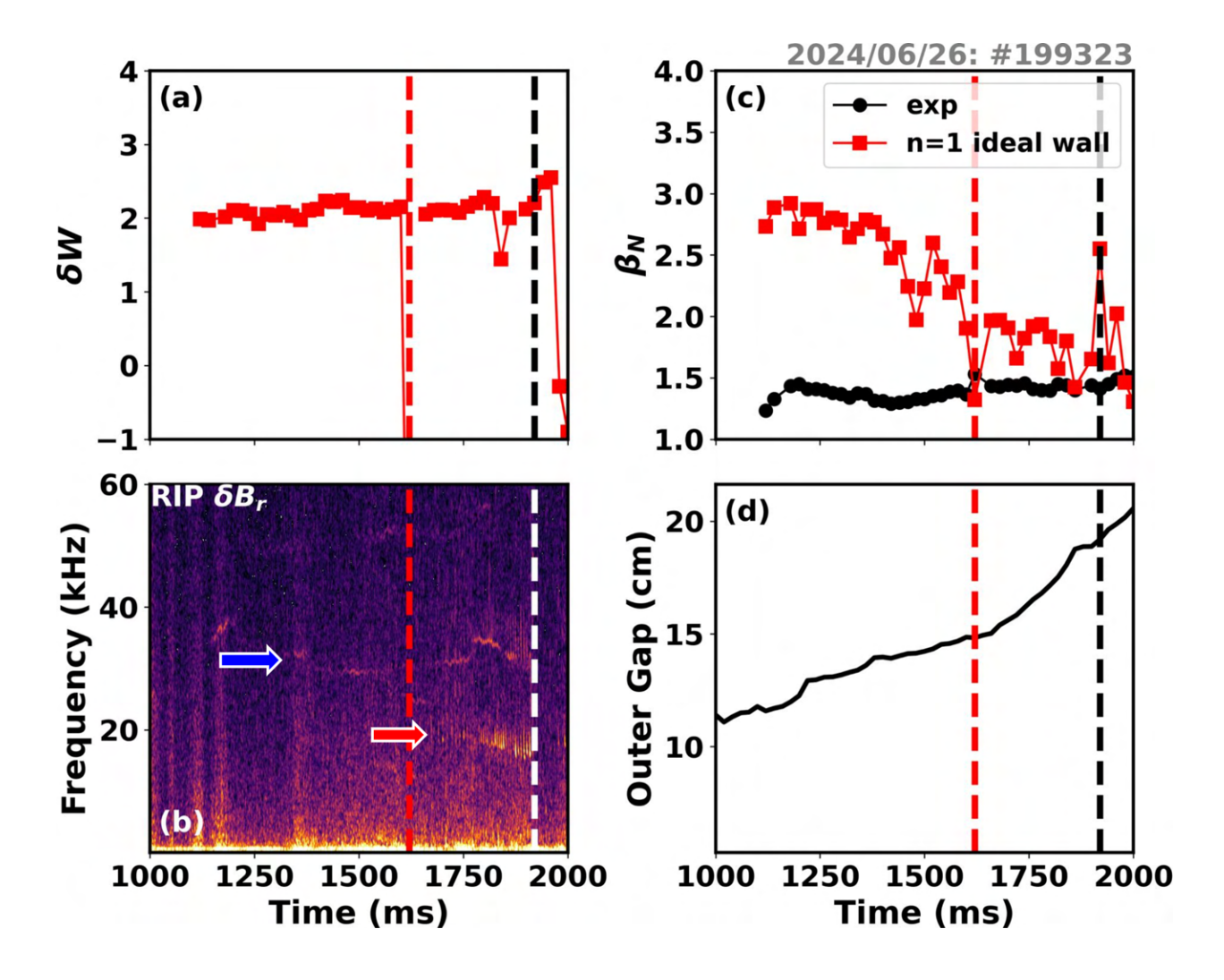


Figure 5.10: (a) Potential energy δW , (b) RIP spectrogram, (c) n=1 ideal-wall β_N limit (red) and experimental β_N (black), and (d) gap between plasma and outer wall for shot #199323 from 1000–2000 ms. Red dashed line marks start of sawtooth precursor. Black dashed line marks first sawtooth crash. Red arrow marks sawtooth precursor. Blue arrow marks tearing mode.

resistivity plays a role, and (2) the drive is classical. Both the precursor and the crash are associated with dips in the limit below the measured β_N ; the drive mechanism appears to be the same for both. An interesting and unusual point about this case is that the experimental β_N remains steady while the n=1 limit drops drastically, from 3 to below 1.5. The plasma current has already hit its flattop, and the neutral beams are injecting at a constant rate. The potential energy δW does not change during this time and only jumps when the plasma is distorted by the sawtooth precursor. One quantity that is changing significantly throughout the first portion of this shot is the shape. In preparation for an increase in elongation and vertical jog across the RIP chords, the plasma is compressed against the inner wall to reduce its radius. The gap between the plasma and the wall increased by a factor of two, as shown in Figure 5.10(d). I posit that a decrease in plasma volume (elongation has not yet increased, so the plasma was shrinking overall) means that a smaller perturbation is required to induce instability.

In the case of the increasing outer gap, the sawtooth was associated with the n=1 limit. The minimum safety factor q_{min} is hovering around 1 during this time, making the plasma susceptible to sawteeth. I provide an example, from my run day, of coincident n=1 and n=2 limits yielding only an n=1 mode, indicating insufficient n=2 drive for a stationary mode despite approaching the limit. The n=2 limit is typically associated with tearing mode triggering, but the plasma appears to be susceptible to n=1 at this time instead. A significant resistive contribution to sawtooth destabilization exists. This indicates that resistivity is strong enough to induce modes, but the sawtooth drive is stronger than the tearing drive. Instead, in most cases, pressure is too low for tearing modes to arise. An example of a dominant n=1 drive is shown in Figure 5.11(a–c), which gives δW and the β_N limit to drive n=1 and n=2 modes in shot #199327, which exhibited fishboning sawteeth like #199323. Here, β_N is lower, around 1.5. The n=2 mode remains stable in the computation with a fixed δW , but both n=1 and n=2 beta limits drop until a sawtooth precursor (red arrow) emerges. An n=3 tearing mode (green arrow) emerges

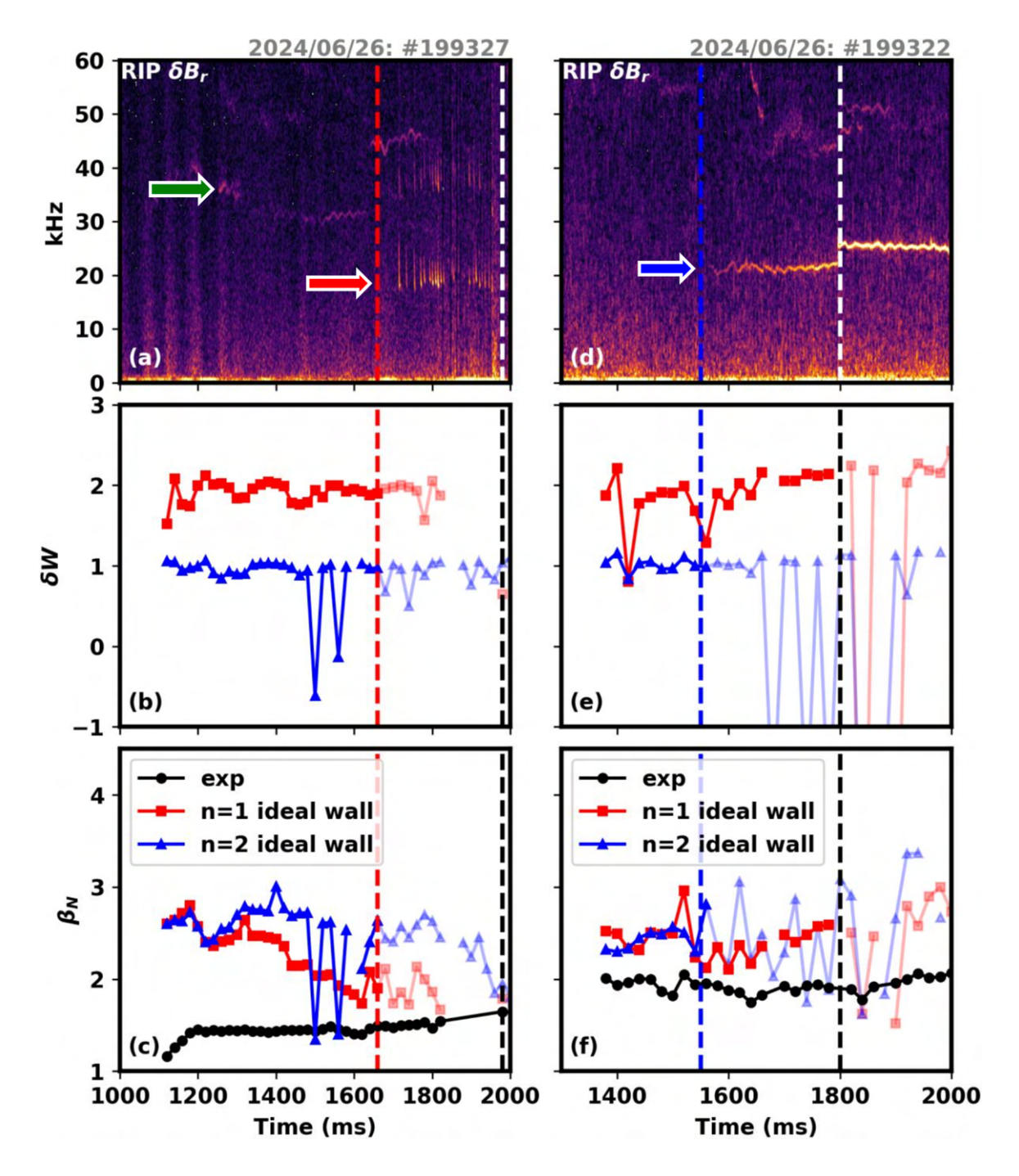


Figure 5.11: Shot #199327: (a) spectrogram. (b) δW for n=1 (red squares) and n=2 (blue triangles) modes, (c) Experimental β_N (black circles) with n=1 (red squares) and n=2 (blue triangles) ideal-wall β_N limits. Red dashed line denotes sawtooth precursor. Black dashed line denotes sawtooth crash. Shot #199322: (d) spectrogram, (e) δW for n=1 (red squares) and n=2 (blue triangles) modes, (f) experimental β_N (black circles) with n=1 (red squares) and n=2 (blue triangles) ideal-wall β_N limits. Blue dashed line denotes tearing mode start. Black dashed line denotes tearing mode jump.

but is weak and vanishes after sawteeth begin. Since the sawtooth appears to have a single frequency, as opposed to the giant sawteeth in shot #199325 which had multiple frequencies, there is no m, n = 2, 1 component present. It is also notable that the ideal-wall limit drops below the experimental β_N just before the sawtooth crash and begins to oscillate around the time of the crash. I hypothesize that this is attributable to time-averaging of profiles both before and after the crash in EFIT. There is no major change in the EFIT profiles before the precursor starts around 1660 ms; core pressure rises, but neither change is dramatic. The central safety factor drops closer to 1, as might be expected at the start of a sawtooth precursor. Since NTMs usually have a lower stability limit than CTMs, it was unexpected that classical modes would emerge first despite the presence of sawteeth, even with the n = 2 β_N limit as a trigger.

I contrast the dominant n=1 sawtooth drive in lower- β_N shots with a higher-pressure case in which an m, n = 3, 2 tearing mode does occur. In Figure 5.11(d-f), an n = 2 tearing mode (blue arrow) is present. It is associated with higher β_N , around 2, and a rise when the mode begins. The rise in β_N coincides with the n=1 and n=2 pressure limits approaching the experimental value, but this time the n=2 is triggered. Later, around 1800 ms, a brief n=1 mode, difficult to detect with RIP but visible on the coils, appears. At this time, the n=2 both jumps in frequency and strengthens. I posit that the n=2 mode interacts with the n=1 mode. Since it is not clear why one limit dominates over the other, it appears that factors other than the stability limit are differentiating tearing and sawtoothing shots. In all cases, after modes arise, the plasma loses axisymmetry and stability fitting becomes less effective, leading to ambiguous oscillations in beta limit. A weak, intermittent n=1mode arises later, but this is after the limits have oscillated for some time. MHD in the IWL plasmas was associated with pressure approaching the ideal-wall limit. This suggests that instead of neoclassical as expected for plasmas with strong triggers, the modes were classical. In the plasmas studied here, it appears that tearing modes do not require a trigger. The fact that tearing modes only arose in shots with $\kappa \approx 1.5$, the higher range within the two run

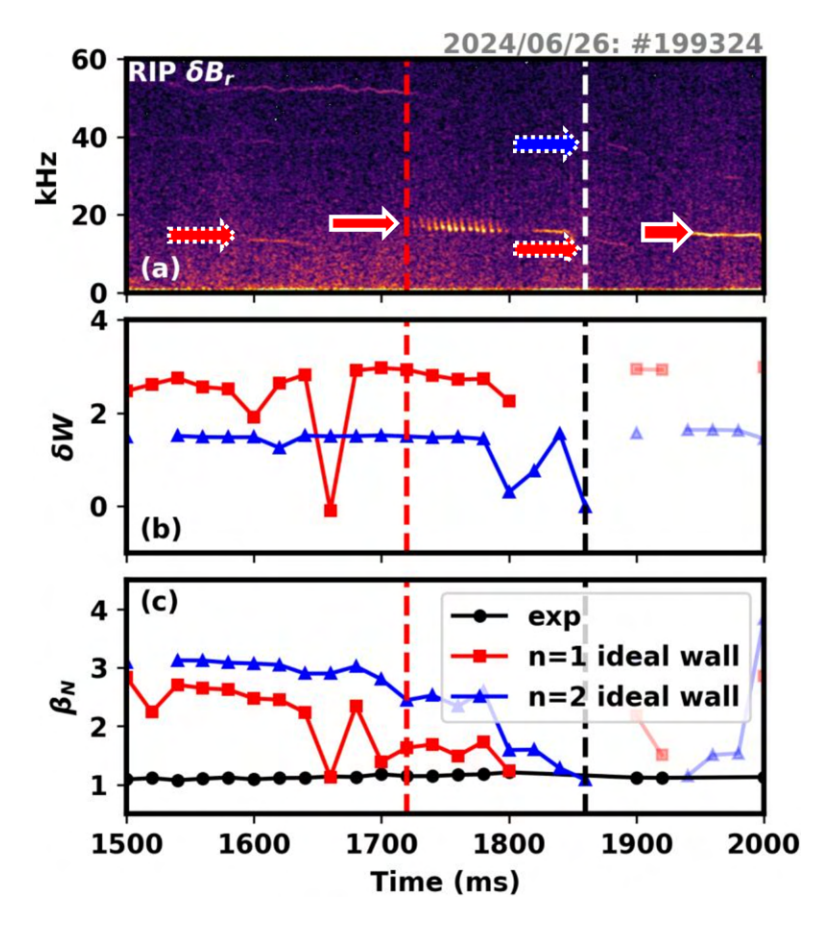


Figure 5.12: (a) RIP spectrogram of a shot with giant sawteeth. (b) δW for n=1 (red squares) and n=2 (blue triangles) modes, (c) Experimental β_N (black circles) with n=1 (red squares) and n=2 (blue triangles) ideal-wall β_N limits. Red arrows mark n=1 sawtooth precursors, blue arrow marks n=2 component of sawtooth. Dotted arrow borders denote precursors to in compound sawtooth. Red dashed line denotes start of primary sawtooth precursor, black/white dashed lines denote primary sawtooth crash.

days, also suggests that there is a boundary around that value below which tearing modes cannot form.

However, even at the higher elongations that were compatible with magnetic tearing, tearing modes sometimes did not arise. I now investigate why the giant sawteeth present in the non-fishboning, non-tearing shots did not trigger tearing modes as intended. The lack of triggering may be attributed to lower elongation than the IBS shots in previous studies, which had a lower limit of $\kappa = 1.6$. In that case, these shots would represent an extension to the existing database to lower elongations. However, higher elongations had both tearing and non-tearing shots, so another factor must have been involved. Figure 5.12(a) gives a

spectrogram of RIP polarimetry data for the first two sawtooth crashes in shot #199324, which had giant sawteeth throughout with no tearing modes. RIP data quality is variable in this shot due to high power, but it is evident that the n=1 sawtooth precursors are strong and have additional harmonics, including n=2. The oscillations have a period of 50-100 ms between crashes, considering the entire shot. The sawteeth in this shot and in many of the other shots in the contingency run day had compound components. In compound sawteeth, a temperature crash is preceded by a smaller crash caused by the same type of mode, with its own precursor [23]. DCON results for the ideal-wall β_N limits are less useful here because the sawteeth are so strong, but they do indicate that the n=1 and n=2 sawtooth precursor components become unstable around the same time, as shown in Figure 5.12(b-c). The kink modes associated with the sawtooth reduce the reliability of the reconstruction because they reduce the axisymmetry of the plasma.

I supplement the DCON results by using multi-device empirical scalings, [24] which include data from DIII-D, to understand the properties that allow sawteeth to trigger NTMs in multiple scenarios. In DIII-D and other devices, tearing mode triggering depends on both β_N and sawtooth period. For a shorter period, higher β_N is required to trigger a tearing mode. The sawtooth period $\tau_{sawtooth}$ is expressed as a fraction of the resistive diffusion time $\tau_r = \mu_0 L^2/\eta$, which is the typical time scale of current redistribution in the plasma. Here, μ_0 is the permittivity of free space, L is the characteristic length scale, and η is the resistivity. In this case, L is the minor radius of the q=1 surface. I used the dataset of all sawteeth in the three shots from my run days demonstrating giant sawteeth: #199324–199326. Between all shots ang times, $\tau_{sawtooth}/\tau_r$ ranges from 0.01–0.09 and β_N ranges from order 1–2. It should also be noted that while no persistent tearing mode emerged in shot #199325, brief m, n=2, 1 components were observed in the sawteeth. The distribution of sawteeth in shots #199324–199326 is plotted in Figure 5.13 alongside the two DIII-D tearing mode trigger cases from the multi-device scaling [24]. Shots in white and black are from my run day, and shots in red are from the previous scaling [24]

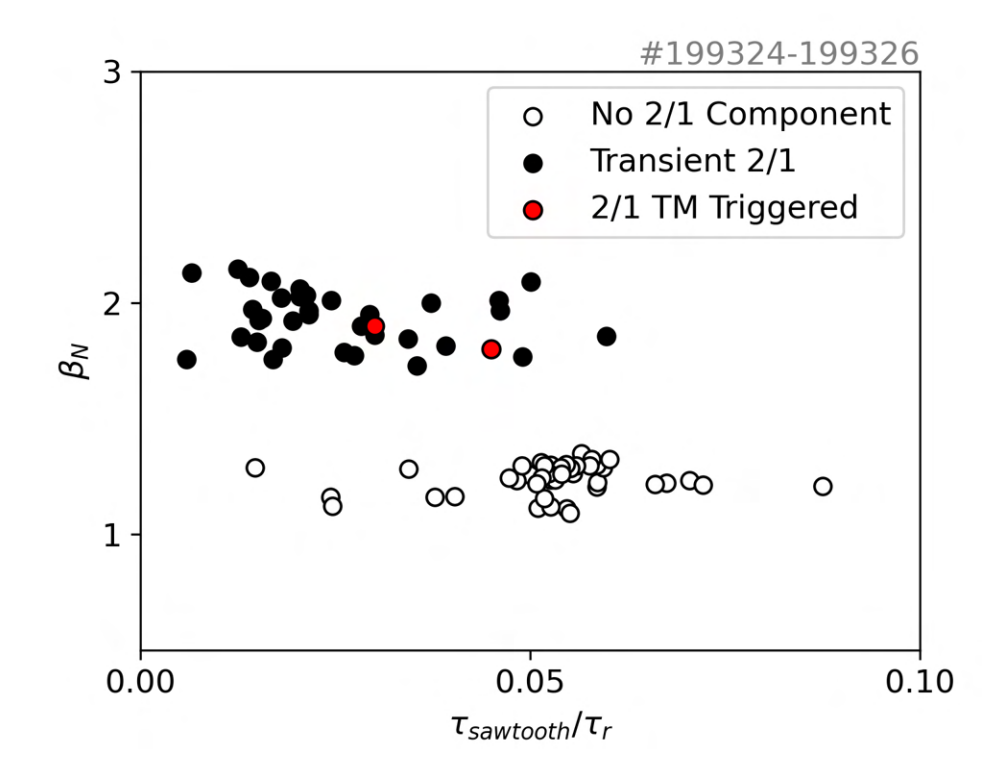


Figure 5.13: Scaling between sawtooth period and β_N for shots #199324–199326 alongside 2,1 NTM trigger shots from the empirical scaling (red) [24]. Shots with no trigger in white, shots with brief 2,1 sawtooth components in black.

The two run day shots without 2,1 components had much lower β_N than the shot with 2,1 components as well as the DIII-D shots used in the original scaling. The run day shot with 2,1 sawtooth components resembled the tearing shots from the scaling, matching expectations that the given β_N values could induce the m, n = 2, 1 mode. While there was no long-lived 2,1 in the run day giant sawtooth shots, this may be related to the q profile, which is steeper in these shots than in the scaling. A steep q profile places the q = 1, q = 1.5, and q = 2 surfaces closer together, so the 1,1 kink of the sawtooth may have disturbed a 3,2 or 2,1 island and caused the island to dissipate. I also posit that limited power and lack of H-mode contributed to the failure of sawteeth to trigger tearing modes. Overall, the sawteeth were too far apart in the run day shots to trigger tearing modes.

Using the EFITs, I tracked the safety factor q throughout the sawtooth cycle to identify whether the sawteeth occurred with a m, n = 1, 1 mode as is typical. I again used shot

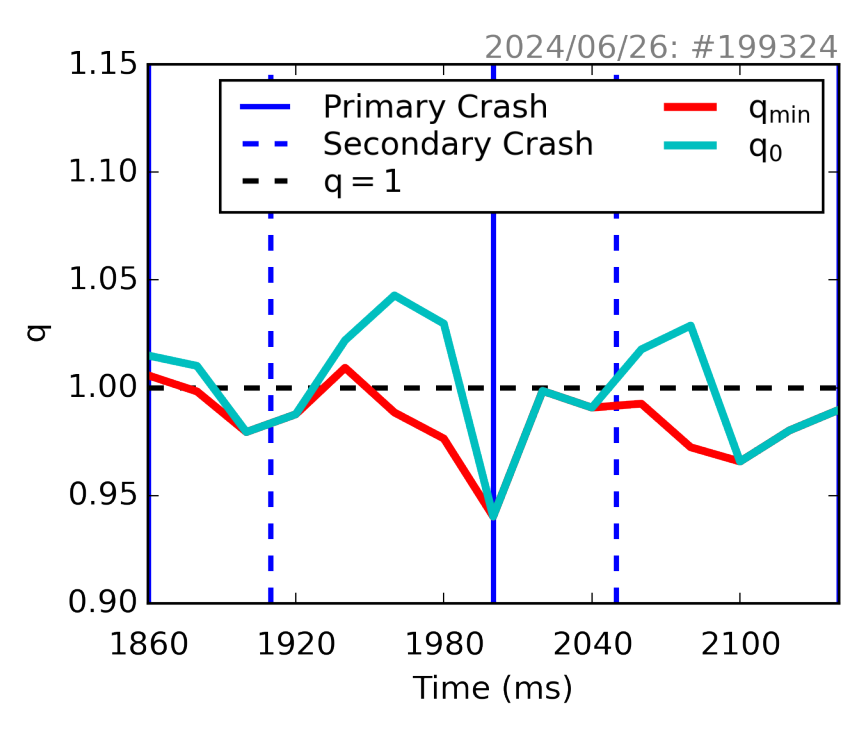


Figure 5.14: Minimum safety factor q_{min} (red) and central safety factor q_0 (cyan) during two compound sawtooth cycles in shot #199324. Solid blue line marks primary sawtooth crash, and dashed blue lines mark secondary crashes. Black dashed line marks q = 1.

#199324 for this study because of the strong sawtooth precursors and crash as well as the presence of compound sawteeth. One subject of study regarding compound sawteeth is the comparative strength in the q_{min} jumps between the primary and secondary sawteeth. I expected that there would be a clear shift from $q_{min} > 1$ to $q_{min} < 1$ around the start of the precursor and $q_{min} < 1$ to $q_{min} > 1$ at the crash for both the primary and secondary sawteeth. Instead, q_{min} jumped more than once and hover near 1; see Figure 5.14 for an example spanning two sawtooth cycles. The second primary crash and both secondary crashes were accompanied by $q_{min} < 1$, but this did not appear to be true for the first crash. Additionally, q_{min} stays low after the second secondary crash. The central shear of the q profile varies during the cycle, with negative shear leading to $q_0 > q_{min}$ for portions of the cycle. There is a greater association between $q_0 > 1$ and the inter-sawtooth period. This may mean that a transition from $q_0 > 1$ to $q_0 < 1$ is a stronger driver for sawteeth than a transition from $q_{min} > 1$ to $q_{min} < 1$.

5.4 Plasma Shape and Mode Detection

The other objective of the shaping experiment was to identify toroidicity, elongation, and triangularity effects in tearing mode amplitudes measured by RIP. Changes in vertical position to sweep the plasma across all three RIP chords were implemented to measure more of the mode structure, with the goal of sweeping across most of an island. I begin with examples from shot #199322, which contained a long-lived m, n = 3, 2 tearing mode, and shot #199328, which contained a long-lived m, n = 2, 1 tearing mode. Mode numbers for all these modes were available from sensing coil analysis, which also proved that the m, n = 3, 2 and 2,1 were tearing modes. Spectrogram and 2D mode structure overviews of these two shots are presented in Figure 5.15. Each has a mode of consistent frequency for the duration of the current flattop. Each tearing mode also had a harmonic at double frequency, which will not be studied in detail here. Both 2D mode structures are taken at t = 2000 ms, before the vertical jog. Both plasmas are modestly elongated, around $\kappa = 1.45$, with triangularities δ_u, δ_l around 0.1. The plasma shape does not change significantly after 2000 ms, the main period where mode amplitudes will be calculated, though there is some movement in boundary location. The inverse aspect ratio is taken in these models to be 0.3, a DIII-D-like value and the same as that used in Section 4.3 and is the maximum value achievable in TJ. Full toroidal sidebands are present.

The mode in #199322, which was also shown at its start in Figure 5.11(d-f), is localized to the core and is generally symmetric in r. The mode in #199328 is also localized and generally antisymmetric in r. Both contain visible toroidicity components, shown as distortions to the structure, and resonant surfaces at which the derivative of B_R is non-continuous. I integrate over these B_R structures to obtain a synthetic version of what RIP and the coils are expected to detect, and then I compare these to the actual ratio of RIP to coil amplitudes. Characteristics of the shot and TJ models for each are depicted in Table 5.3. The ideal wall is located at $b_w = r_{wall}/a$. I take $H_{j>3} = 0$ and $V_j = 0$ to match the experiment. This plasma is vertically symmetric.

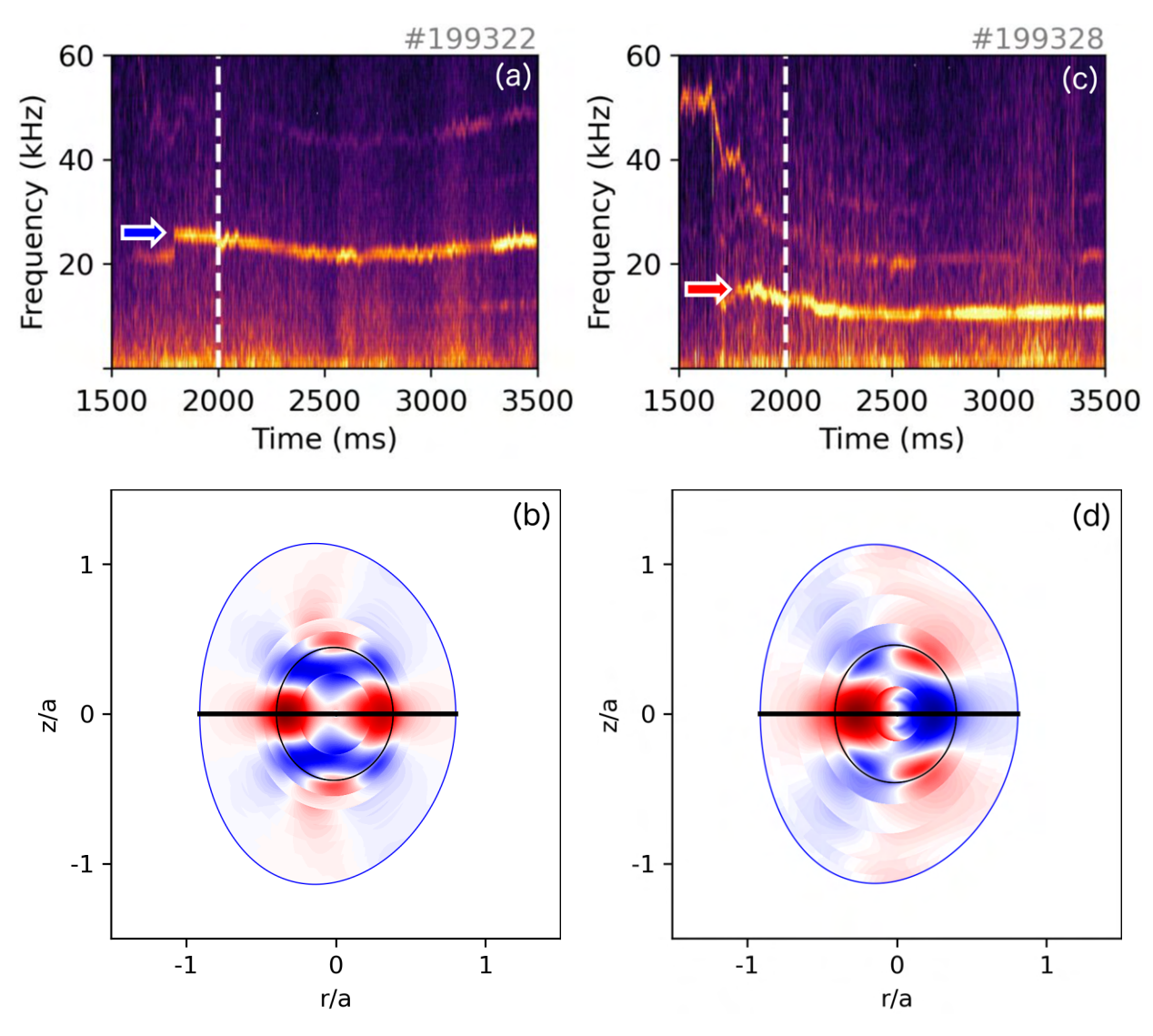


Figure 5.15: (a) Spectrogram and (b) 3,2 tearing mode B_R structure in TJ for shot #199322. (c) Spectrogram and (d) 2,1 tearing mode B_R structure in TJ for shot #199328. Primary modes in spectrograms marked with arrows: blue for 3,2 in #199322 and red for 2,1 in #199328. RIP position marked in structure with black horizontal line.

To track the amplitudes of toroidicity and elongation sidebands, I compare RIP and sensing coil mode amplitudes as in Chapter 4. I give an overview, with all experimental amplitudes, of the tearing modes in shots #199322 (3,2 mode) and #199328 (2,1 mode) throughout the current flattop (see Figure 5.1), when conditions have stabilized. The m, n = 3, 2 mode amplitude is shown in Figure 5.16(a) as a cross-power between the two channels at the same frequency. It is then compared to the amplitude from a single low-noise magnetic coil at the midplane, shown in Figure 5.16(b). The A and B RIP midplane channels have differing

199322; 3,2

Time (ms)	2000	2500	2825	3000	3175	3500
q	0.89-4.93	0.93-4.92	0.85-4.83	0.85 - 4.76	0.94-4.79	0.92-4.96
$H_{2,a}$	0.47	0.45	0.42	0.44	0.45	0.45
κ	1.4	1.39	1.36	1.36	1.38	1.39
$H_{3,a}$	0.08	0.09	0.09	0.09	0.09	0.09
b_w	1.38	1.33	1.35	1.37	1.39	1.36
$B_{ heta b}$	1.75	1.51	2.01	2.05	2.78	0.237

199328; 2,1

Time (ms)	2000	2500	2825	3000	3175	3500
q	0.95 - 5.95	0.91-6.03	0.85 - 5.88	0.86 - 5.83	0.94 - 5.86	0.98-6.14
$H_{2,a}$	0.45	0.41	0.4	0.4	0.4	0.42
κ	1.38	1.37	1.36	1.35	1.36	1.38
$H_{3,a}$	0.09	0.09	0.09	0.09	0.09	0.09
b_w	1.38	1.32	1.35	1.38	1.38	1.35
$B_{\theta b}$	4.80	5.46	6.62	7.22	6.80	7.32

Table 5.3: TJ parameters and $B_{\theta b}$ representing the plasma in shots #199322 and #199328.

magnitudes, but the measurements track together, so I use the cross-power spectral density to calculate a more accurate amplitude. The mode grows up gradually at the beginning of the period, indicating that it does not have a seed and is therefore classical as the DCON results from Section 5.3 indicate. Later, amplitudes with both diagnostics grow, but the mode has significant jumps on the RIP polarimetry, particularly near the end of the shot. There is also a short jump in RIP amplitude near 1900 ms, where the mode also jumps in frequency on all diagnostics. Since this jump is not reflected on the coils, that means that RIP is detecting some internal MHD activity far from the coils, possibly a nonlinear interaction. The RIP polarimetry amplitude is also subject to rapid changes from 1800–2000 ms. The density amplitude on both channels and the cross-power is shown in Figure 5.16(c).

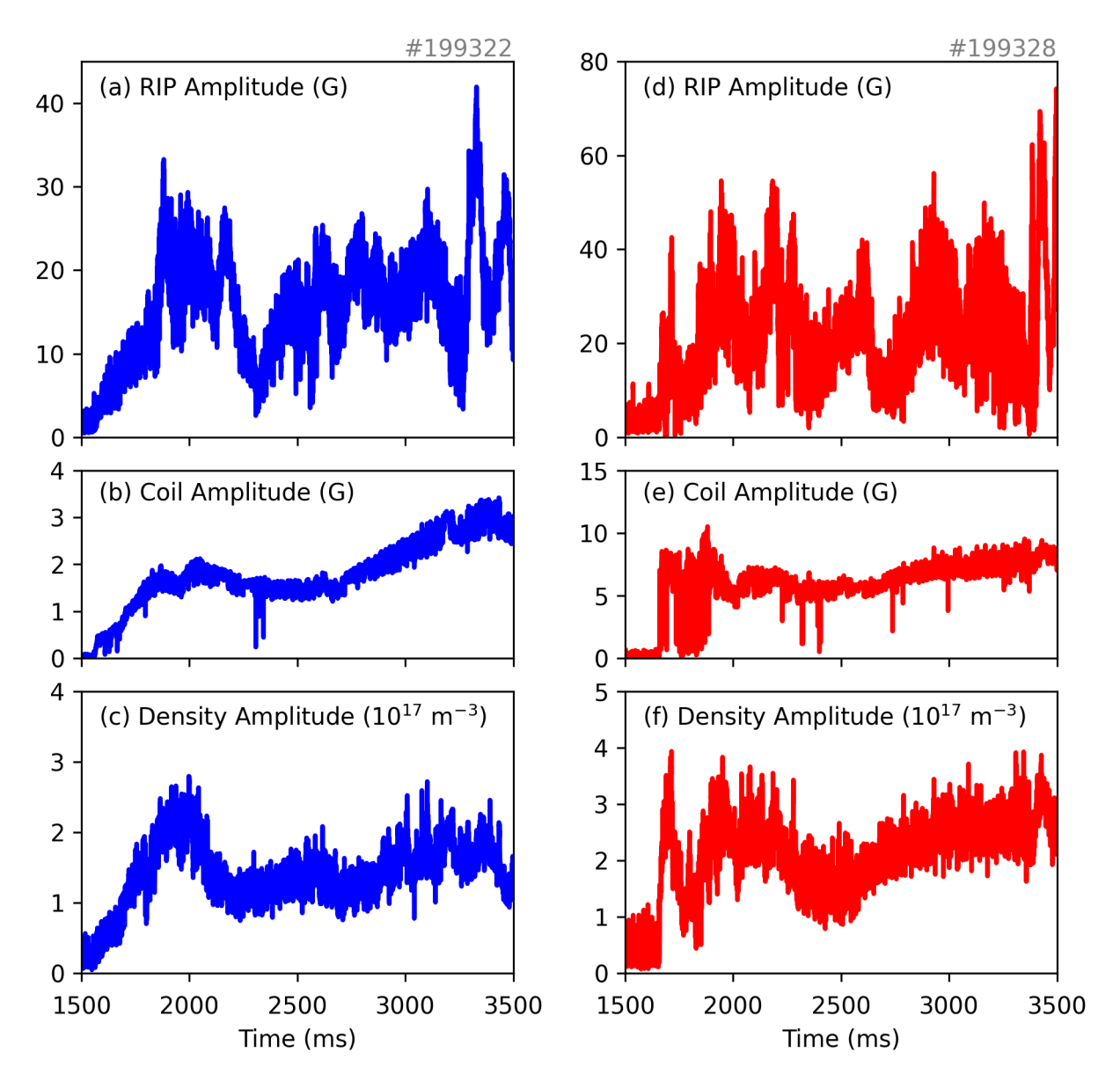


Figure 5.16: (a) 3,2 mode magnetic amplitude from midplane correlation polarimetry, (b) magnetic amplitude at edge on single low-noise midplane sensing coil, (c) and density amplitude from midplane correlation interferometry in shot #199322. (d–f) The same quantities for the 2,1 mode in shot #199328.

The uptick in the density data is less pronounced. There is significantly more variation in the RIP polarimetry amplitude than either the coil or the density.

I investigate possible reasons for the discrepancy between the amplitude tracks in time of the RIP and coil data, particularly the uptick around 1900 ms but also the rise in amplitude from 1800–2000 ms. I first consider the possibility that the mode grows in amplitude and

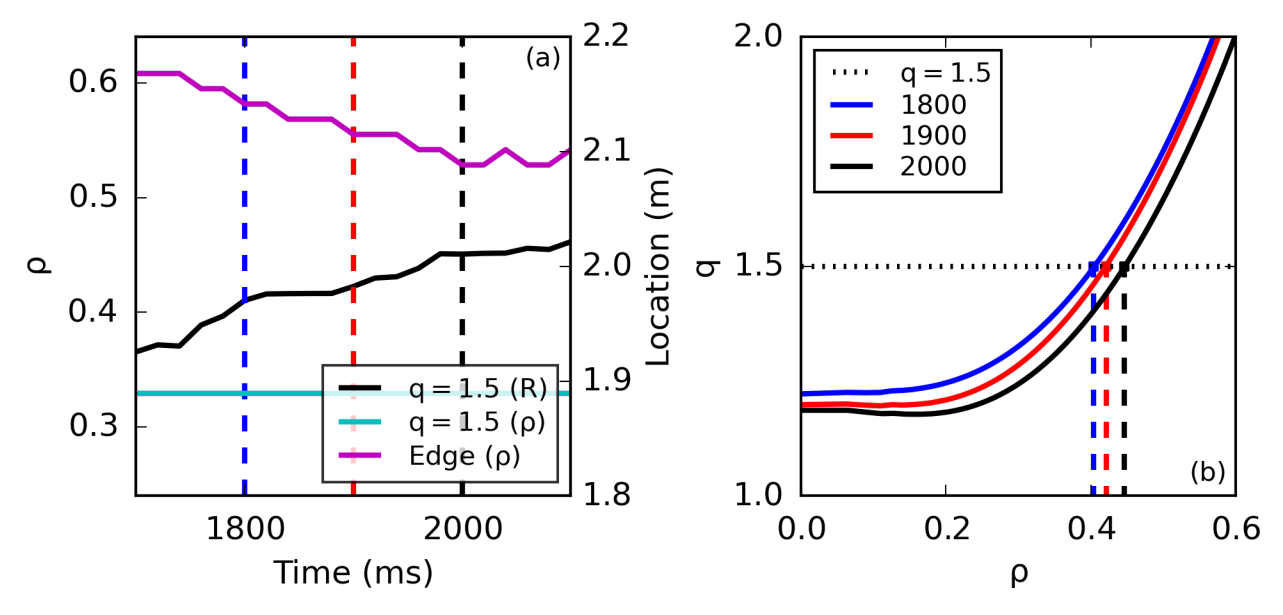


Figure 5.17: (a) Location in ρ of q=1.5 surface (cyan) and locations in R of q=1.5 surface (black) and plasma edge (magenta) in shot #199322. Dashed lines mark 1800 (blue), 1900 (red), and 2000 ms (black). (b) Safety factor profiles at 1800 (blue), 1900 (red), and 2000 ms (black). Dotted line marks q=1.5.

simultaneously moves away from the wall, leading to a relative reduction in coil amplitude relative to RIP that then cancels out with the mode growth. I measure proximity to the wall using the q profile to pinpoint the mode location in both ρ , the flux coordinate, and R, the major radial coordinate. All location and q profile measurements are derived from the kinetic EFITs previously discussed for shot #199322. Figure 5.17(a) depicts the location of the q = 1.5 surface (the tearing mode has m, n = 3, 2) in ρ and R from 1700–2100 ms along with the location of the plasma edge. Figure 5.17(b) plots the q profiles associated with the beginning, middle, and end of the window in ρ with respect to the q = 1.5 surface. The drop in edge R reflects that the plasma is being compressed to increase elongation. However, an overall drop in q means that the q = 1.5 surface remains stationary in R. The uptick in amplitude cannot be attributed to movement away from the coils. The window 1800–2000 ms is also associated with an n = 4 mode fading below the noise floor on RIP but not coils. An interaction between the n = 2 and n = 4 may have drawn energy toward the n = 2 mode. The n = 4 mode may also have shielded the coil from the n = 2 fluctuations.

Shot #199328 displays a dominant 2,1 mode with different dynamics but similar discrep-

ancies between RIP, coil, and density data. In shot #199328, all amplitudes jump noticeably when the mode begins rather than rising gradually. This does not rule out the existence of a seed for the mode. It cannot be determined whether this growth is linear, as expected of an NTM, or quadratic, as expected of a CTM. The density fluctuation amplitude is lowest at 2500 ms, when the magnetic axis is 10 cm above the midplane chord. Interferometry is detecting some structure in the core, inside a 10 cm radius that is equivalent to approximately $\rho = 0.25$. Coil amplitude changes much more smoothly than RIP polarimetry once again, and RIP has several jumps that interferometry does not detect. In both shots, either RIP is detecting internal structural changes that neither interferometry or the coil can detect (likely related to even/odd parity effects), or data quality is causing the changes.

After 2000 ms, the plasma is jogged up and down, from the midplane to 10 cm above the midplane and then down to 10 cm below the midplane before returning to the midplane at 4000 ms as Figure 5.1 shows. For an outboard minor radius of 55 cm (#199322, 2000 ms), this equates to $Z_c/a = \pm 18\%$. The two working chords sweep out a total of 33.5 cm during the jog, which is expected to cover most or all of a magnetic island. I measure the change in RIP magnetic amplitude over time, normalized to the amplitude on the sensing coils, and compare to the corresponding ratio in TJ: $\int B_R dR/B_{\theta,b}$. The relationship between the RIP/coil ratio and the TJ integral/edge ratio, which represents the same quantity with synthetic diagnostics, indicates the strength of nonlinear and higher-order effects on island structure.

I investigate the effect of mode number and even/odd parity on long-lived, steady 3,2 and 2,1 modes. First I directly compare the 3,2 in the steadiest tearing shot (#199322) with the 2,1 (#199328). I begin with the period 2000–2500 ms, where the plasma is rising from the midplane to 10 cm, i.e., the midplane chord is measuring from 0 cm to -10 cm below the magnetic axis. I investigate the symmetry of the mode by comparing this window to the window 3000–3500 ms, where the plasma is falling from 0 cm to -10 cm, i.e., the midplane chord is measuring from 0 to 10 cm above the magnetic axis. In a completely

vertical symmetric plasma, $\int B_R \, dR$ should be the same whether the chord is displaced above or below midplane. Prior to this point, this thesis has only described n > 1 modes. The sideband model encounters a special case in the n = 1 mode. When $q_{min} < 1$, a 1,1 sideband is present. The 1,1 sideband, which appears as a circular formation in the core of Figure 5.15, may contribute significantly to the measured amplitude of the 2,1 mode despite being attenuated by ϵ in the expansion. The 3,1 is also expected to play a role, though it would be detected more strongly by coils than the 1,1. Due to the strong toroidal sidebands, I expect a finite mode and relatively high amplitude and RIP/coil ratio for the 2,1 mode in shot #199328, compared to the 4,2 mode modeled in Chapter 4.

Since the plasma is up-down symmetric, I expect the amplitude to behave similarly when moving up and down from the midplane. For a 3,2 mode, I expect $\int B_R dR$ to be strongest at the midplane and for the ratio between the line integral and the edge coil amplitude, both in experiment and in TJ, to remain approximately the same when accounting for the location of the chord. Since $B_{\theta,b}$ is always measured at the midplane of the vessel, the TJ integrals are divided by B_{θ} at the end of the chord, which represents the vessel midplane for a jogged plasma. The difference between the values at the midplane between 2000 and 3000 ms, and at the top and bottom of the jog between 2500 and 3500 ms, is due to changes in the plasma parameters, most noticeably the q profile, that alter the location of the resonant surfaces. A comparison between the line-integrated B_R and edge B_θ , both in experiment (RIP and coils) and in TJ, for the 3,2 mode in shot #199322 is shown in Figure 5.18. I also consider an even-m mode, the 2,1 in shot #199328. TJ integrates over a function with the appropriate symmetry, so the ratios should be similar, but I expect the raw RIP values to be lower compared to the coil values in the cylindrical model. Figure 5.19 shows the same amplitudes and ratios for a 2,1 mode. In both cases, the TJ models correspond to the midplane and the beginning of the period.

The ratio of the RIP line-integrated value to the coil value ranges from approximately 2–15 for shot #199322, which is greater than for the 3,2 in other plasmas. Since the coil B_{θ}

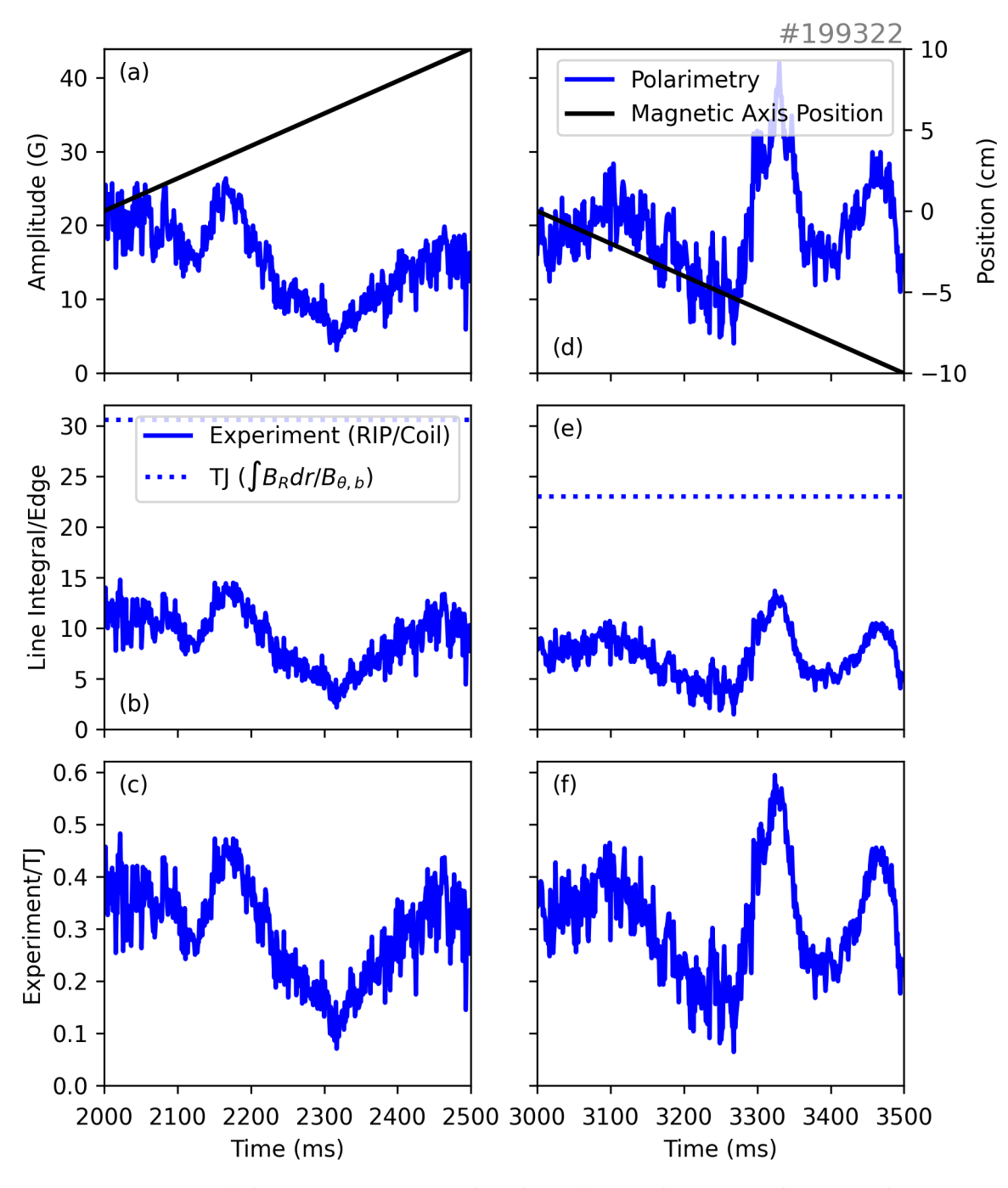


Figure 5.18: RIP midplane magnetic amplitudes, obtained via correlation polarimetry, for the 3,2 mode and relative magnetic axis position (black) from 2000–2500 ms. (b) Ratio of line-averaged B_R to $B_{\theta,b}$ in experiment (RIP/coils) and TJ. (c) Ratio of quantities in (b). (d–f) The same quantities for 3000-3500 ms.

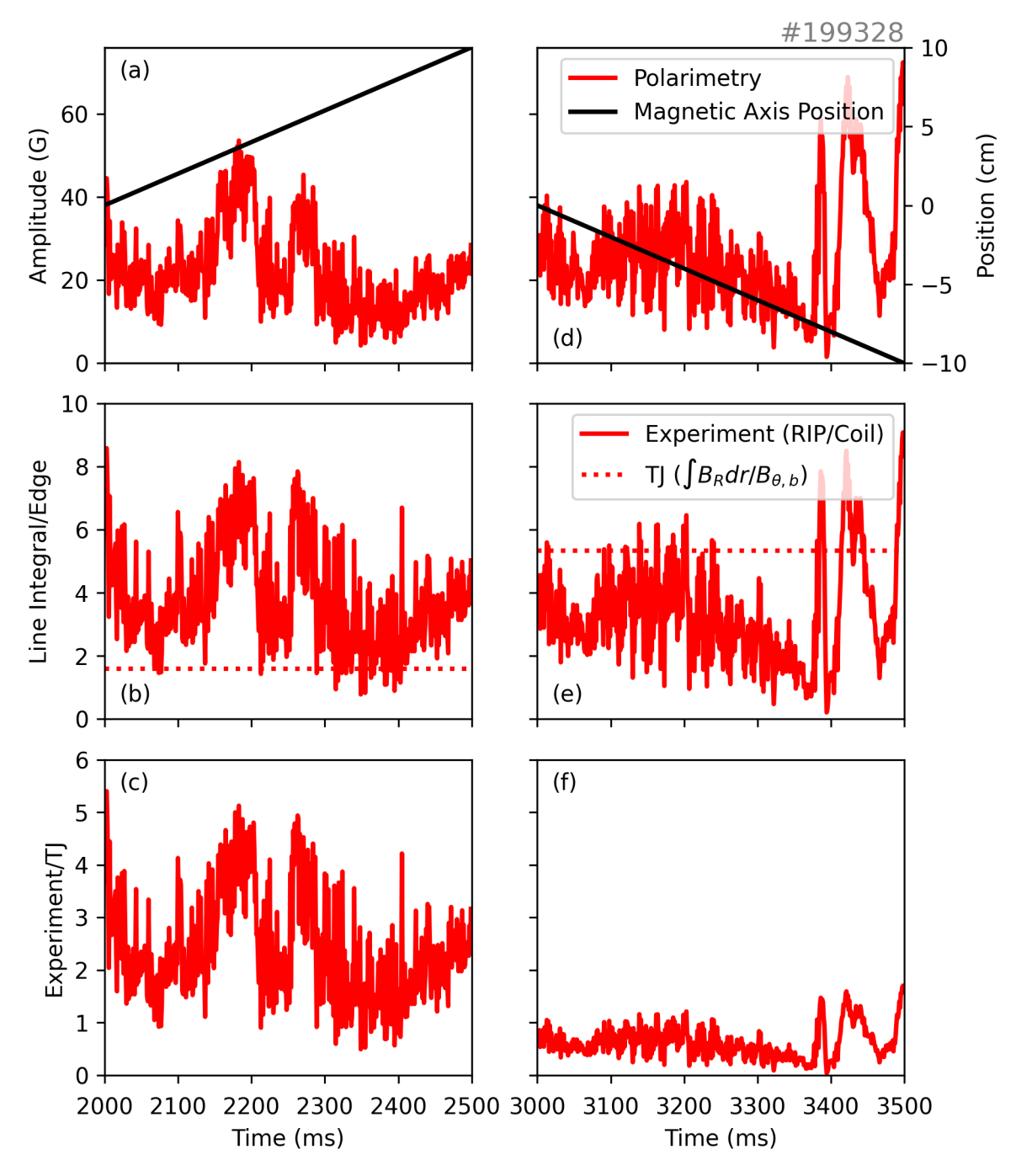


Figure 5.19: RIP midplane magnetic amplitudes, obtained via correlation polarimetry, for the 3,2 mode and relative magnetic axis position (black) from 2000–2500 ms. (b) Ratio of line-averaged B_R to $B_{\theta,b}$ in experiment (RIP/coils) and TJ. (c) Ratio of quantities in (b). (d–f) The same quantities for 3000-3500 ms.

measurement is very high for the 3,2 mode, the ratio between the RIP and TJ measurements is quite low, below 1, suggesting that there is some cancellation in the measurement from RIP. Recall that high elongation in shots such as #182771 produces significant $m \pm 2$ sidebands, which have odd m for odd-m modes and are therefore detectable. Due to comparatively lower elongation in #199322, these sidebands are less prominent and therefore may result in comparatively low RIP measurements at 2000 and 3000 ms, when the RIP midplane chord and magnetic axis coincide. Error in the q profile could move the chord back into the region of high B_R and bring the line-integrated coil amplitude closer to the RIP amplitude. There are significant jumps in the RIP magnetic amplitude during each window that are not attributable to the move off-midplane. It is likely that the major variation on RIP as the plasma moves is due to nonlinear effects. Recall that TJ only calculates harmonics for one n and does not include higher-order effects such as energy transfer, and that torque balance produces structure at the edge that may affect B_{θ} .

In the 2,1 case, $q_{min} < 1$ at all measurement times, so the 2,1 mode amplitude includes a 1,1 sideband. The exaggerated 1,1 sideband, along with the other toroidicity sideband m, n = 3, 1, results in a finite expected value for the line-integrated RIP value based on coils. Other sidebands such as 5,1, formed either by both toroidicity and elongation or by triangularity, are peaked in amplitude in a localized region and may also contribute to RIP but not coils. Combined, these effects result in similar RIP/coil ratios to the 3,2 mode. The 1,1 mode, nonlinear interactions between modes with different n, or error in the EFITs may contribute to the amplitudes. The RIP amplitude decreases as the plasma moves off midplane but jumps near the end of the period; this could be due to interaction with the 1,1 surface. In addition, the TJ-modeled integral/coil ratio rises significantly between 2000 ms and 3000 ms despite the plasma being at the same position with respect to the midplane. The 1,1 mode may be contributing to TJ more strongly here as well, since the RIP amplitudes do not change drastically. Early in the shot, RIP is stronger than TJ would indicate, suggesting that RIP picks up a structure TJ does not, such as a very large island, or the TJ edge value

is too large, as already demonstrated for the TJ model of shot #182771 in Chapter 4. Later, the experiment/TJ ratio at less than 1 but a significant fraction thereof matches the 3,2 mode relatively well, suggesting consistency between the TJ models for both shots.

I also compare amplitudes of the same mode between chords where the plasma location with respect to each chord is the same. For example, at 2500 ms, the plasma is at Z=10cm, 10 cm above the midplane chord. At 3175 ms, the plasma is at Z=-3.5 cm, 10 cm above the lower chord. The midplane chord from 2500–2825 ms is at the same plasma location as the lower chord from 3175–3500 ms. The midplane chord amplitude at 2500 ms and the lower chord amplitude at 3175 ms are therefore analogous, and the relationship between RIP and coil data is expected to be similar. Once again, the TJ models and ratios correspond to the beginning of the period. The RIP amplitudes for each chord, at the time the plasma is descending from 10 cm to 3.5 cm above that respective chord, are shown in Figure 5.20(a) (midplane) and (d) (lower) for #199322 and Figure 5.21 (a) (midplane) and (d) (lower) for #199328. Plots (b) and (e) show the modeled line-integrated amplitude from TJ, normalized to the mode amplitude on the coils. Plots (c) and (f) show the ratio between the RIP and coil amplitudes. Once again, the RIP amplitudes are variable while the coil amplitudes are relatively steady in time. The RIP to coil amplitude ratios are similar in both periods. In shot #199322 for the 3,2 mode, the RIP results are much greater than the results from Figures 5.18, and TJ measures a very low value.

In #199328, the RIP/coil and experiment/TJ ratios are more similar to Figure 5.19. Both chords show similar ratios, to within the same order for the same relative magnetic axis position, indicating a consistent trend in linear mode structure. At 2500 and 3500 ms in shot 199322, the midplane chord lies in a region of low B_R in TJ, meaning that the line integral/coil ratio for TJ is drastically lower than for the experiment (RIP and coils), and the experiment/TJ ratio is higher. The chord has moved off the island. In #199328, the chord is still detecting the island, which is larger than that for the 3,2. This is unexpected because the 1,1 sideband, which would be detected by RIP but less so by coils due to its

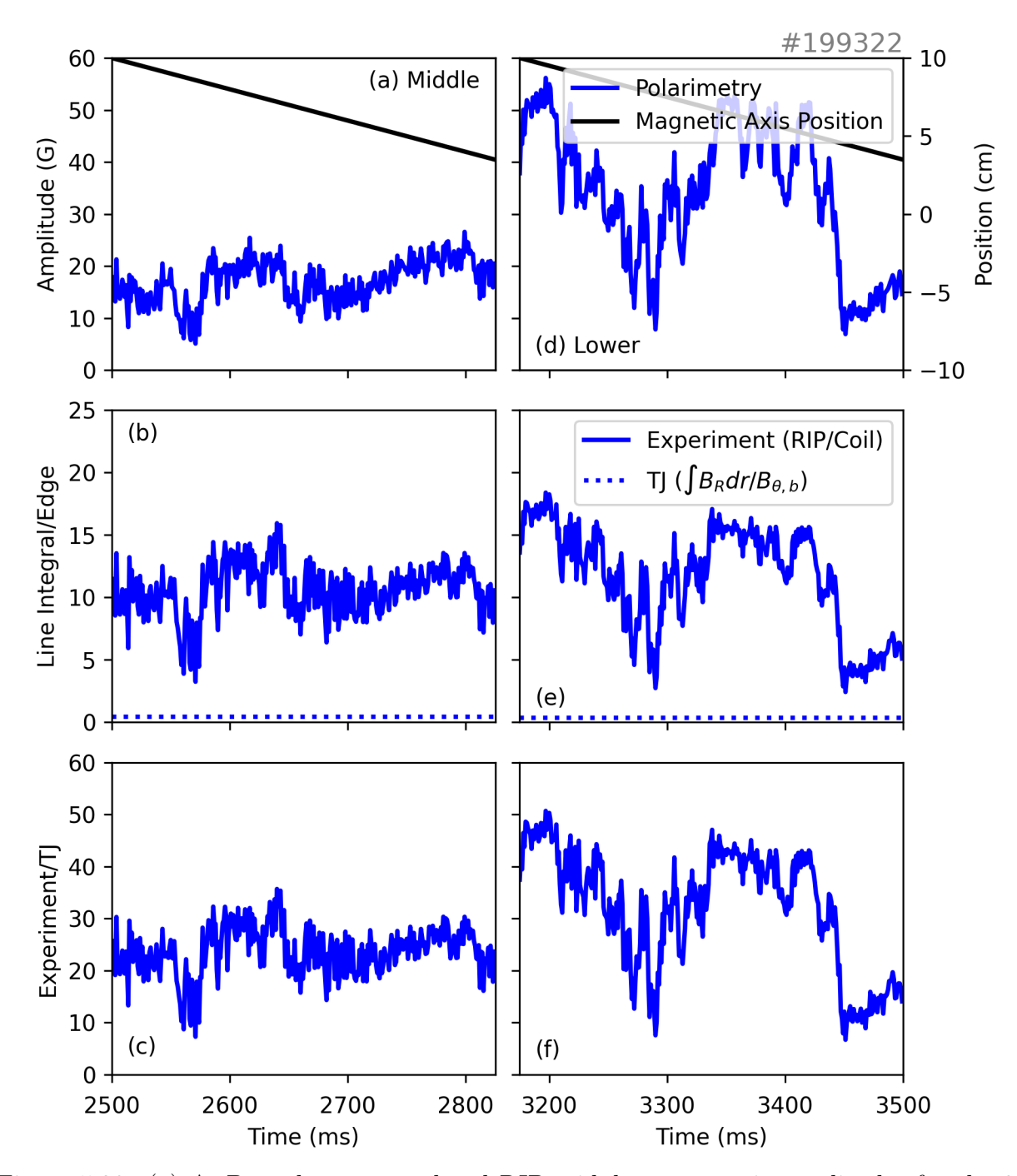


Figure 5.20: (a) A, B, and cross-correlated RIP midplane magnetic amplitudes for the 3,2 mode and relative magnetic axis position (black) from 2500–2825 ms. (b) Line-integrated synthetic coil amplitudes from TJ for the TJ value at the beginning (dotted) and end (solid) of the window. (c) Ratio between RIP and coils for both TJ values. (d–f) The same plots for the lower chord, 3175–3500 ms.

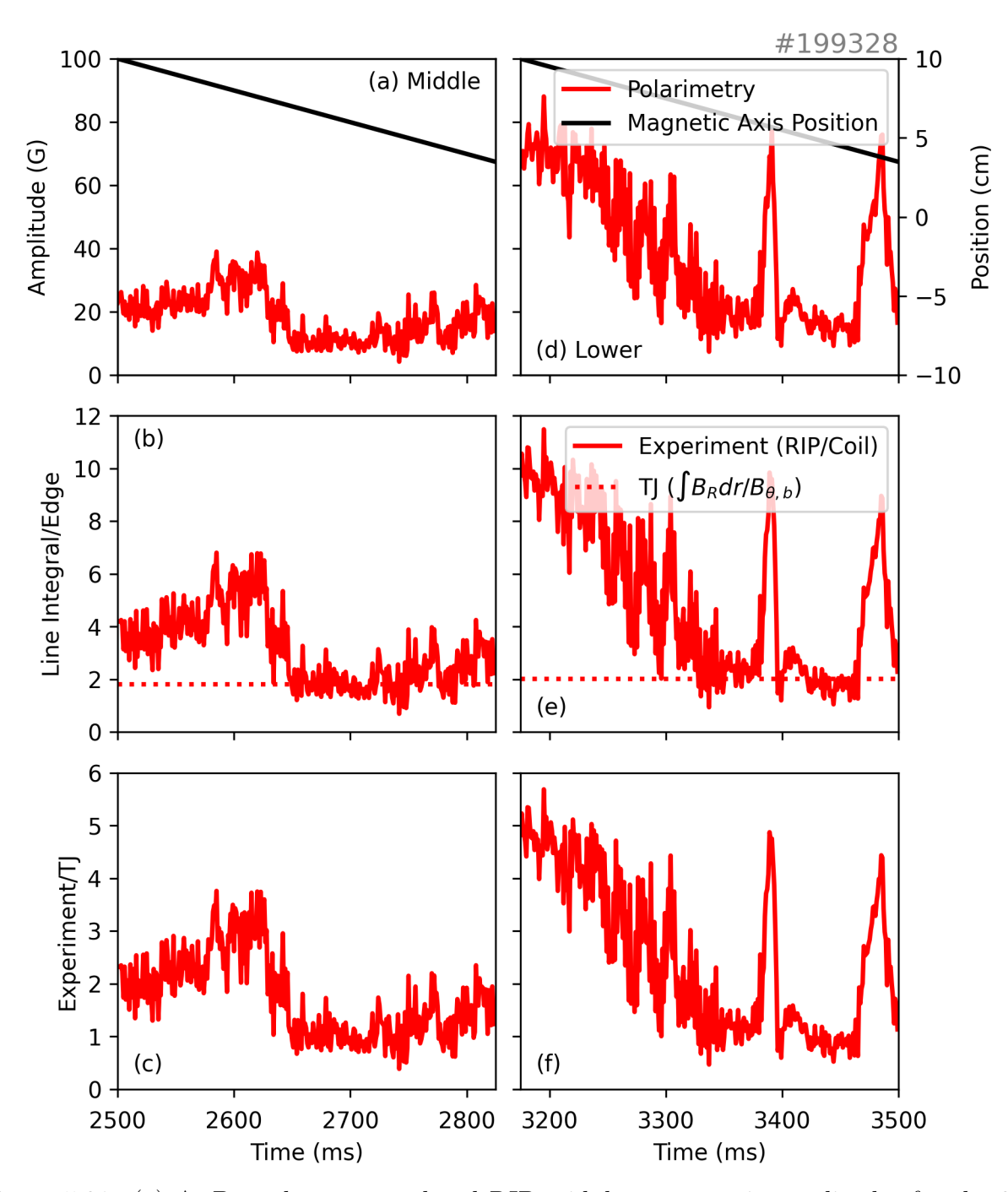


Figure 5.21: (a) A, B, and cross-correlated RIP midplane magnetic amplitudes for the 2,1 mode and relative magnetic axis position (black) from 2500–2825 ms. (b) Line-integrated synthetic coil amplitudes from TJ for the TJ value at the beginning (dotted) and end (solid) of the window. (c) Ratio between RIP and coils for both TJ values. (d–f) The same plots for the lower chord, 3175–3500 ms.

core localization and therefore be a large contributor to RIP, is closer to the core than the 3,2 surface. The 3,1 sideband appears to be dominating instead. The RIP amplitudes and corresponding RIP/coil ratios do not have a clear association with the location of the magnetic axis, indicating nonlinear effects on both chords as the magnetic axis, and therefore the modes, pass each chord. The spikes in the lower chord data indicate sudden bursts of signal, possibly related to radiation bursts visible on the spectrogram and also to a reduction in ELM dither.

Bibliography

- [1] L. L. Lao et al. "Equilibrium analysis of current profiles in tokamaks". *Nuclear Fusion* 30.6 (1990), p. 1035.
- [2] A. H. Glasser. "The direct criterion of Newcomb for the ideal MHD stability of an axisymmetric toroidal plasma". *Physics of Plasmas* 23.7 (2016), p. 072505.
- [3] L. Bardóczi et al. "Empirical probability and machine learning analysis of m, n = 2, 1 tearing mode onset parameter dependence in DIII-D H-mode scenarios". Physics of Plasmas 30.9 (2023), p. 126052.
- [4] R. J. La Haye. "Neoclassical tearing modes and their control". *Physics of Plasmas* 13.5 (2006), p. 055501.
- [5] M. D. Pandya et al. "Early internal detection of magnetic tearing and implications for tokamak magnetohydrodynamic stability". *Physics of Plasmas* 31.7 (2024), p. 070706.
- [6] N. J. Richner et al. "Use of differential plasma rotation to prevent disruptive tearing mode onset from 3-wave coupling". *Nuclear Fusion* 64.10 (2024), p. 106036.
- [7] O. Sauter. "Geometric formulas for system codes including the effect of negative triangularity". Fusion Engineering and Design 112 (2016), pp. 633–645.
- [8] J. Chen, W. X. Ding, and D. L. Brower. "Impact of the Cotton-Mouton effect on Faraday polarimetry measurements using circular polarization". *Plasma Physics and Controlled Fusion* 60.8 (2018), p. 085001.
- [9] O. Gruber et al. "Vertical displacement events and halo currents". Plasma Physics

- and Controlled Fusion 35.SB (1993), B191.
- [10] R. Ding et al. "Advances in understanding of high-Z material erosion and re-deposition in low-Z wall environment in DIII-D". Nuclear Fusion 57.5 (2017), p. 056016.
- [11] R. J. Fonck, A. T. Ramsey, and R. V. Yelle. "Multichannel grazing-incidence spectrometer for plasma impurity diagnosis: SPRED". Applied Optics 21.12 (1982), pp. 2115–2123.
- [12] P. C. de Vries et al. "Survey of disruption causes at JET". Nuclear Fusion 51.5 (2011),p. 053018.
- [13] W. W. Heidbrink and G. Sager. "The fishbone instability in the DIII-D tokamak".

 Nuclear Fusion 30.6 (1990), p. 1015.
- [14] E. Neill et al. "Investigation of Instabilities During Nonstandard Sawtooth Periods in the DIII-D Tokamak". APS Division of Plasma Physics Meeting Abstracts. Vol. 2024. 2024, CP12–119.
- [15] K. H. Burrell et al. "Confinement physics of H-mode discharges in DIII-D". *Plasma Physics and Controlled Fusion* 31.10 (1989), p. 1649.
- [16] E. Parke, W. X. Ding, and D. L. Brower. "Correlation polarimetry for broadband magnetic fluctuation measurements". Review of Scientific Instruments 89.10 (2018), 10B112.
- [17] C. E. Bush et al. Characteristics of the TFTR Limiter H-mode: The transition, ELMs, transport and confinement. Tech. rep. Princeton Univ., NJ (United States). Plasma Physics Lab, 1992.
- [18] H. Zohm. "Edge localized modes (ELMs)". Plasma Physics and Controlled Fusion 38.2 (1996), p. 105.
- [19] D. P. Brennan et al. "Tearing mode stability studies near ideal stability boundaries in DIII-D". *Physics of Plasmas* 9.7 (2002), pp. 2998–3006.

- [20] F. Turco et al. "Sensitivity of transport and stability to the current profile in steady-state scenario plasmas in DIII-D". *Physics of Plasmas* 19.12 (2012), p. 122506.
- [21] B. B. Kadomtsev. "Disruptive instability in tokamaks". Fizika plazmy 1 (1975), pp. 710–715.
- [22] R. J. Hawryluk. "An empirical approach to tokamak transport". *Physics of Plasmas Close to Thermonuclear Conditions*. Elsevier, 1981, pp. 19–46.
- [23] H. Yamada, K. McGuire, D. Colchin, et al. Compound sawtooth study in ohmically heated TFTR plasmas. Tech. rep. Princeton Plasma Physics Laboratory, 1985.
- [24] I. T. Chapman et al. "Empirical scaling of sawtooth period for onset of neoclassical tearing modes". *Nuclear Fusion* 50.10 (2010), p. 102001.

Chapter 6

Detection and Role of Nonlinear Coupling in QH-Mode Development

Fluctuations of all kinds can interact with each other nonlinearly in both unmagnetized fluids and plasmas. Nonlinear coupling governs fluid and plasma behavior at scales ranging from microturbulence to systemic flows. In fusion configurations including the reversed-field pinch [1–4] and tokamaks [5, 6], interactions between fluctuations are often fundamental to system dynamics. They can seed other tearing modes or form large-scale coherent structures. As discussed in Section 2.4, nonlinear coupling is measured using bicoherence analysis. Here, I apply bicoherence of RIP data in quiescent H-mode (QH-mode) to detect two macroscopic nonlinear coupling mechanisms not previously seen in experiment. Section 6.1 outlines the characteristics of QH-mode¹. It also describes the importance of coupling in maintaining the edge harmonic oscillation (EHO), which has been predicted experimentally, and the discovery of which forms the first part of this chapter. In Section 6.2, I detail bicoherence analysis, which is used to measure nonlinear coupling strength. In Section 6.3 I observe nonlinear coupling of the EHO to core-resonant tearing modes, the first time coupling has been observed between coherent modes in the core and edge. Section 6.4 details the detec-

¹Sections of this chapter are reproduced from a manuscript submitted to Physical Review Letters and talks given at the 2023 and 2024 Workshops on MHD Stability Control.

tion, using RIP, and identification of a returning EHO in post-QH ELMy H-mode. Lastly, Section 6.5 demonstrates that coupling to tearing modes interrupts coupling between the edge harmonics, resulting in their desaturation and the return of ELMs. While coupling of EHO harmonics is measured with multiple diagnostics, EHO coupling to tearing modes is measured internally with RIP but not detected on external magnetic sensing coils.

6.1 QH-Mode and the EHO

Recall from Chapter 1 that H-mode is a high-confinement regime sustained by a steep temperature and density gradient, called the pedestal, at the edge. The gradient is maintained by a transport barrier that reduces particle and energy loss from the plasma at the edge. However, the pedestal gradient provides free energy to ELMs. Damage caused by ELMs to system components will likely be prohibitive in a reactor. In addition, ELMs can trigger tearing modes that cause the plasma to disrupt. To prevent these events, advanced scenarios and control mechanisms to avoid ELMs are being investigated. This section discusses QH-mode, one attractive ELM-free scenario candidate. QH-mode maintains the H-mode temperature and density pedestal without ELMs and is marked by external and, typically, internal transport barriers [7, 8]. Tearing modes are rare in QH-mode due to the typically high safety factor value, but core-resonant tearing modes sometimes occur [9].

This quiescent state is maintained by the EHO, which is a saturated, continuous edge magnetic fluctuation. The EHO, similarly to other magnetic modes, causes density and temperature fluctuations by modifying temperature and pressure gradients [10]. It is non-sinusoidal, so in Fourier analysis it does not reduce to a single component. Though it is a coherent oscillation, it appears as a superposition of components, which due to the coherent structure are harmonics of a single fundamental frequency. Typically, the fundamental has n = 1 or n = 2 [11]. On average, the EHO induces faster particle transport across the separatrix than ELMs, ensuring density control while thermal confinement remains high [11]. If the EHO disappears, ELMs and the standard H-mode can return as edge transport weakens, and the pedestal density rises [12]. Linear modeling [13–16] and experiments [17] have

validated the saturated EHO as an external kink-peeling mode, driven by current gradients in the pedestal and distinct from the peeling-ballooning ELM [16]. The EHO is strongest at the pedestal top and drops off in amplitude toward the last closed flux surface [18].

Experimentally, the EHO arises at low collisionality and high rotation shear at the edge [19]. Typically, this high shear results from high toroidal rotation, though it can also be induced by applied nonresonant magnetic perturbations [20]. Whenever both **E** and **B** fields are present in a plasma, particles drift in the $\mathbf{E} \times \mathbf{B}$ direction [21], which results in a rotation. The $\mathbf{E} \times \mathbf{B}$ rotation shearing rate, $\omega_{\mathbf{E} \times \mathbf{B}}$, inside the E_r well at the pedestal is the primary driver of the EHO [22]. A critical value of $\mathbf{E} \times \mathbf{B}$ shear is required to sustain and saturate the EHO in experiment; this is linked to destabilization of low-n (n = 0 - 10) ideal modes and stabilization of higher-n modes [19]. If the shear is below the threshold, the EHO desaturates [23]. Linear eigenvalue analysis and nonlinear simulations with JOREK have also found that $\mathbf{E} \times \mathbf{B}$ shear is important in EHO saturation [24–26]. If the EHO disappears, ELMs and the standard H-mode can return as edge transport weakens and the pedestal density rises [12]. The back-and-forth transition from EHO (QH-mode) to ELMs (H-mode) can occur repeatedly [23]. The $\omega_{\mathbf{E} \times \mathbf{B}}$ threshold for the QH-H transition is the same as that for the H-QH back-transition [23, 27]. A steady EHO is vital to re-establishing sustained QH-mode.

Nonlinear magnetohydrodynamic simulations [24, 25, 28–32] of the edge harmonic oscillation (EHO) in DIII-D [33] and other tokamaks describe EHO saturation by nonlinear coupling. Several kink-peeling harmonics grow linearly at first, with $n \geq 4$ dominating and pressure-driven ballooning as the primary driver of instability. In this model, nonlinear coupling between the higher harmonics transfers energy in an inverse cascade to the three lowest-n harmonics ($n \leq 3$, or $n \leq 6$ when even n dominate), which saturate and sustain the oscillation [25, 28–30]. The steady lower-n harmonics form a sustained edge oscillation, the EHO. This is reminiscent of other large-scale coherent structures formed by nonlinear coupling, such as zonal flow. Large-scale zonal flow, has a profound impact on transport processes, exemplified in the atmospheres of Earth and the gaseous giant planets. Zonal flow

in magnetically confined fusion plasmas, reduces heat and particle transport to help make fusion conditions accessible [34]. In the case of the EHO, the large magnetic fluctuation component enables particle transport across the H-mode transport barrier [35]. Zonal flows are maintained by $\mathbf{E} \times \mathbf{B}$ shear through both Kelvin-Helmholtz instability mitigation and decorrelation of turbulent eddies [34, 35]. The same appears to be true of the EHO, where the two processes suppress the peeling-ballooning ELM [26, 29, 36].

In simulations directly replicating coupling within the EHO [29], the summed bicoherence between each mode and all other modes increased between the linear growth and nonlinear saturation phases, indicating that coupling strengthened. In other simulations where bicoherence was not calculated explicitly [25], energy still flowed from higher to lower n. The lower-n harmonics i.e., the kink-peeling modes, retained the energy transferred to them by the higher-n harmonics and dominated throughout the remainder of the simulation. Both papers were related to DIII-D results. The former used DIII-D-like radial electric field profiles in the BOUT++ framework [37], and the latter used JOREK [38] to simulate the EHO directly in an experimental DIII-D equilibrium. In both cases, nonlinear coupling and EHO saturation emerged spontaneously when several mode numbers were included. When nonlinear coupling was restricted, higher harmonics remained dominant, and the coherent EHO did not form. If the lower harmonics desaturated, the higher-n harmonics gained energy, dominating again, and the EHO desaturated [25]. The lowest frequency, or fundamental, similarly saturated in a simulated ITER plasma, but the inverse cascade was incomplete [25]. The lack of energy transfer restricted the maximum amplitude of the lower frequencies and hampered particle transport, demonstrating the importance of the nonlinear cascade. The modeled nonlinear coupling between the EHO's harmonics [25, 29] has not until now been confirmed experimentally.

6.2 Bicoherence Analysis

The bispectrum of three components of frequencies $f_1, f_2, f_1 + f_2$ in a single signal is the two-dimensional analogue of the power spectral density for a single frequency. It is the product of the Fourier transforms of the three components: $B(f_1, f_2) = F(f_1)F(f_2)F^*(f_1 + f_2)$, where F^* is the conjugate. However, the bispectrum cannot account for phase, since it is a product of transforms over an entire time window. It is also not normalized, so a strong component that is weakly coupled still produces a strong bispectrum. Both of these issues are solved using the bicoherence, or normalized bispectrum. Small time samples covering the period where the bispectrum would be calculated are ensemble-averaged:

$$b^{2}(f_{1}, f_{2}) = \frac{|\langle F_{j}(f_{1})F_{j}(f_{2})F_{j}^{*}(f_{1} + f_{2})\rangle_{j}|^{2}}{\langle |F_{j}(f_{1})F_{j}(f_{2})|_{j}^{2}\rangle\langle |F_{j}^{*}(f_{1} + f_{2})|_{j}^{2}\rangle}$$
(6.1)

where F_j are the Fourier transforms of each time series, and angle brackets represent averaging over samples. To understand how ensemble-averaging includes the effect of phase, consider a case where components f_1 , f_2 are present in a signal along with a component at $f_1 + f_2$. If $f_1 + f_2$ is always in phase with f_1 and f_2 , then $F_j(f_1)F_j(f_2)F_j^*(f_1 + f_2)$ always has the same value when normalized. However, if $f_1 + f_2$ is always out of phase or always tangential to f_1 and f_2 , then the $F_j(f_1)F_j(f_2)F_j^*(f_1+f_2)$ still add to a finite value, that then normalizes to 1, because all samples add rather than subtract. The waves are still correlated but have locked with a constant offset. For the bicoherence to drop below 1 or equal zero, $f_1 + f_2$ must be uncorrelated to some degree with f_1 and f_2 . Uncorrelated modes entail a random phase for at least one component such as might be found with noise or with multiple modes at the same frequency. In this case, successive components of the ensemble average cancel, and the remaining bicoherence is insignificant when normalized.

Note that bicoherence is symmetric over exchange of f_1 and f_2 : the coupling at (f_1, f_2) equals the coupling at (f_2, f_1) . Bicoherence is normalized such that $b^2 = 1$ represents perfect phase locking. The nonlinear coupling of the triplet represented by (f_1, f_2) is statistically significant if $b^2(f_1, f_2)$ is above the 99% significance value, which for ensemble sample size N is 9.2/(2N) [39]. Bicoherence can also be calculated for the space f < 0 in the Fourier transform, since for real signals $F(-f) = F^*(f)$. When a coupling (f_1, f_2) is present, couplings at $(f_1 + f_2, -f_2)$ and $(f_1 + f_2, -f_1)$ are also present. Coupled modes are expected to be visible

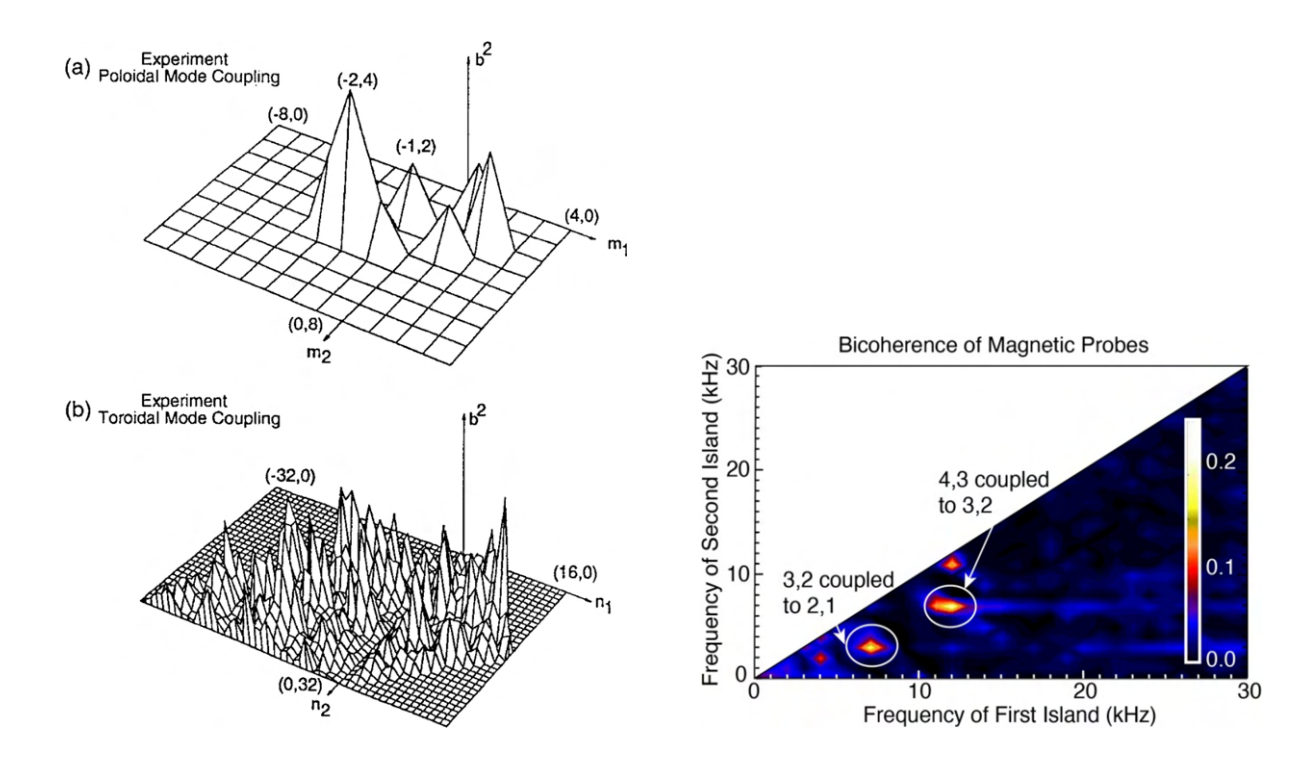


Figure 6.1: Left: Plots of bicoherence in MST magnetic probe data averaged over an ensemble of sawtooth crashes, with signals classified by mode number. (a) shows bicoherence with respect to m_1, m_2 . (b) shows bicoherence with respect to n_1, n_2 . Reproduced from [2]. Right: A plot of bicoherence in DIII-D magnetic probe data during a case of multiple coupled tearing modes. Bright spots represent coupling of modes at the given frequencies. Adapted from [40].

at both positive and negative frequencies. Modes can couple to themselves, producing a coupling with frequency triplet (f, f, 2f) and negative-frequency equivalent (2f, -f, f).

Bicoherence is usually represented as a two-dimensional height or color plot, with the frequencies f_1 and f_2 on the x and y axes [1, 2, 6]. The color or height of the plot at (f_1, f_2) marks the bicoherence strength at that point. If mode numbers are easily identifiable, (m_1, m_2) or (n_1, n_2) may be used instead. Figure 6.2 gives two examples of bicoherence plots. Figure 6.2(a-b) were taken in the Madison Symmetric Torus (MST) reversed-field pinch (RFP) and highlight negative-frequency space. Figure 6.2(c) was taken on DIII-D and highlight color bicoherence plots in frequency. In (a-b), negative mode numbers represent the negative-frequency space in the Fourier transform in the same way that negative frequency space does. Note the wide spectrum of finite bicoherence in (b) due to the complexity of the

coupling during an RFP sawtooth. Also note the negative coupling (-2, 4) alongside the positive coupling (2, 2). The right plot demonstrates coupling of coherent tearing modes at 4 kHz (m, n = 1, 1 and 2, 1), 7 kHz (3, 2), and 11 (4, 3) kHz. The finite bicoherence at these frequency pairs represents interactions between the modes whose frequencies are marked on the axes and their sum. (11, 7) is a coupling between the 4,3; the 3,2; and another mode at 18 kHz. (7, 4) is a coupling between the 3,2; the 2,1; and the 4,3 at 11 kHz.

6.3 Nonlinear Coupling Between Edge Harmonics

The analysis shown in this section derives from a single DIII-D discharge, an overview of which is shown in Figure 6.2. Other DIII-D plasmas that enter QH-mode (at least eleven shots in the database that have a robust EHO and the necessary diagnostic complement for the analysis reported here) also exhibit nonlinear coupling within the EHO. All database shots that contained EHO exhibited some coupling between EHO components. EHOs that were less robust demonstrated weaker coupling at the EHO frequencies, relative to the statistical significance level, than robust EHOs.

The plasma parameters are designed to produce QH-mode, with plasma current $I_p = 1.1$ MA in the reverse direction, toroidal magnetic field $B_t = 2$ T in the standard direction, and maximum injected neutral beam power of 7 MW. Neutral beam injection was in the counter- I_p direction, as is more often used in QH-mode and and which was the original beam configuration in which QH-mode was discovered [7, 11]. Both injection directions are viable for QH-mode [41], but as of now the counter- I_p direction is better studied. All available beams were used to ensure high power with long duration. The 150 beamline, which can be tilted off-axis, was placed on axis; all beams injected into the core. Plasma shape was ITER-similar. #184791 was the first shot of the day, intended to produce robust QH-mode using proven experimental parameters [42].

Figure 6.2(a–b) show spectrograms of magnetic fluctuations measured by the RIP midplane chord and a low-noise midplane magnetic sensing coil. Figure 6.2(c) shows a spectrogram of density fluctuations measured by a BES channel viewing the plasma at the outboard midplane and normalized radial coordinate $\rho = 0.92$, situated near the pedestal top. The first three harmonics of the coherent EHO are evident around 17 kHz, 34 kHz, and 51 kHz. The absence of deuterium-alpha emission (D_{α}) [43] spikes in Fig. 6.2(d) in this window indicates lack of ELMs. I conclude that the observed fluctuation is the EHO, as it consists of multiple harmonics, occurs during H-mode without ELMs, and produces local density fluctuations in the pedestal as shown in Figure 6.2(c).

QH-mode with a persistent EHO lasts until around 1800 ms, marked by another dashed line, when a programmed shape change is imposed, marked by another dashed line. The gap between the outboard plasma boundary and wall was reduced, which was intended to be compatible with QH-mode. Controls are held constant afterwards. There is then a quiet period until ELMs appear around 2100 ms, marked by a dotted line. Several tearing modes and an intermittent mode at 22 kHz are visible with RIP. As shown later, the 22 kHz intermittent mode is a returning EHO. One tearing mode is visible on the coils, and the EHO is visible faintly on a few coils. The electron density pedestal height, measured using Thomson scattering [44], remains constant during QH-mode and rises when the EHO dissipates; see Figure 6.2(d). Figure 6.2(d) also shows spikes in divertor D_{α} emission due to ELMs starting around 2100 ms.

I calculate using experimental data the nonlinear coupling between the three lowest harmonics of the EHO using bicoherence analysis. Between 1100–1800 ms, as shown in Fig. 6.2, the EHO fundamental frequency varies gradually in time between 17–19 kHz, with second harmonic 34–38 kHz, and third harmonic 51–57 kHz. I henceforth identify each harmonic by its minimum frequency. The toroidal mode numbers of the harmonics are n=2,4,6, measured by Fourier analysis of the sensing coil array data. Fig. 6.3(a) shows the evolution of the bicoherence between the EHO fundamental and the harmonics, calculated from RIP data. Each 50 ms time step represents an ensemble of 100 segments of length 0.5 ms. The 99% significance level is 0.046, indicated with a red dashed line. The bicoherence at (34,17) is statistically significant the entire time between when the EHO appears until it

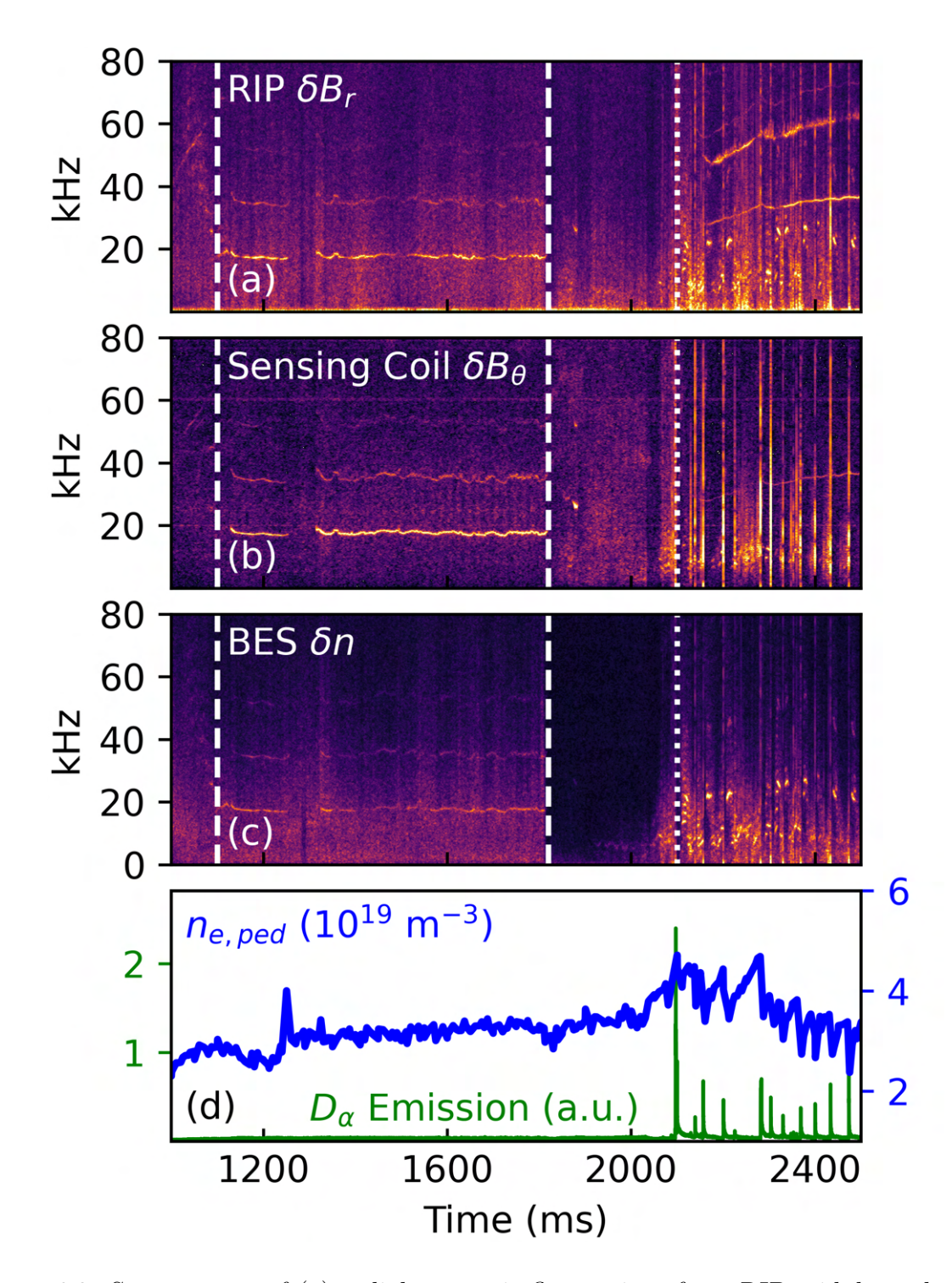


Figure 6.2: Spectrogram of (a) radial magnetic fluctuations from RIP midplane chord, (b) poloidal magnetic fluctuations from one low-noise outboard midplane sensing coil, and (c) density fluctuations from one midplane BES channel near pedestal top. Dashed lines denote QH-mode. Dotted line denotes ELMy H-mode. Horizontal lines on sensing coils at 20 kHz and 60 kHz are artifacts. (d) Divertor D_{α} emission and electron pedestal density. Data from DIII-D discharge #184791.

dissipates; the EHO harmonics remain coupled throughout. Variation in bicoherence reflects variation in coupling strength.

The entire-period bicoherence values in RIP data for each frequency pair, calculated using 1600 time segments of length 0.5 ms, are shown in Figure 6.3(b). Bicoherence for the (34,17) kHz component, which represents coupling of the 34 kHz second harmonic and the 17 kHz fundamental to the 51 kHz third harmonic, is 0.016. This bicoherence value is well above the 99% significance level for the sample size, which for 1600 segments is 0.0029. The coupling is also identifiable in negative frequency space at (51,-17) and (51,-34) kHz. The bicoherences at (17,17) and (34,-17) kHz arise from the fundamental coupling to itself and do not involve the third harmonic. Broadening at (17,17) and (34,-17) kHz, i.e., adjacent data points showing significant bicoherence, is due to variation in EHO frequency within the window. The EHO harmonics remain coupled throughout, both at every time slice in the window and averaged over time. However, the absolute value of the bicoherence is small $(b^2 \ll 1)$, suggesting that the harmonics are weakly coupled. The same coupling is also identifiable with magnetic sensing coils and BES. The fundamental frequency of the EHO corresponds to m, n = 11, 2 according to the magnetic coils. EHO mode numbers generally correspond to q = m/n at the pedestal top [45], which during this time is between 5–5.5, compatible with the measured m, n = 11, 2 EHO or with an m, n = 10, 2 EHO. Note that mode numbers m > 6 are approximate on coils.

The time-dependent and entire-period bicoherences between the EHO harmonics for one low-noise midplane sensing coil, whose spectrogram is shown in Figure 6.2(b), are shown in Figure 6.4(a-b). The same values for the midplane BES channel at the pedestal top are shown in Figure 6.4(c-d). Once again, statistically significant bicoherences are found at (17,17) and (34,17) kHz as well as their negative-space counterparts. The entire-period bicoherences for the BES signal also demonstrate some broadband coupling to noise of the 17 kHz fundamental. There is also a bicoherence value just above significance (lighter purple) at (51,17), suggesting that the fundamental and 51 kHz harmonic are also coupled to higher

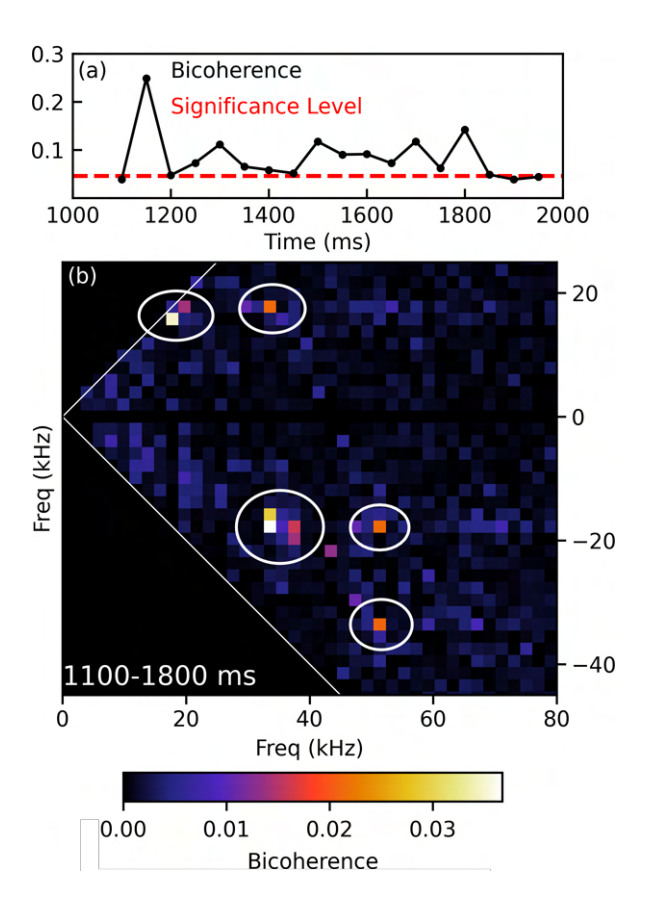


Figure 6.3: From the discharge in Figure 6.2, (a) bicoherence (black) and 99% significance level (red dashed line) for RIP data over time in 50 ms segments at (34,17) kHz. (b) Bicoherence in RIP data from 1100–1800 ms. Couplings are circled. Plot (b) is symmetrical across y = x and y = -x, so f_2 (y-axis) f_3 (y-axis) sections are removed. White diagonal lines distinguish sections. Row $f_2 = 0$ is obscured to remove artifacts.

harmonics not visible in spectrograms. This bolsters the evidence of an inverse cascade. Note that in this case the bicoherence values are much higher, with respect to the significance level, on both the coil and BES than on RIP. RIP shows the EHO relatively strongly but has significant background noise, evident from the strong broadband in the RIP signal during the QH period. The coil and BES experience less noise during this period than RIP. This is particularly relevant for the 51 kHz harmonic, which is more clearly visible to the eye on the coil and BES than on RIP. In addition, both the coil and BES measure at the plasma edge, which results in less pickup from the rest of the plasma. For all diagnostics, the bicoherence over time drops when the mode amplitude drops near or below the noise floor. I conclude that all three signals demonstrate nonlinear coupling between the EHO's first three

harmonics and the inverse cascade from higher to lower harmonics.

6.4 EHO and Mode Identification in Post-QH-Mode

After the EHO vanishes, the plasma transitions to ELMy H-mode. Figure 6.2 shows the EHO dissipating around 1800 ms, marked by a dashed line, after which there is little MHD activity and density begins to rise, reflecting the steady growth in the pedestal due to reduced edge transport. ELMy H-mode begins around 2100 ms, as marked by a dotted line, and density drops. Coherent magnetic modes follow soon after, visible as bright bands. The lowest-frequency mode, visible on RIP and BES but not coils, is intermittent. This mode appears a consistent 5–10 ms after each ELM and lasts about 10 ms, with inter-ELM periods where this mode appears lasting tens of ms. Tearing modes are also detected at this time. RIP reveals tearing modes beyond the single mode seen with sensing coils or BES. The frequencies of the principal modes to be discussed in this chapter are 26 kHz, 48 kHz, and 70 kHz. Magnetic activity below 20 kHz during this time, appearing on both RIP and the sensing coils, does not have signatures associated with tearing modes according to sensing coil analysis and is not considered here. This period is shown in more detail in Figure 6.9(a).

The intermittent mode emerges from 2164–2175 ms at 22 kHz, near the previous EHO fundamental frequency; this suggests that it, too, is the EHO. It is visible clearly with RIP and BES but only faintly on a few magnetic sensing coils. The sensing coils that detect the intermittent mode are close to each other in space; this suggests that it is toroidally localized. Strong localization of the mode, which would result in a sharp radial decay towards the edge, may also make it difficult to detect the mode at the wall. RIP detects its second harmonic, another EHO characteristic, at 44 kHz but no visible third harmonic. I detect the 22 kHz mode at the pedestal top using BES [46] to measure its associated density fluctuations. Density fluctuation amplitudes, as shown in Figure 6.5, are calculated from the power spectrum via the short-time Fourier transform using 1 ms windows. Fluctuations at 22 kHz are shown from normalized radial coordinate $\rho = 0.92$, near the pedestal top, to the last closed flux surface, $\rho = 1$, in Figure 6.5(a). This structure characterizes the EHO, which

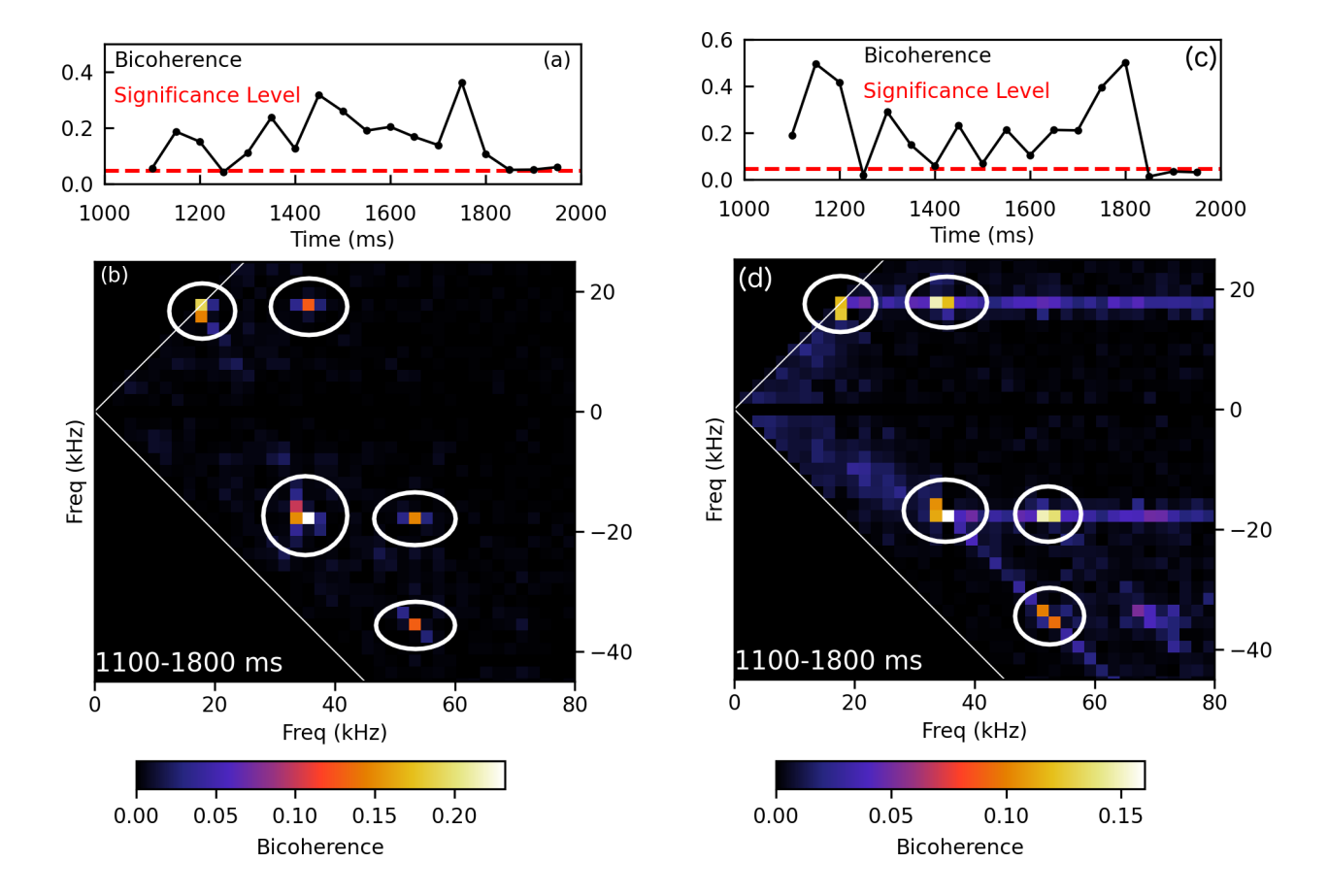


Figure 6.4: From the discharge in Figure 6.2, (a) bicoherence (black) and 99% significance level (red dashed line) for data from a single coil over time in 50 ms segments at (34,17) kHz. (b) Bicoherence in single coil data from 1100–1800 ms. (c) Bicoherence (black) and 99% significance level (red dashed line) for data from a single midplane BES channel at the pedestal top over time in 50 ms segments at (34,17) kHz. (d) Bicoherence in single BES channel data from 1100–1800 ms. Couplings are circled. Plot (b) is symmetrical across y = x and y = -x, so f_2 (y-axis) > f_1 (x-axis) sections are removed. White diagonal lines distinguish sections. Row $f_2 = 0$ is obscured to remove artifacts.

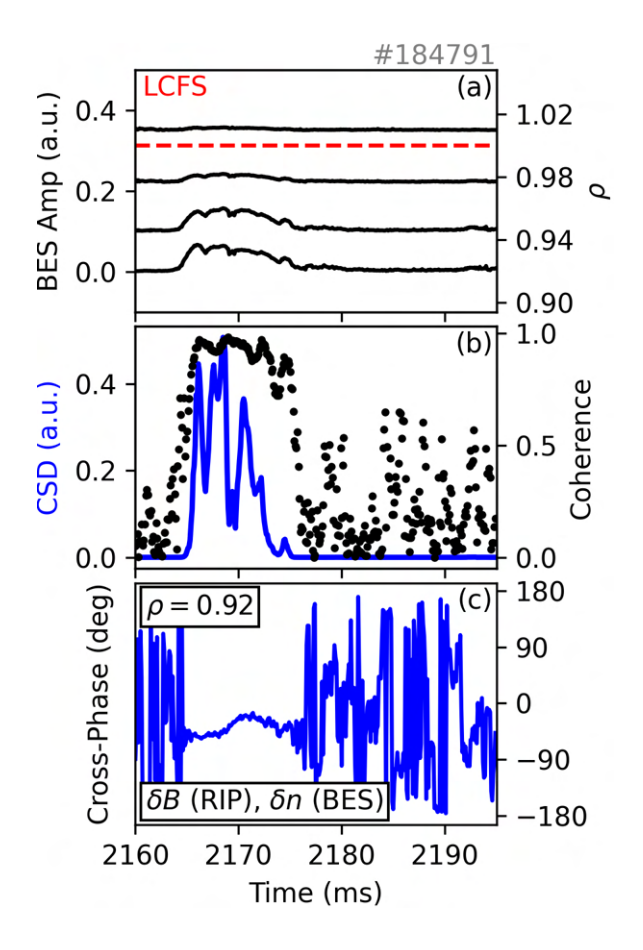


Figure 6.5: From the discharge in Figure 6.2, (a) 22 kHz EHO amplitudes on four midplane BES channels at plasma edge. Red dashed line marks last closed flux surface (normalized radial coordinate $\rho=1$), and blue dashed line marks pedestal top. EHO (b) cross-power spectral density and coherence between RIP magnetic and BES density fluctuations ($\rho=0.92$). EHO (c) cross-phase between RIP magnetic and BES density fluctuation measurements ($\rho=0.92$).

peaks in amplitude at the pedestal top and drops off toward the last closed flux surface [19]. Correlation of the internal magnetic fluctuation measurements, taken with RIP, and the pedestal density fluctuation measurements, taken with BES, at 22 kHz is shown in Figure 6.5(b) to confirm that the same mode appears on both diagnostics. The signals' cross-power spectral density is finite, their coherence is high, and their cross-phase is constant, only when the 22 kHz mode is present. The approximately constant phase between the internal magnetic and edge density fluctuations indicate that they arise from the same mode. The cross-power spectral density's trajectory matches the BES amplitude trajectory, as seen in Figure 6.5(a), and the RIP amplitude trajectory, as shown in Figure 6.9(b).

BES data from the innermost channels shows that the mode 1 signal is offset in phase between vertically spaced channels. Figure 6.6 illustrates these phase shifts with respect to the poloidal spacing between the innermost channels in a manner typically used for the magnetic sensing coils. Eight equally-spaced channels at a minor radius of 0.49 m have a vertical span of 11 cm, corresponding to a channel separation of 1.6 cm. The mode rotation is measured at 4.3 km/s, corresponding to a poloidal wave number of $k_{\theta} = 2\pi f/v = 0.32$ cm⁻¹. The positive phase shifts between BES channels reveal that the possible EHO rotates counterclockwise in the poloidal plane, or in the electron diamagnetic direction, which is characteristic of the EHO but not other modes such as the geodesic acoustic mode or quasicoherent mode [18, 47]. Diamagnetic drift is large-scale, parallel to $\nabla p \times \mathbf{B}$, and represents pressure-induced particle motion. Motion in the electron diamagnetic direction matches the direction of sheared $\mathbf{E} \times \mathbf{B}$ flow, an important EHO driver [26].

For poloidal mode number m and assuming poloidal uniformity in both the mode and the BES array, the phase shift between channels is $m\Delta\theta$, where $\Delta\theta=1.8^{\circ}$ is the angular distance between channels. Under this assumption, the shifts between the channels are fit to an estimated m=14. However, BES may overestimate the mode number due to toroidicity-related elliptical distortion, similar to the distortion seen in tearing modes [48], and poloidal localization of kink modes like the EHO. The estimate from the q profile of m=10-11 is appropriate. Given the resemblance of mode 1 to the previously existing n=2 EHO, I estimate n=2 for this mode as well.

I now identify the nature of the coherent fluctuations with frequencies above the EHO. I first confirm that the modes are core-resonant tearing modes and determine the approximate location of their resonant surfaces. The strong magnetic fluctuations seen on RIP, as shown in Figure 6.2(b), indicate MHD activity. From the poloidal and toroidal coil arrays, mode 2 has m, n = -3, 2. According to the q profile at 2170 ms, determined using MSE-constrained EFIT [49], a mode at q = 3/2 = 1.5 could lie at $\rho = 0.13$ or $\rho = 0.36$ (see Figure 6.7), which gives a benchmark for the location of mode 2's resonant surface. For tearing modes,

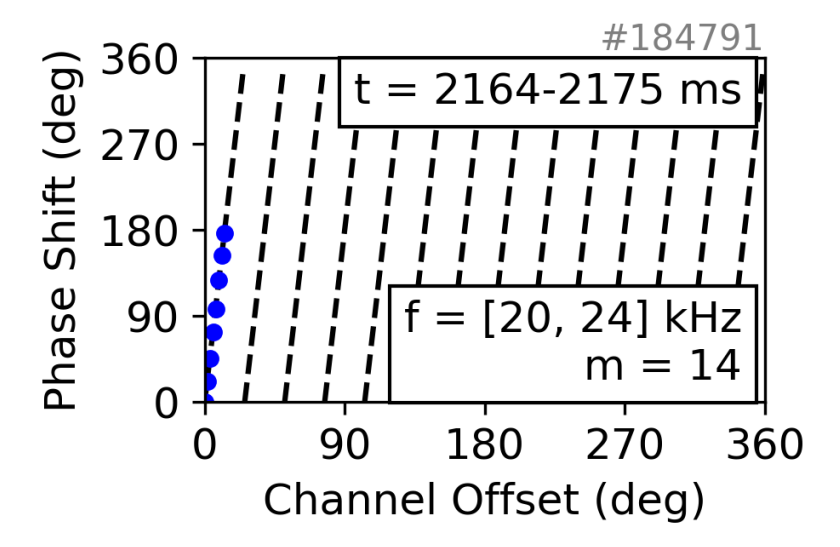


Figure 6.6: EHO phase shifts on each BES channel at $\rho = 0.92$ versus channel poloidal spacing.

 $f_{mode} \approx n f_{plasma}$, where n is the toroidal mode number and f_{plasma} is the plasma rotation. An n=2 mode at 26–28 kHz would be expected to resonate where $f_{plasma}=13$ –14 kHz; this is roughly true at the locations indicated for mode 2 by the q profile. In this section, I incorporate data from other diagnostics to confirm the location of mode 2 and identify features of mode 3, since the latter's mode numbers cannot be identified using coils.

I also incorporate RIP and the CO_2 interferometer to find the locations of mode resonant surfaces. To detect fluctuations from a rotating MHD mode using either RIP or the CO_2 interferometer, a chord must detect fluctuations above the noise floor and must therefore intersect or approach the mode's resonant surface. The locations of the three vertical interferometry chords V1, V2, and V3, shown on DIII-D in Figure 3.1, correspond in shot #184791, 2170 ms to minimum normalized radii of $\rho = 0.41$, 0.30, and 0.58 respectively. The horizontal RIP chords at $z = \pm 13.5$ cm intersect the plasma at minimum normalized radii of $\rho = 0.16$ and 0.14. The midplane RIP chord and the R0 CO_2 interferometer chord lie at $\rho = 0$. For any of these chords, if a mode is visible on the midplane chord but not an offset chord, then the mode is too weak to be detected at any surface crossed by that offset chord and therefore lies inside its minimum radius. I use this to estimate the resonant surface location of each RIP-identified mode.

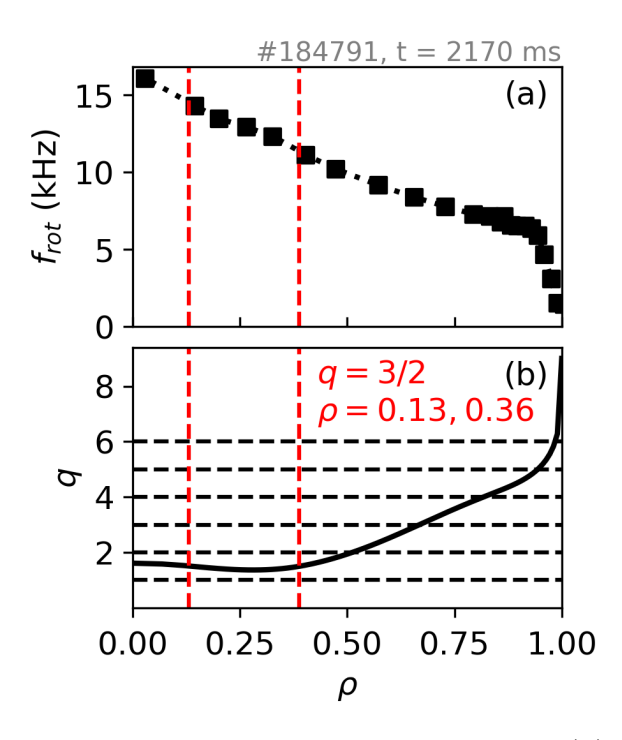


Figure 6.7: (a) Toroidal impurity rotation profile at 2170 ms. (b) Safety factor profile at 2170 ms. Red dashed lines denote q = 3/2 surfaces. Gray dashed lines denote integer q.

To narrow down resonant surface locations using RIP and the CO₂ interferometer, I compare the density fluctuation amplitudes measured with the two diagnostics, as shown in Figure 6.8. I use the RIP midplane chord for comparison instead of the CO₂ interferometer midplane chord because the CO₂ chord has significant pickup from optical component vibration [50] during this time. All modes are detected along the RIP upper, midplane, and lower chords. The 26 kHz mode is detected on chord V2 but not chords V1 or V3, indicating that it lies in the approximate range $\rho = 0.30$ –0.41. The mode location identified from the q profile falls within this range, but the mode location from the rotation profile falls just outside it. This can be attributed to the use of the toroidal rotation profile as an approximation for the true profile. The 48 kHz mode is not detected on any of the vertical chords but is detected on all three RIP chords, indicating that it lies in the approximate range $\rho = 0.16$ –0.30. The 70 kHz mode is detected on the RIP midplane chord but not the upper and lower chords, indicating that it lies inside $\rho = 0.14$. The EHO is detected on all chords of both RIP and CO₂ interferometer. It therefore lies outside $\rho = 0.58$, the location of V3, the outermost

chord, matching the edge location appearing on BES.

Since the 48 kHz and 70 kHz modes are not detected on coils, their mode numbers are not available. I estimate the mode numbers of each mode given the available information. Given that the previous EHO fundamental has n=2, the toroidal rotation and safety factor profiles indicate approximately that $(n_1, n_2, n_3) = (2, 3, 5)$ or (2, 4, 6). The EHO is expected to have m, n = 10, 2 or 11,2 if it is resonant near the pedestal at the q = 5 or q = 5.5 surface [45]. A 48 kHz mode at n=3 would lie on a surface where $v_{\phi}=16$ kHz, and at n=4would lie at $v_{\phi} = 12$ kHz. A mode between $\rho = 0.16 - 0.3$ would resonate at a surface closer to 16 kHz, suggesting n=3. The core location suggests q near or above 1.5, which matches best with m, n = 5, 3 for the 48 kHz mode. The 70 kHz mode should therefore have $m, n = m_1 + m_2, n_1 + n_2 = 15, 5$ or 16,5. A mode near the q = 3 rational surface should lie around $\rho = 0.7$, which is not consistent with the mode's visibility on the RIP midplane chord but not the side chords or any interferometry chord. It is also not consistent with an estimated resonant frequency of 70/5 = 14 kHz. Instead considering n = 6 for the 70 kHz mode, the resonant surface frequency is 11.7 kHz, and the resonant surface outside $\rho = 0.5$. In that case, n = 4 for the 48 kHz mode, yielding a resonant surface at 12 kHz, just inside $\rho = 0.5$, and approximate mode numbers of m, n = 7, 4. The 70 kHz mode would therefore have m, n = 17, 6 or m, n = 18, 6, which is still not consistent with the mode's perceived location but more closely matches the plasma frequency at the mode location. I hypothesize that the 48 kHz and 70 kHz modes are not visible on coils or interferometry due to their localization and/or low amplitude instead of their location.

6.5 Coupling to Tearing Modes Interrupting EHO Development

The EHO first appears alongside tearing modes during the window 2164–2175 ms, which is characterized by rapidly changing tearing mode amplitudes. Figure 6.9(a) shows these modes in RIP data just after an ELM crash at 2160 ms. One clear tearing mode and one

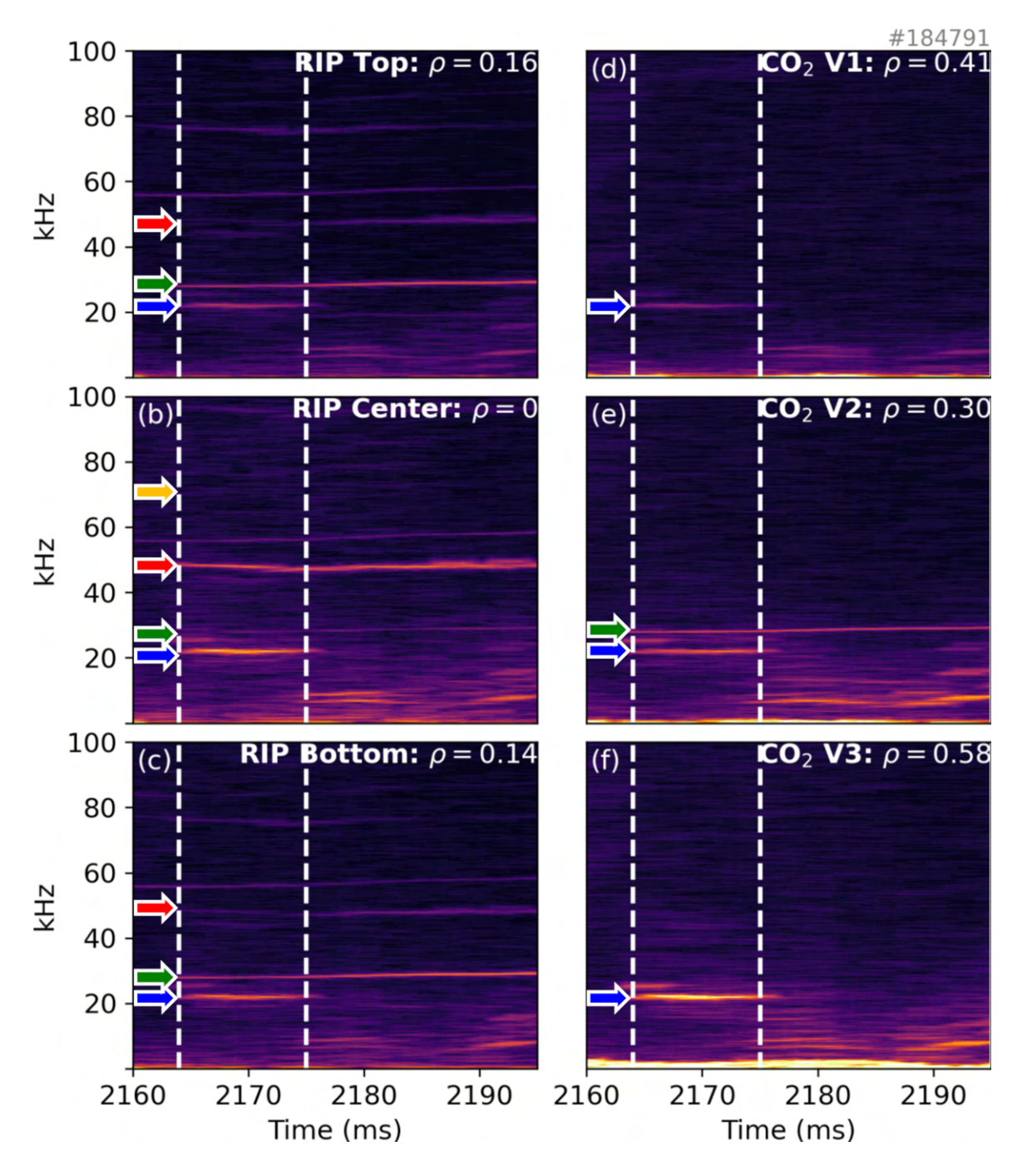


Figure 6.8: During coupling, spectrograms of RIP upper (a), (b) midplane, and (c) lower interferometry chord; (d) CO₂ interferometer V1, (e), V2, and (f) V3 chord. Coupling period marked by dashed lines. EHO in blue, 26 kHz mode in green, 48 kHz mode in red, and 70 kHz mode in yellow.

weak tearing mode emerge at 48 kHz and 70 kHz respectively and are not visible on coils. The mode visible on coils emerges around 28 kHz and does not interact directly with the 22 kHz mode, nor does its harmonic that appears on RIP at around 56 kHz. 22 kHz, 48 kHz, and 70 kHz mode amplitudes, calculated using the short-time Fourier transform, are shown in Figure 6.9(b) along with density pedestal height measured with Thomson scattering. Growth of the 48 kHz mode as the EHO and 70 kHz mode amplitudes drop suggests energy transfer between coupled modes. Density pedestal height remains lower during the EHO, suggesting that the EHO increases particle transport.

To calculate bicoherence, I divide the 2164–2175 ms window into 22 segments of length 0.5 ms. Bicoherence values from RIP are shown in Figure 6.9(c). Bicoherence is 0.62 at (48,22) kHz, the frequencies of one tearing mode and the EHO respectively, well above the 99% significance level of 0.21. The frequency pair corresponds to coupling to the 70 kHz mode. While significant bicoherence at (22,22) indicates EHO self-coupling, there is no significant bicoherence at (44,22) kHz, the frequencies of the EHO second harmonic and fundamental. Rather, the EHO fundamental couples to tearing modes. Other, isolated high bicoherence values are visible in Figure 6.9(c). The value at (76,48) is a higher tearing mode coupling that does not appear to affect the EHO. Elevated bicoherences at (44,-22), (70,-22), and (70,-48) are negative-space counterparts of the EHO self-coupling and tearing mode coupling. The other elevated values do not correspond to tearing and do not appear to affect the EHO.

I address the transient EHO's role in the temporary back-transition into QH-mode by measuring density pedestal height. The amplitude of the EHO is ensemble-averaged over 8 ELM cycles, i.e., all ELM cycles before the 48 kHz mode disappears and that contain the EHO. Since each ELM cycle has a different length, between 16 and 43 ms, amplitudes are binned by the fraction of the ELM cycle that has passed. They are plotted in Figure 6.10 along with the height of the density pedestal, measured using Thomson scattering [44]. The EHO returns consistently, and its amplitude rises soon after each ELM. After the EHO disappears, the pedestal rises and leads into the next ELM. The pedestal height remains

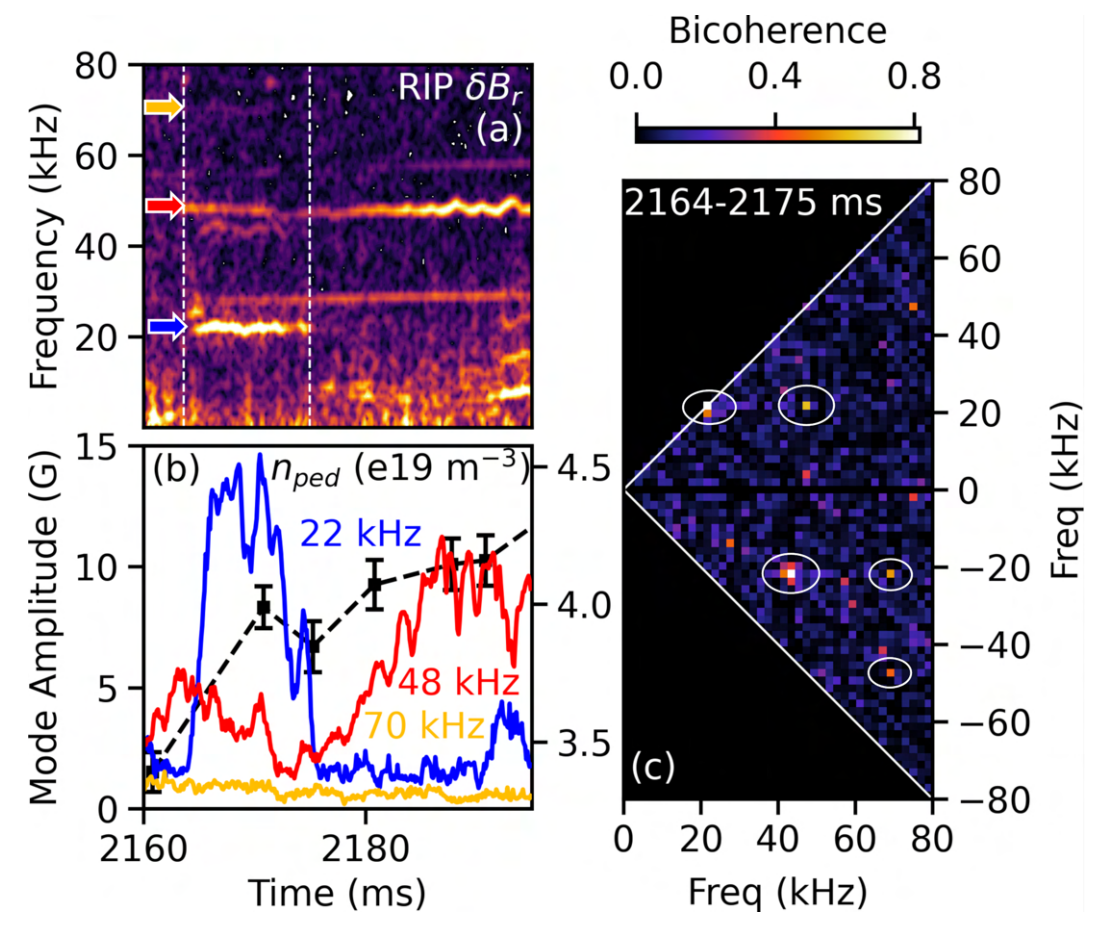


Figure 6.9: From the discharge in Figure 6.2, (a) spectrogram of RIP z=0 polarimetry. Blue arrow marks EHO fundamental, red arrow marks 48 kHz mode, and yellow arrow marks 70 kHz mode. (b) EHO fundamental (blue), 48 kHz (red), and 70 kHz (yellow) mode amplitudes and electron density pedestal height (black, dashed). (c) Bicoherence in RIP z=0 data for 2164-2175 ms. EHO couplings are circled.

nearly constant in time during the EHO, indicating a return to QH-mode. However, when the EHO couples to tearing modes, it loses energy and the emerging QH-mode cannot be maintained. Similar intermittent EHOs appear in two other DIII-D shots in the QH-mode database. In both shots, the intermittent EHO was associated with an EHO early in the shot with weak nonlinear coupling before a transition to ELMy H-mode, just as in shot #184791. The presence of similar MHD in other shots motivates further investigation of the role of tearing mode coupling in the return of the intermittent EHO.

Limitations of this analysis include the difficulty of measuring bicoherence with small sample sizes. Another limitation was the spatial coverage of BES in this shot, which pre-

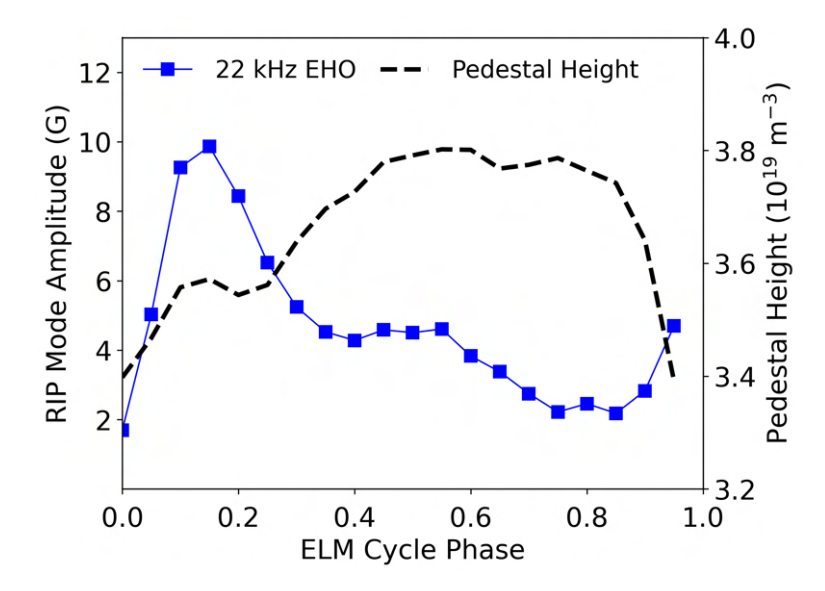


Figure 6.10: Ensemble-averaged EHO amplitude and density pedestal height for 8 ELM cycles with EHO. Phase ranges from 0 (end of last ELM) to 1 (beginning of next ELM).

vented full coverage of the edge mode but was nonetheless sufficient to track its motion. In future shots intended to track the EHO, it could be advantageous to center BES's viewing channels at the top of the pedestal. Electron cyclotron emission (ECE) [51] measurements of the pedestal were inconclusive; the EHO did not appear at 2170 ms in a channel viewing the pedestal but did appear later in the shot. This may be attributable to noise or localization of the mode. The line-integrated RIP measurements, and the different time bases between diagnostics, prevented quantitative measurements of cross-phase between RIP and BES. Qualitative measurements of high correlation and consistent cross-phase were sufficient to identify that the same mode was observed on RIP and BES. I have addressed possible error in mode number calculations using BES and regard them as estimates.

Bibliography

- [1] S. Assadi, S. C. Prager, and K. L. Sidikman. "Measurement of nonlinear mode coupling of tearing fluctuations". *Physical Review Letters* 69.2 (1992), p. 281.
- [2] J. S. Sarff et al. "Nonlinear coupling of tearing fluctuations in the Madison Symmetric Torus". *Physics of Fluids B: Plasma Physics* 5.7 (1993), pp. 2540–2545.
- [3] W. X. Ding et al. "The Hall dynamo effect and nonlinear mode coupling during sawtooth magnetic reconnection". *Physics of Plasmas* 13.11 (2006), p. 112306.
- [4] L. Lin et al. "Role of nonlinear coupling and density fluctuations in magnetic-fluctuation-induced particle transport". *Physical Review Letters* 108.17 (2012), p. 175001.
- [5] M. F. F. Nave et al. "Triggering of neo-classical tearing modes by mode coupling". Nuclear Fusion 43.3 (2003), p. 179.
- [6] L. Bardóczi, N. C. Logan, and E. J. Strait. "Neoclassical tearing mode seeding by nonlinear three-wave interactions in tokamaks". *Physical Review Letters* 127.5 (2021), p. 055002.
- [7] C. M. Greenfield et al. "Quiescent double barrier regime in the DIII-D tokamak".

 Physical Review Letters 86 (20 May 2001), pp. 4544–4547.
- [8] B. A. Grierson et al. "Impurity confinement and transport in high confinement regimes without edge localized modes on DIII-D". *Physics of Plasmas* 22.5 (2015), p. 055901.
- [9] K. H. Burrell et al. "Quiescent H-mode plasmas in the DIII-D tokamak". *Plasma Physics and Controlled Fusion* 44.5A (2002), A253.

- [10] K. H. Burrell et al. "Quiescent double barrier high-confinement mode plasmas in the DIII-D tokamak". *Physics of Plasmas* 8.5 (2001), pp. 2153–2162.
- [11] K. H. Burrell et al. "Advances in understanding quiescent H-mode plasmas in DIII-D".

 Physics of Plasmas 12.5 (2005), p. 056121.
- [12] W. M. Solomon et al. "Extending the physics basis of quiescent H-mode toward ITER relevant parameters". *Nuclear Fusion* 55.7 (2015), p. 073031.
- [13] P. B. Snyder et al. "Stability and dynamics of the edge pedestal in the low collisionality regime: physics mechanisms for steady-state ELM-free operation". *Nuclear Fusion* 47.8 (2007), p. 961.
- [14] N. Aiba et al. "Impact of rotation and ion diamagnetic drift on MHD stability at edge pedestal in quiescent H-mode plasmas". *Nuclear Fusion* 60.9 (2020), p. 092005.
- [15] N. Aiba et al. "Stabilization of kink/peeling modes by coupled rotation and ion diamagnetic drift effects in quiescent H-mode plasmas in DIII-D and JT-60U". *Nuclear Fusion* 61.12 (2021), p. 126044.
- [16] N. Aiba, X. Chen, T. H. Osborne, and K. H. Burrell. "Comparison of MHD stability properties between QH-mode and ELMy H-mode plasmas by considering plasma rotation and ion diamagnetic drift effects". Nuclear Fusion 63.4 (2023), p. 042001.
- [17] K. Kamiya et al. "Unveiling the structure and dynamics of peeling mode in quiescent high-confinement tokamak plasmas". Nature Communications Physics 4.1 (2021), p. 141.
- [18] G. Yu et al. "ECEI characterization of pedestal fluctuations in quiescent H-mode plasmas in DIII-D". *Plasma Physics and Controlled Fusion* 64.9 (2022), p. 095014.
- [19] X. Chen et al. "Rotational shear effects on edge harmonic oscillations in DIII-D quiescent H-mode discharges". *Nuclear Fusion* 56.7 (2016), p. 076011.
- [20] A. M. Garofalo et al. "Advances towards QH-mode viability for ELM-stable operation in ITER". Nuclear Fusion 51.8 (2011), p. 083018.

- [21] R. J. Goldston and P. H. Rutherford. *Introduction to Plasma Physics*. Bristol, UK and Philadelphia, PA, USA: Institute of Physics Publishing, 2000.
- [22] K. H. Burrell et al. "Reactor-relevant quiescent H-mode operation using torque from non-axisymmetric, non-resonant magnetic fields". Physics of Plasmas 19.5 (2012), p. 056117.
- [23] X. Chen et al. "Bifurcation of quiescent H-mode to a wide pedestal regime in DIII-D and advances in the understanding of edge harmonic oscillations". Nuclear Fusion 57.8 (2017), p. 086008.
- [24] F. Liu et al. "Nonlinear MHD simulations of quiescent H-mode plasmas in DIII-D".

 Nuclear Fusion 55.11 (2015), p. 113002.
- [25] F. Liu et al. "Nonlinear MHD simulations of QH-mode DIII-D plasmas and implications for ITER high Q scenarios". Plasma Physics and Controlled Fusion 60.1 (2018), p. 014039.
- [26] G. S. Xu et al. " $\mathbf{E} \times \mathbf{B}$ flow shear drive of the linear low-n modes of EHO in the QH-mode regime". *Nuclear Fusion* 57.8 (2017), p. 086047.
- [27] T. M. Wilks et al. "Scaling trends of the critical E × B shear for edge harmonic oscillation onset in DIII-D quiescent H-mode plasmas". Nuclear Fusion 58.11 (2018), p. 112002.
- [28] J. R. King et al. "MHD modeling of a DIII-D low-torque QH-mode discharge and comparison to observations". *Physics of Plasmas* 24.5 (2017), p. 055902.
- [29] J. G. Chen et al. "Impact of $E \times B$ shear flow on low-n MHD instabilities". Physics of Plasmas 24.5 (2017), p. 050704.
- [30] L. Meier et al. "MHD simulations of formation, sustainment and loss of quiescent H-mode in the all-tungsten ASDEX Upgrade". Nuclear Fusion 63.8 (2023), p. 086026.
- [31] A. Cathey et al. "Non-linear MHD investigations of high-confinement regimes without type-I ELMs in ASDEX Upgrade and JT-60SA". *Nuclear Fusion* 64.9 (2024),

- p. 096003.
- [32] Z. Liang et al. "Predictive nonlinear MHD simulations of quiescent H-mode plasma in the HL-3 tokamak". *Physics of Plasmas* 32.1 (2025), p. 012502.
- [33] J. L. Luxon. "A design retrospective of the DIII-D tokamak". Nuclear Fusion 42.5 (2002), p. 614.
- [34] P. W. Terry. "Suppression of turbulence and transport by sheared flow". Rev. Mod. Phys. 72.1 (2000), p. 109.
- [35] K. Burrell. "Effects of $E \times B$ velocity shear and magnetic shear on turbulence and transport in magnetic confinement devices". Physics of Plasmas 4.5 (1997), pp. 1499–1518.
- [36] P. W. Xi, X. Q. Xu, X. G. Wang, and T. Y. Xia. "Influence of equilibrium shear flow on peeling-ballooning instability and edge localized mode crash". *Physics of Plasmas* 19.9 (2012).
- [37] B. D. Dudson et al. "BOUT++: A framework for parallel plasma fluid simulations".

 *Computer Physics Communications 180.9 (2009), pp. 1467–1480.
- [38] G. T. A. Huysmans and O. Czarny. "MHD stability in X-point geometry: simulation of ELMs". *Nuclear Fusion* 47.7 (2007), p. 659.
- [39] S. Elgar and R. T. Guza. "Statistics of bicoherence". *IEEE Transactions on Acoustics*, Speech, and Signal Processing 36.10 (1988), pp. 1667–1668.
- [40] L. Bardoczi et al. "The root cause of disruptive NTMs and paths to stable operation in DIII-D ITER baseline scenario plasmas". Nuclear Fusion 64.12 (2024), p. 126005.
- [41] K. H. Burrell et al. "Quiescent H-mode plasmas with strong edge rotation in the cocurrent direction". *Physical Review Letters* 102.15 (2009), p. 155003.
- [42] X. Chen et al. DIII-D Miniproposal 2019-31-05. 2021.

- [43] R. J. Colchin et al. "The filterscope". Review of Scientific Instruments 74.3 (2003), pp. 2068–2070.
- [44] T. N. Carlstrom et al. "Design and operation of the multipulse Thomson scattering diagnostic on DIII-D". Review of Scientific Instruments 63.10 (1992), pp. 4901–4906.
- [45] Z. Li. Private communication. 2024.
- [46] G. McKee et al. "The beam emission spectroscopy diagnostic on the DIII-D tokamak".

 *Review of Scientific Instruments 70.1 (1999), pp. 913–916.
- [47] N. Winsor, J. L. Johnson, and J. M. Dawson. "Geodesic acoustic waves in hydromagnetic systems". *Physics of Fluids* 11.11 (1968), pp. 2448–2450.
- [48] J. W. Connor et al. "Tearing modes in toroidal geometry". *Physics of Fluids* 31.3 (1988), pp. 577–590.
- [49] L. L. Lao et al. "Equilibrium analysis of current profiles in tokamaks". *Nuclear Fusion* 30.6 (1990), p. 1035.
- [50] M. A. Van Zeeland et al. "Fiber optic two-color vibration compensated interferometer for plasma density measurements". Review of Scientific Instruments 77.10 (2006), 10F325.
- [51] M. E. Austin and J. Lohr. "Electron cyclotron emission radiometer upgrade on the DIII-D tokamak". Review of Scientific Instruments 74.3 (2003), pp. 1457–1459.

Chapter 7

Conclusions

7.1 Summary

Faraday-effect polarimetry measures rotation of the polarization of a light beam in the presence of a magnetic field. Faraday rotation fluctuates as the magnetic field or density fluctuates. As a line-integrated, internal measurement, polarimetry therefore provides a unique opportunity to measure magnetic and density fluctuations at any location in a plasma. A recently installed diagnostic on DIII-D, the Radial Interferometer-Polarimeter (RIP) [1], has allowed the first internal magnetic measurements on that device. RIP measures lineintegrated magnetic and plasma density and their fluctuations across the radius of DIII-D. Simultaneous interferometry and polarimetry allow the magnetic component of the rotation measurement to be extracted, and it can be shown that density fluctuation contributions to RIP measurements are negligible. When compared to magnetic sensing coils, the other main magnetic diagnostic on DIII-D, RIP has a higher bandwidth. In addition, the sensing coils only measure magnetic field at a single point, in contrast to RIP, which measures across the entire plasma. As RIP is location-agnostic, it can measure modes such as high-order tearing modes that are spatially localized and resonant far from the coils. Low-frequency coherent MHD modes are the subject of this thesis. Primary emphasis is placed on tearing modes, but also other coherent modes like the edge harmonic oscillation (EHO) in quiescent H-mode (QH-mode). Of particular interest are neoclassical tearing modes, which grow quickly but require a trigger.

Fluctuation amplitudes and spectra are calculated using the short-time Fourier transform. The amplitude is equal to the integrated power spectral density over all frequencies corresponding to the mode, divided by the line-integrated density. As RIP is averaged, it cannot measure mode structure. Instead, I use a series of increasingly detailed computational mode structure models to understand what RIP is expected to measure. Cylindrical models predict that even-m modes should not be visible with RIP; however, they are visible but attenuated. I use linear toroidal models incorporating plasma shape using the code TJ [2] to understand the mechanisms behind RIP even-m mode detection and attenuation. In the TJ model, the main mode couples to toroidicity, ellipticity, triangularity, and higher-order shaping effects to generate sidebands with $m \pm 1$, 2, 3, and so on. The strength of each sideband is related to the size of the shaping parameter.

TJ uses an asymptotic expansion to generate a composite eigenfunction made up of all sidebands. In the linear expansion, even-m modes have odd-m sidebands which can be visible with line-integrated diagnostics such as RIP. The magnetic field B_R can be measured at every point in the plasma cross-section, and a synthetic RIP diagnostic was constructed to integrate over the model. The TJ model can be normalized to the coil-measured magnetic field at the edge and then used to construct a synthetic, line-integrated coil value to compare directly to RIP. I confirm that the odd-m, visible sidebands of even-m modes generated by toroidicity scale with the inverse aspect ratio in TJ. It is found experimentally that compared to odd-m modes, even-m modes are also attenuated by a factor of somewhat less than the inverse aspect ratio, which approaches the theoretical scaling. The even-m modes have a low amplitude in TJ when line-integrated (analogous to RIP) compared to the edge value (analogous to coils) even in the triangular model, matching predictions that the sign of the mode plays a major role. Higher-m modes are also much stronger on RIP than the coils in general, which is related to localization of the mode and difficulty detecting it with coils.

I also discuss cases other than varying mode number in which a discrepancy between RIP and the coils occurs. In particular, RIP can be used successfully to detect ELMs an average of 0.33 ms before they are detected using filterscopes, which is a significant fraction of the ELM duration. In addition, RIP detects tearing modes and other MHD activity not seen with coils.

I then discuss experiments carried out on DIII-D to test plasma shaping effects on tearing mode stability and relative amplitude measurements between RIP and the external sensing coils. This experiment prioritized m, n > 2, 1 tearing modes in weakly shaped plasmas, which could approach the circular limit studied in the TJ modeling. An inner-wall limited plasma was selected to allow a weakly shaped plasma. Elongation was varied from 1.25, which is typically called circular, to 1.5. Weak shaping also expanded the range of stability research, since previous work prioritized the ITER Baseline Scenario, which is diverted and has higher elongation ($\kappa > 1.6$). The experiment also jogged the magnetic axis up and down to scan as much of the mode structure as possible. The plasma was run at high rotation and neutral beam fueling, which was intended to enable tearing modes but avoid nonlinear coupling. The initial experimental run contained large impurity influxes, primarily carbon and iron, related to an exposed tile and wire on the vessel floor. RIP data was compromised due to high impurity radiation and density in the plasma core, resulting in both pickup at the RIP detectors and refraction of the beam. Pickup generated noise, whereas refraction attenuated the portion of the signal due to magnetic fluctuations. Impurity radiation also led to disruptions. As a result, this thesis primarily used results from a later contingency run day. The contingency day experienced much less impurity influx, though some was still present due to plasma contact with the wall. There were no disruptions in the contingency.

The plasmas had low q and were sawtoothing, with the intention of using sawteeth to trigger tearing modes. MHD stability was measured using the DCON [3] code, incorporating precise equilibrium reconstructions with kineticEFIT [4]. While DCON is an ideal MHD code, the ideal-wall β_N limit is a good proxy for tearing stability as the tearing index Δ'

increases drastically near the limit [5, 6]. MHD stability and experimental parameter results from the experiment were unexpected. In most of the shots, sawteeth dominated but did not trigger tearing modes. Circular shots were not expected to experience tearing modes, but the lack of sawtooth triggering of tearing modes in elongated shots was unexpected. It was identified using DCON that in most cases, the n=1 stability limit was reached at the same time as the n=2 limit, causing sawteeth to dominate over tearing modes. In addition, the sawtooth period was found to be too short to trigger tearing modes. As the sawteeth were triggered at the ideal-wall limit despite the wall distance being larger than usual, it can be surmised that the sawteeth contained a resistive component. Tearing modes, in the shots where they occurred, appeared also to be associated with approach to the n=2 ideal-wall β_N limit, indicating that their initial trigger was classical rather than neoclassical. Another unusual result was that the ideal-wall limit varied with time despite β_N remaining steady and the plasma already having reached the I_p and B_t flattop. The limit instead was affected by the plasma size and distance from the wall as it was compressed in preparation for elongation increases and vertical jog. A plasma with the same energy in less volume is unstable at a lower pressure. Some shots entered H-mode, which is unusual for limited plasmas. It was found that the input neutral beam power matched previous DIII-D scalings with density and magnetic field for H-mode in limited plasmas. This was in contrast to scalings from TFTR, which ran circular plasmas like those in the recent IWL experiment but operated at much higher temperatures than DIII-D [7].

For the shots that did include tearing modes, RIP-measured mode amplitudes were compared to coil amplitudes, using a synthetic line-integrated model in TJ. This was conducted for shots with 3,2 and 2,1 tearing modes and for magnetic axis position both above and below midplane. In both cases, there were significant jumps in RIP amplitude that did not correspond to similar jumps in coil amplitude. The 3,2 mode had RIP/coil values less than the synthetic $\int B_R dR$ values. This may be attributable to the weaker $m \pm 2$ sidebands, which contributed to the RIP amplitude in IBS, while the $m \pm 1$ sidebands, invisible on RIP,

were still subtracted from the expected value. However, the 2.1 mode, which was expected to be significantly attenuated in all experiments, was quite strong and even outperformed the 3.2 mode when the ratio of RIP to coil amplitudes was compared to TJ. This is likely due to a strong 1.1 sideband, which frequently occurs in 2.1 modes at low safety factor, and a core 3.1 sideband detected by RIP but weaker on coils. Distance from midplane did not significantly affect the 2.1 mode, which is hypothesized to be visible from the detectable sidebands and which would be covered by all chord locations. However, moving the plasma off midplane significantly reduced the TJ 3.2 amplitude as the chord is no longer in contact with the island. RIP was still strong, suggesting the island was larger in experiment than in the model. Nonlinear effects are also expected to play a role. In particular, the TJ model includes only a single n. A mode at a given frequency can contain components from or have gained or lost energy from multi-wave interactions with modes of different n, which is not contained in the linear TJ model.

I conclude that linear mode structure is useful for benchmarking RIP amplitudes but that other factors must be considered. I also have not considered pressure or density profile effects. The TJ amplitudes were calculated with zero pressure, and $\int B_R dR$ was directly calculated without the interferometric density-weighting incorporated in experimental results with RIP. Density weighting is possible using either experimental density profiles obtained from the Thomson scattering diagnostic [8] or synthetic DIII-D-like input density profiles. Since some sidebands are most prominent in the edge, it will be interesting to identify whether the density drop associated with the pedestal reduces the measured amplitudes of those sidebands on RIP.

I next discuss use of RIP to measure nonlinear coupling of coherent modes in the core and edge through bicoherence analysis. Specifically, I measure coupling first between components of the edge harmonic oscillations (EHO) in quiescent H-mode (QH-mode), which is predicted by nonlinear magnetohydrodynamic simulations to cause EHO saturation [9, 10]. This supports the assertion that the EHO saturates through an energy cascade between

harmonics. Based on data from later in the shot, I measure nonlinear coupling between two core-resonant tearing modes and an intermittent EHO, which is confirmed by measurements with beam-emission spectroscopy to lie at the edge. The edge mode's location at the pedestal top, frequency near the previous EHO frequency, and estimated mode numbers lead us to conclude that it is a developing EHO. In contrast, the tearing modes are resonant in the core according to the q profile and to comparisons between RIP and interferometry amplitudes. The pedestal height remains near constant in time during the intermittent EHO appearance, indicating that a transition back to QH-mode is occurring. The EHO returns after each ELM, but the coupling between its harmonics is no longer detectable, and the EHO loses energy through interaction with core-resonant tearing modes. I conclude that coupling to tearing modes interrupts the nonlinear interaction between the EHO's harmonics, causing it to desaturate and then dissipate. As a result, the EHO is unable to maintain particle transport across the pedestal, and ELMs continue. When the EHO couples to tearing modes, it can no longer gain energy by coupling to its harmonics. ELMs continue, and re-entry to QH-mode is halted. I propose that nonlinear coupling of the two tearing modes to the EHO removes the energy cascade sustaining the EHO and causes the EHO to dissipate, preventing the return of QH-mode.

7.2 Future Work

I have described three different, promising use cases of interferometry-polarimetry as well as their results, advantages, and disadvantages. I now describe their possible expansions.

Linear eigenmode analysis in TJ is effective for estimating comparative amplitudes of sidebands generated by coupling to toroidicity and shaping parameters such as elongation. It has been used to identify, with reasonable accuracy, the degree to which even-m modes should be visible on RIP by predicting the size of their toroidal sidebands, the dominant odd-m contributor. This modeling will continue to be benchmarked against both theoretical expectations and RIP data. The inverse aspect ratio scaling for odd-m modes will be better understood. Elongation scalings for both odd- and even-m modes will be performed; so far,

these scalings are complicated by boundary conditions that change the sign of B_{θ} near the outboard midplane to conserve angular momentum. In addition, TJ can be used to calculate Δ' , the resistive stability parameter. TJ makes two approximations that DCON does not make: it linearizes the MHD equations, and it generates its own equilibrium rather than taking in an experimental EFIT. Regardless, it is likely to produce more accurate results for equilibrium stability than ideal analysis.

In the cases demonstrated in this thesis, the line integrals of the eigenfunctions were calculated from the output data, which required coordinate transforms that introduced error to the model. A synthetic RIP diagnostic is planned for a further upgrade of TJ, which will be helpful for obtaining the most accurate sideband amplitudes. The RIP/synthetic coil model may be applied to more shots and times to further assess the linear contribution to mode amplitudes. For example, the tearing mode in shot #180704, asserted to have m, n = 6, 3[11], should be expected to have low amplitude when considering TJ cylindrical and possibly even shaped models. It is clearly detected with RIP and relatively strong compared to the coils, so this indicates a strong effect on RIP amplitude from mode localization. An alternative interpretation, related to the mode's strength on RIP and since the coils did not identify the mode number clearly, is that the early-detected mode has m, n = 5, 3. Further comparison to TJ models may be able to resolve the mode number question. Also of note is that in linear TJ models of shaped plasmas, there is significant poloidal structure near the edge for the entire poloidal circumference of the plasma. This structure is generated by shaping-induced sidebands and expected to be detected by the sensing coils. Mode amplitudes from the poloidal coil array may be compared to output values from TJ to determine how much of the modeled poloidal structure exists and is detectable in experiment. Beyond further use of TJ, I would like to expand my eigenfunction models to encompass nonlinear effects such as interactions between modes. Nonlinear codes such as Nimrod [12] will be useful for such modeling.

Future experimentation with RIP on DIII-D will encompass as many scenarios as possible

to add to a database of examples in which RIP shows advantages, or disadvantages, with respect to the coils. This database will include IBS, QH-mode, and other previously discussed scenarios but also other high-performance scenarios such as wide-pedestal QH-mode and high- β_p . This will also include inner-wall limited plasmas, ideally configured to produce less impurity radiation and increase plasma susceptibility to tearing modes compared to the experiments covered in this thesis. Boronization may be helpful in increasing the robustness of the wall to heat fluxes experienced in IWL. Using improved toroidicity and elongation scalings in TJ as well as a built-in synthetic RIP diagnostic, the expected shaping components of RIP data in the experiments described here will also be calculated and compared to the experimental line-integrated mode amplitudes.

EHO dissipation through coupling, discovered using RIP as described in this thesis, is a concern for future QH-mode plasmas. I posit that if QH-mode is transiently lost, tearing modes can couple to a returning EHO and inhibit QH-mode. I posit also that coupling to tearing modes during sustained QH-mode could cause the EHO to be lost, as coupling within the EHO is relatively weak. Recent predictive modeling advances [13, 14] may allow specific study of tearing mode effects on EHOs. While long-range tearing mode interactions are immediately relevant to QH-mode, their relevance may extend to other scenarios with localized tearing modes, edge fluctuations, or turbulence. These findings illustrate the need to reduce coupling risk for higher-order tearing modes, particularly in advanced tokamak scenarios where the m, n = 2, 1 mode and its acute risk to the plasma have been avoided. Coupling's role in EHO disappearance motivates use of differential rotation, electron cyclotron current drive, and other control techniques to reduce detrimental interactions in ITER or a fusion pilot plant [15–17]. QH-mode is robust to ECCD, and ECCD has been used successfully to modify density and temperature profiles in the doublebarrier configuration [16]. Injected neutral beam power can be used to offset the reduction in stored energy caused by ECCD [16]. Since $\mathbf{E} \times \mathbf{B}$ flow shear is vital to maintaining QH-mode, strengthening the shearing rate may also strengthen coupling and make QH- mode more robust. In ELMy H-mode in EAST, higher $\mathbf{E} \times \mathbf{B}$ shear was found to increase summed bicoherence across the turbulence spectrum. In BOUT++ [18] simulations of similar conditions, shear suppressed the ballooning mode [19]. Diagnostics such as RIP that are sensitive to fluctuations resonant in the core will be vital to measuring core-edge interactions, as core-resonant modes may not be detected by sensing coils. Strong bicoherence within the EHO might serve as a marker for robust QH-mode, while coupling to tearing modes might be a warning sign that QH has become marginal. Future work will investigate more cases of coupling in QH-mode to determine thresholds for EHO persistence, both with and without tearing modes.

Further analysis of nonlinear coupling will incorporate short-lived modes through wavelet analysis, which has been used successfully to measure ELM spectral content [20] and nonlinear coupling of Alfvén eigenmodes (AE) on the millisecond scale on DIII-D [21]. Wavelet methods may be useful to study tearing mode-ELM interactions, which occur on a similar timescale to AE coupling. The goal of this research will be to identify a potential link between tearing mode seeding and either coupling within ELMs or coupling between tearing modes and ELMs. Wavelet analysis may also be useful for measuring transient couplings between longer-lived modes, such as tearing mode frequency jumps associated with sawtooth precursors and crashes.

Bibliography

- [1] J. Chen et al. "Faraday-effect polarimeter diagnostic for internal magnetic field fluctuation measurements in DIII-D". Rev. Sci. Instrum. 87.11 (2016), 11E108.
- [2] R. Fitzpatrick. "Calculation of tearing mode stability in an inverse aspect-ratio expanded tokamak plasma equilibrium". *Physics of Plasmas* 31.10 (2024), p. 102507.
- [3] A. H. Glasser. "The direct criterion of Newcomb for the ideal MHD stability of an axisymmetric toroidal plasma". *Physics of Plasmas* 23.7 (2016), p. 072505.
- [4] L. L. Lao et al. "Equilibrium analysis of current profiles in tokamaks". *Nuclear Fusion* 30.6 (1990), p. 1035.
- [5] D. P. Brennan et al. "Tearing mode stability studies near ideal stability boundaries in DIII-D". Physics of Plasmas 9.7 (2002), pp. 2998–3006.
- [6] F. Turco et al. "Sensitivity of transport and stability to the current profile in steady-state scenario plasmas in DIII-D". *Physics of Plasmas* 19.12 (2012), p. 122506.
- [7] D. M. Meade et al. Recent TFTR results. Tech. rep. Princeton University, 1991.
- [8] T. N. Carlstrom et al. "Design and operation of the multipulse Thomson scattering diagnostic on DIII-D". Review of Scientific Instruments 63.10 (1992), pp. 4901–4906.
- [9] J. G. Chen et al. "Impact of $E \times B$ shear flow on low-n MHD instabilities". *Physics of Plasmas* 24.5 (2017), p. 050704.
- [10] F. Liu et al. "Nonlinear MHD simulations of QH-mode DIII-D plasmas and implications for ITER high Q scenarios". *Plasma Physics and Controlled Fusion* 60.1 (2018),

- p. 014039.
- [11] M. D. Pandya et al. "Early internal detection of magnetic tearing and implications for tokamak magnetohydrodynamic stability". *Physics of Plasmas* 31.7 (2024), p. 070706.
- [12] C. R. Sovinec et al. "Nonlinear magnetohydrodynamics simulation using high-order finite elements". *Journal of Computational Physics* 195.1 (2004), pp. 355–386.
- [13] A. Cathey et al. "Non-linear MHD investigations of high-confinement regimes without type-I ELMs in ASDEX Upgrade and JT-60SA". Nuclear Fusion 64.9 (2024), p. 096003.
- [14] Z. Liang et al. "Predictive nonlinear MHD simulations of quiescent H-mode plasma in the HL-3 tokamak". *Physics of Plasmas* 32.1 (2025), p. 012502.
- [15] R. J. La Haye et al. "Control of neoclassical tearing modes in DIII-D". *Physics of Plasmas* 9.5 (2002), pp. 2051–2060.
- [16] T. A. Casper et al. "Density and temperature profile modifications with electron cyclotron power injection in quiescent double barrier discharges on DIII-D". *Plasma Physics and Controlled Fusion* 48.5A (2006), A35.
- [17] N. J. Richner et al. "Use of differential plasma rotation to prevent disruptive tearing mode onset from 3-wave coupling". *Nuclear Fusion* 64.10 (2024), p. 106036.
- [18] B. D. Dudson et al. "BOUT++: A framework for parallel plasma fluid simulations".

 *Computer Physics Communications 180.9 (2009), pp. 1467–1480.
- [19] D. F. Kong et al. " $E \times B$ flow shear mitigates ballooning-driven edge-localized modes at high collisionality: experiment and simulation". Nuclear Fusion 59.1 (2019), p. 016016.
- [20] F. M. Poli, S. E. Sharapov, S. C. Chapman, JET-EFDA Contributors, et al. "Study of the spectral properties of ELM precursors by means of wavelets". *Plasma Physics* and Controlled Fusion 50.9 (2008), p. 095009.
- [21] G. Riggs et al. "Time-resolved biphase signatures of quadratic nonlinearity observed in

coupled Alfvén eigenmodes on the DIII-D tokamak". Physics of Plasmas 31.4 (2024), p. 042305.

Appendix A

Resources and Shot Plan: 2024-34-03

This Appendix gives the Resources and Shot Plan sections of the DIII-D "miniproposal" written for Experiment 2024-34-03, results from which are described in Chapter 5. The sections presented below are reproduced from the contingency miniproposal. Bold and strikethrough refer to differences between the contingency and the original due to a better understanding of limitations from the previous experimental day. The "Appendix" mentioned in the Resources section refers to the Beam Plan.

Resources

<u>Tokamak</u>: All discharges will be run with standard plasma current and **standard** toroidal field. Initial shape will correspond to target shot #**198614** as specified in Section 3. Plasma magnetic axis height will be swept from z = +10 cm to -10 cm.

NBI:

See Appendix for exact beam settings and timings.

30L and at least three other beams are essential, with preference to 330L and 330R if vertical CER is operational, and whichever 150 is optimal for BES that day if BES is operational. All beams aside from 30R are requested. 30R is not requested.

30L should run at 81 kV for all shots. If 330L, 330R, and/or the optimal 150 are available, they should be run at 75 kV for all shots, with 330R on a 50% duty cycle. The other 150 and 210R should be run at 0-75 kV depending on the shot. 210L should be run at 0 or 70 kV depending on the shot and time if available.

Initial source voltages should match reference shot #198614. The 150 beams will be positioned on-axis. The 210 beams will be run in the co-Ip direction. Voltages will be changed throughout the day and may be modulated by the PCS in real time to maintain steady rotation profiles.

No other heating is requested.

Required Diagnostics:

Operational diagnostics: magnetics, CO2 interferometer

Profile diagnostics: CER (tangential). At least one of core Thomson scattering and reflectometry must be operational.

Other diagnostics: RIP. At least one of ECE-I, BES, and DBS must be operational.

Important Diagnostics:

Operational diagnostics: filterscopes, core SPRED

Profile diagnostics: ECE, high-res ECE (for piggyback), CER (vertical), Thomson scattering (core, tangential), profile reflectometry

Edge diagnostics: ECE-I, BES (in near-edge, fully inside SOL), DBS, fast SXR

Other diagnostics: RIP toroidally separated chord (TRIP), fast magnetics from 500ms

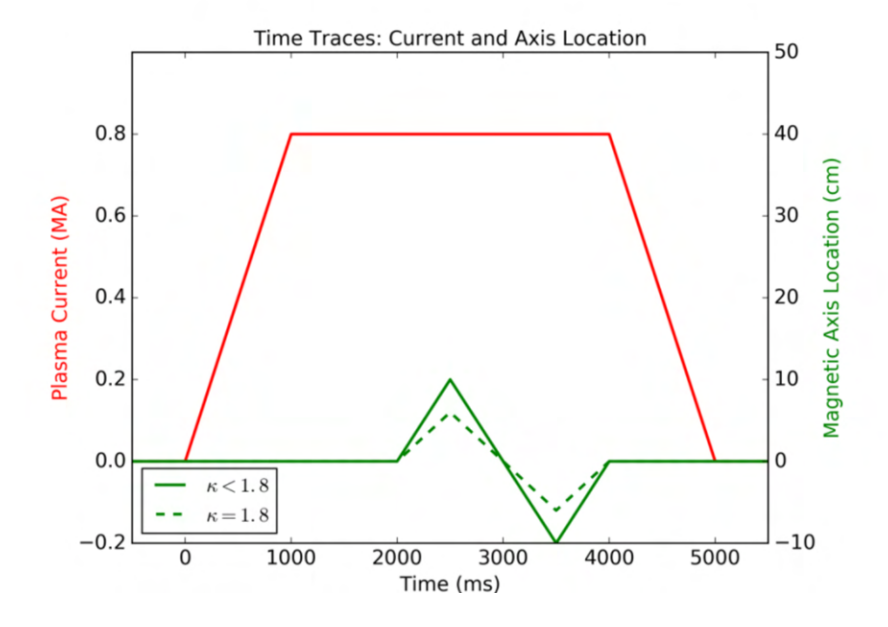
<u>Desired Diagnostics:</u> UF-CHERS, MICER

Other: Gas system should be the standard configuration with deuterium in GASA. Error field correction should be in the standard configuration. All cryopumps will be required to be on at helium temperature.

Experimental Plan

- 1. Initialize circular shot and NBI power benchmarks based on shot #198614 (4-8 shots)
- 1.1. Recreate target shot #**198614**. (1-2 shots)
- 1.2. Raise the density target to 4×10^{19} m⁻³ and drop minor radius to 0.54. Scan NBI voltages. Sweep the magnetic axis in each shot from z = 0 to +10 cm from 2000 to 2500 ms, then from +10 to -10 cm from 2500 to 3500 ms, then from -10 cm to 0 cm from 3500 ms to 4000 ms. Exact beam timings are **listed in the Appendix** and include some power early to avoid locked modes. Time traces of axis location are shown in Figure 1. (2-6 shots)
 - 1.2.1. NBI configuration #1: lowest beam power
 - 1.2.2. NBI configuration #2: highest beam power
 - 1.2.3. NBI configuration #3: only if 1.2.1 and 1.2.2 successfully run and show marked differences
 - 1.2.4. NBI configuration #4: only if 1.2.1, 1.2.2, and 1.2.3 successfully run and show marked differences

Decision Point 1: Select two beam settings to use in the next steps: 1. The setting with the richest MHD (tearing), either the most modes or the strongest modes with the choice to be made the day of experiment, and 2. The setting with the lowest beam power that still induces modes aside from sawteeth, or NBI configuration #1 if modes are induced in only one configuration. If no modes are induced at all, use configurations #1 (0 on extra beams) and #4 (75 on extra beams). If modes are induced and the richest MHD/lowest power are the same configuration, use the next highest beam power as the second setting.



Above: A time trace of the sweep in plasma magnetic axis location for every shot during and after Step 1.2, with plasma current as a timing reference. Note that the sweep height is reduced for the highest elongation.

- 2. Scan rotation and plasma shape for NBI power values chosen in Decision Point 1 (4-8 shots)
 - 2.1. Scan rotation using the NBI configurations found in step 1.2, elongation of 1.7, and current of 1.27 MA. Reduce sweep height if needed to fit the plasma. (2-4 shots)
 - 2.2. Skip 1.6 as that was completed the previous experimental day with good shape response and RIP data. If time permits and the plasma runs with good RIP data, repeat step 2.1 for elongation of 1.4 and current of 0.94 MA. Optionally, if another elongation range has particularly rich MHD, investigate it instead. (2-4 shots)

If shot disrupts, stop performing sweep, decrease density, and/or move to the next step, depending on the cause of the disruption. If shot encounters a locked mode, add extra beam power from 150 ms onward. One beam will be applied early by default.

Check RIP after every shot before starting up for the next one. If RIP is having trouble, lower density target to $3.5 \times 10^{19} \, \text{m}^{-3}$ before troubleshooting further.

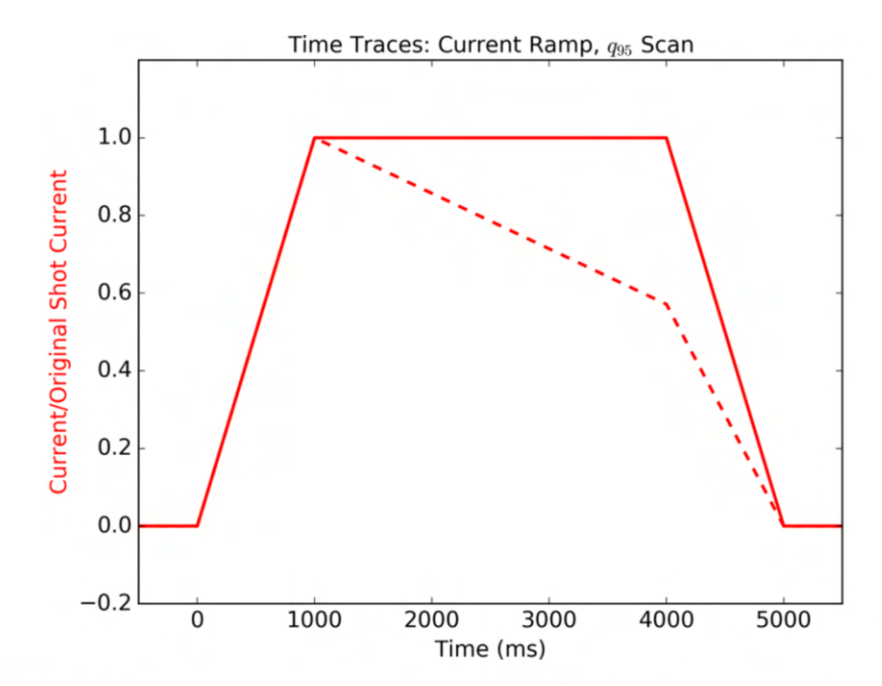
If shot does not show MHD, decrease I_p to 0.6 MA for $\kappa = 1.25$. To maintain consistent q_{95} across elongations, the corresponding currents for the higher elongations will change to:

- 1. 0.95 for $\kappa = 1.7$
- 2. 0.705 for $\kappa = 1.4$
- 3. Any other values investigated: see SL

At this point we have met our main goal – following points desirable for documentation, more complete measurement, or useful extensions

Decision Point 2: If time is available for extensions, select the combination of NBI power and elongation values associated with most interesting tearing activity as the basis for steps 3-4. Any of steps 3-5 may be prioritized at this time subject to SL preference.

- 3. Using the shot from Decision Point 2: modify triangularity, enforce up-down asymmetry (0-4 shots)
 - 3.1. Change upper plasma triangularity to **0.2** and change lower triangularity to **0.2**. Use the NBI power and elongation values associated with richest tearing activity and perform the vertical sweep as in step 2. (0-2 shots)
 - 3.2. Repeat Step 3.1 for upper triangularity of 0.1 and lower triangularity of **0.2**. (0-1 shots)
 - 3.3. Repeat Step 3.1 for upper triangularity of **0.2** and lower triangularity of 0.1. (0-1 shots)
- 4. Recreate the shot from Decision Point 2 with q_{95} rising steadily from 4 to 7 after 1000 ms (current rampdown from $I_{p,shot}$ to $I_p = \frac{4}{7}I_{p,shot}$, see figure below) to vary MHD susceptibility and triggers (0-2 shots)



5. Return to Steps 2-3 and repeat shots or increase density for any elongation/triangularity ranges with particularly strong, rich, or variable MHD. (0+ shots)

Yang piggyback: High-res ECE will be tuned to the q=2 surface throughout. No additional shots are requested.

Total 12-16 shots

Beam Plan: By Beam

30L: 1100-4000 ms. 81 kV in every shot.

30R: Not requested.

150L: Not operational.

150R: 900-4000 ms. 75 kV in every shot.

210L: This beam starts early to prevent locked modes and burn off any residual graphite. Lower to a maximum of 70 kV to let it run the entire time.

Steps 1, 3, and 4: 150-1200 ms, 70 kV. Turn off at 1200 ms.

Step 2: 150-4000 ms, 70 kV.

210R: 1050-4000 ms. 0, 75, 65, 50 kV.

330L: 1000-4000 ms, 0, 75, 65, 50 kV.

330R: 1000-4000 ms, 50% duty cycle with a 20ms period. 75 kV in every shot.

Beam Plan: By Time

150: Turn on 210L at 70 kV.

900: Turn on 150R at 75 kV.

1000: Turn on 330R at 75 kV with a 50% duty cycle and a 20ms period.

1050: Skip this for step 1. Turn on 210R at 75 kV if step 2, 65 kV if step 3, or 50 kV if step 4.

1100: Turn on 30L at 81 kV.

1200:

- 1. Steps 1 and 3-4: Turn off 210L.
- 2. Step 2: Do not make any change. 210L will run through at 70 kV.

4000: Turn off all beams.

If the working maximum for a beam is lower than the designated value for the given step, set that beam to the working maximum.

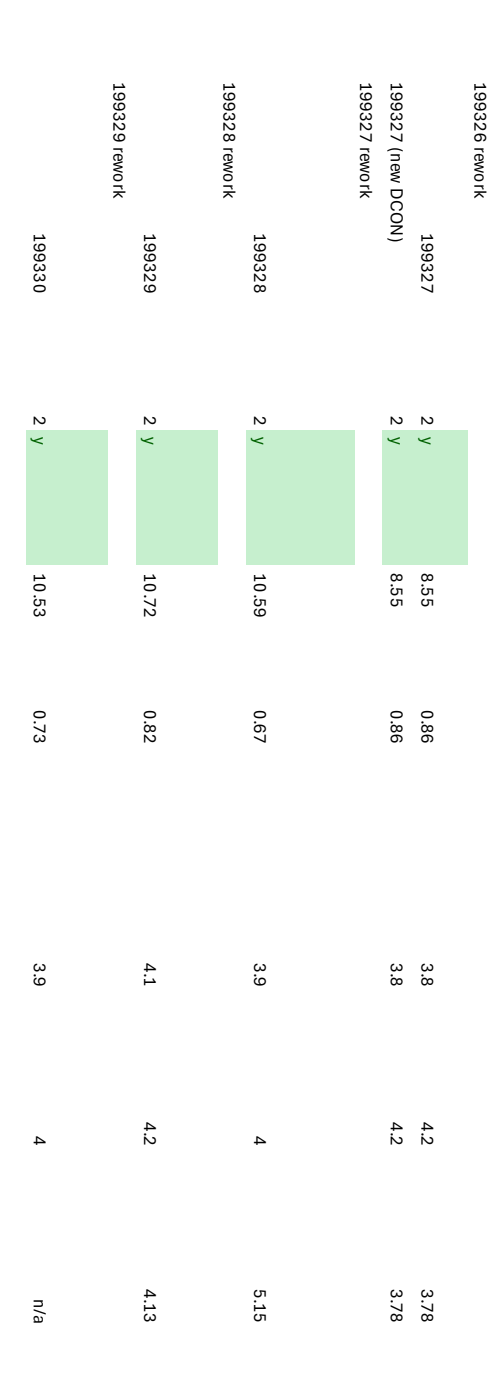
Appendix B

Database Spreadsheet: 2024-34-03

This Appendix gives the original spreadsheet of descriptive notes taken for each shot in series 2024-34-03, described in Chapter 5. These notes comprise shot parameters, tearing mode descriptions, and notes on the progress of each shot's kineticEFIT and DCON runs.

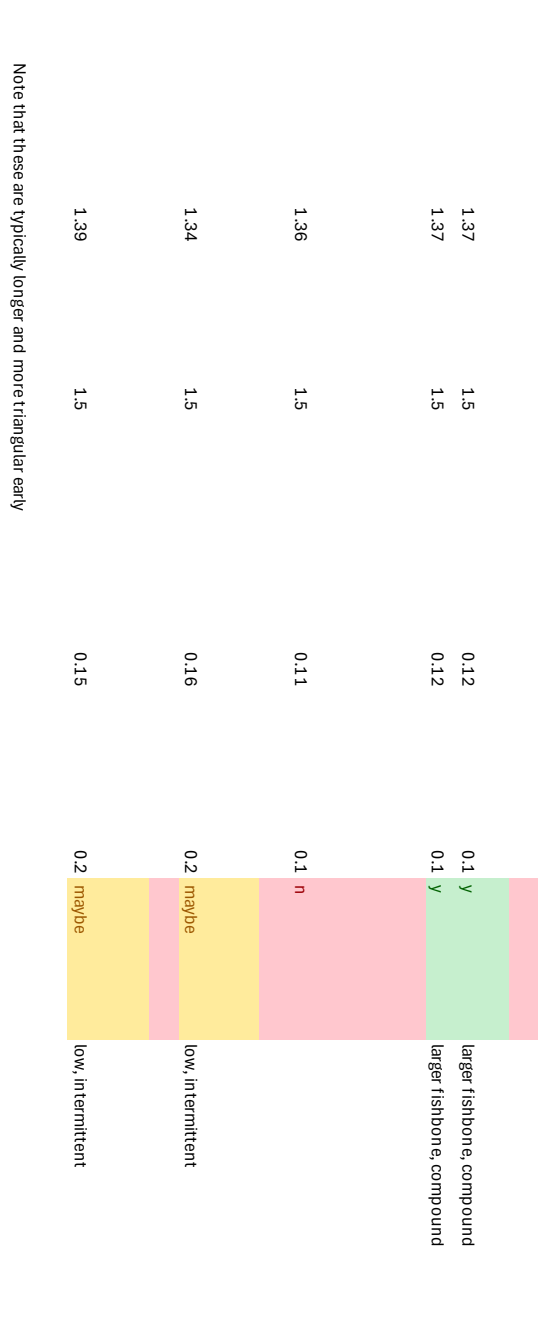
																			Shot Number
199319	199318	198629	198628	198627	198626	198625	198624	198623	198622	198621	198620	198619	198618	198617	198616	198615	198614	198613	Series
N	2	1	ц	ц	<u> </u>	_		<u>ц</u>	ш	ᆸ	ь	_		1	<u> —</u>	1	Д	Н	
2 y	п	partial	×	<	<	ם	×	partial	1 partial	1 partial	D	ם	Y	Ψ	Ψ	ח	У	V	Survived?
5.69	2.06	5.43	9.29	9.53	9.45		9.40	9.35	9.54	9.34	6.85	6.79	8.13	8.02	7.67	6.17	7.64	6.71	Beam Power
0.80	0.44	0.84	0.81	0.83	0.81	0.01	0.81	1.14	1.19	1.19	1.13	1.14	0.69	0.80	0.89	0.94	0.81	0.81	Current
					(1)										(P		N		Density (2000)
2.5			4.5	4.4	3.9		4.6		5.5				4.8	σ	5.1		2.5	2.5	Density (2000) Density (3000)
2.5			4.5	4.5	4.1		3.8						4.9	5.1	4.9		2.7	2.5	q95_02er (3000)
n/a	n/a	n/a	3.96	3.63	4.21	n/a	3.99	n/a	n/a	n/a	n/a	n/a	5.58	n/a	n/a	n/a	n/a	4.52	Ö.

19 199326 (new DCON)			199323 rework	199322 rework		19 199321 (new DCON) 199321 (new EFIT)	
199326 V)	199325	199324	199323		199322	199321 N)	199320
2 2	2	2	2 <	2 <	N Y	N N	Ν
y y	Ψ					ч ч	Ψ
7.15 7.15	10.80	ထ ယ ယ	& .3 3	10.54	10.54	6.97 6.97	6.08
1.27 1.27	1.27	1.27	0.80	0.81	0.81	0.80	0.91
3.9 3.9	ហ ហ	5.1	ယ္	4.5	4.5	ω ω ο ο	4.1
4.8	6 .4	დ	4.3	4.5	4.5	4 4 3	4.4
2.82 2.82	2.93	2.85	4.06	4.19	4.19	4 4	4.04



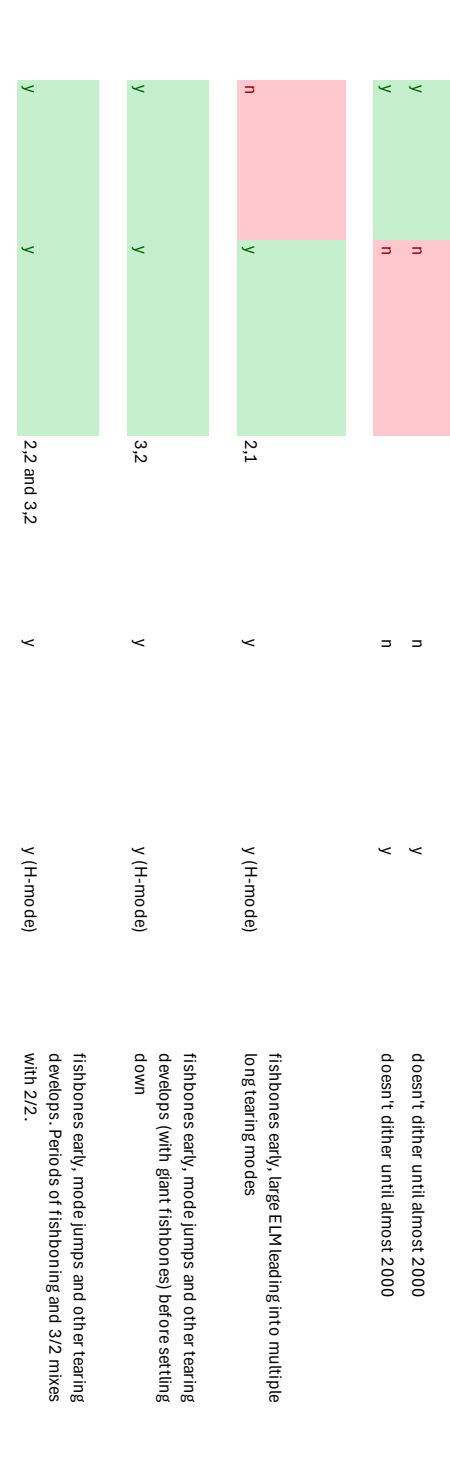
1.27 1.25	1.25	1.6	1.37 1.6	1.3 1.6	1.5 1.6	1.6	1.5 1.6	1.6	1.7	1.7	1.8	1.8	1.26 1.25	1.27 1.25	1.26 1.25	1.25	1.3 1.25	1.3 1.25	Etongation (3000) Godi Etongation Op	Goal Elongation
0.084			0.16/0.2	0.16	0.14		0.15						0.13	0.087	0.085		0.13	0.12	opper manguanty (3000) Goat manguanty	
0.1 y		0.3 y	0.3 y	0.1 y	0.1 maybe	0.1 y	0.1 y	0.1 y	0.1 n	0.1 n	0.1	0.1	0.1 y	0.1 y	0.1 y	0.1	0.1 y	0.1 y	Sawree III ?	Courtootho
small		small	giant, blurry fishbone	giant, blurry fishbone	low, intermittent		giant, blurry fishbone	giant					small/not compound , fishbone early	weak fishbone	small/compound, fishbone early		small/compound, fishbone early	small/compound	оамион туре	Douglas Tuno

1.47 1.47	1.49	1.48	1.37	1.37	1.37	1.37	1.36
1.7 1.7	1.7	1.7	1.25	1.25	1.25	1.25 1.25	1.25
0.07 0.07	0.08	0.07	0.11	0.11	0.11	0.11	0.11
0.1 y 0.1 y	0.1 y	0.1 y	0.1 y	0.1	0.1	0.1 y 0.1 y	0.1 y
				0.1 maybe	0.1 maybe		
giant, compound giant, compound	giant, compound	giant, compound	larger fishbone, compound	low, in termittent	low, in termittent	clear fishbone, compound clear fishbone, compound	clear fishbone, compound



п	n	n	Y	У	n	ח	V	n	n	n	n	B	У	V	٧	п	Y	3	Fishbones?
п	п	n	D	n	у	D	=	У	У	У	a a	D	n n	Э	ם	п	П	3	Tearing Modes?
					3,2			2,1 locking	2,1 locking	2,1 locking									Tearing Mode Type
3	n	n	n	n	J	n	n	n	n	ח	ח	n	n	ח	ח	п	ח	n	H-Mode Transition?
п	ח	п	Y	У	У		Y	3	D .	ח	III	n	n	n	II	J	J	n	Any Dalpha Dither?
no 30L		Francesca ECH attempt	EFIT 3000 vs 2600				shape wobbles												Notes





٧	п	п	٧	У	٧	n	٧	٧	~	У	п	n	٧	~	У	ח	~	٧	EFIT desired?
n/a	n/a	n/a	У	٧	У	n/a	٧	hold	hold	У	n/a	n/a	hold	hold	٧	n/a	Y	У	EFIT started?
n/a	n/a	n/a	hold	hold	hold	n/a	TRANSP	hold	hold	hold	n/a	n/a	hold	hold	hold	n/a	hold	n/a	Transport completed?
n/a	n/a	n/a	hold	hold	hold	n/a	(Z03) M01	hold	hold	hold	n/a	n/a	hold	hold	hold	n/a	hold	n/a	TRANSP ID
		n/a	n/a	n/a	n/a	n/a	low (0 best but really bad and noisy)	n/a	n/a	n/a	n/a	n/a	n/a	n/a	n/a	n/a	n/a	n/a	Fast Ion Diffusion
n/a	n/a	n/a	hold	hold	hold	n/a	hold probably	hold	hold	hold	n/a	n/a	hold	hold	hold	n/a	hold	n/a	EFIT completed?

Y	٧	٧	< <
hold	<	¥	y y
hold	TRANSP	TRANSP	TRANSP
hold	Z01-Z03, M01-M03, M04	Z01-Z05, M01	Z06-Z10, M01 Z06-Z10, M01
n/a	time-dependent (0-10000, may want a 2000 to fill in the gaps if it's bad)	time-dependent	time-dependent time-dependent
hold * first attempt done, ** how quality	<	٧	v v

٧	Υ.	~	~ ~
hold	¥	٧	ν ν
hold	TRANSP	TRANSP	TRANSP TRANSP
hold	Z01-Z03, M01-M03, M04	Z01-Z05, M01	Z06-Z10, M01 Z06-Z10, M01
n/a	time-dependent (0-10000, may want a 2000 to fill in the gaps if it's bad)	time-dependent	time-dependent time-dependent
hold * first attempt don ** how guality	nta y	Ψ.	~ ~

n/a	n/a	n/a				n/a					n/a	n/a				n/a			EFIT Start
_	_	_	1120	1120	1120	_	1280	1120	1120	1120	_	_			1100	_	2160	1120	
n/a	n/a	n/a	400	400	400	n/a	398	360	192	170	n/a	n/a			400	n/a	376	200	EFIT End
		n/a	4000 hold	4000 hold	4000 hold	n/a	3980 ???	3600 hold	1940 hold	1700 hold	n/a	n/a	hold	hold	4000 hold	n/a	3760 hold	2000 n/a	Next Step
																			:ep
																			D
																			DCON started?
																			DCO
																			DCON Finished?
																			DCON n=1 dW
																			=1 dW

1120	1120	1760	1480	1120	1380	1380		1120	1120	1120
4000 DCON	4000 done	4000 done	4000 done	4000 done	4000 DCON	4000 done including n=4	EFIT refining	4000 DCON	4000 done	4000 done
~ ~	<	≺	Y	¥		Ψ.		У	~	y
ų	<	٧	У	٧		Υ			У	У
illossy probably too illossy	messy probably too messy	almost nothing	not consistent	rises to 2000 then all over the place		always a mess			2ish except for a couple of blips, loses points in the middle	2-2.5 early, loses a lot of points 2000- 3000 and eventually rises to 2.5-3

1120 4000 hold in in progress	1120 2400 done y y almost r	low patc up, som 1120 4000 done y y otherwi	done justed as including n=4 but i don't good, ~ 1120 4000 think so] y y in them 1120 4000 DCON y
	y almost nothing	low patch -3 1100-1600ish then back up, some noise but above 1 throughout otherwise	good, ~2 to 2000, loses a lot of points y in the middle, good ~2.5 after 3000

noisy throughout, small patch of coherency around 1500 (>exp)	many points missing and noisy	dip at 1600, starts completely oscillating at 2000	steadily drops to 2000 when it hits exp and then stays there	dips and then starts oscillating after 1800	starts high and drops to near exp at 2000 starts high and drops to near exp at 2000 then hovers around there
1-2ish except for a quick drop at 1500 and increasing noise after 2500	1.5 ish except for some oscillations and a gap in the middle	quite consistent to 3200, 1.5-2	1 rising to 1.5, some oscillations	no major change when the n=2 mode arises but oscillates more when the n=2 mode jumps	1-1.5 throughout, losing points every so often 1ish throughout, losing points every so often
noisy throughout	noisy throughout	high and oscillatory	oscillates throughout, even early	dip at 1600 and again after 1800	usually high but oscillates, sometimes dropping to exp consistently high until 1600ish then noisy

followed exp to 1500 then got too noisy		consistently dropping until it rises just before 2000 and then goes oscillatory
almost nothing	also <0 in the low patch and high after	good just above 1 throughout, a few blips
noisy throughout		consistently well above exp until 2000 then oscillatory. A couple of blips early.

OCON n=3 dW
DCON n=3 beta
DCON n=4 dW
DCON n=4 beta

increasing noise after 2500	just above 1 except for some oscillations and gap in the middle	quite consistent to 3200, ~1	0.5-1 throughout, some oscillations	many points missing but stays steady throughout	just below 1 throughout, loses points	0.5-1 throughout, losing points every so often
noisy throughout	noisy throughout	high and oscillatory	oscillates throughout; first goes unstable when the early TM arises	oscillates throughout but quite high	exp	usually high but oscillates, sometimes dropping to exp
unused	just below 1 except for some oscillations and a gap in the middle; fewer points survive than n=2 and n=3	unused	unused	many points missing but stays steady throughout	unused	unused
unused	noisy throughout	unused	unused	oscillates throughout	unused	unused

almost nothing	not visible in low patch, otherwise tracks n=2 but lower	good just below 1 throughout, a few blips
noisy throughout		consistently well above exp until 2000 then oscillatory. A couple of blips early.
unused	unused	unused
unused	unused	unused

EFIT/TRANSP Notes

DCON Notes

30L not working after 2000. Segfaults in kfile creation when I try to do anything before that.

30L blocking, CER not reporting until
2160, CER tangential missing
n/a
30L working, MSE data exists, EFIT02 not
present. Ask Brian about how to do efit

#1 UPDATE it seems to be CER

30L working, MSE data exists, EFIT02 not present. Ask Brian about how to do efit #1 UPDATE it seems to be CER
30L working, MSE data exists, EFIT02 not present. Ask Brian about how to do efit #1 UPDATE it seems to be CER

EFIT02 present as it was re-run, but ER was not. CER was unusable after 1250ish; pause for now.

EFIT02 present as it was re-run, but ER

No EFITO2, but CER is usable
Redo the whole thing. TRANSP neutrons
are very messed up. UPDATE: it
happened again

was not. CER was unusable after 1250ish; pause for now.

CER unusable; pause for now.

CER unusable; pause for now.

no 30L and no CER. EFIT beyond 01 is not possible.

any particular part of the sawtooth cycle. n=1 beta dip matches the rise of compound sawteeth, suggesting the compound sawtooth is a genuine mode. N=2 and n=3 go unstable intermittently and don't appear to correspond to

Still better without current constraint. constraint problems were due to dither. Some ion densities go negative in

as well given it does dither and some

to 1e-8 about as easily as the other one pedestals are visible. UPDATE: it's getting using Lmode snapfile; this may not work

ONETWO. I wonder if the reduced current side note, try to save 1560 if at all possible. N=1 and n=2 thresholds are very very similar early. not accompanied by the beta limit drop!); also expected to be noisy, jumps down when the 3/2 starts (note the early part has 5/2 or 7/2 and is Run ends at 2500

rerunning 322 for 1e-8. Edge q is still got to 1e-5. Finish this, then consider

during the jog. Failed on 15000 and 1900, 20000 (1) likely due to server disconnect crash

5000-10000 debatable; 10000 is better Note that there is an n=3 tearing mode until 1900, the time of the first sawto oth-fishbone

All seem mostly stable by beta definitions

striking. What is happening at 1500? It's quite

EFIT is perfect

note that the drops below 0 in n=2 and n=3 in dW match up pretty well, both with each other in time and within the mode # in size

30L working, MSE data exists, EFIT02 not present. Ask Brian about how to do efit #1 UPDATE it seems to be CER